**TECHNISCHE
UNIVERSITÄT
DRESDEN**

Advances in Organic Displays and Lighting

Towards Planar Lithographic Integration of

Organic Light-Emitting Diodes

Dissertation
zur Erlangung des akademischen Grades
DOCTOR RERUM NATURALIUM

vorgelegt von

Simonas Krotkus
geboren am 28.10.1987 in Vilnius

Institut für Angewandte Physik
der Technischen Universität Dresden
2016

Abstract

This work focusses on the advances of organic light-emitting diodes (OLEDs) for large area display and solid-state-lighting applications. OLED technology has matured over the past two decades, aided by the rapid advances in development of the novel material and device concepts. State-of-the-art OLEDs reach internal efficiencies of 100% and device lifetimes acceptable for commercial display applications. However, further improvements in the blue emitter stability and the device performance at the high brightness are essential for OLED technology to secure its place in the lighting market. As the current passing through the device increases, a rapid decrease in OLED efficiency, so-called efficiency roll-off, takes place, which hinders the use of OLEDs wherever high brightness is required. In addition, white OLEDs comprising multiple emitter molecules suffer from the emission colour change as the operating conditions are varied or as the devices age. Despite side-by-side structuring of the monochrome OLEDs could in principle circumvent most of bespoke issues, the limitations imposed by the shadow mask technique, employed to structure vacuum deposited films, renders such approach impractical for fabrication of the devices on a large scale.

In order to address these issues, photolithographic patterning of OLEDs is implemented. Highly efficient state-of-the-art devices are successfully structured down to tens of micrometers with the aid of orthogonal lithographic processing. The latter is shown to be a promising alternative for the shadow mask method in order to fabricate the full-colour RGB displays and solid-state-lighting panels. Photo-patterned devices exhibit a virtually identical performance to their shadow mask counterparts on a large scale. The high performance is replicated in the microscale OLEDs by a careful selection of functional layer sequence based on the investigation of the morphological stability and solubility of vacuum deposited films. Microstructured OLEDs, fabricated in several different configurations, are investigated and compared to their large area counterparts in order to account for the observed differences in charge transport, heat management and exciton recombination in bespoke devices. The role of the Joule heat leading to the quenching of the emissive exciton states in working devices is discussed. Structuring the active OLED area down to 20 μm is shown to improve the thermal dissipation in such devices, thus enabling the suppression of the efficiency roll-off at high brightness in white-emitting electroluminescent devices based on side-by-side patterned OLEDs.

Kurzfassung

Die vorliegende Arbeit beschäftigt sich mit den neusten Errungenschaften von organischen Licht-emittierenden Dioden (OLEDs) für großflächige Beleuchtungs- und Displayanwendungen. Die OLED-Technologie hat sich in den letzten zwei Jahrzehnten, begünstigt von neuartigen Material- und Bauteilkonzepten, weit entwickelt. Im aktuellen Stand der Technik erreichen OLEDs sowohl interne Effizienzen von 100% als auch Lebensdauern die für die kommerzielle Nutzung in Displays ausreichend sind. Nichtsdestotrotz sind weitere Verbesserungen für die Stabilität blauer Emitter und die Leistungsfähigkeit bei hohen Leuchtstärken erforderlich, damit die OLED Technologie ihren Platz auf dem Markt behaupten kann. Mit steigender Stromstärke, die durch ein solches Bauteil fließt, sinkt die Effizienz rapide (der sogenannte Effizienz-Roll-Off), was die Nutzung von OLEDs verhindert, wann immer hohe Leuchtstärken erforderlich sind. Zusätzlich verändern weiße OLEDs ihre Farbkomposition durch die unterschiedliche Alterung der unterschiedlichen Emittermoleküle oder veränderte Einsatzbedingungen. Obwohl die laterale Strukturierung nebeneinander aufgebrachter, monochromer OLEDs diese Probleme umgehen könnte, ist diese Herangehensweise durch die aktuelle Schattenmasken-Technologie limitiert, welche zur Strukturierung vakuumprozessierter Dünnschichten eingesetzt wird, und somit unpraktikabel für die Massenproduktion.

Um diese Problemstellungen zu umgehen, wird hier die photolithographische Strukturierung von OLEDs angewendet. Mithilfe der orthogonalen Lithographie können hocheffiziente Bauteile damit erfolgreich auf Größenordnungen von 10 µm strukturiert werden. Dies zeigt, dass die orthogonale Prozessierung eine vielversprechende Alternative für die Schattenmasken-Technologie darstellt und für die Herstellung von RGB-Displays und Beleuchtungspanelen geeignet ist. Photostrukturierte Bauteile zeigen dabei eine nahezu identische Leistungsfähigkeit zu solchen, die großflächig mittels Schattenmasken hergestellt wurden. Diese hohe Leistungsfähigkeit kann hierbei durch eine sorgfältige Auswahl der einzelnen funktionellen Schichten erreicht werden, welche auf Untersuchung von morphologischer Stabilität und Löslichkeit dieser Schichten basiert. Mikrostrukturierte OLEDs in verschiedenen Konfigurationen werden mit ihren großflächigen Gegenstücken verglichen, um beobachtete Abweichungen im Ladungstransport, der Wärmeverteilung, sowie der Exzitonenrekombination zu erklären. Die Rolle der Joule'schen Wärme, die zur Auslöschung der emittierenden Exzitonenzustände führt, wird hier diskutiert. Die thermische Dissipation kann dabei verbessert werden, indem die aktive Fläche der OLED auf 20 µm herunterstrukturiert wird. Folglich kann der Effizienz-Roll-Off bei hohen Leuchtstärken in lateral strukturierten weißen elektrolumineszenten Bauteilen unterdrückt werden.

Contents

List of Publications

Articles

1. Renata Karpicz, Skomantas Puzinas, Simonas Krotkus, Karolis Kazlauskas, Saulius Jursenas, Juozas V. Grazulevicius, Saulius Grigalevicius, and Vidmantas Gulbinas, "Impact of intramolecular twisting and exciton migration on emission efficiency of multifunctional fluorene-benzothiadiazole-carbazole compounds", *The Journal of Chemical Physics*, **134**(18), 204508, (2011).

2. Ramunas Aleksiejunas, Simonas Krotkus, Saulius Nargelas, Saulius Miasojedovas, and Saulius Jursenas, "Impact of doping on carrier recombination and stimulated emission in highly excited GaN:Mg", *Physica B: Condensed Matter*, **406**(15), 2990, (2011).

3. Saulius Miasojedovas, Christof Mauder, Simonas Krotkus, Arunas Kadys, Tadas Malinauskas, Kestutis Jarasiunas, Michael Hauken, Holger Kalisch, and Andrei Vescan, "High-excitation luminescence properties of m-plane GaN grown on $LiAlO_2$ substrates", *Journal of Crystal Growth*, **329**(1), 33, (2011).

4. Simonas Krotkus, Karolis Kazlauskas, Arunas Miasojedovas, Alytis Gruodis, Ausra Tomkeviciene, Juozas V. Grazulevicius, and Saulius Jursenas, "Pyrenyl functionalized fluorene and carbazole derivatives as blue light emitters", *The Journal of Physical Chemistry C*, **116**(13), 7561, (2012).

5. Simonas Krotkus, Saulius Miasojedovas, Saulius Jursenas, "Threshold of stimulated emission in GaN layers grown by various techniques", *Physica B: Condensed Matter*, **450**, 16, (2014).

6. Simonas Krotkus, Fabian Ventsch, Daniel Kasemann, Alexander A. Zakhidov, Simone Hofmann, Karl Leo, and Malte C. Gather, "Photo-patterning of highly efficient state-of-the-art phosphorescent OLEDs using orthogonal hydrofluoroethers", *Advanced Optical Materials*, **2**(11), 1043, (2014).

7. Simonas Krotkus, Frederik Nehm, Robby Janneck, Shrujan Kalkura, Alexander A. Zakhidov, Matthias Schober, Olaf R Hild, Daniel Kasemann, Simone Hofmann, Karl Leo, and Sebastian Reineke, "Influence of bilayer resist processing on pin OLEDs: towards multicolor photolithographic structuring of organic displays", *Proceedings of the SPIE, Organic Photonic Materials and Devices XVII*, 93600, (2015).

8. Simonas Krotkus, Daniel Kasemann, Simone Lenk, Karl Leo, and Sebastian Reineke, "Adjustable white-light emission from a photo-structured micro-OLED array", *Light: Science and Applications*, **5**(7), 16121, (2016).

Patents

Daniel Kasemann, Simone Hofmann, Malte C. Gather, Simonas Krotkus, Fabian Ventsch, and Alexander A. Zakhidov, "Fotolithografieverfahren zum Herstellen organischer Leuchtdioden", DE 102014117096 A1, (2015).

Conference contributions

(Presenting author is underlined)

1. <u>Simonas Krotkus</u>, Fabian Ventsch, Daniel Kasemann, Alexander A. Zakhidov, Simone Hofmann, Karl Leo, and Malte C. Gather, "Photolithographic structuring of organic electroluminescent devices with state-of-the-art efficiency", *DPG Spring Meeting, Dresden, Germany*, oral presentation, (2014).

2. <u>Simonas Krotkus</u>, Fabian Ventsch, Daniel Kasemann, Alexander A. Zakhidov, Simone Hofmann, Karl Leo, and Malte C. Gather, "Highly-efficient organic light-emitting devices patterned via photolithography", *SPIE Photonics Europe, Bruxelles, Belgium*, invited talk, (2014).

3. <u>Simonas Krotkus</u>, Frederik Nehm, Robby Janneck, Shrujan Kalkura, Alex A. Zakhidov, Matthias Schober, Olaf R. Hild, Daniel Kasemann, Simone Hofmann, Karl Leo, and Sebastian Reineke, "Influence of bilayer resist processing on p-i-n OLEDs: towards multicolor photolithographic structuring of organic displays", *SPIE OPTO, San Francisco, USA*, oral presentation, (2015).

4. Simonas Krotkus, Daniel Kasemann, Simone Lenk, Karl Leo, <u>Malte C. Gather</u>, and Sebastian Reineke, "Photo-patterned two-color micro-OLED array for lighting applications" *MRS Fall, Boston, USA*, poster presentation (2016).

5. Simonas Krotkus, Tim Schaefer, Tobias Schwab, Fabian Ventsch, Daniel Kasemann, Alexander A. Zakhidov, Simone Lenk, Karl Leo, and <u>Malte C Gather</u>, "Orthogonal hydrofluoroethers enable photo-patterning of state-of-the-art phosphorescent small molecule OLEDs and deposition of outcoupling enhancement structures", *MRS Fall, Boston, USA*, poster presentation (2016).

1 Introduction

Since the dawn of modern organic light-emitting diodes (OLEDs) dating back more than two decades [1], the OLED technology based on thermally evaporated small-molecule organic films has experienced a rapid development, which culminated in a number of commercial applications, including OLED displays in smartphones, tablets and TVs. On the other hand, the structuring of OLEDs, i.e. the way devices are positioned and integrated into multi-component arrays, remained virtually unaltered. Namely, patterning of vacuum deposited films via shadow mask is employed, which results in serious limitations of the substrate size and display resolution which can be achieved. On the contrary, photolithography, which is a well established patterning technique in inorganic semiconductor and liquid crystal display (LCD) industries, enables parallel, high throughput and high resolution structuring, which can be scaled to large area substrates. State-of-the-art OLEDs comprise a multilayered structure, with each of the thermally evaporated layers representing certain functions within the device. Vacuum deposition enables precise control of the thickness and the deposition rate of each of the functional films, which allows to achieve the highest OLED performance in terms of efficiency and lifetime. This is because even slight deviations from the desired film thickness or quality results in a significant decline of OLED performance. However, photolithography is a wet-processing based technique, which requires multiple steps employing organic or water-based solvents, etchants and photoresists, which are known to be detrimental to the OLEDs, in order to achieve pre-determined structures. For this reason, photolithography was seldom used to structure organic electronic devices in the past. Recently, however, a modified lithographic approach, coined orthogonal processing, started to gain interest in organic semiconductor community [2, 3]. It is based on using highly fluorinated materials as resist layers and as development solvents, which are shown to be compatible with many organic molecules, thus enabling photolithographic structuring of organic semiconductor devices. The aim of this work is to gain the understanding of the prerequisites for lithographic structuring of state-of-the-art OLEDs and to reap the benefits by utilising the best of both worlds, i.e. highly efficient electroluminescence of vacuum deposited devices, and scalability and high resolution provided by photolithography.

Following this introduction, Chapter 2 summarises the main theories and physical mechanism employed to describe the electrical and optical response of organic solid films, the fundamental building blocks of modern organic electronic devices. The main differences, relevant for the optoelectronic systems, between the "classical" group IV and III-V semiconductors and their organic molecule based counterparts are highlighted. Chapter 3 gives a brief overview of the classical description of the electromagnetic field based on partial differential Maxwell's equations, which form the basis for the understanding and prediction of most of the optical phenomena relevant for OLEDs. Two specific cases, i.e. guided optical waves and electromagnetic field interactions with charges, are described in more detail as they represent the two major optical loss channels in organic electroluminescent devices. Based on the fundamental principles described in Chapters 2 and 3, Chapter 4 presents the main working principles behind the operation of state-of-the-art OLEDs. Current research efforts, especially in developing novel emitter systems and light extraction structures, as well as the main current and future OLED applications are discussed. Chapter 4 closes with a brief discussion on the current limitations of the shadow mask patterning technique, which is followed by the overview of the alternative structuring methods of OLEDs. Chapter 5 covers the functional materials and the experimental techniques, including sample fabrication and characterisation procedures, used in this work.

Chapter 6 describes the initial efforts of patterning organic semiconductor films and simple single heterojunction devices, based on archetypal Alq$_3$ emitter, using orthogonal photolithography. Simple proof-of-concept devices serve as a platform to investigate the impact of certain lithographic processing steps. The doped p-type transport layer and a thick metal cathode are shown to be essential in order to successfully demonstrate the photo-patterned OLEDs fabricated in bottom-emitting architecture. Based on these findings, state-of-the-art p-i-n OLEDs are fabricated and investigated in Chapter 7. The large area devices are fabricated by photolithography and investigated in terms of the electrical, optical and lifetime parameters in order to compare their performance to the reference OLEDs fabricated by the shadow mask technique. It is followed by the study on microscale OLEDs structured down to the dimensions relevant for display applications. Chapter closes with the investigation of the impact of the additional lithographic steps required to achieve full-colour OLED displays. Chapter 8 discusses the investigations of white light generation from two-colour OLED array based on lateral alignment of fluorescent blue and phosphorescent yellow subunits fabricated using photolithography. Hansen solubility parameter approach is introduced for screening of the materials compatible with orthogonal processing. The possibility to tune emission colour of the optimised two-colour OLED array is investigated, as well as its colour stability at higher brightness. Chapter 9 focusses on the

role of the OLED dimension in determining the device performance, especially at elevated current density and brightness. While Joule heat is usually omitted when discussing the OLED efficiency decline at higher currents, a phenomena known as efficiency roll-off, a systematic study on the performance of large area and microscale devices, operated in DC and pulsed mode, show that thermal management plays an important role already in the milimeter scale devices. A better heat management attributed to the smaller OLED dimension enables demonstration of the suppression of efficiency roll-off at elevated currents in microstructured OLEDs, which is supported by an exciton recombination model including a Joule heat quenching term.

The final Chapter 10 summarises this work and aims to give an overview of the future prospects of the OLEDs fabricated by the orthogonal photolithography and the microstructured OLEDs in general.

2 Organic Semiconductors

This chapter summarises the main properties of organic semiconductors, starting from the basic molecular considerations. Section 2.1 describes intramolecular and intermolecular forces binding the molecules in organic semiconductor films. The resulting spectral properties of organic molecules in UV and visible range, relevant for device applications, are presented in Section 2.2. The concept of the exciton is introduced and is followed by the discussion about energy transfer in organic solids in Section 2.3. Section 2.4 summarises the main mechanisms and theoretical models of charge transport in organic semiconductors, which play a vital role in understanding the operation of organic electronic devices.

2.1 Molecular Bonding

Organic molecules is a loosely defined term to describe a vast class of compounds, which all have a common carbon backbone structure and often include additional common elements, such as hydrogen, oxygen, nitrogen, etc. Organic molecules, made out of tens, hundreds or even thousands atoms, are the basic structural elements of organic solids. Organic solids are characterised by a strong bonding inside the molecules and relatively weak and short-ranged forces binding different molecules together. Such mixture of strong and weak forces present in organic semiconductors, give rise to their distinct properties as compared to those of "classical" semiconductors such as Si or GaAs, whose electronic and optical properties are a result of the strong covalent interaction between the constituent atoms fixed in a crystal lattice. Due to the strong covalent intramolecular interactions, the molecular dimensions, vibrational frequencies and optical properties, such as emission or absorption of organic semiconductor films, are essentially those of the free molecules. Charge transport as well as energy transfer depend on the overlap of the conjugated π-π electron orbitals which give rise to the conductivity of organic films, and are influenced by intermolecular interactions. Crystal packing of the molecules depends on both intra- and intermolecular forces, which then can result in both highly-ordered crystalline films as well as amorphous solids.

What follows is a discussion about the main interactions on the atomic and molecular

level, relevant for understanding the structure and properties of organic semiconductor films. The treatment is mainly focussed on the low-weight organic molecules, which form the basis of modern organic optoelectronic devices. While another distinct class of materials researched since the 80's of the previous century [4], namely, conductive polymers, is omitted in this discussion, it is important to note, that the fundamental aspects of the mechanisms involved in explaining the physical properties are essentially identical between the two classes of materials. The main difference between low-weight small-molecules and conductive polymers arise when comparing the fabrication procedures of thin films, with the former being mostly deposited from a gaseous phase via sublimation [1](see Chapter 4), while the latter is based on a solution-processing. The following description is kept at a general level and is well-founded to a large extent for both small-molecule and polymeric materials.

2.1.1 Intramolecular Interactions

Electronic structure of the molecules is assessed by the quantum mechanical approaches, which are based on solving the *time-dependent Schrödinger equation*, which can be written in its general form as

$$i\hbar\frac{\partial\Phi_{\text{total}}(\boldsymbol{r},t)}{\partial t} = \hat{H}\Phi_{\text{total}}(\boldsymbol{r},t), \qquad (2.1.1)$$

where $\hbar = \frac{h}{2\pi}$ is the reduced Planck's constant ($h \approx 6.626 \cdot 10^{-34}$ m^{2}kg s^{-1}), $\hat{H}$ is the *Hamiltonian operator*, and $\Phi_{\text{total}}(\boldsymbol{r},t)$ is the wavefunction of the electron system, which contains all of the information about the spatial distribution of each electron at any instant of time t. Therefore, Eq. (2.1.1) represents a many-body problem, in which the electron-electron as well as electron-nucleus interactions have to be evaluated and, except for a few trivial cases, it is not possible in reality. For this reason, a number of approximations have to be introduced, in order to access the molecular states with the available computational resources. First of all, since the outer shell electrons (*valence* electrons) are less strongly coupled to the rest of the electronic system, they tend to interact more with the outer stimuli, and therefore are responsible for most of the chemical and optical properties of the molecules. Therefore, the problem is reduced to the calculation of the wavefunction only of the valence electron of the atomic constituents comprising the molecule in question. Secondly, the solutions which are constant in time (modes or orbitals), represented by the spatial wavefunction $\Phi(x,y,z) = \Phi(\boldsymbol{r})$ are calculated by solving the *stationary* Schrödinger

---

[1]In fact, small molecular compounds can be also deposited via solution-processing; however the contrary is not applicable for polymers

equation for a single electron

$$\hat{H}\Phi(\boldsymbol{r}) = \mathcal{E}\Phi(\boldsymbol{r}), \tag{2.1.2}$$

where $\mathcal{E}$ is the energy of the electron system. The Hamilton operator can then be expressed as

$$\hat{H} = -\frac{\hbar^2}{2m}\Delta - \frac{\hbar^2}{2M}\Delta - V(\boldsymbol{r},\boldsymbol{R}), \tag{2.1.3}$$

where m is the mass of the electron, M is the mass of the nucleus, and $\Delta = \left(\frac{\partial^2}{\partial x^2} + \frac{\partial^2}{\partial y^2} + \frac{\partial^2}{\partial z^2}\right)$ is a Laplace operator in cartesian coordinates. The first two terms represent the kinetic contribution of electrons and nuclei, respectively, while $V(\boldsymbol{r},\boldsymbol{R})$ is the potential energy operator which depends on both electronic and nuclear positions, $\boldsymbol{r}$ and $\boldsymbol{R}$, respectively. *Adiabatic* or *Born-Oppenheimer approximation* is based on the fact that the mass of the nucleus M is commonly $10^3 - 10^4$ times higher than the mass of the electron m, *i.e.* $m \ll M$. It enables a description of motion of the electron separately from the movement of the nuclei background, since all the electronic events are expected to occur on a timescale several orders of magnitude faster than the nuclei motion. It allows one to separate the electronic and nuclear contributions and consider them separately from one another. The Hamiltonian of the electronic system simplifies to

$$\hat{H}_e = -\frac{\hbar^2}{2m}\Delta - \frac{Z}{4\pi\epsilon_0\,|\boldsymbol{R}-\boldsymbol{r}|} + \sum_{j}^{N_e}\frac{1}{4\pi\epsilon_0\,|\boldsymbol{r_l}-\boldsymbol{r}|}, \tag{2.1.4}$$

where Z denotes the atomic number of the chemical element, N_e is the number of electrons in the system. The total energy of the system can then be expressed as the combination of electronic and nuclear contribution, $\mathcal{E}_e$ and $\mathcal{E}_M$, respectively,

$$\mathcal{E} = \mathcal{E}_e + \mathcal{E}_M. \tag{2.1.5}$$

After solving Eq. (2.1.2) for the wavefunction, $\left|\Psi(\boldsymbol{r})\Psi^*(\boldsymbol{r})\right|^2$ will then give a probability density of finding an electron, where $\Psi(\boldsymbol{r})^*$ denotes the complex conjugate of the wave function. The corresponding valence electron orbitals of carbon is depicted in Figure 2.1.1 (a). The *linear combination of atomic orbitals* (LCAO) approximation is then used to calculate the resulting molecular orbitals. According to the LCAO approach, the molecular orbital

can be expressed as

$$\Psi(\boldsymbol{r}) = \sum_i C_i \Phi_i(\boldsymbol{r_i}). \tag{2.1.6}$$

The coefficients C_i and molecular energies can be found by applying a *variational principle*, which is the corner piece of all of the computational approaches in quantum chemistry. The principle states, that the energy computed using an arbitrary wavefunction Ψ_{trial} will set an upper bound to the true energy of the ground state of the molecule, $\mathcal{E}_0$

$$\langle \Psi_{\text{trial}} | \hat{H} | \Psi_{\text{trial}} \rangle = \mathcal{E}_{\text{trial}} > \mathcal{E}_0 = \langle \Psi_0 | \hat{H} | \Psi_0 \rangle, \tag{2.1.7}$$

where Ψ_0 is the true wavefunction of the ground state. Therefore, minimizing the energy by varying Ψ_{trial} one can expect to get a good approximation of the ground state of the molecule.

To understand the nature of the bond formation in organic materials, let's first take a look at methane (chemical formula CH_4), one of the most simple carbon based compounds. In the methane molecule, carbon forms four covalent bonds with four 1s valence electrons of hydrogen. To explain such bonding, one assumes valence electron configuration of carbon to have four unpaired electrons $(s^1 2p_x^1 2p_y^1 2p_z^1)$ which then form bonds with 1s atomic orbitals of hydrogen. The difference from the ground state of carbon, which have only two unpaired electrons in p orbitals and fully occupied 2s state $(s^2 2p_x^1 2p_y^1)$ is explained by the *promotion* of one electron in 2s orbital to a higher energy orbital 2p. Such electron promotion to a higher energy level helps to minimise the electron-electron repulsion which C molecule would otherwise experience having fully occupied 2s orbital. Therefore, $s^1 2p_x^1 2p_y^1 2p_z^1$ configuration of carbon results in overall minimal energy state of the CH_4 molecule. Such electron promotion to a higher energy orbital and subsequent formation of 4 bonds is a characteristic property of carbon. In general, when several electrons occupy degenerate orbitals, the configuration comprising the largest number of parallel electron spins (see below) is the most stable. The latter statement is known as *Hund's rule*.

The interaction of four atomic orbitals (one 2s and three 2p orbitals) results in a constructive and destructive interference of the wavefunctions, which leads to the formation of the four sp^3 hybridized molecular orbitals, which is depicted in Figure 2.1.1 (b). As result of the hybridization each hybrid orbital is composed of a large lobe pointing in the direction of one corner of a regular tetrahedron. The angle between the axes of hybrid orbitals is equal to 109.47°. Due to the constructive wavefunction interference, wavefunction of the hybrid orbital has enhanced amplitude compared to the 2s and 2p orbitals (see

(a)

(b)

(c)
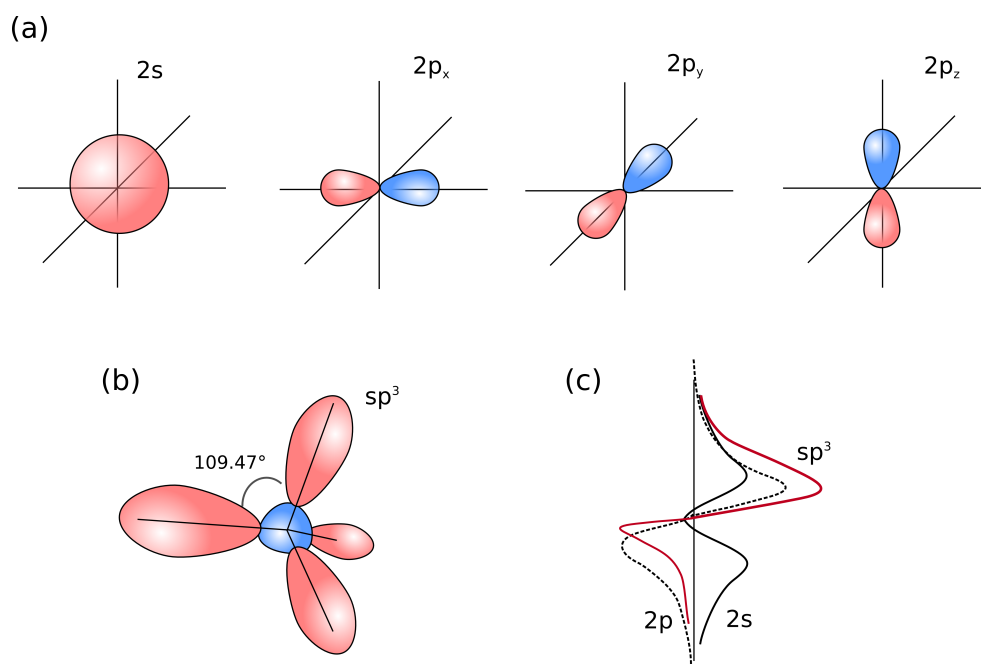
Figure 2.1.1: Formation of molecular orbital model for methane molecule (chemical formula CH_4) by linear combination of atomic orbitals of carbon. (a) Atomic orbitals of carbon valence electrons; (b) resulting sp^3 hybridized molecular orbital made out of three $2p-$ and one $2s-$orbital; (c) the cross-section of the corresponding electron wavefunctions for atomic $2p$, $2s$ and hybrid molecular sp^3 orbital. Constructive interference of atomic wavefunctions results in enhanced amplitude of the wavefunction of the hybridised orbital $\Psi(\boldsymbol{r})$ and therefore stronger bond of the hybrid orbital described by probability density $\left|\Psi(\boldsymbol{r})\Psi^*(\boldsymbol{r})\right|^2$. After [5].

Figure 2.1.1 (c)), which leads to the stronger bond compared to s or p bonds alone.

Ethene with a chemical formula H_2-C=C-H_2 represents one of the most simple molecular systems comprising double carbon-carbon bond. Each of two electron systems of carbon in the ethene molecule takes part in the sp^2 hybridized orbital, which is combined of two 2p and one 1s atomic orbitals. Shown in Figure 2.1.2 (a), the three lobes of the hybrid molecular orbitals are lying in a plane and are separated by 120°. The 2p orbital which doesn't participate in the hybridization is then positioned normal to the sp^2 orbital plane. The double bond is then combined between σ bond arising from the interaction of two sp^2 orbitals and a π bond formed from two 2p orbitals (Figure 2.1.2 (b)). Such double bond is responsible for the relative rigidity and the resulting planar structure of the molecule. The schematic representation of the energy level diagram of molecular orbitals, which can be calculated by the process described above is shown in Figure 2.1.2. The σ bond is stronger than the π bond, which manifests in higher gap between the bonding and antibonding (higher energy) orbital levels. Since the energy required to excite the

(a)   (b)   (c)

Figure 2.1.2: Molecular orbitals and energy level diagram of ethene (C_2H_4). (a) Planar hybrid sp^2 orbital resulting from the interaction of the two $2p$ and one $2s$ orbitals; (b) double bond resulting from π bond for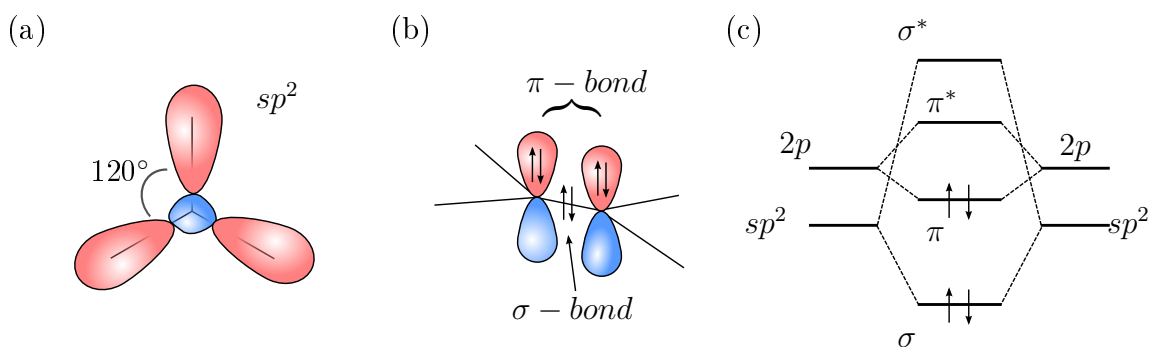med from two $2p$ orbitals and σ bond formed from two sp^2 orbitals (not shown for simplicity). The arrows pointing upward and downward represent two electron spin states in each orbital according to the exclusion principle; (c) corresponding energy level diagram of the valence orbitals of ethene molecule. After [5].

electron to a higher energy level is lower for $\pi \to \pi^*$ transition, the chemical and optical properties are mainly determined by the π orbitals. The resulting frontier orbital levels are respectively called *highest occupied molecular orbital* (HOMO) and *lowest unoccupied molecular orbital* (LUMO).

The arrows pointing upward and downward in Figure 2.1.2 represent the fact that there can be two electrons with different intrinsic angular momentum, called spin, in the same orbital. The electrons are *fermions* with a half integral spin, which results in the requirement for a wavefunction of an electron system to be asymmetrical, i.e. $\Psi(\boldsymbol{r_1}, \boldsymbol{r_2}) = -\Psi(\boldsymbol{r_2}, \boldsymbol{r_1})$ (for two electron system). The requirement for wavefunction asymmetry results in what is called *Pauli's exclusion principle*, which states that no more than two electrons may occupy any given orbital, and if two do occupy one orbital, then their spins must be paired [5]. A two-electron system then can have respective configurations where the electron spins are aligned parallel or anti-parallel, which differ in their overall spin angular momentum. The vector model for the spin configurations is presented in Figure 2.1.3. In anti-parallel or paired configuration, spins of the electrons cancel each other out, resulting in total angular momentum being zero ($S = 0$). The resulting electron state is called *singlet*, since there's only single combination of electron spins which fulfill the anti-parallel configuration (Figure 2.1.3 (a)). The resulting spin function of the singlet state can be written as

$$\sigma_S(\boldsymbol{r_1}, \boldsymbol{r_2}) = \frac{1}{\sqrt{2}}\Big(\alpha(\boldsymbol{r_1})\beta(\boldsymbol{r_2}) - \alpha(\boldsymbol{r_2})\beta(\boldsymbol{r_1})\Big), \qquad (2.1.8)$$
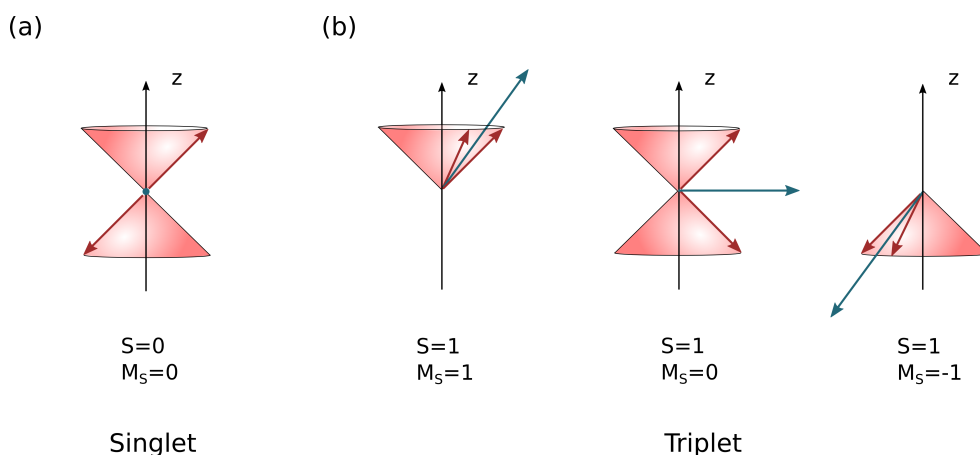
Figure 2.1.3: Vector model for spin coupling of two-electron system. Red arrows represent spins of the two electrons, blue arrow is the resulting spin of the system; (a) Anti-parallel or singlet configuration results in a zero spin system ($S = 0$); (b) three possible parallel spin arrangements (triplet state) resulting in $S = 1$ configuration.

where α and β represents two possible electron states with spin angular momentum $m_s = 1/2$ and $-1/2$, respectively.

On the other hand, parallel spin configuration can be achieved in three different combinations, in which two parallel spins add together (Figure 2.1.3 (b)). The resulting state is hence called *triplet*, and the corresponding spin operator can be written as

$$\sigma_T(\boldsymbol{r_1}, \boldsymbol{r_2}) = \begin{cases} \alpha(\boldsymbol{r_1})\alpha(\boldsymbol{r_2}) \\ \frac{1}{\sqrt{2}}\Big(\alpha(\boldsymbol{r_1})\beta(\boldsymbol{r_2}) + \alpha(\boldsymbol{r_2})\beta(\boldsymbol{r_1})\Big) \\ \beta(\boldsymbol{r_1})\beta(\boldsymbol{r_2}). \end{cases} \tag{2.1.9}$$

The electron states are represented by *spin orbitals*, which is a product of spatial wavefunction $\phi(\boldsymbol{r})$ and a spin function

$$\Phi(\boldsymbol{r}) = \phi(\boldsymbol{r})\sigma. \tag{2.1.10}$$

For larger and more complicated molecules than the ones that were presented so far, more complicated calculations involving the many-body interactions have to be performed. For this, numerical approaches to calculation of both intermolecular and intramolecular interactions are successfully implemented, based on various approximations. A common approach to approximate a wavefunction of N-electron system, is to use an anti-symmetrised product of N one-electron spin orbitals, which is represented by the *Slater determinant*
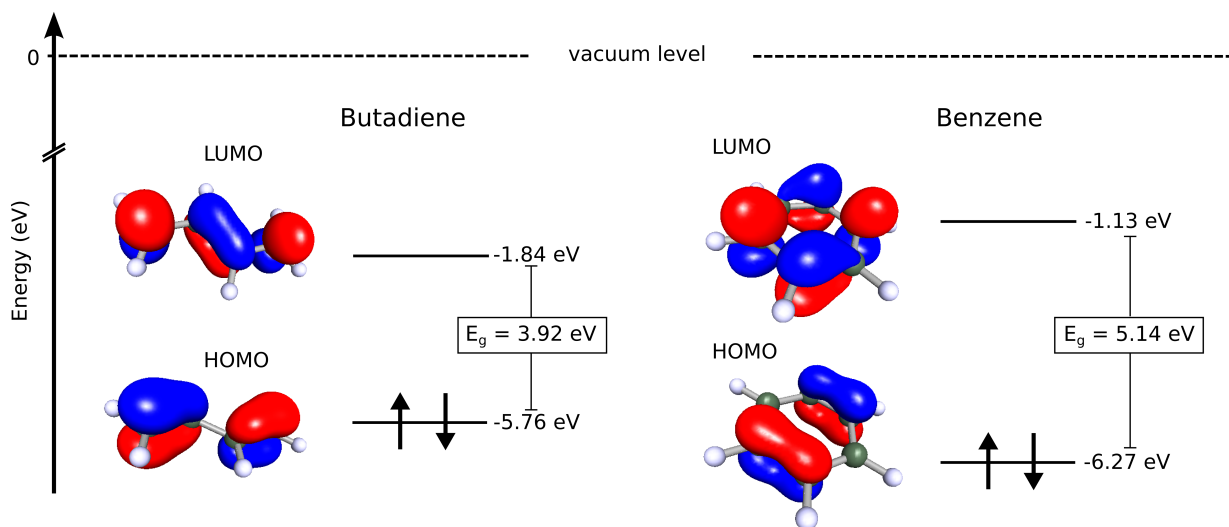
Figure 2.1.4: HOMO and LUMO of butadiene (left) and benzene (right) molecules, representing the most simple examples of linear and cyclic conjugated π-orbital systems, respectively. The calculated values are obtained using Turbomole software, based on a DFT approach.

$$\Psi(\boldsymbol{r_1}, \boldsymbol{r_2}, \ldots, \boldsymbol{r_N}) = \frac{1}{N!} \begin{vmatrix} \Phi_1(\boldsymbol{r_1}) & \Phi_2(\boldsymbol{r_1}) & \cdots & \Phi_N(\boldsymbol{r_1}) \\ \Phi_1(\boldsymbol{r_2}) & \Phi_2(\boldsymbol{r_2}) & \cdots & \Phi_N(\boldsymbol{r_2}) \\ \vdots & \vdots & \ddots & \vdots \\ \Phi_1(\boldsymbol{r_N}) & \Phi_2(\boldsymbol{r_N}) & \cdots & \Phi_N(\boldsymbol{r_N}) \end{vmatrix} \tag{2.1.11}$$

Hartree-Fock approach is based on the variational principle applied to the many electron system wavefunction based on Slater determinant approximation. While this method forms the basis of the modern computational approaches, calculation based on *density functional theory* (DFT) is commonly used to study organic molecules [6]. DFT approach is based on Hohenberg-Kohn theorem [7], which states that the total energy of the system in its ground state is a functional of the electronic density $\rho(\boldsymbol{r})$ of that system, and that any density other than the true density will necessarily lead to a higher energies. Thus, a variational principle applies here, as the molecular state is calculated by minimizing the energy functional $E\left[\rho((r))\right]$ [8]. Naturally, such approach is very sensitive to the initial form of the functional, therefore considerable effort has been spent developing the energy functional in a approximate way. One of the most commonly used functionals in DFT calculations is B3LYP [9].

The crucial role in determining optical and electrical properties of organic semiconductors is played by the alternate single and double carbon-carbon bonds, which are present

in so-called *conjugated molecular systems.* In such molecules, π orbitals overlap which enables partial or full de-localization of the electron wave over the molecular structure. Figure 2.1.4 shows the HOMO and LUMO orbitals of butadiene and benzene, which represent the most simple linear and cyclic π-conjugated systems, respectively. Since there is no overlap between σ and π orbitals, the de-localized π system can be studied independently. The larger E_{g} values for benzene as compared to those of butadiene (Fig.2.1.4) comes from the greater larger length of the conjugated system in the latter molecule. The greater the extent of the the π conjugated chain, the lower the "band-gap" E_{g} (determined by the difference between the HOMO and LUMO levels) and the corresponding energy of the $\pi \rightarrow \pi*$ transition (larger absorption wavelength). This effect is even more clear in the polyacene molecule family. There benzene, naphtalene and antracene, representing 1,2 and 3 conjugated rings, respectively, have their absorption peaks in the UV spectral range ($\lambda_{abs} = 255$, 315 and 380 nm, respectively), while tetracene and pentacene absorbs in the visible (4 and 5 conjugated rings, $\lambda_{\mathrm{abs}} = 480$ and 580 nm). This phenomena can be qualitatively understood by a simplified particle-in-a-box analogy, with electron being free along the length of the conjugated system a. As known from the quantum mechanics, writing the Hamiltonian for such a system and solving the corresponding Schödinger equation, leads to the quantified energy levels of the electron, and if the box has the infinite barriers, the energy spacing is proportional to a^{-2}, that is, inverse square of the conjugated system length.

2.1.2 Intermolecular Interactions

All of the forces relevant for the discussion of the intramolecular interactions are of electromagnetic origin and arise from the electrostatic interaction between the particles comprising the two interacting molecules [10]. The electrostatic attraction between the molecules is governed by the *Coulomb's law* of the interaction between opposite charges. According to the Coulomb's law, the potential energy between two point charges q_1 and q_2 can be written as

$$V = -\frac{q_1 q_2}{4\pi\epsilon_0 r} \propto -\frac{1}{r}, \tag{2.1.12}$$

where r is the distance between the charges. The inverse proportionality of the interaction energy to the distance between the charges leads to the fact that such interaction persist over the long distances (in the molecular scale). Such interaction can be found in compounds comprising ions, and the resulting interaction is called ionic bond. When present, the ionic bonding dominates over all other interactions and since it is a long-range inter-

action, it often results in closely-packed crystalline solids. However, in the case of organic molecules and molecular solids, the molecular constituents are in most cases non-polar or have partial charges, therefore ionic bonding does not play a role. In the following, the main forces holding organic molecules together are described, namely, *dipole-dipole*, *dipole-induced dipole* and *induced dipole-induced dipole* interactions. All aforementioned interactions contribute to the attractive long-range forces between molecules which collectively are often called *van der Waals forces*. They are named after the scientist who introduced the well-known gaseous state equation, which accounts for the deviations from the ideal gas behaviour by introducing the correlation factors due to an attraction between molecules [11]. Finally, hydrogen bonding is discussed as it plays a crucial role in bio-molecules and, when present, is a dominant interaction in organic compounds.

Dipole-dipole interactions, also known as Keesom forces [12], as name suggests, originates from the electrostatic interaction between two dipoles. In organic molecules, such dipoles are formed due to the attraction between partial charges in bonds between C and electronegative atoms, such as O, N or halogens (F, Cl, Br, I). The dipole-dipole interactions play a role in a large number of organic materials, including amines, amides, alkyl halides, ethers, esters, ketones and aldehydes. The original Keesom interaction is derived for the gas molecules, where molecules exhibit a rotational degree of freedom. Since the mutual potential energy depends on the orientation of each of the two interacting molecules, there is the preferential orientation of the dipoles, which minimises the overall interaction energy E_{Keesom}. Therefore, the average interaction is not zero as it would be in the case of independently rotating dipoles, and is found by averaging the possible orientations weighted by the Boltzmann factor $\exp(-\frac{E_{\mathrm{Keesom}}}{k_B T})$, which describes the probability of each orientation. The resulting interaction energy then depends on the dipole moment of each of the molecules $\mu_{1,2}$, distance between them and temperature

$$V_{\mathrm{Keesom}} = -\frac{2\mu_1^2\mu_2^2}{3(4\pi\epsilon)^2 r^6 k_B T} \propto -\frac{1}{r^6}. \qquad (2.1.13)$$

In solid state, however, the molecules can be regarded to be in a fixed orientation specified by spherical coordinates ϕ_i and θ_i, where $i = 1, 2$ corresponds to the different dipoles. The resulting interaction potential is then

$$V_{\mathrm{Keesom}}^{\mathrm{solid}} = -\frac{\mu_1\mu_2}{4\pi\epsilon r^3} f(\phi_1, \phi_2, \theta_1, \theta_2, T) \propto -\frac{1}{r^3}. \qquad (2.1.14)$$

The term $f(\phi_1, \phi_2, \theta_1, \theta_2)$ includes the information about the particular orientation of the molecules in the solid, which could also depend on the temperature T. Result in Eq.

(2.1.14) is different from the case in the solution, where $V \approx \frac{1}{r^6}$, therefore the dipole-dipole interaction is more pronounced for polar molecules in the solid state compared to the gaseous state. However, the interaction described by Eq. (2.1.14) is proportional to r^{-3} and so it fades faster with increasing separation of the interacting entities as compared to the point charge interaction, where the interaction is inversely proportional to the separation (Eq. (2.1.12)). The dipole-dipole interaction energy approaches zero more rapidly, since both interacting dipoles appear neutral to each other at large distances. Similar trend also hold true for the quadrupole and higher order polar interactions. In general, the interaction between the n-pole and m-pole molecules varies with distance as

$$V_{\text{multipole}} \propto -\frac{1}{r^{n+m+-1}}.$$ (2.1.15)

In molecules that can be polarised, a dipole can induce a dipole in an otherwise neutral molecule, which is proportional to the polarizability of the molecule α. Such dipole-induced dipole (or Debye) interaction must also be added to the (2.1.14) expression of the interaction energy [13]. Then the interaction of two dipolar molecules can be described by

$$V = V_{\text{Keesom}} + \sum_{i,j} V_{\text{Debye}}^{i,j},$$ (2.1.16)

with

$$V_{\text{Debye}}^{i,j} = -\frac{\alpha_i \mu_j^2}{4\pi\epsilon r^6} \propto -\frac{1}{r^6}.$$ (2.1.17)

The Debye interaction is independent of temperature. It is also a weaker interaction compared to the force between permanent dipoles. The r^{-6} dependence can be understood by the combination of dipole's electric field r^{-3} dependence, which influences the magnitude of the induced dipole, and the r^{-3} dependence of the potential energy between the permanent and the induced dipoles [5].

Formation of the condensed phases of non-polar substances, such as condensation of benzene to a liquid in room temperature or existence of anthracene crystals, are a clear manifestation of a cohesive forces holding such compounds together. However, they cannot be explained by the dipole-dipole and dipole-induced dipole interactions since the molecules don't have a permanent multipole moment. Therefore, so-called *London or dispersion forces* were introduced to account for the interactions between two varying fluctuating multipoles [14]. The interaction can be understood by considering a molecule with a

fluctuating dipole moment. At some instant of time it can induce the dipole state in the neighbouring molecule. This leads to the attraction between the two dipoles. The two dipoles are also correlated in the direction of interaction, since one dipole of one molecule will follow the change in the other. The general description of such dispersion force is rather complicated and can be written as

$$V_{\text{dispersion}} = \frac{c_6}{r^{-6}} + \frac{c_8}{r^{-8}} + \frac{c_{10}}{r^{-10}} + ..., \qquad (2.1.18)$$

where c_6, c_8... are constants. A good approximation of the interaction is given by the *London's formula*, which is based on a quantum mechanical second-order perturbation treatment

$$V_{\text{London}} = \frac{3}{2} \frac{\alpha_1 \alpha_2}{r^6} \frac{I_1 I_2}{I_1 + I_2}, \qquad (2.1.19)$$

where $I_{1,2}$ denotes the ionisation energy of the corresponding molecules. The dispersion interaction is independent of temperature, and depends mainly on the size of the atomic components and to a lesser degree the size of the molecules. Larger molecules, with higher surface area have more dispersed electronic systems and they exhibit higher polarisabilities. The London forces are weaker compared to Keesom or Debye interactions, however, they are present in all of the compounds, regardless of their constituency, while the polar interactions require at least one polar entity for the interaction. For this reason, dispersion forces are the dominant contribution to the overall binding of the hydrocarbons, which are essentially non-polar compounds. The effect of the molecule's size to the strength of the interaction can be illustrated by taking the example of the common aromatic hydrocarbons. Benzene comprising ring of 6 C atoms (see Figure 2.1.4) is a liquid at room temperature and atmospheric pressure. The naphthalene consists of two phenyl rings. The increase of size in the molecule leads to the formation of the crystalline solid at similar conditions, with a melting point of 78.2 °C. Moreover, anthracene (three ring structure) crystal have a melting point of 215.76 °C, which further exemplifies the role of the dispersion forces in such compounds. Figure 2.1.5 compares different intermolecular interactions in various organic molecules.

Whenever molecules comprising solid are constituted of highly electronegative atom covalently linked to a hydrogen atom H, they can form a bond with a neighbouring molecule, comprising another electronegative atom B which often contains a lone pair of electrons. Such linkage A-H$\cdots$B is known as *hydrogen bond* and since its introduction [16] it has been widely accepted in explaining a number of cohesive effects in molecular solids [17]. Only certain elements A and B can participate in hydrogen bonding effectively, most prominent
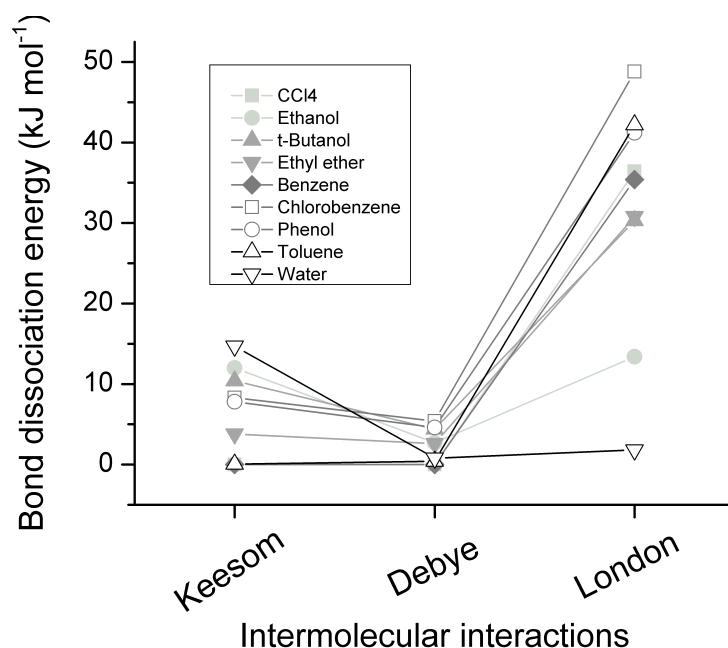
Figure 2.1.5: Bond strength comparison in various organic molecules. Based on [15].

being N, O and F. Due to such molecular structure selectivity, the hydrogen bonding is even less universal than dipole-dipole or dipole-induced dipole interactions. The bonding can originate from a number of different physical effects. The most simple explanation is that of the interaction between partial positive charge of H and a partial negative charge of B. Alternatively, LCAO model can be used to represent hybrid molecular orbitals and resulting bond formation [5]. The detailed nature of the hydrogen bond is still a matter of debate [18], since it is dependent on a subtle interplay between both electrostatic and covalent contributions [19]. The detailed quantum mechanical description of the hydrogen bonding is beyond the scope of this work. It is suffice to mention, that it is a short-range, contact-like interaction, and whenever present, it dominates over the van der Waals forces. For this reason, it is essential in understanding structure of water, nucleic acids as well as various hydrocarbons, if the structure of the latter allows A-H$\cdots$B formation.

Often, both atomic and molecular interactions are modelled by so-called *Lennard-Jones* potential [20]. Its explicit form is as follows

$$V_{\mathrm{L-J}} = 4\xi_0 \Big[\Big(\frac{\sigma_0}{r}\Big)^{12} - \Big(\frac{\sigma_0}{r}\Big)^6 \Big], \tag{2.1.20}$$

where ξ_0 denotes the depth of the potential well with a minimum at $r_0 = 2^{1/6}\sigma_0$, and σ_0 is the value of r at $V_{\mathrm{L-J}}(r) = 0$. Due to its convenience, Lennard-Jones potential, also known as (12-6) potential, has been widely used in many physical and chemical applications. In
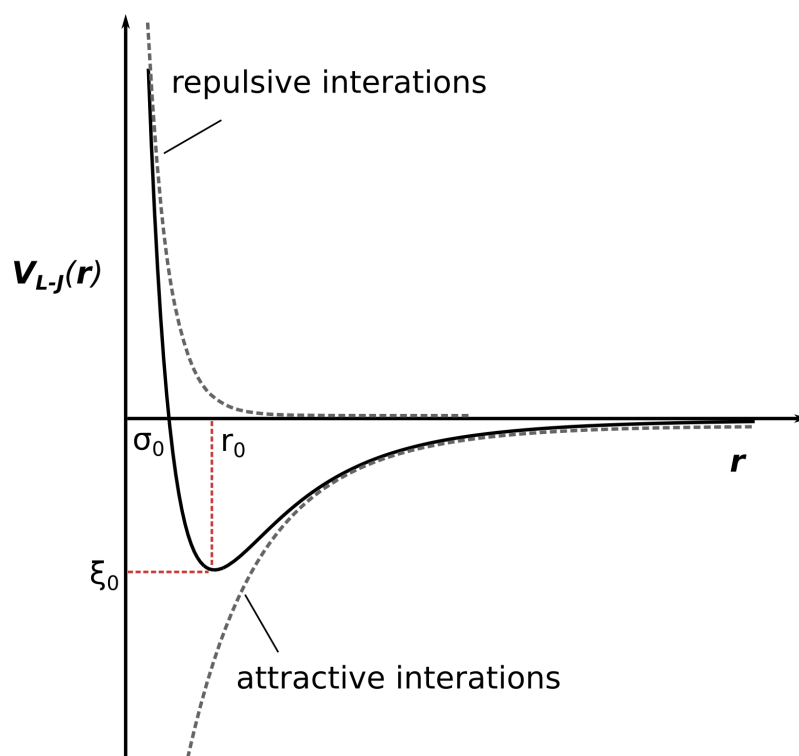
Figure 2.1.6: Empirical Lennard-Jones potential, which is used to model intermolecular interactions. Attractive molecular forces are mediated by the Coulomb interaction between opposite charges. At short intermolecular distance, electron wavefunctions start to overlap and strong repulsive force, due to Pauli principle, dominate.

the region where $V_{L-J}(r) > 0$ the repulsive force dominates. Alternatively, if $V_{L-J}(r) < 0$, then the interaction is attractive. As can be seen from Figure 2.1.6, at short intramolecular distances the forces are repulsive, while the attractive interactions dominate at large distances. In the intermediate region, the attractive and repulsive forces balance each other, which results in the distance r_0, at which the potential energy is minimal, which can be found from the condition $\frac{dV(r_0)}{dr} = 0$.

2.2 Optical Properties of Organic Semiconductors

The electronic structure of molecules is determined by the interaction between the atomic orbitals of molecular constituents. The combination of atomic orbitals then forms the basis for the understanding of the molecular orbitals (MO). The so-called σ orbital is formed either from the combination of two s-type atomic orbitals, from s and p type orbitals, or of two p-type orbitals lying along the collinear axis of symmetry. The binding arising between the atoms due to σ orbital is called σ bond. Another type of MO is called π orbital and is formed by the laterally overlapped p-type atomic orbitals. The corresponding bond is called a p-bond. Absorption of the visible light can promote the electron from π to anti-bonding $\pi*$ orbital representing the higher energy level. On the other hand, σ bond is stronger and the transition $\sigma \rightarrow \sigma*$ occurs via absorption in the deep ultraviolet radiation. There might also occur transition between non-bonding electrons situated in the vicinity of heteroatoms such as oxygen or nitrogen which possess free radicals. Such a transition (commonly to $\pi*$ orbital) is then denoted as $n \rightarrow \pi*$. Usually, in terms of transition energies, $n \rightarrow \pi* < \pi \rightarrow \pi* < n \rightarrow \sigma* < \sigma \rightarrow \pi* < \sigma \rightarrow \sigma*$ [21]. Commonly, in organic semiconductors, the most important transitions occur between frontier HOMO and LUMO orbitals, analogous to the valence and conductions bands in inorganic counterparts, respectively.

The transitions between the states are governed by the *Fermi's Golden Rule*, which gives the probability of the transition from the initial state i to the final state f. In the *bra-ket* notation

$$W_{if} = \frac{2\pi}{\hbar} \left| \langle f | \, \boldsymbol{M} \, | i \rangle \right|^2 \rho_f, \qquad (2.2.1)$$

where ρ_f is the density of the final states and $\boldsymbol{M} = \sum_j \boldsymbol{r_j}$ denotes the dipolar moment of the molecule. So according to Eq.(2.2.1), the transition probability is directly proportional to the square of the *transition moment* matrix element from initial to the final states, which is dependant on wave function overlap of the corresponding states Ψ_i and Ψ_f and can be written explicitly as

$$\mu_{if} = \int \Psi_f^*(\boldsymbol{r}, \boldsymbol{R}) \boldsymbol{M} \Psi_i(\boldsymbol{r}, \boldsymbol{R}) d\boldsymbol{r}. \qquad (2.2.2)$$

The intensity of each transition is then characterised by the oscillator strength f, which is connected to the transition moment via

$$f = \frac{4\pi mc}{3\hbar e^2 \lambda} \left| \mu_{if} \right|^2. \qquad (2.2.3)$$

Experimentally, one measures the absorption of light, characterised by the molar absorption coefficient $\epsilon_{\mathrm{abs}}(\lambda)$ measured in L mol^{-1}cm^{-1}, in a solution comprising absorbing molecules of concentration C. Then, according to *Beer-Lambert law*, the measured intensity of light I which passes the length L is described by

$$\log \frac{I}{I_0} = \epsilon_{\mathrm{abs}}(\lambda)LC, \tag{2.2.4}$$

where, I_0 is the initial light intensity entering the solution. The oscillator strength (and transition moment) can then be calculated from the absorption spectrum for each absorption peak, according to

$$f = \frac{4 \ln 10 \epsilon_0 m c^2}{N_A e^2 \lambda} \int \epsilon_{\mathrm{abs}}(\lambda) d\lambda. \tag{2.2.5}$$

From the perspective of quantum mechanical treatment, using adiabatic approximations allows one to separate the electronic and vibrational wave functions, $\boldsymbol{\Phi}$ and $\boldsymbol{\chi}$. Then the wave function of the molecular system $\boldsymbol{\Psi}$ can be written

$$\Psi(\boldsymbol{r}, \boldsymbol{R}) = \Phi_e(\boldsymbol{r}, \boldsymbol{R}) \cdot \chi_{\nu,e}(\boldsymbol{r}, \boldsymbol{R}), \tag{2.2.6}$$

where $\boldsymbol{r}$ denotes the electronic coordinate and $\boldsymbol{R}$ is a set of nuclear coordinates. The indexes e and ν denote the electronic state and the vibrational quantum number, respectively. Within the approximation, the transition dipole matrix element for the transition from the initial state $|i, m\rangle$ (which can be assumed to be the ground electronic state of the molecule as it is usually the case) corresponding to the vibrational level m to the final electronic state $\langle f, n|$ in the vibrational level n, can be written as

$$\mu_{im,fn} = \langle \chi_n(\boldsymbol{R})| \, \mu_{if} \, |\chi_m(\boldsymbol{R})\rangle \,. \tag{2.2.7}$$

The latter holds true for the case when $i \neq f$, that is the transition involves the change in the electronic levels. $\mu_{if} = \langle \Phi_e(\boldsymbol{r}, \boldsymbol{R})| \, M_e \, |\Phi_e(\boldsymbol{r}, \boldsymbol{R})\rangle$ is the electronic transition dipole moment. In general, the electronic wavefunction depends on the nuclear coordinates, therefore also $\mu_{if} = \mu_{if}(\boldsymbol{R})$. However, the dependence is relatively weak, thus allowing to expand the electronic transition dipole into a series $\mu_{if}(\boldsymbol{R}) = \mu_{if}^0 + \mu_{if}^1 \boldsymbol{R} + ...$ To a first approximation, Equation (2.2.7) can be rewritten as

$$\mu_{im,fn} = \mu_{if}^0 \, \langle \chi_n(\boldsymbol{R})\rangle \, \chi_m(\boldsymbol{R}), \tag{2.2.8}$$
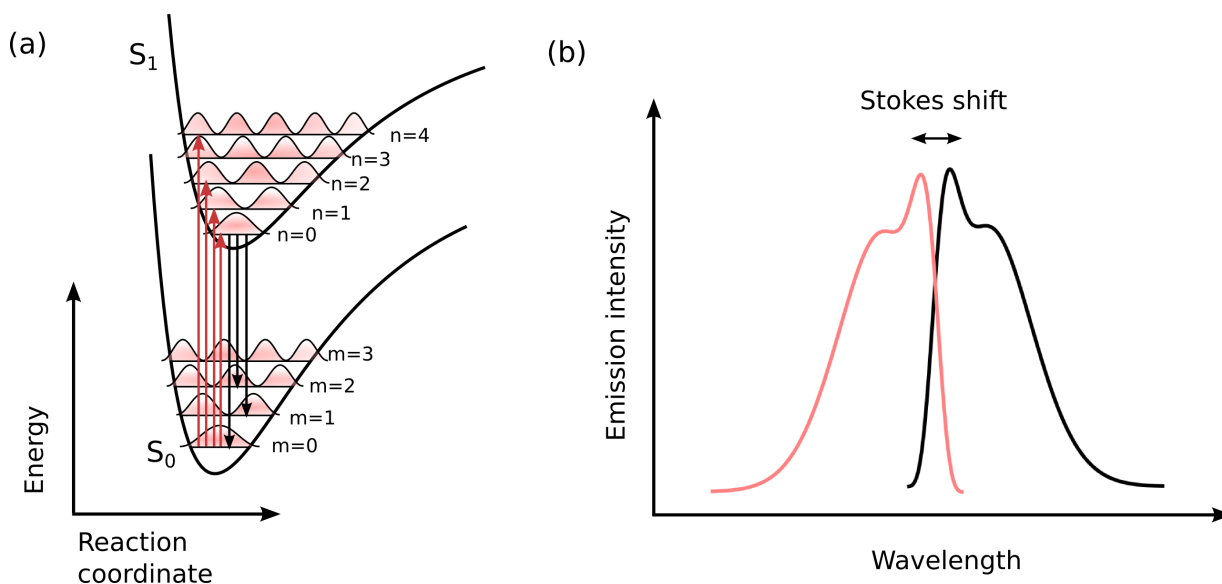
Figure 2.2.1: Origin of molecular absorption and emission spectra. (a) Energy level diagram representing molecular ground state S_0 and first excited state S_1. Electronic transitions between different vibrational levels $n \leftrightarrow m$ are represented by the vertical arrows. The intensity of the transitions are proportional to the square of the transition dipole moment μ_{if}, which is dependent on the overlap between electron wavefunctions (represented by the shaded area) in ground and excited states; (b) resulting absorption (shaded red area) and emission (shaded blue area) spectra. Stokes shift characterises the difference between the absorption and emission peaks.

which leads to the final estimation of the probability of such transition

$$W_{if} \propto \left| \mu_{if}^0 \right|^2 \cdot F_{nm}, \tag{2.2.9}$$

where $F_{nm} = \left| \langle \chi_n(\boldsymbol{R}) \rangle \, \chi_m(\boldsymbol{R}) \right|^2$ is Frank-Condon integral, which represents the square of the overlap between vibrational wavefunctions. The approximation $\mu_{if} = \mu_{if}^0 = \text{const}(\boldsymbol{R})$ is valid in many situations, since the time it takes to promote an electron to the higher energy level is in the range of $\approx 10^{-15}$ s while the characteristic time of a molecular vibration is $\approx 10^{-12} - 10^{-10}$ s, therefore an electronic transition can be described separately from any changes in nuclear configuration. This, together with a subsequent result in Eq.(2.2.9), that the transition probability is proportional to the square root of the electronic transition moment weighted by the Frank-Condon integrals, forms the basis of the *Frank-Condon principle*. It follows that the electronic transition can be depicted as a vertical in a configuration coordinate space. Due to the nuclear displacement induced by the electronic transition, Frank-Condon integrals are finite. Using the simplified displaced harmonic

oscillator model, for a $m = 0 \to 1$ transition

$$F_{n0} = \frac{e^{-S} S^n}{n!}, \text{ with } S = \frac{\Delta^2}{2}. \qquad (2.2.10)$$

Here Δ is the nuclear displacement in the reaction coordinate space, represented in the dimensionless units $\Delta = \sqrt{\frac{m\omega}{\hbar}} \delta R$ and S is the *Huang-Ryss factor*, which represents the average number of photons, generated by the vibronic transition $S = \frac{m\omega^2 \delta R^2}{2\hbar\omega} = \frac{\Delta E}{\hbar\omega}$. $\Delta E = E_{fn} - E_{00}$ is the *relaxation energy, i.e.* energy required to distort the configuration of the ground state into the configuration of the excited state without the electronic transition.

2.2.1 Excited State Dynamics

The transition of the electron between two different electronic states happens in the time of $\tau \approx 1$ fs $= 10^{-15}$ s. As the probability of the transition is governed by the transition dipole moment from initial to the final state (Eq. 2.2.1), it is identical for both absorption ($S_0 \to S_n$ transition) and emission ($S_n \to S_0$) processes (assuming that the excitation does not change the ground state of the molecule). However, due to the subsequent processes following light absorption, the excited state lifetime, which is measured in time-dependent spectroscopic methods is few orders of magnitude longer than the time for the electron jump. In the following, the radiative and nonradiative mechanisms leading to the depopulation of the excited state of the molecule are discussed.

With a few exceptions, following the excitation of one of the vibrational levels of higher energy singlet states S_n, the excitation is transferred nonradiatively to the lowest lying vibrational level of the first excited state S_1. Therefore, one expects the subsequent emission of the molecule to occur from the S_1. The latter statement, proposed in 1950, is known as *Kasha's rule* [22]. A corollary of Kasha's rule is the *Vavilov rule*, which states that the quantum yield of the molecule (ratio between the emitted and absorbed photons) is independent of the excitation wavelength [23]. Mechanisms responsible for a relatively fast recombination of the excitation are *internal conversion* and *vibrational relaxation*. The latter is the transition between different vibrational in the same electronic configuration, which occurs in 10^{-12}-10^{-10} s time. The former is the nonradiative transition between two electronic states of the same multiplicity, which ultimately leads to $S_n \to S_1$. Internal conversion probability is higher for a lower energy gap between the states and the corresponding transition lifetime can vary from $\tau \approx 10^{-13}$ to 10^{-9} s [21].

The radiative transition from a singlet state $S_1 \to S_0$ is called *fluorescence*. Its characteristic lifetime is from sub-nanosecond to few tens of nanoseconds. The separation between vibrational levels in ground and excited states are usually similar, which leads to

the "mirror image" between absorption and fluorescence spectra. The fluorescence spectrum is red-shifted with respect to the absorption spectrum, and the difference between the emission and absorption peaks is called *Stoke's shift* (Figure 2.2.1 (b)). Stoke's shift is a direct consequence of the Kasha's rule. In some cases, the emission wavelength can be blue-shifted with respect to the absorption (*Anti-Stoke's shift*), by the process is called *optical refrigeration* [24].

Intersystem crossing (ISC) refers to crossing between two potential energy surfaces of different multiplicity, often $S_1 \rightarrow T_n$. While such transition is forbidden due to the requirement of spin conservation (see above), the probability of ISC is not zero, due to the *spin-orbit coupling*. The latter is the coupling between orbital magnetic moment and spin magnetic moment of the electron. The spin-orbit coupling is enhanced and the ISC becomes more efficient if the heavy atom is present in the molecule, such as Pb, Pt or Ir. The ISC rate then can be of the similar order to the fluorescence rate, and therefore compete with the radiative recombination process. Once the triplet state is populated, it can also recombine radiatively, a process known as *phosphorescence*. Its spectrum is red shifted in comparison to fluorescence emission, $T_1 < S_1$. Phosphorescence lifetime can range from $\tau \approx 1$ ms to even 10 s. Due to it is such a slow process, other competing mechanisms usually dominate over phosphorescence, however it can observed at low temperatures and in the rigid media.

Reverse process of ISC also occurs, called *reverse intersystem crossing* (RISC). Similar selection rules apply to $T_n \rightarrow S_1$ transition as was described above. Additionally, RISC is a thermally activated process, since triplet state lies below the singlet excited state, and therefore energy difference ΔE_{ST} have to be overcome. Therefore, systems of low ΔE_{ST} are required for efficient RISC to occur, such as systems involving $\pi \rightarrow n$ transitions or charge transfer states, characterised by a low values of exchange integral K_{ex}. Emission from the singlet state due to the RISC process is called *E-type delayed fluorescence* or *thermally activated delayed fluorescence* (TADF). Alternatively, another type of delayed fluorescence exists which is called *P-type*. It is due to the triplet excitation upconversion resulting from the *triplet-triplet annihilation* (TTA) and subsequent relaxation to the singlet state. The spectrum of delayed fluorescence matches the prompt fluorescence emission, while the lifetime is between that of fluorescence and phosphorescence.

2.3 Energy Transfer in Organic Solids

The elementary excitations are responsible for the energy transport in the organic solid, which occur from an excited (donor) molecule, denoted D^* to the recipient (acceptor)
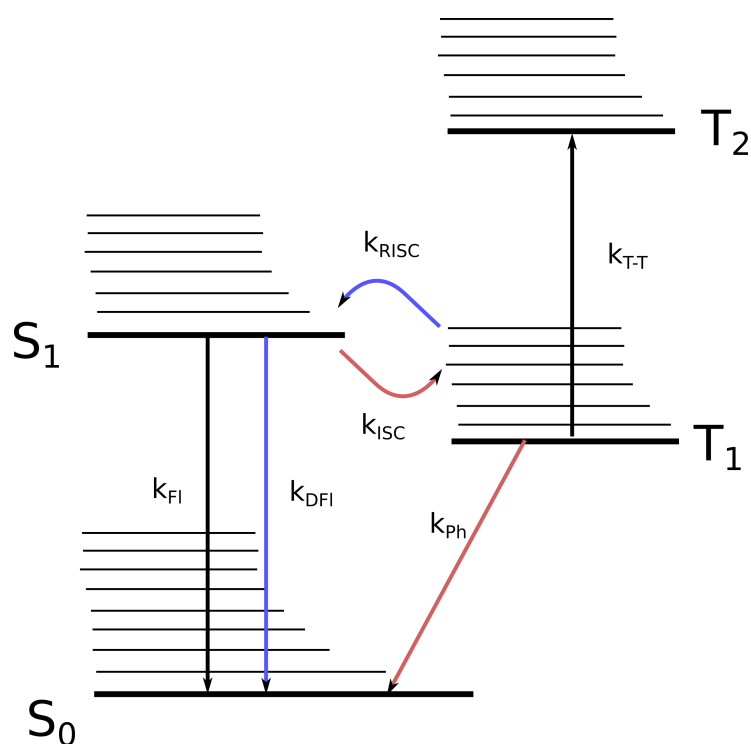
Figure 2.2.2: Jablonski diagram of excited state recombination pathways in organic molecules.

molecule A. The energy transfer process can then formally be described as

$$D^* + A \rightarrow D + A^*. \tag{2.3.1}$$

If D and A represent molecules of the same chemical structure, the energy transfer is called *homotransfer*. Otherwise, is molecules are different, the energy transfer is said to be *heterotransfer*. Energy migration occurs if the energy is being transported repeatedly from donor to acceptor molecules. Such excitation transfer plays a major role in the photosynthesis phenomena.

Energy among molecules can be transferred via process of emission and absorption of the photon of the energy $E = h\nu$. It is a two-step process and in this case, equation (2.3.1) can be rewritten to

$$D + h\nu \rightarrow D^* \tag{2.3.2}$$

$$h\nu + A \rightarrow A^*. \tag{2.3.3}$$

Due to its easy-to-grasp mechanism, radiative energy transfer is also known as *trivial transfer*, however, consistent description of the energy transfer is complicated and involves

use of the stochastic approaches when self-absorption effects have to be considered [25].

Nonradiative energy transfer can be grouped into two different types of interactions, namely, Coulombic interaction and interactions dependent on intermolecular orbital overlap. The former can prevail both in long (dipole-dipole interaction) and short (multipole interaction) range, while the latter occurs only when there's orbital contact at molecular scale. The universal description of the nonradiative transfer processes can be achieved by the quantum mechanical perturbation theory.

2.3.1 Förster Energy Transfer

The Coulombic dipole-dipole interaction leading to the energy transfer was first described by Förster using semi-classical quantum approach [26]. The schematic representation of such energy transfer mechanism is depicted in Figure 2.3.1 (a). The transfer rate of the *Förster transfer* is

$$k_{\mathrm{dd}} = k_D \left(\frac{R_{\mathrm{FRET}}}{r} \right)^6, \tag{2.3.4}$$

where k_D is the spontaneous decay rate of the donor emission, and R_{FRET} is the *critical* or *Förster radius*, which is a distance at which the spontaneous de-excitation and energy transfer decay of the donor is equally probable, i.e. $k_{\mathrm{dd}} = k_D$. R_{FRET} depends on the orientation of donor and acceptor molecules, described by the orientation factor κ_F, radiative decay efficiency of the donor in absence of transfer, η_{rad}, and the spectral overlap between the normalised emission of the donor $I_{\mathrm{norm}}^D(\lambda)$ and the absolute absorption of the acceptor $\epsilon_{\mathrm{abs}}^A(\lambda)$

$$R_{\mathrm{FRET}} \approx \frac{\kappa_F^2 \eta_{\mathrm{rad}}^D}{n^4} \int I_{\mathrm{norm}}^D(\lambda) \epsilon_A(\lambda) \lambda^4 d\lambda, \tag{2.3.5}$$

where n is the refractive index of the medium. The orientation factor $\kappa_F^2 = 1$ when the interacting dipoles are parallel, $\kappa_F^2 = 0$ when they are perpendicular to each other, and $\kappa_F^2 = 4$ for the collinear orientation of donor and acceptor. In a rigid medium, assuming isotropic random distribution of the donor and acceptor molecules, it can be shown that $\kappa_F = 0.476$. Typically, R_{FRET} is around 1-8 nm, but it some cases it can act up to separation of around 20 nm [21].

It is important to note, that Förster energy transfer depends on the oscillator strength of the transition in acceptor molecules, which is related to the absolute absorption coefficient of the molecule (Eq. 2.2.5). This implies that only the allowed transition under the spin

conservation condition are allowed for the energy transfer to occur. While, the process is called nonradiative, in fact it depends on a number of emission properties of the donor molecule (k_D, $\eta_{\rm rad}$). This is fully explained by the quantum electrodynamic treatment, which describes the Coulombic interaction as the exchange between virtual, rather than real photons.

2.3.2 Dexter Energy Transfer

Figure 2.3.1 (b) schematically depicts another type of energy transfer, which is based on short range electron exchange between interacting species. The exchange mechanism, often called *Dexter transfer*, is characterised by the exponentially decaying transfer rate with increasing separation between donor and acceptor molecules [27]

$$ k_{\rm ex} = \frac{2\pi}{h} {\rm K} e^{-(\frac{2r}{L_B})} \int_0^\infty I_{\rm norm}^D(\lambda) \epsilon_{\rm norm}^A \lambda d\lambda, \qquad (2.3.6) $$

here K is a constant, L_B is an average *Bohr's radius* and $\epsilon_{\rm norm}^A \lambda$ is the normalised absorption spectrum of the acceptor. Contrary to the resonant transfer, Dexter-type transfer allows energy migration between different spin states as long as the total spin of the system is kept constant. The exchange mechanism is relevant only at the very short distances (< 1 nm) as it is dependent on the orbital overlap. However, it is dominant for the spin forbidden transitions, such as $S_0 \to T_1$, as it is independent of the transition moments (oscillator strengths) of interacting molecules. For the allowed transitions, exchange interaction is also present, however it is dominated by the Coulombic interactions.
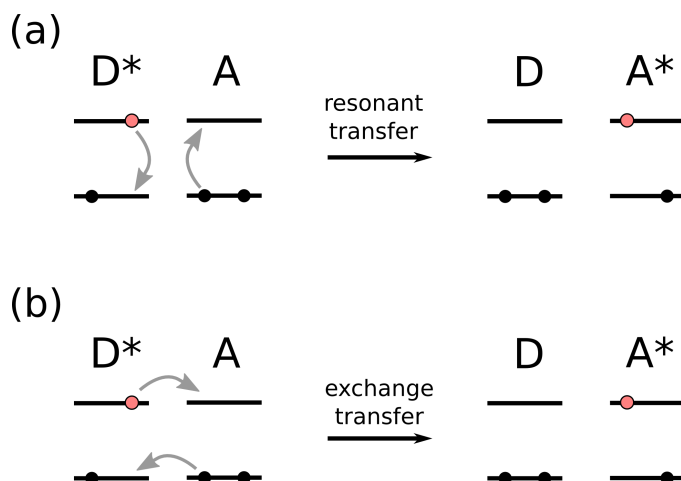

Figure 2.3.1: Schematic representation of main energy transfer mechanisms in organic solids: (a) Förster or resonant energy transfer and (b) Dexter or exchange mechanism.

2.4 Charge Transport Phenomena

As discussed previously in Section 2.1, organic solids are characterised by strong intramolecular interactions and relatively weak Van der Waals interactions between molecules. This is in stark contrast to the forces holding together the atoms in standard semiconductor crystals, composed of the elements from IV and III-V groups of the periodic table, bound by the sp^3 hybridized orbitals. The strong overlap between these orbitals leads to the energy splitting of the atomic energy levels resulting in the energy continuum representing the solid state. Occupation of those so-called energy bands by electrons are then used to consistently described the wide range of electronic and optical phenomena of semiconductor crystals. In contrast, due to the different nature of weak bonding between the constituents, charge transport in organic semiconductors is better described by the electron hopping or tunneling through the different perturbed energy levels attributed to separate molecules. Additionally, *polaronic* transfer effects, instead of free electron picture are better suited to account for the interaction between the charge and the environment in the solid state. Due to its complicated nature, charge transport phenomena in organic semiconductors need more sophisticated models as compared to the relatively simple band transport picture. The consistent theoretical description of charge transport in organic solids forms the field of study of its own, and the specifics of it is beyond the scope of this work. This section aims to summarise the most prominent features of describing the charge transport in organic semiconductors, which makes them distinct from the classical semiconducting materials. For a comprehensive review of the field of charge transport in organic semiconductors, the reader is referred to the reviews by Karl [28], Coropceanu *et al.* [29], and Tessler *et al.* [30].

2.4.1 Polarization and Energetic Disorder

The neutral molecular states can be ionised, i.e. loose an electron and become positively charged. The energy required to remove the electron from the molecule is called the *ionisation potential* of the molecule, E_{IP}^M. The energy released when electron is added to the molecule, is known as *electron affinity*, E_{EA}^M. The schematic of the energy levels for the single molecules in the gaseous state or in solution is depicted in Figure 2.4.1. The energy levels in the solution can be different to the situation in gas, since the interaction between the molecules and the environment (solvent molecules) might lead to the more stable potential energy configuration, leading to the downward shift in energy for electron (upward shift for holes), the effect known as *solvation*. Similarly, when considering the electronic states in the molecular solids, one has to account for the polarisation changes due to the
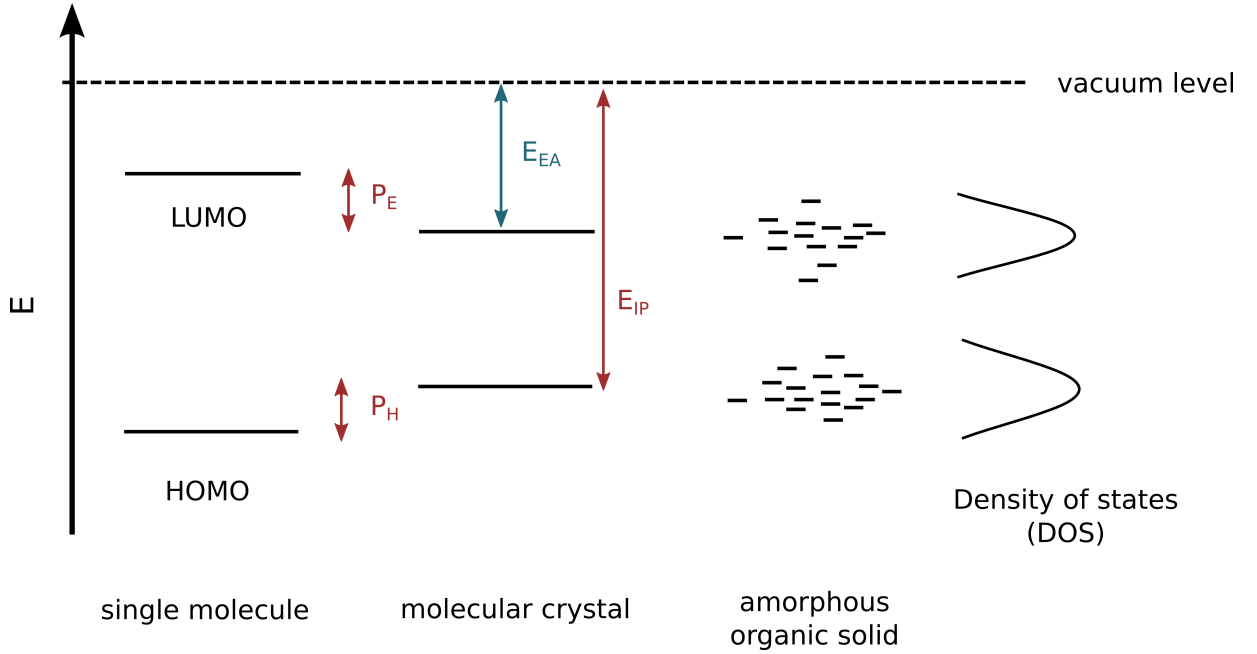
Figure 2.4.1: Schematic illustration of differences between electron energy states in single molecules, molecular crystals and amorphous solids.

environment, i.e. the electron density of the neighbouring molecules [31]. The energy level shift in the crystal for electrons and holes is characterised by the respective *polarisation energies* P_E and P_H (Figure 2.4.1). The polarisation energy P_H can be experimentally determined by comparing the ionisation potentials of the molecule in the gaseous and solid states

$$P_H = E_{\text{IP}}^M - E_{\text{IP}},\tag{2.4.1}$$

where E_{IP} is the ionisation potential of the molecular solid. As a first approximation, $P_E \approx P_H = P$ can be assumed. In such case, the energy gap E_g of the crystalline solid can be estimated to be

$$E_g = E_{\text{IP}} - E_{\text{IP}}^M - 2P.\tag{2.4.2}$$

Therefore, by measuring ionisation potential of solid, one can estimate the polarisation energy.

In crystalline solids, molecular interaction results in the splitting of the degenerate energy levels, which leads to the formation of the energy bands. However, in amorphous organic semiconductors, the molecular energy sites are localised in space due to the weak intermolecular interactions (Figure 2.4.1). The energetic disorder arises due to the vary-

ing spacing, orientation of different molecules. The energetic sites are described using a Gaussian density of states function

$$N(E) = \frac{N_{\text{eff}}}{\sqrt{2\pi\sigma_G^2}} \exp\left[- \frac{(E - E_0)^2}{2\sigma_G^2} \right], \tag{2.4.3}$$

which peaks around E_0 and has a width σ_G (which is ≈ 150 meV)Therefore, often transport via hopping through the separate energy levels, as opposed to the band transport, is used to describe the charge transport in organic semiconductors. The following section briefly describes two most successful models used to describe the hopping mechanism.

2.4.2 Charge Transport Models

Miller-Abrahams hopping rate is used to describe the rate of the charge carrier hopping between two states $\mathcal{E}_i$ and $\mathcal{E}_f$, separated by $r_{i,f}$, which is enabled by the thermal excitation

$$k_{i,f} = \nu_0 \exp\left(-2Jr_{i,f}\right) \begin{cases} \exp\left(- \frac{\mathcal{E}_f - \mathcal{E}_i}{k_B T} \right) & , \mathcal{E}_f > \mathcal{E}_i \\ 1 & , \mathcal{E}_f < \mathcal{E}_i, \end{cases} \tag{2.4.4}$$

where, ν_0 is the vibrational jump probability, J is the wavefunction overlap, assuming exponential decay (inverse localisation radius). In the case of applied electric field $\boldsymbol{E}$, for $\mathcal{E}_f > \mathcal{E}_i$, the expression of the hopping rate changes to

$$k_{i,f} = \nu_0 \exp\left(-2Jr_{i,f}\right) \exp\left(- \frac{(\mathcal{E}_f - \mathcal{E}_i - e\boldsymbol{E}\boldsymbol{r})}{k_B T} \right). \tag{2.4.5}$$

Using Miller-Abrahams formalism and Monte Carlo simulations, Bässler [32] was able to demonstrate the temperature dependence of the mobility of the charge carrier

$$\mu(T) = \mu_0 \exp\left[- \left(\frac{2\sigma}{3k_B T} \right)^2 \right] = \mu_0 \exp\left[- \left(\frac{T_0}{T} \right)^2 \right] \tag{2.4.6}$$

Also, dependence on square root of the electric field (*Poole-Frenkel law*) can also be demonstrated using similar approach

$$\mu = \mu_0 \exp(\gamma_T \sqrt{E}), \tag{2.4.7}$$

where

$$\gamma_T = \left[\frac{1}{k_B T} - \frac{1}{k_B T_0}\right].$$

(2.4.8)

However, Miller-Abrahams rate calculation does not include polaronic effects, that is, electron interaction with the environment during the transfer. To account for polaronic interactions, rate formalisms, based on *Marcus theory* of charge transfer is used

$$k_{i,f} = \frac{J_M^2}{\hbar} \frac{\pi}{\sqrt{2U_p k_B T}} \exp\left(-\frac{U_p}{2k_B T}\right) \exp\left(-\frac{\mathcal{E}_f - \mathcal{E}_i}{2k_B T} - \frac{(\mathcal{E}_f - \mathcal{E}_i)^2}{8k_B T U_p}\right),$$

(2.4.9)

where U_p is the polaron binding energy and J_M is function related to overlap integral J.

3 Electromagnetic Field Propagation in Layered Media

This chapter summarizes the properties of the electromagnetic field and its propagation in layered media relevant for the understanding of optical phenomena in OLEDs. A general overview of classical theory of the electromagnetic radiation propagation in a media based on a seminal work of Maxwell [33] is presented in Section 3.1. Following the discussion on boundary conditions of the electromagnetic field propagating at the interface between two media, Section 3.2 describes the reflection and transmission amplitudes in a stratified medium, essential for understanding light propagation within the organic semiconductor device. Guided optical modes and plasmonic excitations, two main contributions to the optical loss of the electroluminescent devices, are described in detail in Sections 3.3 and 3.4. If not stated otherwise, the description below follows the treatment found in [34] and [35].

3.1 Maxwell's Equations

Properties of electromagnetic field in a medium are described by four differential Maxwell equations. This is often referred to as the classical description as opposed to the treatment of quantum electrodynamics. The full quantum mechanical description of the electromagnetic field is beyond the scope of this work, as for most of the cases presented (*e.g.* optical modes in OLEDs, interaction of charges and electromagnetic fields), the classical framework is fully sufficient for a firm understanding of the involved phenomena. The four macroscopic Maxwell equations describing electric field strength $\boldsymbol{E}$ and magnetic field strength $\boldsymbol{H}$ in a medium with a dielectric constant ϵ and magnetic permeability μ can be

written in the following form

$$\nabla \cdot \boldsymbol{D} = \rho \tag{3.1.1}$$

$$\nabla \cdot \boldsymbol{B} = 0 \tag{3.1.2}$$

$$\nabla \times \boldsymbol{E} = -\frac{\partial \boldsymbol{B}}{\partial t} \tag{3.1.3}$$

$$\nabla \times \boldsymbol{H} = \boldsymbol{j} + \frac{\partial \boldsymbol{D}}{\partial t}, \tag{3.1.4}$$

where $\boldsymbol{D}$ and $\boldsymbol{B}$ denotes electric displacement and magnetic induction, respectively, ρ is charge density, $\boldsymbol{j}$ is the electrical current density and ∇ represents vector of partial derivative operators, $i.e.$ $\nabla = \left(\frac{\partial}{\partial x}, \frac{\partial}{\partial y}, \frac{\partial}{\partial z} \right)$. Electric and magnetic field strengths are connected to electric displacement and magnetic induction, respectively, by the following relations

$$\boldsymbol{D} = \epsilon_0 \boldsymbol{E} + \boldsymbol{P} = \epsilon \epsilon_0 \boldsymbol{E}, \tag{3.1.5}$$

$$\boldsymbol{B} = \frac{1}{\mu_0} \boldsymbol{H} - \boldsymbol{M} = \mu \mu_0 \boldsymbol{H}, \tag{3.1.6}$$

where $\boldsymbol{P}$ denotes electric dipole moment per unit volume (polarization density of the medium) and $\boldsymbol{M}$ denotes magnetic dipole moment per unit volume (magnetization density of the medium). ϵ_0 is the permittivity of vacuum ($\approx 8.859 \times 10^{-12}$ As/Vm) and μ_0 is permeability of vacuum ($\approx 4\pi \times 10^{-7}$ Vs/A). Equations (3.1.5) and (3.1.6), together with the *Ohm's law*, which can be stated in its differential form as

$$\boldsymbol{j} = \sigma \boldsymbol{E}, \tag{3.1.7}$$

are sometimes called *material relations* or *constitutive relations*, since they specify the response of the bound charges and currents within the material to the external electromagnetic field. σ in Eq. (3.1.7) denotes the conductivity of the material.

The physical interpretation of the Maxwell's equations (3.1.1)-(3.1.4) is as follows. Equation (3.1.1) represents the *Gauss law* (electric flux is directly proportional to the charge inside the closed surface), which is a direct consequence of the *Coulomb's law* of attraction or repulsion between two electric charges. Eq. (3.1.2) represents the fact that the magnetic field has no discrete sources, in contrast to the electric field, which is generated by point electric charges. This sometimes is referred to as *Gauss law for magnetism* in analogy to the first Maxwell's equation. Equations (3.1.3) and (3.1.4) relate electric and magnetic

fields. The former equation represents the *Faraday's law of induction*: a changing magnetic flux induces an electromotive force and therefore a current in a conductor. The latter equation is a representation of the *Ampere's law*, which states that electrical currents generate magnetic fields. The last term in the equation, namely $\frac{\partial \boldsymbol{D}}{\partial t}$, is called displacement current, and accounts for generation of the magnetic field by the varying electric field.

The classical description of the electromagnetic field is completed by *the Lorentz' law* and the charge continuity equation. The former states that the electromagnetic field exerts a mechanical force $\boldsymbol{F}$ on a charged particle in motion, with a charge q and a velocity $\boldsymbol{v}$. Lorentz's force is then

$$\boldsymbol{F} = q\big(\boldsymbol{E} + \boldsymbol{v} \times \boldsymbol{B}\big). \tag{3.1.8}$$

The current continuity equation can be derived from the fourth Maxwell's equation (3.1.4) by applying ∇ operator and having in mind that according to the Gauss' law $\nabla \cdot \boldsymbol{D} = \rho$ and also that $\nabla \cdot (\nabla \times \boldsymbol{X}) \equiv 0$ for arbitrary $\boldsymbol{X}$. Then one gets

$$\frac{\partial \rho}{\partial t} + \operatorname{div} \boldsymbol{j} = 0. \tag{3.1.9}$$

This shows that Maxwell equations are consistent with a charge conservation, one of the fundamental conservation laws.

3.1.1 Wave Character of Electromagnetic field

One of the most important consequences of the Maxwell's equations is the demonstration that the propagation of the electromagnetic field can be described by the wave equation. This can be shown for the electric field $\boldsymbol{E}$ by applying the curl operator $\nabla \times$ to Eq. (3.1.3). Taking into account definition of the magnetic induction (Eq. (3.1.6)) for the isotropic, non-magnetic material ($\mu = 1$) one gets:

$$\nabla \times \nabla \times \boldsymbol{E} = -\nabla \times \left(\frac{\partial \boldsymbol{B}}{\partial t}\right) = -\mu_0 \frac{\partial}{\partial t}\big(\nabla \times \boldsymbol{H}\big). \tag{3.1.10}$$

Using definition of $\boldsymbol{D}$ (Eq.(3.1.5)) and the relation (3.1.4) in the absence of the external currents ($\boldsymbol{j} = 0$), Equation (3.1.10) becomes

$$\nabla \times \nabla \times \boldsymbol{E} = -\mu_0 \epsilon_0 \epsilon \frac{\partial^2 \boldsymbol{E}}{\partial t^2}. \tag{3.1.11}$$

Finally, using vector identities $\nabla \times \nabla \times \boldsymbol{E} \equiv \nabla\left(\nabla \cdot \boldsymbol{E}\right) - \nabla^2 \boldsymbol{E}$ and $\epsilon \nabla \boldsymbol{E} \equiv \nabla\left(\epsilon \boldsymbol{E}\right) - \boldsymbol{E}\nabla\epsilon$, the relation (3.1.11) can be written as

$$\nabla\left(\nabla \cdot \boldsymbol{E}\right) - \nabla^2 \boldsymbol{E} = \nabla\left(\frac{1}{\epsilon}\left\{\nabla\left(\epsilon \boldsymbol{E}\right) - \boldsymbol{E}\nabla\epsilon\right\}\right) - \nabla^2 \boldsymbol{E} = -\mu_0 \mu\epsilon \frac{\partial^2 \boldsymbol{E}}{\partial t^2}. \tag{3.1.12}$$

In the isotropic case $\nabla\epsilon = 0$ and in the absence of external charges $\nabla \boldsymbol{D} = \epsilon_0 \epsilon \nabla \boldsymbol{E} = 0$, according to the Gauss law (Eq. (3.1.1)). Therefore, Equation (3.1.12) simplifies to the wave equation

$$\nabla^2 \boldsymbol{E} - \frac{\epsilon}{c^2}\frac{\partial^2 \boldsymbol{E}}{\partial t^2} = 0, \tag{3.1.13}$$

where $c = \frac{1}{\sqrt{\mu_0 \epsilon_0}}$ denotes propagation speed of the electromagnetic wave in vacuum, one of the fundamental constants of nature, equal to $c = 299792458 \text{ m/s} \approx 3 \cdot 10^8 \text{ m/s}$.

3.1.2 Energy of Electromagnetic Field

The energy law of the electromagnetic field can be derived in the following way. From Eqs. (3.1.3) and (3.1.4) one gets

$$\boldsymbol{E}(\nabla \times \boldsymbol{H}) - \boldsymbol{H}(\nabla \times \boldsymbol{E}) = (\boldsymbol{E} \cdot \boldsymbol{j}) + \boldsymbol{E}\frac{\partial \boldsymbol{D}}{\partial t} + \boldsymbol{H}\frac{\partial \boldsymbol{B}}{\partial t}. \tag{3.1.14}$$

Using vector identity $\text{div}\left(\boldsymbol{E} \times \boldsymbol{H}\right) \equiv \boldsymbol{H}(\nabla \times \boldsymbol{E}) - \boldsymbol{E}(\nabla \times \boldsymbol{H})$ to rewrite the right side of the equation and then integrating over the arbitrary volume V, Equation (3.1.14) becomes

$$\int\left(\boldsymbol{E}\frac{\partial \boldsymbol{D}}{\partial t} + \boldsymbol{H}\frac{\partial \boldsymbol{B}}{\partial t}\right)dV + \int(\boldsymbol{E} \cdot \boldsymbol{j})dV + \int \nabla(\boldsymbol{E} \times \boldsymbol{H})dV =$$
$$\int\left(\boldsymbol{E}\frac{\partial \boldsymbol{D}}{\partial t} + \boldsymbol{H}\frac{\partial \boldsymbol{B}}{\partial t}\right)dV + \int(\boldsymbol{E} \cdot \boldsymbol{j})dV + \int(\boldsymbol{E} \times \boldsymbol{H})\boldsymbol{n}dS = 0 \tag{3.1.15}$$

The last integral is obtained by applying the *Gauss theorem*, S denotes the surface defined by the boundary of the volume, over which the integral is evaluated and $\boldsymbol{n}$ is the unit vector pointing outward normal to the surface. Finally, using constitutive relations (Eqs. (3.1.5) and (3.1.6)), Eq. (3.1.15) becomes

$$\frac{\partial W}{\partial t} + \int(\boldsymbol{j} \cdot \boldsymbol{E})dV + \int(\boldsymbol{S} \cdot \boldsymbol{n})dS = 0, \tag{3.1.16}$$

where

$$W = \int (w_{\mathrm{e}} + w_{\mathrm{m}}) dV \tag{3.1.17}$$

is the total energy within the volume and

$$w_{\mathrm{e}} = \epsilon \epsilon_0 \frac{1}{2} \frac{\partial}{\partial t} (\boldsymbol{E} \cdot \boldsymbol{E}) \tag{3.1.18}$$

$$w_{\mathrm{m}} = \mu \mu_0 \frac{1}{2} \frac{\partial}{\partial t} (\boldsymbol{H} \cdot \boldsymbol{H}) \tag{3.1.19}$$

denotes electric and magnetic energy densities, respectively. The second term of the Eq.(3.1.16) is the resistive dissipation of energy, known as *Joule's heat*, while in the last term

$$\boldsymbol{S} = \boldsymbol{E} \times \boldsymbol{H} \tag{3.1.20}$$

is so-called *Poynting vector*. It describes the amount of energy which crosses per second a unit area normal to the directions of $\boldsymbol{E}$ and $\boldsymbol{H}$.

3.1.3 Boundary Conditions of Electromagnetic Fields

While Maxwell's equations describe the electromagnetic field in the regions of space where physical properties of the medium (characterized by ϵ and μ) are continuous, in most cases in optics, one has to deal with the discontinuities due to abrupt changes of material properties across one or more surfaces. When propagating through a boundary between a medium, characterized by ϵ_1 and μ_1, and a medium with ϵ_2 and μ_2, electromagnetic field is a subject to the boundary conditions. The boundary conditions for the electric and magnetic fields in the corresponding medium, respectively $\boldsymbol{E_{1,2}}$ and $\boldsymbol{H_{1,2}}$, are as follows:

$$\boldsymbol{e_n} \cdot (\boldsymbol{D_2} - \boldsymbol{D_1}) = \sigma \tag{3.1.21}$$

$$\boldsymbol{e_n} \cdot (\boldsymbol{B_2} - \boldsymbol{B_1}) = 0 \tag{3.1.22}$$

$$\boldsymbol{e_n} \times (\boldsymbol{E_2} - \boldsymbol{E_1}) = 0 \tag{3.1.23}$$

$$\boldsymbol{e_n} \times (\boldsymbol{H_2} - \boldsymbol{H_1}) = \boldsymbol{j}. \tag{3.1.24}$$

The vector $\boldsymbol{e_n}$ is the normal to the boundary surface. In case of no external charges present, (*i.e.* $\sigma = 0$ and $\boldsymbol{j} = 0$), equations 3.1.21 and 3.1.22 show that the normal components of $\boldsymbol{D}$ and $\boldsymbol{B}$ are continuous at the boundary. Similarly, equations 3.1.23 and 3.1.24 require

tangential components of $\boldsymbol{E}$ and $\boldsymbol{H}$ to be continuous at the boundary.

3.2 Reflection and Refraction of Plane Waves

When electromagnetic wave passes from one medium to the other, with differing optical constants, it undergoes partial reflection and transmission. The corresponding amplitudes can be evaluated based on the boundary conditions of the electromagnetic field described in the previous section. Considering the simplest case of a plane wave, which has a wavefront defined by $\boldsymbol{k} \cdot \boldsymbol{r} = const$, where $\boldsymbol{r}$ is the position vector and $\boldsymbol{k} = nk_0\boldsymbol{e_i}$ is the wave vector of the wave propagating in a medium with a refractive index n. e_i is the unit vector fixed in a direction of a propagating wave. Further, a perfectly planar and infinite boundary between two media described by ϵ_1, μ_1 and ϵ_2, μ_2 is considered, depicted in Figure (3.2.1). The planarity condition is fulfilled as long as the curvature radius of the interface is much higher than the wavelength of the incoming electromagnetic wave.
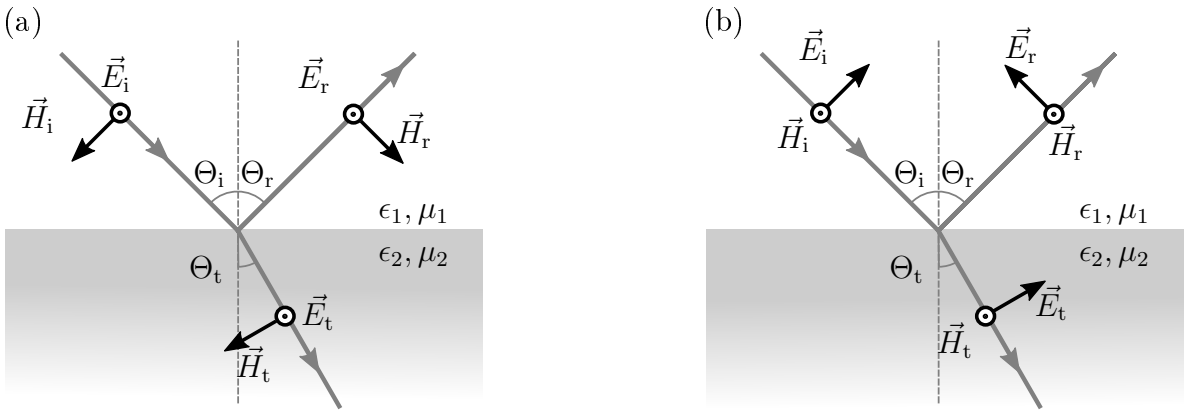

Figure 3.2.1: Electromagnetic field propagation at an interface of two dielectric materials, characterised by $\epsilon_{1,2}$ and $\mu_{1,2}$. Electric and magnetic field vector directions are depicted for incident E_i, H_i, relfected E_r, H_r and transmitted fields E_t, H_t directions, respectively, for (a) s- and (b) p-polarized light.

Let $\boldsymbol{k_i}$, $\boldsymbol{k_r}$ and $\boldsymbol{k_t}$ be wave vectors of incident, reflected and transmitted waves. Field continuity requires at $\boldsymbol{r} = (x, y, 0)$

$$\boldsymbol{k_i} \cdot \boldsymbol{r} = \boldsymbol{k_t} \cdot \boldsymbol{r} = \boldsymbol{k_r} \cdot \boldsymbol{r}. \tag{3.2.1}$$

For the tangential components of the wave vectors of the incident and reflected fields, this leads to $n_1 \sin \Theta_i = n_1 \sin \Theta_t \Rightarrow \Theta_t = \Theta_t$. This, together with the result from Eq.(3.2.1)

that $\boldsymbol{k_i}$ and $\boldsymbol{k_t}$ lie in the same plane, known as *the plane of incidence*, constitutes what is called *the law of reflection*. Similarly, for the tangential components of $\boldsymbol{k_i}$ and $\boldsymbol{k_t}$

$$n_1 \sin \Theta_i = n_2 \sin \Theta_t, \tag{3.2.2}$$

which is known as *the Snell's law*. Without a loss of generality the planar wave can be described as a superposition of two perpendicularly polarized fields. In case of TE (transverse electric) or s-polarized wave (from German word *senkrecht* for *perpendicular*) the electric field vector is lying perpendicular to the plane of incidence (Fig. 3.2.1(a)). In TM (transverse magnetic) or p-polarization (for parallel) the magnetic field is perpendicular to the plane of incidence while electric field is lying parallel to it (Fig. 3.2.1(b)). Boundary conditions (Eqs. (3.1.23-3.1.24)) require continuity of the tangential components E_x, E_y, H_x and H_y at the interface. For the s-polarized wave this leads to

$$E_i + E_r = E_t \text{ , and} \tag{3.2.3}$$

$$\sqrt{\frac{\epsilon_1}{\mu_1}}(E_i - E_r) \cos \Theta_i = \sqrt{\frac{\epsilon_1}{\mu_1}} E_t \cos \Theta_t. \tag{3.2.4}$$

The latter equation results from the continuity of $\boldsymbol{H}$ field components and the relation between electric and magnetic field strength (Eq.(3.1.4)), rewritten for the case of planar waves ($\nabla \times \rightarrow i\boldsymbol{k}\times$) with harmonically varying amplitudes ($\frac{\partial}{\partial t} \rightarrow -i\omega$):

$$\boldsymbol{H} = \sqrt{\frac{\epsilon}{\mu}} \frac{\boldsymbol{k}}{k} \times \boldsymbol{E}. \tag{3.2.5}$$

Then, defining reflection (transmission) coefficient r_s (t_S) as a ratio between reflected (transmitted) and incident field amplitude, leads to

$$r_s = \left(\frac{E_r}{E_i}\right) = \frac{n_1 \cos \Theta_i - n_2 \cos \Theta_t}{n_1 \cos \Theta_i + n_2 \cos \Theta_t} \tag{3.2.6}$$

$$t_s = \left(\frac{E_t}{E_i}\right) = \frac{2n_1 \cos \Theta_i}{n_1 \cos \Theta_i + n_2 \cos \Theta_t} \tag{3.2.7}$$

Similarly, for p-polarized wave, applying boundary conditions leads to:

$$(E_\mathrm{i} - E_\mathrm{r}) \cos \Theta_\mathrm{i} = E_\mathrm{t} \cos \Theta_\mathrm{t}, \tag{3.2.8}$$

$$\sqrt{\frac{\epsilon_1}{\mu_1}}(E_\mathrm{i} + E_\mathrm{r}) = \sqrt{\frac{\epsilon_2}{\mu_2}} E_\mathrm{t}. \tag{3.2.9}$$

Then, the corresponding reflection and transmission coefficients are:

$$t_\mathrm{p} = \frac{2n_1 \cos \Theta_\mathrm{i}}{n_2 \cos \Theta_\mathrm{i} + n_1 \cos \Theta_\mathrm{t}} \tag{3.2.10}$$

$$r_\mathrm{p} = \frac{n_2 \cos \Theta_\mathrm{i} - n_1 \cos \Theta_\mathrm{t}}{n_2 \cos \Theta_\mathrm{i} + n_1 \cos \Theta_\mathrm{t}} \tag{3.2.11}$$

Equations (3.2.6), (3.2.7), (3.2.11) and (3.2.10) are collectively known as *Fresnel formulae* and corresponding ratios r_s, r_p and t_s, t_p are called Fresnel reflection and transmission coefficients, respectively. While Fresnel coefficients describe the ratios of the reflected and the transmitted wave to the amplitude of the incident wave, amplitude of the propagating field is not accessible in an experiment. Instead, the energy of the propagating field can be measured, which is proportional to the square of the electric field strength, as can be shown using by the time-averaged Poynting's vector (Eq.(3.1.20)). For a plane wave with a real wave vector:

$$\boldsymbol{S} = \frac{\boldsymbol{k}}{2\omega\mu}|\boldsymbol{E}|^2. \tag{3.2.12}$$

Then, defining experimentally measured reflectance R and transmittance T as a ratio between the normal component of the Poynting vector of a reflected or transmitted field, $S_{r,x}$ or $S_{t,x}$, respectively and that of the incident field $S_{t,x}$, one gets

$$R_s = |r_s|^2 \text{ , and } R_p = |r_p|^2 \tag{3.2.13}$$

$$T_s = \frac{n_2 \cos \Theta_t}{n_1 \cos \Theta_r}|t_s|^2, \tag{3.2.14}$$

$$T_p = \frac{n_2 \cos \Theta_t}{n_1 \cos \Theta_r}|t_p|^2, \tag{3.2.15}$$

where subscripts s and p denote corresponding polarization state.

3.2.1 Total Internal Reflection

In case the light is propagating from an optically denser medium n_1 into an optically less dense medium n_2, *i.e.* $n_1 > n_2$ in Fig. 3.2.1, according to the Snell's law (Eq.3.2.2), at higher angle of incidence

$$\sin \Theta_{\mathrm{ic}} = \frac{n_2}{n_1} = n, \tag{3.2.16}$$

where Θ_{ic} is the critical angle at which $\sin \Theta_{\mathrm{t}} = 1$. When incident light exceeds the critical value, no light propagates in the second medium and so such situation is known as *Total internal reflection.* The electric field in the less optically dense medium n_2 can be written as

$$\boldsymbol{E_{\mathrm{t}}} = \boldsymbol{E_0} e^{i(\omega t - \boldsymbol{k} \cdot \boldsymbol{r})} = \boldsymbol{E_0} e^{i(\omega t - k_x x - k_z z)} = \boldsymbol{E_0} e^{i(\omega t - |k| x \sin \Theta_{\mathrm{t}} - |k| z \cos \Theta_{\mathrm{t}})} \tag{3.2.17}$$

Following Snell's law:

$$\sin \Theta_{\mathrm{t}} = \frac{\sin \Theta_{\mathrm{i}}}{n} \text{ and} \tag{3.2.18}$$

$$\cos \Theta = \sqrt{1 - \sin^2 \Theta_{\mathrm{t}}} = \pm i \sqrt{(\frac{\sin^2 \Theta_{\mathrm{i}}}{n} - 1)}. \tag{3.2.19}$$

The last equation is written, having in mind, that then $\Theta_{\mathrm{i}} > \Theta_{\mathrm{c}}$, and $\sin \Theta_{\mathrm{t}} > 1$. Since the propagation vector component in z direction is purely imaginary, the electric field decays exponentially into the optically less dense media:

$$E_{\mathrm{t}} = E_{\mathrm{t}0} e^{-i(\omega t - \frac{|k| x}{n} \sin \Theta_{\mathrm{i}})} e^{-\frac{|k| z}{L}} \tag{3.2.20}$$

with a decay length L:

$$L = \left(\sqrt{\frac{\sin^2 \Theta_{\mathrm{i}}}{n^2} - 1} \right)^{-1} \tag{3.2.21}$$

The Fresnel reflection coefficients in the optically dense medium for TE and TM polarized

radiation reads

$$r_{\mathrm{s}} = \frac{\cos\Theta_{\mathrm{i}} - i\sqrt{\sin^2\Theta_{\mathrm{i}} - n^2}}{\cos\Theta_{\mathrm{i}} + i\sqrt{\sin^2\Theta_{\mathrm{i}} - n^2}} \tag{3.2.22}$$

$$r_{\mathrm{p}} = \frac{n^2\cos\Theta_{\mathrm{i}} - i\sqrt{\sin^2\Theta_{\mathrm{i}} - n^2}}{n^2\cos\Theta_{\mathrm{i}} + i\sqrt{\sin^2\Theta_{\mathrm{i}} - n^2}}. \tag{3.2.23}$$

$$\tag{3.2.24}$$

Then, experimentally relevant reflectance value, according to Eq. (3.2.14), is $R_{\mathrm{s,p}} = 1$, for both s- and p-polarized light. Hence, upon the total internal reflection all of the light is reflected back to the optically dense medium. However, the field also extends into the medium with lower refractive index and decays exponentially with a characteristic decay length usually in the range of $10 - 100$ nm. As will be discussed in the following section, this so-called *evanescent* field decay gives rise to the ways of coupling the radiation into or out of the waveguiding structure.

3.3 Guided Optical Waves

As demonstrated in the previous section, when light travels from a material with a high optical density to a low optical density medium, total internal reflection occurs at the boundary between the two media, when the angle of the incident light exceeds the critical value. In case the film of high refractive index n_{f} is sandwiched between layers of lower refractive indexes n_{c} and n_{s}, called the cover and the substrate, respectively, under certain conditions total internal reflection can occur on both sides of the film. Depending on the geometry, this leads to the field being trapped inside one or two dimensions, allowing wave propagation only in the lateral direction. Therefore, such a structure is called a *waveguide*. From the perspective of the wave theory, only certain discrete solutions exist for the standing wave pattern inside the waveguide, corresponding to the constructive interference of waves reflected from the two boundaries. These solutions of the wave equation (3.1.13) corresponds to the so called optical modes, which are characterized by the spatial distribution of the optical energy that remain constant in time. In the following, complete electromagnetic field description of the guided fields inside the planar slab guide is discussed. Simplified ray optics approach is also briefly mentioned for a more intuitive picture of the problem. The planar waveguide represents the most primitive problem for the guided electromagnetic fields, however, despite its relative simplicity, it is also one of the most common examples encountered in the practical applications, and good familiarity

with the planar guides are a prerequisite for a good understanding of the optical losses in the OLEDs, as well as integrated sensing applications, discussed in the forthcoming chapters. Most of the following is based on [36, 37].

3.3.1 Modes of Planar Waveguide

Assuming harmonic time dependence of the electric field $\boldsymbol{E}(\boldsymbol{r}, t) = \boldsymbol{E}(\boldsymbol{r})e^{iwt}$ for the monochromatic waves with a frequency ω, wave equation Eq. (3.1.13) becomes

$$\nabla^2 \boldsymbol{E} + k_0^2 n^2 \boldsymbol{E} = 0, \tag{3.3.1}$$

where $k_0 = \frac{w}{c}$ is the wave vector of the propagating wave in vacuum and $n = \sqrt{\epsilon}$ is the refractive index of the material. Equation (3.3.1) is known as *Helmholtz equation*.
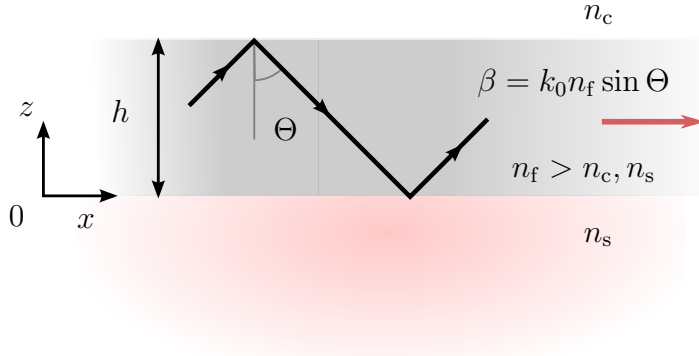
Figure 3.3.1: Electromagnetic wave propagation in a waveguide structure. See text for details.

Further, defining the propagation geometry as depicted in the Figure 3.3.4, for the plane wave with a propagation constant $\beta = n_f k_0 \sin \Theta$ travelling in the x direction $\boldsymbol{E}(\boldsymbol{r}) = \boldsymbol{E}(y, z)e^{-i\beta x}$, Equation (3.3.1) becomes

$$\frac{\partial^2 \boldsymbol{E}(y, z)}{\partial y^2} + \frac{\partial^2 \boldsymbol{E}(y, z)}{\partial z^2} + (k_0^2 n^2 - \beta^2)\boldsymbol{E}(y, z) = 0. \tag{3.3.2}$$

Similar relation also holds for the magnetic field strength $\boldsymbol{H}$. For the sake of simplicity the waveguide is assumed to be infinite in the y direction, so that the field along this direction is constant ($\frac{\partial}{\partial y} = 0$). Therefore, rewriting Eq. (3.3.2) for the three separate regions in z
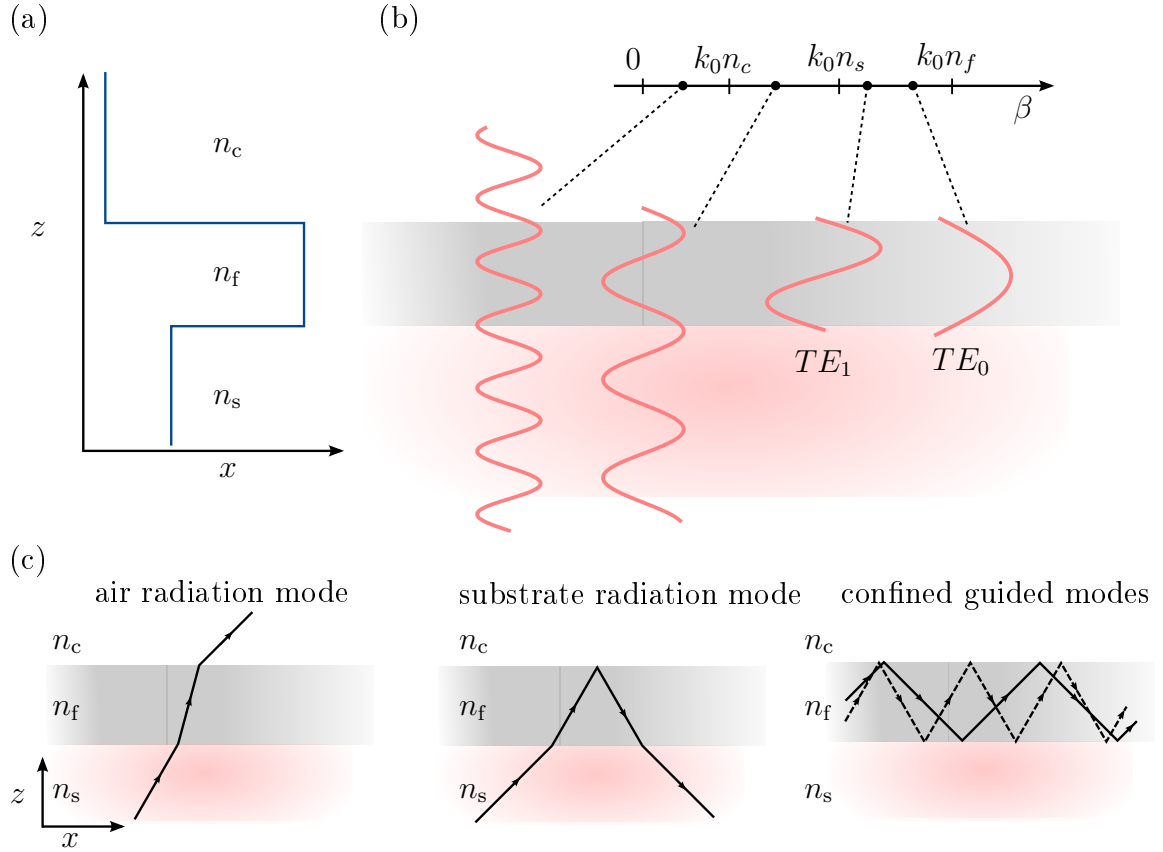
Figure 3.3.2: (a) Refractive index profile of a waveguide structure comprising cover layer with refractive index n_c, substrate (n_s), and core film $(n_f > n_s, n_c)$. (b) Solutions of the wave equation for the electric field distribution $E(z)$ and corresponding propagation constant β values for air radiation mode $(0 < \beta < k_0 n_c)$, substrate radiation mode $(k_0 n_c < \beta < k_0 n_s)$, and guided modes confined in the core layer $(k_0 n_s < \beta < k_0 n_f)$ for the TE polarised light. Solutions for $\beta > k_0 n_f$ are omitted as they are not physically realisable. (c) Ray optics picture of the modes described in (b).

and skipping notation for the electric field dependence on y, one gets

$$\frac{\partial^2 \boldsymbol{E}(z)}{\partial z^2} + (k_0^2 n_c^2 - \beta^2)\boldsymbol{E}(z) = 0 \quad , \text{for } z > h, \tag{3.3.3}$$

$$\frac{\partial^2 \boldsymbol{E}(z)}{\partial z^2} + (k_0^2 n_f^2 - \beta^2)\boldsymbol{E}(z) = 0 \quad , \text{for } 0 < z < h, \tag{3.3.4}$$

$$\frac{\partial^2 \boldsymbol{E}(z)}{\partial z^2} + (k_0^2 n_s^2 - \beta^2)\boldsymbol{E}(z) = 0 \quad , \text{for } z < 0. \tag{3.3.5}$$

Electromagnetic field profile in each of the regions of x is then accessed by solving each of the corresponding differential equations (3.3.3)-(3.3.5), whose solutions are oscillatory if $(k_0^2 n_i^2 - \beta^2) > 0$ and exponential if $(k_0^2 n_i^2 - \beta^2) < 0$, where $i = c, f, s$. Solutions of

46

the above equations are depicted in Figure 3.3.2. The refractive index profile is shown in Figure 3.3.2 (a). Corresponding electric field distribution for both radiation and waveguide modes, together with the corresponding propagation constant values is depicted in Figure 3.3.2 (b). *Air radiation modes* are represented by the oscillatory solutions for $E(z)$ in all three regions. Such modes are not considered to be confined, as the energy is free to spread out of the core region. *Substrate radiation modes* are confined at the interface with cover region (usually air), and propagate in the substrate. There is a continual loss of energy from the waveguide core region to substrate, therefore light in the core region is damped out over a short distances. For these reasons, substrate radiation modes are not useful for signal transmission, however they may be employed in coupler applications (e.g. tapered coupler [38]). Finally, solutions to the wave equation for the propagation constant values $k_0 n_s < \beta < k_0 n_f$ represents situation where $E(z)$ is confined at both interfaces. The number of the possible waveguide modes is determined by the core layer thickness, and polarisation and wavelength of the light wave. Figure 3.3.2 (b) shown first two modes for the TE polarised field, TE$_0$, also known as *fundamental mode* and TE$_1$. It should be noted, that solutions for propagation constant $\beta > k_0 n_f$ do exist. However, in such case, $E(z)$ must be exponential in all three regions. This leads to the exponentially increasing electric field outside the core region, which ultimately leads to the infinite energy values, and therefore such solutions are not physically realisable.

The explanation of the solution can be easily understood considering ray optics picture, shown in Figure 3.3.2 (c). For the case of air radiation modes, the propagation angle Θ in the core film is lower than the critical value Θ_c for both interfaces. Therefore total internal reflection does not occur and guiding of light is not possible. For the substrate radiation mode, TIR occurs at core/cover interface, and $\Theta \geq \arcsin(n_c/n_f)$. For the guided modes TIR occurs at both interfaces and $\Theta \geq \arcsin(n_s/n_f)$. While ray optics picture offers an intuitive explanation, wave optics approach will be used from now on to describe guided modes, as it offers more complete picture, especially when the optically lossy media is considered.

For the guided waves, one expects to find propagating wave solutions in the $0 < z < h$ region and exponentially decaying fields in $x > h$ and $x < 0$. Hence, it is reasonable to define the propagation constant of the guided mode as

$$\kappa_f = k_0^2 n_f^2 - \beta^2, \tag{3.3.6}$$

with the corresponding decay constants for the electric field at film/cover and substrate/film

interfaces:

$$\gamma_c = \beta^2 - k_0^{c2}, \tag{3.3.7}$$

$$\gamma_s = \beta^2 - k_0^2 n_s^2. \tag{3.3.8}$$

For the TE polarized field ($H_y = E_x = E_z = 0$), using the curl relation for the electric field (Eq. (3.1.3)), one can write

$$\beta E_y = \omega\mu H_z, \tag{3.3.9}$$

$$\frac{\partial E_y}{\partial z} = i\omega\mu H_x, \tag{3.3.10}$$

with E_y component obeying the wave equation

$$\frac{\partial^2 E_y}{\partial z^2} = (\beta^2 - n^2 k_0^2)E_y. \tag{3.3.11}$$

For the guided modes we have

$$E_y = \begin{cases} E_c e^{-\gamma_c(z-h)}, \text{ for } z < h, \\ E_f \cos(\kappa_f z - \phi_s), \text{ for } 0 < z < h, \\ E_s e^{\gamma_s z}, \text{ for } z < 0. \end{cases} \tag{3.3.12}$$

The boundary conditions require continuity of E_y and $\frac{\partial E_y}{\partial z}$ across the film boundaries at $z = 0$ and $z = h$. Application of the boundary conditions yields the dispersion relation for the guided modes:

$$\kappa_f h - \phi_s - \phi_c = \pi\nu, \text{ with } \nu = 0, 1, 2... \tag{3.3.13}$$

with the corresponding phase shifts at the interfaces

$$\phi_s = \arctan\left(\frac{\gamma_s}{\kappa_f}\right), \tag{3.3.14}$$

$$\phi_c = \arctan\left(\frac{\gamma_c}{\kappa_f}\right), \tag{3.3.15}$$

and a relation between the peak electric fields:

$$E_f^2(n_f^2 - N_{eff}^2) = E_s^2(n_f^2 - n_s^2) = E_c^2(n_f^2 - n_c^2), \tag{3.3.16}$$

where $N_{\mathrm{eff}} = \beta/k_0$ is called effective refractive index. Similarly, by writing Eq.(3.1.3) explicitly for the TM modes ($E_y = 0, H_x = 0$ and $H_z = 0$) one gets

$$E_z = i\frac{1}{\omega\epsilon_0\epsilon}\frac{\partial H_y}{\partial z}, \tag{3.3.17}$$

$$E_x = \frac{\beta}{\omega\epsilon_0\epsilon}H_y, \tag{3.3.18}$$

with H_y component obeying the wave equation

$$\frac{\partial^2 H_y}{\partial z^2} = (\beta^2 - n^2 k_0^2)H_y. \tag{3.3.19}$$

The field solutions for the modes guided in the film are

$$H_y(z) = \begin{cases} H_{\mathrm{c}}e^{-\gamma_{\mathrm{c}}(z-h)} \text{ for } z < h, \\ H_{\mathrm{f}}\cos(\kappa_{\mathrm{f}}z - \phi_{\mathrm{s}}) \text{ for } 0 < z < h, \\ H_{\mathrm{s}}e^{\gamma_{\mathrm{s}}z} \text{ for } z < 0. \end{cases} \tag{3.3.20}$$

Using the boundary conditions at $z = 0$ and $z = h$, which demand continuity of both, H_y and $n^{-2}\frac{\partial H_y}{\partial z}$, dispersion relation, similar to Eq. (3.3.13) for the TM guided modes is derived, with the corresponding phase shifts:

$$\phi_{\mathrm{s}} = \arctan\left[\left(\frac{n_{\mathrm{f}}}{n_{\mathrm{s}}}\right)^2\frac{\gamma_{\mathrm{s}}}{\kappa_{\mathrm{f}}}\right], \tag{3.3.21}$$

$$\phi_{\mathrm{c}} = \arctan\left[\left(\frac{n_{\mathrm{f}}}{n_{\mathrm{c}}}\right)^2\frac{\gamma_{\mathrm{c}}}{\kappa_{\mathrm{f}}}\right] \tag{3.3.22}$$

Figure 3.3.3 shows allowed modes calculated for a $\lambda = 407$ nm light traveling in a planar waveguide, comprising of TiO_2 core sandwiched between SiO_2 and air, for different core thickness h values. As this case represents the asymmetric waveguide, mode cut-off thickness exists $\lambda_{\mathrm{cut-off}}$, below which no modes are supported. Shown in Fig.3.3.3, $d_{\mathrm{cut-off}} \approx 30$ nm for s-polarised light, and $d_{\mathrm{cut-off}} \approx 50$ nm for p-polarised light. Below *ca.* 120 nm only one mode is supported in SiO_2/TiO_2/air structure, and as will be elaborated further in the results section, this makes it interesting for use in sensing applications.

3.3.2 Multilayer Waveguides

It is not convenient to solve Maxwell's equations and calculate Fresnel coefficients for each interface when the number of interfaces of interest is high. Instead, so-called transfer matrix approach is used for numerical calculations of the relevant optical properties of the layered
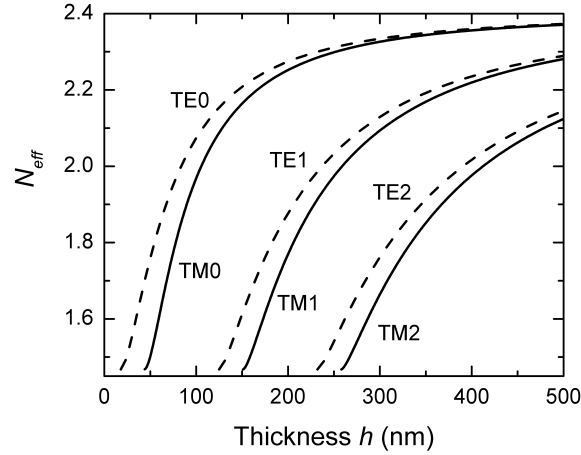
Figure 3.3.3: Modes of the planar waveguide, consisting of TiO$_2$ core film and SiO$_2$ substrate layer. N_{eff} is the effective refractive index of the waveguide film, $N_{\text{eff}} = \beta/k_0$. The allowed modes at different core layer thickness values d were calculated according to the dispersion relation Eq. (3.3.13) for TM (black solid line) and TE (black dashed line) modes for $\lambda = 407$ nm light.

media. For a thorough treatment of the method, the reader is referred to [34, 39]. Here we give an example for the s-polarized light of how transfer-matrix algorithm is used to calculate transmission and reflection coefficients for a structure with an arbitrary number of layers, together with a discussion about calculation of waveguide modes in a multilayer system.

Starting with the Eqs. (3.3.9)-(3.3.10) for TE polarized light and defining the field parameters which are continuous at the interfaces as $U = E_y$ and $V = \omega\mu H_x$, one can shown that the wave equation (Eq.(3.3.11)) has a solution of the form

$$U = Ae^{-i\kappa z} + Be^{i\kappa z} \tag{3.3.23}$$

$$V = \kappa\big(Ae^{-i\kappa z} - Be^{i\kappa z}\big), \tag{3.3.24}$$

where $\kappa^2 = n^2 k_0^2 - \beta^2$ is the propagation constant of the layer. It is clear that A and B describe the amplitudes of the field propagating in $+z$ and $-z$ direction, respectively. The light propagation in the layer then can be described by the matrix equation

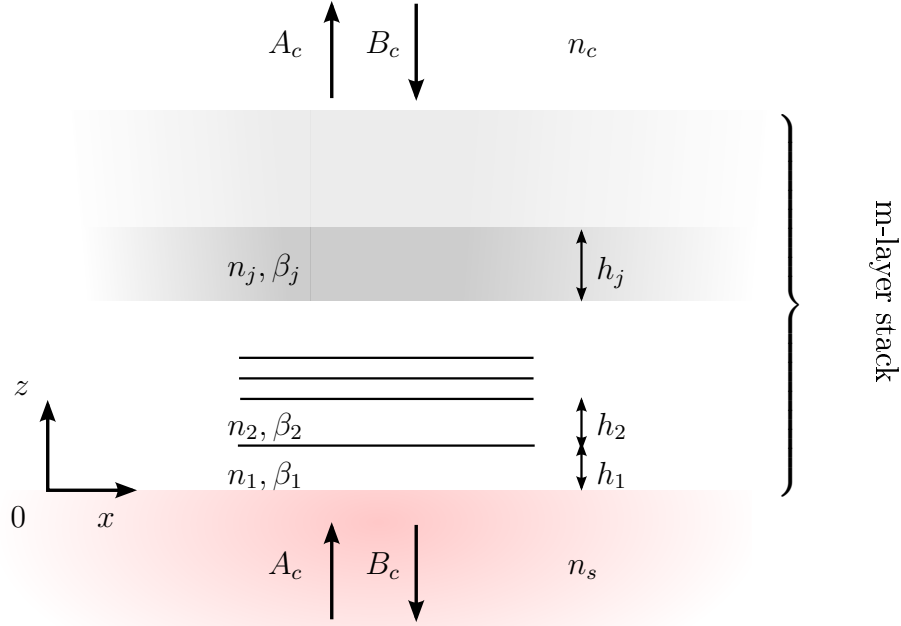$$\begin{pmatrix} U_0 \\ V_0 \end{pmatrix} = M \begin{pmatrix} U \\ V \end{pmatrix}, \tag{3.3.25}$$

Figure 3.3.4: Multilayer stack with arbitrary layer thicknesses used for transfer-matrix method calculations.

where U_0 and V_0 are the input field variables, defined at $z = 0$ and

$$M = \begin{vmatrix} \cos(\kappa z) & \left(\frac{i}{\kappa}\right)\sin(\kappa z) \\ i\kappa\sin(\kappa z) & \cos(\kappa z) \end{vmatrix} \tag{3.3.26}$$

is the characteristic matrix of the layer. For a stack of n layers sandwiched between n_s and n_c, one can then write for $j-$layer the characteristics matrix equation

$$\begin{pmatrix} U_{j-1} \\ V_{j-1} \end{pmatrix} = M_j \begin{pmatrix} U_j \\ V_j \end{pmatrix}, \tag{3.3.27}$$

where

$$M_j = \begin{vmatrix} \cos(\kappa_j h_j) & \left(\frac{i}{\kappa_j}\right)\sin(\kappa_j h_j) \\ i\kappa_j\sin(\kappa_j h_j) & \cos(\kappa_j h_j) \end{vmatrix} \tag{3.3.28}$$

is the matrix of $j-$layer and h_j, n_j and $\kappa_j^2 = n_j^2 k_0^2 - \beta_j^2$ are thickness, refractive index and the propagation constant in the respective layer. Using the matrix manipulation, one arrives at the final input-output relationship between incident field variables U_0 and V_0 and

field leaving the n-layered structure U_n, V_n using transfer matrix approach, which reads

$$\begin{pmatrix} U_0 \\ V_0 \end{pmatrix} = \bar{M} \begin{pmatrix} U_n \\ V_n \end{pmatrix}. \tag{3.3.29}$$

Here,

$$\bar{M} = \prod_{j=1}^{n} M_j = \begin{vmatrix} m_{11} & m_{12} \\ m_{21} & m_{22} \end{vmatrix}. \tag{3.3.30}$$

is the characteristics matrix of the multi-layer stack. The corresponding transmission and reflection coefficients are then calculated using the matrix elements of the characteristic matrix $\bar{M}$ and propagation constants of the surrounding media, $\kappa_{\rm s}$ and $\kappa_{\rm c}$, respectively.

$$t = \frac{2\kappa_{\rm s}}{m_{21} + m_{11}\kappa_{\rm s} + m_{22}\kappa_{\rm c} + m_{12}\kappa_{\rm c}\kappa_{\rm s}} \tag{3.3.31}$$

$$\tag{3.3.32}$$

$$r = -\frac{t}{2\kappa_{\rm s}} \Big(m_{21} + m_{22}\kappa_{\rm c} - m_{11}\kappa_{\rm s} - m_{12}\kappa_{\rm c}\kappa_{\rm s} \Big). \tag{3.3.33}$$

Following similar procedure, waveguide modes in the multilayer structures are calculated assuming exponentially decaying rather than propagating fields outside the layered structure. The solutions to the wave equation then reads

$$U = Ae^{\gamma z} + Be^{\gamma z} \tag{3.3.34}$$

$$V = i\gamma\big(Ae^{\gamma z}\big), \tag{3.3.35}$$

with decay constants defined as before $\gamma = -\kappa$. The field solutions outside the waveguide becomes $U_0 = A_s$, $V_0 = i\gamma_{\rm s}A_s$ and $U_n = B_c$, $V_n = -i\gamma_{\rm c}B_c$, with $\gamma_{\rm c}$ and $\gamma_{\rm s}$ defined in Eq.(3.3.8) and (3.3.8), respectively. Feeding this into the matrix relation (3.3.29) leads to the general dispersion relation

$$i(\gamma_{\rm s}m_{11} + \gamma_{\rm s}\gamma_{\rm c}m_{12}) = m_{21} - i\gamma_{\rm c}m_{22}. \tag{3.3.36}$$

The preceding discussion on TE polarised field propagation can be easily extended to account for TM modes in the multilayer stack, with the aid of a simple substitution. For the TM modes, one has $E_y = H_x = H_z = 0$. Then, defining the field variables as $U = H_y$

and $V = \omega\epsilon_0 E_x$, one arrives at the general solution to a traverse wave equation (3.3.19):

$$U = Ae^{-i\kappa z} + Be^{i\kappa z} \tag{3.3.37}$$

$$V = -\left(\frac{\kappa}{n^2}\right)\left[Ae^{-i\kappa z} - Be^{i\kappa z}\right]. \tag{3.3.38}$$

Comparing the latter expressions to the result for the TE modes (Eq.(3.3.24)), one can see that a simple substitution applied to the propagation and decay constants, namely

$$TE \to TM, \tag{3.3.39}$$

$$\kappa \to -\left(\frac{\kappa}{n^2}\right), \tag{3.3.40}$$

$$\gamma \to -\left(\frac{\gamma}{n^2}\right) \tag{3.3.41}$$

leads to the similar expression of the general solution. This means that all of the results obtained from solving wave equation for TE modes are also valid for the TM case after applying the substitution described in Eq.(3.3.40)-(3.3.41). For example, the corresponding dispersion relation for the TM modes

$$-i\left(m_{11}\frac{\gamma_{\mathrm{s}}}{n_{\mathrm{s}}^2} + m_{22}\frac{\gamma_{\mathrm{c}}}{n_{\mathrm{c}}^2}\right) = m_{21} - \left(\frac{\gamma_{\mathrm{s}}\gamma_{\mathrm{c}}}{n_{\mathrm{s}}^2 n_{\mathrm{c}}^2}\right)m_{21}. \tag{3.3.42}$$

Here, the matrix elements representing the multilayer stack can be calculated from the multiplication of the characteristics matrices for the $j-$layer, which can be calculated from

$$M_j = \begin{vmatrix} \cos(\kappa_j h_j) & -i\left(\frac{n_j^2}{\kappa_j}\right)\sin(\kappa_j h_j) \\ -i\left(\frac{\kappa_j}{n_j^2}\right)\sin(\kappa_j h_j) & \cos(\kappa_j h_j). \end{vmatrix} \tag{3.3.43}$$

It should be noted, that the substitution Eq.(3.3.40)-(3.3.41) is applied only to the prefactor terms and should not be applied for the phase terms, as these are identical for general solutions for TE and TM modes.

3.3.3 Mode Coupling

From the theory point of view, the problem of light coupling into the waveguide is similar to that of light out-coupling from the waveguide structure. The difference arises only then considering experimental techniques used to achieve in- or out-coupling of the radiation.

In order to couple the light into or out of the waveguide structure, phase matching condition $k_z = \beta$ for the incoming and guided light has to be fulfilled. It can be written

explicitly as

$$nk_0 \sin \Theta = n_{\text{core}} k_0 \sin \Theta_{\text{core}}, \tag{3.3.44}$$

where k_0 is the wave vector, n and n_{core} denotes refractive indexes of outer and core layers, Θ is the incident angle of light and Θ_{core} is the propagation angle of the guided mode. Since the guiding condition requires that $\sin \Theta_{\text{core}} > \frac{n}{n_{\text{core}}}$, it is easy to show that then the incident angle

$$\sin \Theta = \frac{n_{\text{core}}}{n} \cdot \sin \Theta_{\text{core}} > 1 \tag{3.3.45}$$

and therefore direct beam coupling into or out of the the waveguide is not possible and hence special techniques have to be implemented to alter the in-plane component of the $k-$vector of the incoming light.

The condition for the incident angle (Eq.3.3.44) can be satisfied if the light is incident in the material with a higher refractive index than the core layer of the waveguide: $n = n_p > n_{\text{core}}$. Then, at a certain incident angle Θ_{p},

$$n_{\text{p}} k_0 \sin \Theta_{\text{p}} = n_{\text{core}} k_0 \sin \Theta_{\text{core}}. \tag{3.3.46}$$

Naturally, the n_{p} material cannot be brought into the optical contact with the waveguide, otherwise the guiding condition for the light in the core layer is not fulfilled. For this reason, an angle higher than the critical value for the n_p/n interface is used, *i.e.* $\Theta_{\text{p}} > \arcsin\left(\frac{n}{n_{\text{p}}}\right) = \Theta_{\text{critical}}^{n_{\text{p}}/n}$, and the coupling is then achieved via the evanescent field associated with the high refractive index material. The penetration depth of the evanescent wave can be estimated according to the Eq. (3.2.21):

$$L = \frac{\lambda_0}{4\pi\sqrt{n_{\text{p}}^2 \sin^2 \Theta_{\text{p}} - n^2}}. \tag{3.3.47}$$

For the most cases L is in the subwavelength range of $10 - 100$ nm.

In practice, prism of the high refractive index material is pressed onto the surface of the waveguide, hence the name *prism coupling*. The relation between the Θ_{p} and out-coupling angle of the prism Θ_0 is

$$\Theta_{\text{p}} = \alpha + \arcsin\left(\frac{n}{n_{\text{p}}} \sin \Theta_0\right), \tag{3.3.48}$$

where α is the inclination angle of the prism. As discussed above, light coupling occurs at $\Theta_{\text{p}} > \Theta_{\text{critical}}^{n_{\text{p}}/n}$, so that if $\alpha \geq \Theta_{\text{critical}}^{n_{\text{p}}/n}$ the phase matching condition (Eq.3.3.44) is achieved for all of the out-coupled angles.

Similar to the prism coupler, light can also be coupled out of the waveguide by using

the lens of the high refractive index material. However, the range of the out-coupling angles is narrow and the available Θ_0 values tend to be high, as shown for the case of the hemispherical lens. This limits the application of the lens coupler, and therefore for most practical purposes a prism is used instead.

3.4 Electromagnetic Fields in Presence of Charges

Conductive materials used in OLED devices, such as metal or metal oxide electrodes, as well as doped organic semiconductors, posses excessive amount of free charges, which then can interact with the incident electromagnetic radiation. The study of electromagnetic field interactions with charges is loosely called *plasmonics*. Electromagnetic field oscillations propagating along metal/dielectric interface, called *surface plasmon polaritons* can be excited either by coupling to the evanescent dipole field of the emitter molecules or by an external coupling structure. Plasmonic effects at the organic/metal interfaces play a major role in determining the outcoupling efficiency of OLEDs and affect greatly the intensity and distribution of the outcoupled field emission from the device. On the other hand, plasmonic effects found a great number of applications in sensing, where both surface plasmon polariton and *localised plasmon* effects can be employed for a sensitive measurement of the changes of the optical properties induces by various specimen. This section aims to account for the basic description of the plasmonic phenomena relevant for electroluminescent device and sensing applications. Most of this section is based on Ref. [40].

Free Electron Gas Approximation

Electric and optical response of metals can be modelled using electron gas approximation, where the density of electrons n is about 10^{23} cm^{-3}. In the most simple approach electrons in such a system are considered to move freely in the fixed background of nucleus cores of the metal atoms. Then, one can write the equation of motion for a single electron:

$$\frac{d\boldsymbol{p}}{dt} + \frac{\boldsymbol{p}}{\tau} = -e\boldsymbol{E}, \tag{3.4.1}$$

where e is the charge of the electron and τ is the relaxation constant of the electron's momentum $\boldsymbol{p}$ due to the collisions and is inversely proportional to the collision frequency γ, $\tau = 1/\gamma$. Typically, in metals at room temperature $\tau \approx 10^{-14}$ s and $\gamma \approx 100$ THz. At the steady state conditions ($\frac{d}{dt} = 0$), from Eq.(3.4.1)

$$\boldsymbol{p} = m^*\boldsymbol{v} = -\tau e\boldsymbol{E}, \tag{3.4.2}$$

where m^* denotes the effective mass of the electron, which depends on the lattice potential and electron-electron interactions and can be calculated from the band structure of the metal. Using this result together with the definition of the current density from the kinetic theory, $\boldsymbol{j} = -en\boldsymbol{v}$ and combining it with the differential form of the Ohm's law (Eq.(3.1.7)), one arrives at the expression for the conductivity of the metal

$$\sigma = \frac{ne^2\tau}{m^*}. \tag{3.4.3}$$

Assuming a harmonic time dependence of the driving electric field $\boldsymbol{E}(t) = \boldsymbol{E_0}e^{-i\omega t}$, electrons will oscillate accordingly and their response can be described by a solution to the equation of motion (Eq.(3.4.1)) $\boldsymbol{x}(t) = \boldsymbol{x_0}e^{-i\omega t}$, with complex amplitude x_0 incorporating any phase shifts between the driving field and response via

$$\boldsymbol{x}(t) = \frac{e}{m^*(\omega^2 + i\gamma\omega)}\boldsymbol{E}(t). \tag{3.4.4}$$

Free electrons contribute to the macroscopic polarization $\boldsymbol{P} = -en\boldsymbol{x}$. Inserting this expression into Eq.(3.1.5) yields

$$\boldsymbol{D} = \epsilon_0\Big(1 - \frac{\omega_p^2}{\omega^2 + i\gamma\omega}\Big)\boldsymbol{E}, \tag{3.4.5}$$

where ω_p is called the *plasma frequency* of the free electron gas and is equal to

$$\omega_p = \sqrt{\frac{ne^2}{\epsilon_0 m^*}}. \tag{3.4.6}$$

Typically, ω_p is in the range of $5 - 15$ eV for most of the metals. Comparing definition of the dielectric displacement and Eq.(3.4.5) we arrive at the main result of the free electron model, *i.e.* the frequency-dependant complex dielectric function $\epsilon(\omega) = \epsilon'(\omega) + i\epsilon''(\omega)$

$$\epsilon(\omega) = 1 - \frac{\omega_p^2}{\omega^2 + i\gamma\omega}. \tag{3.4.7}$$

Its real and imaginary components, respectively

$$\epsilon'(\omega) = 1 - \frac{\omega_p^2\tau^2}{1 + \omega^2\tau^2}, \tag{3.4.8}$$

$$\epsilon''(\omega) = \frac{\omega_p^2\tau}{\omega(1 + \omega^2\tau^2)}. \tag{3.4.9}$$

Free electron model predicts $\epsilon(\omega \gg \omega_p) \to 1$. For nobel metals (*e.g*, Au, Ag) extension to the model is needed to account for the additional polarization due to the filled d electron band close to the Fermi surface, which results in higher than predicted values of ϵ in this frequency regime. This residual polarized background of the ion cores is accounted for by introducing the corresponding term $\boldsymbol{P_\infty}$ to the dielectric displacement

$$\boldsymbol{D} = \epsilon_0 \boldsymbol{E} + \boldsymbol{P} + \boldsymbol{P_\infty}, \tag{3.4.10}$$

$$\text{with } \boldsymbol{P_\infty} = \epsilon_0(\epsilon_\infty - 1)\boldsymbol{E}. \tag{3.4.11}$$

Typically, $\epsilon_\infty = 1 - 10$ for most metals. Corresponding corrected dielectric function is then

$$\epsilon(\omega) = \epsilon_\infty - \frac{\omega_p^2}{\omega^2 + i\gamma\omega}. \tag{3.4.12}$$

Simplified electron plasma model, also known as *Drude's model*, works fairly well for the alkali metals up to the ultraviolet regime, while for most of the metals (noble metals, Cu, etc.) it breaks down in the visible, due to the interband transitions limiting the validity of this approach. The free electron approach can be extended to account for the interband transitions by adding an additional term containing the resonant frequency of the electronic transition ω_0 for the restoring force to the electrons equation of motion (Eq.(3.4.1)), yielding

$$m^*\frac{\partial^2 \boldsymbol{x}}{\partial t^2} + m^*\gamma\frac{\partial \boldsymbol{x}}{\partial t} + m^*\omega_0^2\boldsymbol{x} = -e\boldsymbol{E} \tag{3.4.13}$$

Then, the corresponding dielectric function accounting for multiple resonances can be written as

$$\epsilon(\omega) = \epsilon_\infty + \sum_j \frac{\omega_p^2 f_j}{(\omega_{0j}^2 - \omega^2 - i\gamma\omega)}, \tag{3.4.14}$$

where f_j is the oscillator strength which describes the intensity of the different transitions. Full description of f_j is beyond the classical picture and requires quantum mechanical description [41].

3.4.1 Volume Plasmons

For large frequencies close to plasma frequency ω_p, the product $\omega\tau \gg 1$, which leads to negligible damping, *i.e.* dielectric function of idealised metal can be written as

$$\epsilon(\omega) = 1 - \frac{\omega_p^2}{\omega^2}. \tag{3.4.15}$$

Equation (3.4.15) describes the dielectric function of undamped free electron plasma. It is predominantly real - effect known as *UV transparency of metals*. However, for real metals, as discussed above, interband transitions leads to the finite imaginary part of $\epsilon(\omega)$ and corresponding absorption in the UV range. One can see that at $\omega = \omega_p$, ϵ becomes zero. Rewriting the wave equation (3.1.11) one gets

$$\boldsymbol{k}(\boldsymbol{k} \cdot \boldsymbol{E}) - k^2 \boldsymbol{E} = \epsilon \frac{\omega^2}{c^2} \boldsymbol{E}. \tag{3.4.16}$$

It is clear that zeros in the $\epsilon(\omega)$ correspond to longitudinal collective oscillations, *i.e.* $\boldsymbol{k}(\boldsymbol{k} \cdot \boldsymbol{E}) = k^2 \boldsymbol{E}$. Thus, the plasma frequency ω_p is the natural frequency of a oscillation of a free electron see. The quanta of these oscillations are known as *bulk* or *volume plasmons*, to distinguish it from surface and localized plasmons described in the following sections. Due to its longitudinal nature, volume plasmons cannot be excited by light, since it is a transverse electromagnetic field. Instead, plasma oscillations are studied experimentally using electron loss spectroscopy. For the transverse field $(\boldsymbol{k} \cdot \boldsymbol{E}) = 0$, Eq.(3.4.16) leads to the general dispersion relation $k^2 = \epsilon \frac{\omega^2}{c^2}$. Inserting the dielectric function (3.4.15), one gets the dispersion relation of free electron gas:

$$\omega^2 = \omega_p^2 + k^2 c^2. \tag{3.4.17}$$

One can see that transverse electromagnetic waves are allowed to propagate in metals in the transparency region $\omega > \omega_p$ with a group velocity $\frac{\partial\omega}{\partial k} < c$.

3.4.2 Surface Plasmon Polaritons

Similar the discussion of the guided optical waves which propagate in the core region of the waveguide and are localized at the interfaces between core and the cladding layers, we now look at the interface between dielectric and metal (Figure 3.4.1). It is the most simple system which sustains surface plasmon polaritons (SPPs) - the electron plasma fluctuations localized at the metal and dielectric interface. Electronic fluctuations are coupled to the electromagnetic field and propagate along the interface with the propagation constant $\boldsymbol{\beta}$

and can be indirectly excited by light if phase matching conditions are fulfilled. Therefore, SPPs represent the highest radiative energy loss in OLED structures and big research effort is devoted to study and fabricate various light outcoupling structures.
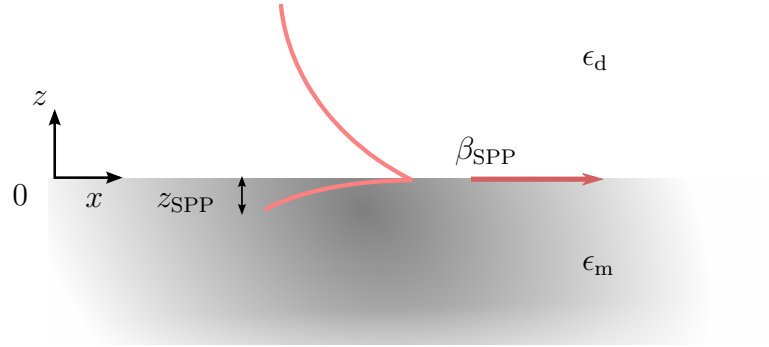

Figure 3.4.1: Electric field distribution representing surface plasmon polaritons at the single metal/dielectric interface.

The starting point is equation sets (3.3.9)-(3.3.11) for s-polarization and (3.3.17)-(3.3.19) for p-polarization. Using the latter equation set, for TM modes in both half spaces of the metal/dielectric interface, one gets for $z > 0$:

$$H_y(z) = A_2 e^{i\beta x} e^{-k_2 z} \tag{3.4.18}$$

$$E_x(z) = iA_2 \frac{1}{\omega \epsilon_0 \epsilon_\mathrm{d}} k_2 e^{i\beta x} e^{-k_2 z} \tag{3.4.19}$$

$$E_z(z) = -A_2 \frac{\beta}{\omega \epsilon_0 \epsilon_\mathrm{d}} e^{i\beta x} e^{-k_2 z} \tag{3.4.20}$$

and for $z > 0$:

$$H_y(z) = A_1 e^{i\beta x} e^{k_1 z} \tag{3.4.21}$$

$$E_x(z) = -iA_1 \frac{1}{\omega \epsilon_0 \epsilon_\mathrm{m}} k_1 e^{i\beta x} e^{k_1 z} \tag{3.4.22}$$

$$E_z(z) = -A_1 \frac{\beta}{\omega \epsilon_0 \epsilon_\mathrm{m}} e^{i\beta x} e^{k_1 z}. \tag{3.4.23}$$

Continuity requirement for H_y and corresponding $\epsilon_\mathrm{m} E_z$ and $\epsilon_d E_z$ leads to the dispersion relation of the surface plasmons
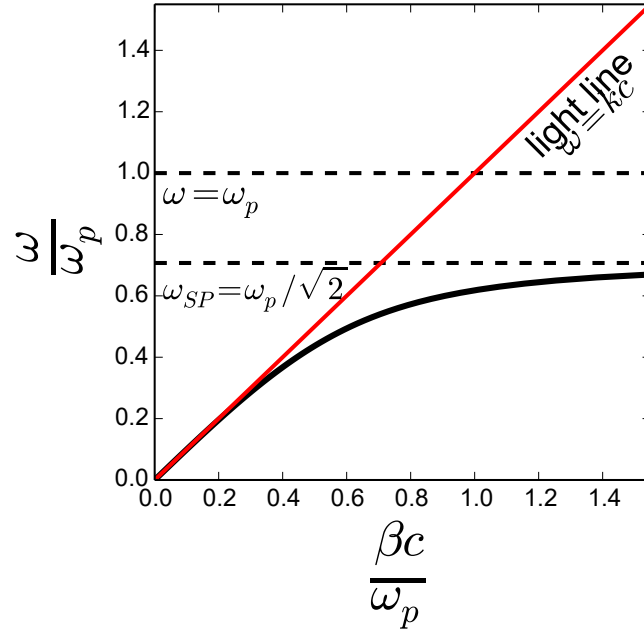
Figure 3.4.2: Plasmon energy dispersion curve (black solid line). The upper part represents dispersion of the volume plasmons, described by the Eq. (3.4.17). The lower branch is the SPP dispersion. In long wavelength region it approaches the light line (red solid line). At short wavelengths SPP approaches the characteristic surface-plasmon frequency ω_{SP}.

$$\frac{k_2}{k_1} = -\frac{\epsilon_2}{\epsilon_1}, \tag{3.4.24}$$

with k_1 and k_2 defined so that the H_y obey the wave equation 3.3.19:

$$k_1^2 = \beta^2 - k_0^2 \epsilon_{\text{d}} \tag{3.4.25}$$

$$k_2^2 = \beta^2 - k_0^2 \epsilon_{\text{m}}. \tag{3.4.26}$$

This allows to rewrite the dispersion relation

$$\beta = k_0 \sqrt{\frac{\epsilon_{\text{d}} \epsilon_{\text{m}}}{\epsilon_{\text{d}} + \epsilon_{\text{m}}}} \tag{3.4.27}$$

The plasmonic dispersion is shown in the Figure 3.4.2. At small wave vector values

corresponding to mid-infrared and lower frequencies, SPP dispersion branch is linear and is close to the light line $\omega = k_0 c$. It extends over many wavelengths into dielectric space and acquires the character of a grazing-incidence surface light field, known as *Sommerfeld-Zenneck* wave. However, SPP excitations always lie to the right side of light line, therefore it is not possible to excite them by direct radiation and special coupling techniques are required to excite surfaces plasmon modes, such as prism or grating coupling described in section 3.3.1. At large wave vectors, the SPP mode acquires the fully electrostatic character, as wave vector goes to infinity and the frequency of SPPs approach the characteristic *surface plasmon* frequency:

$$\omega_{\text{sp}} = \frac{\omega_{\text{p}}}{\sqrt{1 + \epsilon_{\text{m}}}}. \tag{3.4.28}$$

Solving similar set of equation for the TE mode, one arrives at the condition $A_1(k_1 + k_2)$. With both $Re[k_1]$ and $Re[k_2]$ being positive by definition, this leads us to conclude that surface plasmon polaritons exist only for the p polarization.

In the case of systems containing alternating metal/dielectric interfaces, each interface can sustain SPP propagation. Different SPP modes couple if the gap between the interfaces is comparable to the mode decay length $z_{SPP} = \frac{1}{|k|}$. For the insulator/metal/insulator (IMI) system, where the thin (of thickness h) metal film described by ϵ_{m} is sandwiched between two semi-infinite insulator layers with ϵ_2 and ϵ_3 with corresponding decay constants k_2 and k_3. Assuming symmetric structure (*i.e.* $\epsilon_2 = \epsilon_3 = \epsilon_{\text{d}}$ and thus $k_1 = k_3$) the dispersion relation reads:

$$\tanh k_1 h = -\frac{k_1 \epsilon_{\text{m}}}{k_2 \epsilon_2} \tag{3.4.29}$$

$$\tanh k_1 h = -\frac{k_2 \epsilon_{\text{d}}}{k_1 \epsilon_{\text{m}}}. \tag{3.4.30}$$

The former equation describes modes of odd vector parity ($E_x(z)$ is odd, $H_y(z)$ and $E_z(z)$ are even functions) while the latter describes modes of even vector parity ($E_x(z)$ e even, $H_y(z)$, $E_z(z)$ - odd). For large β values:

$$\omega_{\text{odd}} = \frac{\omega_p}{\sqrt{1 + \epsilon_{\text{m}}}} \sqrt{1 + \frac{2\epsilon_{\text{m}} e^{-2\beta h}}{1 + \epsilon_{\text{m}} r}} \tag{3.4.31}$$

$$\omega_{\text{even}} = \frac{\omega_{\text{p}}}{\sqrt{1 + \epsilon_{\text{m}}}} \sqrt{1 + \frac{2\epsilon_{\text{m}} e^{-2\beta h}}{1 - \epsilon_{\text{m}}}} \tag{3.4.32}$$

61

3.4.3 Localized Plasmons

Together with SPP modes, *localized plasmons (LP)* respresent the two fundamental excitations of plasmonics. LP modes are present when electromagnetic radiation is interacting with sub-wavelength size conductive particles, resulting in lateral electron plasma oscillations. In contrast to SPPs, LPs can be directly excited by illumination, without the need of additional phase matching techniques. LPs are characterised by a non-propagating electromagnetic response (hence, the name *localized*) and an accompanied electromagnetic field enhancement. The corresponding field enhancement is extremely sensitive to the dielectric properties of the surrounding medium, where minor changes in the latter results in the well defined changes in the plasmonic resonances. The easily detectable LP resonance shifts lead to the development of the wide range of sensing platforms. On the other hand, as will be demonstrated in the experimental section, inhomogeneities in OLED electrode films, based on thin metal layers, lead to the parasitic LP absorption bands, reducing the device performance. Therefore, the study of LPs is of great practical importance. The aim of this subsection is to briefly describe LP modes at the most basic level.

The most simple system to study LPs is that of a conductive sphere, described by a dielectric constant ϵ_m and a radius d, surrounded by dielectric medium ϵ. If the condition $d \ll \lambda$ is fulfilled, where λ is the wavelength of the incident radiation, the phase of the electromagnetic field can be assumed constant over the volume of the conductive particle and any phase-related phenomena can be neglected. Under this assumption, known as *quasi-static approximation*, electrostatic approach based on solving *Laplace equation* for electrostatic potential is then applied to calculate the electromagnetic response inside and outside of particle, $\boldsymbol{E_{in}}$ and $\boldsymbol{E_{out}}$, respectively, induced by the incident electromagnetic field with amplitude $\boldsymbol{E_0}$

$$\boldsymbol{E_{in}} = \frac{3\epsilon}{\epsilon_m + 2\epsilon} \boldsymbol{E_0} \tag{3.4.33}$$

$$\boldsymbol{E_{out}} = \boldsymbol{E_0} + \frac{3\boldsymbol{e_n}(\boldsymbol{e_n} \cdot \boldsymbol{p}) - \boldsymbol{p}}{4\pi\epsilon_0\epsilon} \frac{1}{r^3}, \tag{3.4.34}$$

here, $\boldsymbol{e_n}$ is the vector normal to the particle surface, r is the distance from the center of the sphere and $\boldsymbol{p}$ denotes the dipole moment of the particle induced by the incident electromagnetic field. It can be shown that the latter can be expressed as

$$\boldsymbol{p} = 4\pi\epsilon_0\epsilon d^3 \frac{\epsilon_m - \epsilon}{\epsilon_m + 2\epsilon}. \tag{3.4.35}$$

It can be seen from equations (3.4.33)-(3.4.35) that the resonance in both, field inside and

outside of the sphere, is achieved then

$$Re[\epsilon_{\mathrm{m}}(\omega)] = -2\epsilon, \tag{3.4.36}$$

which is known as the *Frölich* condition. For the idealised (Drude) metal, whose dielectric response is described by Eq.(3.4.7), resonance frequency of the localized plasma oscillation is then

$$\omega_{\mathrm{res}}^2 = \frac{\omega_{\mathrm{p}}^2}{2\epsilon + 1}. \tag{3.4.37}$$

Slight change of dielectric constant (refractive index) of the surrounding medium will result in the change of the LP resonance frequency. For example, as seen from Eq.(3.4.37), increase in ϵ will shift the resonance ω_{res} to the lower frequency range (red shift). This sensitivity to the environment is the key mechanism behind a number of sensors based on the plasmonic resonance. A small conductive sphere ($d \ll \lambda$) under oscillating plane-wave illumination, will act as an point dipole with an oscillating dipole moment. The resulting dipole excitation of the incident field and subsequent radiation of the dipole leads to the absorption and scattering of the electromagnetic field, respectively. It can be shown, that within the near field ($kr \ll 1$) the resulting field are predominantly electric, while for far-field regime, dipole radiates spherical waves. The corresponding cross-sections for absorption and scattering can be derived to be

$$C_a = 4\pi k d^3 Im\left[\frac{\epsilon_{\mathrm{m}} - \epsilon}{\epsilon_{\mathrm{m}} + 2\epsilon}\right], \tag{3.4.38}$$

$$C_s = \frac{8\pi}{3} k^4 d^6 \left(\frac{\epsilon_{\mathrm{m}} - \epsilon}{\epsilon_{\mathrm{m}} + 2\epsilon}\right)^2, \tag{3.4.39}$$

respectively. It can be seen that for metal nanoparticles both absorption and scattering of light are enhanced at Frölich resonance condition (Eq.(3.4.36)).

4 Organic Light-Emitting Diodes

In this Chapter, the basic principles of OLEDs are discussed. Section 4.1 aims to summarize the main mechanisms responsible for the device operation and the choice behind the material combinations used in modern OLEDs. The main factors which influence device efficiency are presented. Additionally, Section 4.3 gives a general overview of the OLED structuring techniques. The chapter is closed with a more detailed description of the principles and materials used in the emerging orthogonal photolithography technique, as it forms the basis of the work presented in the subsequent chapters.

4.1 Principle of Operation

Since the first demonstration of the OLED in 1987 [1], the OLED technology based on thermally evaporated small-molecule organic films has experienced tremendous improvement. It culminated in a number of commercial applications. Most prominent are OLED displays used in modern smartphones, tablets and TVs. OLEDs are electroluminescent devices, i.e. they produce light from the passage of the electrical current running through the diode. The principle behind the OLED operation can be divided into several distinct physical mechanisms:

1. Charge (electron and hole) injection

2. Charge transport

3. Exciton formation

4. Exciton recombination

5. Light extraction.

The simplified energy diagram of the OLED and the scheme of its operation is presented in Figure 4.1.1. In the following, more details about the above mentioned mechanisms are given and their role in determining device efficiency are discussed.

4.1.1 Electroluminescence Efficiency

The OLED performance is evaluated by its efficiency to convert electricity into light. All of the aforementioned mechanisms, except for the light extraction, influence the so-called internal quantum efficiency η_{IQE} which describes the ratio between the number of photons emitted and the number of the charges injected. Not all of the emitted photons can escape the device, and are lost mainly due to the waveguide modes inside organic layers and losses to the absorptive metal electrodes. Therefore, the external quantum efficiency η_{EQE}, defined as the ratio between the extracted photons and the injected charges, is used to compare OLED performance. η_{EQE} accounts for the optical losses via light outcoupling efficiency η_{out} and can be written as

$$\eta_{\mathrm{EQE}} = \eta_{\mathrm{IQE}} \cdot \eta_{\mathrm{out}}. \tag{4.1.1}$$

The internal efficiency can be expressed as [42, 43]

$$\eta_{\mathrm{IQE}} = \gamma \cdot r_{\mathrm{ST}} \cdot \eta_{\mathrm{rad}}^*, \tag{4.1.2}$$

where γ is the charge balance factor, r_{ST} denotes the probability to form an emissive excited state and η_{rad}^* is the effective radiative efficiency of the emitter. In the following, the processes influencing the internal and external efficiencies of OLEDs are presented in more detail together with the material and device concept developments, which led to the steady increase of the device performance during more than two decades of OLED research.

4.1.2 Charge Injection and Transport

Charge balance factor γ is defined as the ratio between the current consumed by charge recombination j_{r} and the total injected current j. The latter can be written as

$$j = j_{\mathrm{h,a}} + j_{\mathrm{e,a}} = j_{\mathrm{e,c}} + j_{\mathrm{e,a}}, \tag{4.1.3}$$

where $j_{\mathrm{h,a}}$ and $j_{\mathrm{e,c}}$ are the hole current injected from the anode and the electron current injected from the cathode, respectively. Similarly, $j_{\mathrm{h,c}}$ and $j_{\mathrm{e,a}}$ denote the number of holes crossing the cathode or electrons crossing the anode per second per surface area, respectively. The recombination current is then

$$j_{\mathrm{r}} = j_{\mathrm{h,a}} - j_{\mathrm{h,c}} = j_{\mathrm{e,c}} - j_{\mathrm{e,a}}. \tag{4.1.4}$$

anode   HIL/   EBL   EML   HBL   ETL/   cathode
          HTL   EIL
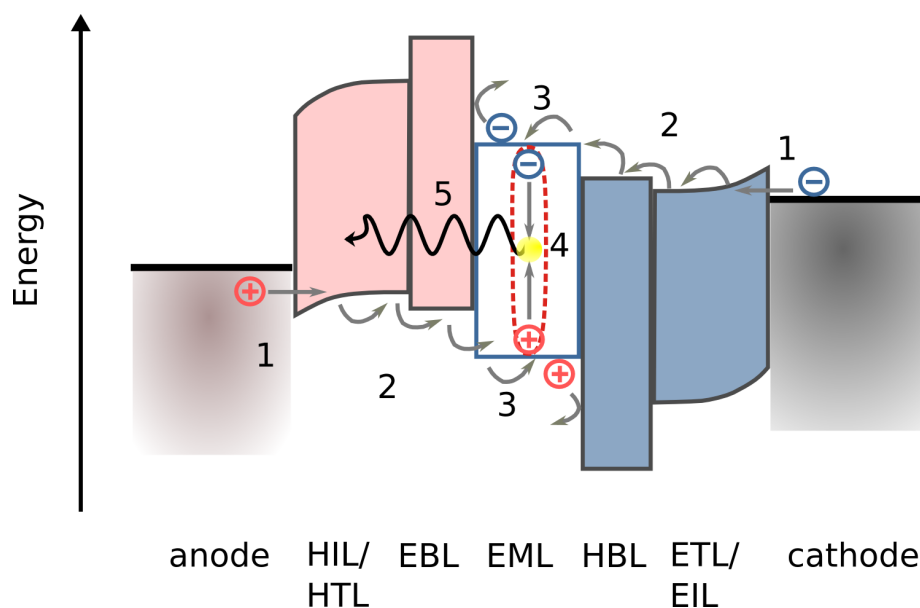
Figure 4.1.1: Energy scheme of the p-i-n diode comprised of functional organic layers sandwiched between two electrodes; HIL/HTL - hole injection and transport layer, EBL- electron blocking layer, EML - emission layer, HBL - hole blocking layer, and ETL/EIL - electron transport and injections layers. Schematic illustration of the physical processes involved in the working OLED: (1) charge (electron and hole) injection, (2) charge transport, (3) exciton formation, (4) exciton recombination and light emission, and (5) light extraction.

One can see that when $j_{h,c} = j_{e,a} = 0$, that is, all of the holes and electrons are consumed by recombination events and do not reach the opposing electrodes, the charge balance factor $\gamma = j_r/j$ is unity. However, in case of the disproportional recombination of electrons and holes, e.g. due to the trap states, $j_{h,c} \gg j_{e,a}$ leads to $\gamma \ll 1$.

The p-i-n concept using doped organic films was introduced to optimise the electrical performance of OLEDs [44]. It relies on using doped charge transport layers. Doping is usually achieved via co-evaporation of the host matrix and dopant molecules. The scheme of the molecular doping process is illustrated in Figure 4.1.2. The general principle behind doping organic semiconductors is similar to the doping of their inorganic counterparts. Excess electron producing n-type doping is achieved by the donation of the electron by the dopant to the LUMO level of the matrix molecule. P-type dopants extract electrons from the HOMO states of the matrix, therefore creating holes.

Doped charge transport layers enable efficient transport of electrons and holes through the organic film as well as relaxes the requirements of the electrode materials for efficient charge injection [44, 45]. It also allows arbitrary thickness of the electron and hole transport layers (ETL and HTL, respectively), without significant electrical losses [46, 47]. The
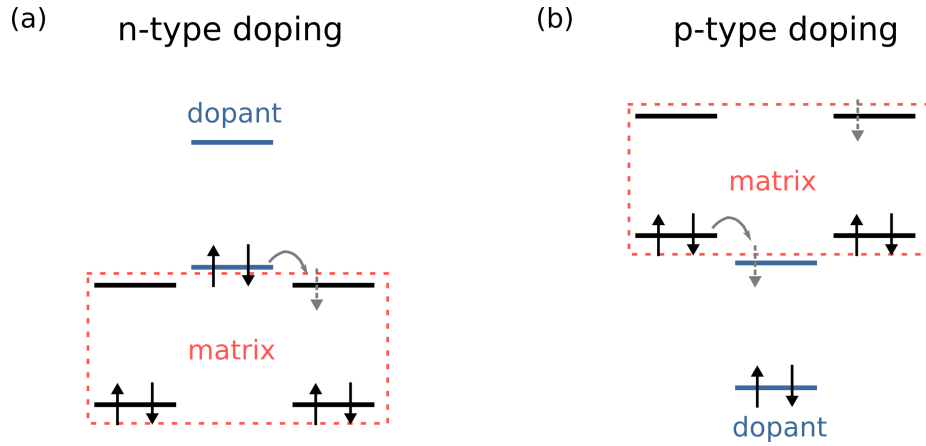
Figure 4.1.2: Schematic illustration of (a) n-type doping and (b) p-type molecular doping of organic semiconductors. In n-type doping, the dopant acts as an donor, while in p-type doping, the dopant acts as an donor. After [44].

charge transport layer thickness can then be varied to optimise the optical mode inside the OLED cavity [48]. Since the electron mobility in the organic semiconductor ETLs usually is at least one order of magnitude lower than the hole mobility in HTLs, additional electron and hole blocking layers (EBL and HBL, respectively) are introduced on p- and n- sides, respectively, to confine the electron-hole recombination within the emission layer (EML).

The charge balance factor γ is known to be dependent on the driving conditions in the OLED, namely, lower γ values are attributed to cause the low η_{EQE} at lower injection levels [49]. However, in modern OLEDs based on the p-i-n device concept, the majority of charges are expected to recombine into excitons in the EML leading to $\gamma \approx 1$ at higher injection levels relevant for applications.

4.1.3 Radiative Efficiency

The effective radiative efficiency of the emitter can be expressed as

$$\eta_{\text{rad}}^* = \frac{F\eta_{\text{rad}}}{1 - \eta_{\text{rad}} + F\eta_{\text{rad}}} \tag{4.1.5}$$

which includes the radiative rate dependency on the microcavity via the *Purcell factor F*. Radiative efficiency η_{rad} of the emitter in the homogeneous media describe the probability for the excited molecule to emit a photon and is expressed as a the ratio between the number of emitting molecules to the number of excited molecules [50]. Experimentally, it can be determined from the competing radiative and non-radiative rates, k_{r} and k_{nr},

respectively

$$\eta_{\text{rad}} = \frac{k_r}{k_r + \sum_j k_{\text{nr,j}}}.$$

(4.1.6)

Strong wavefunction overlap between excited and ground states of organic molecules can be achieved by appropriate chemical design. This leads to the high k_r values which out-competes the non-radiative processes $k_{\text{r}} \gg \sum_j k_{\text{nr,j}}$. Thus, $\eta_{\text{rad}} \approx 1$ can be achieved [21]. However, the concentration of the emissive species have to be kept low, due to the emission quenching mechanisms at higher emitter concentration Valeur, Photochemistry. Similarly to electrical doping, emitter molecules are mixed with a matrix host film to prevent concentration quenching. The matrix molecule is characterised by the higher HOMO-LUMO gap compared to the emitter.

With the balanced charge within the device and the radiative efficiency close to 1, the electroluminescence from the OLED is limited by the number of the generated excited states and the number of photons escaping the device, represented by r_{ST} and η_{out} in Eqs.(4.1.1)-(4.1.2). Therefore, material and device architecture development to increase r_{ST} and η_{out} is still in progress. The following sections briefly summarize the main aspects of the ongoing research efforts.

4.1.4 Excited State Formation

In contrast to LEDs based on inorganic semiconductors where light is generated from the recombination of free carriers, the emission from the OLED arises from the recombination of neutral excitons. This is the result of the significantly greater exciton binding energies found in molecular solids (Chapter 2). The exciton formation in the low mobility organic semiconductors is a process of the recombination of the polaron pair, which can be described by the *Langevin recombination model*. It assumes, that due to the short mean free path of charge carriers, the recombination is limited by the probability of electron and hole finding one another. This is contrary to the recombination in inorganic semiconductors which is limited by the intrinsic rate of the recombination event [51]. The capture radius r_c, which relates to the electron-hole recombination probability, is then derived by equating the Coulomb and thermal energies and reads

$$r_c = \frac{e^2}{4\pi\epsilon k_B T}.$$

(4.1.7)
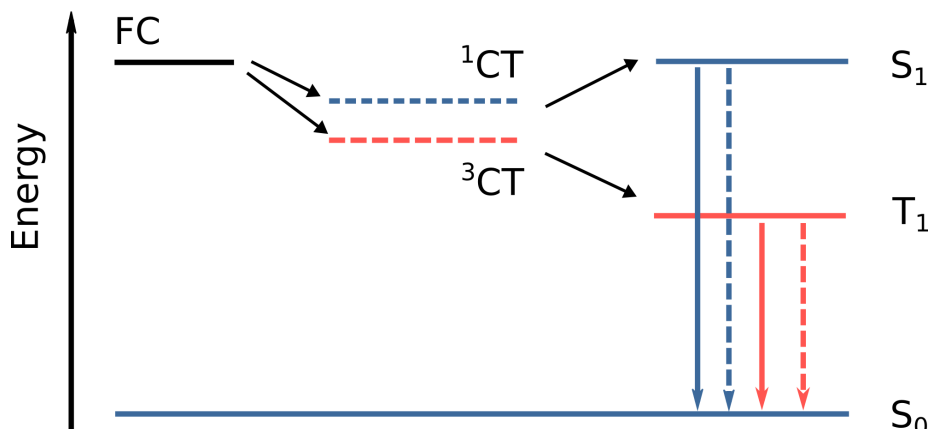
Figure 4.1.3: Energy diagram of the exciton formation and recombination in the electroluminescent device. The injected free charges (FC) recombine to form intermediate singlet and triplet charge transfer states (^{1}CT and ^{3}CT, respectively). CT states recombine rapidly to form singlet and triplet excitons, represented by S_1 and T_1, respectively. Solid and dashed arrows then represent the radiative and non-radiative transitions from the corresponding singlet and triplet states. After [52]

For organic semiconductors at room temperature r_c is the range of 15-20 nm. The bimolecular recombination rate is then

$$k_L = \frac{e(\mu_e + \mu_h)}{\epsilon}. \tag{4.1.8}$$

Excitons formed from the free charge carriers are neutral molecular excitations which carry a total spin S of the molecule, and as described in Chapter 1, can be singlet ($S = 0$) or triplet ($S = 1$). Contrary to optically excited molecules, where triplet state formation from the singlet ground state is forbidden due to the spin conservation, in case of electrical excitation both singlet and triplet excitons are equally probable. Statistically, the singlet/triplet ratio is 1:3, since there are three different spin configurations resulting in triplet state and a unique singlet state configuration (Chapter 1). As a result, η_{IQE} is limited to 25 % using fluorescent emitters, since 75 % of excited states form "dark" triplets, which recombine non-radiatively due to forbidden $T_1 \rightarrow S_0$ transition. Therefore, r_{ST} is introduced in Eq. (4.1.2) to formally account for the efficiency loss associated with singlet/triplet statistics.

4.1.5 Organic Emitters

Phosphorescent emitters, which use both singlet and triplet emissive states were introduced to increase r_{ST}. These "second generation" emitters are organometallic compounds usually comprising a heavy metal atom (Ir, Pt, Pd) in their core [53]. The heavy atom effect enhances the spin-orbit coupling, thus increasing the probability of the forbidden $T_1 \rightarrow S_0$ transition, in addition to increasing the intersystem crossing rate between S_1 and T_1. As a result, r_{ST} and subsequently η_{IQE} close to unity has been demonstrated in phosphorescence OLEDs. However, a number of issues are attributed to the use of phosphorescent emitters in electroluminescent devices. Triplet states exhibit radiative lifetimes $\tau_{Ph} \approx$ 1-10 μs, which leads to high exciton density at elevated driving conditions. This results in the onset of triplet-triplet annihilation (TTA) events which is the main responsible mechanism of the efficiency "roll-off" at high brightness in phosphorescent OLEDs [54]. Additionally, phosphorescent OLEDs suffer from the thermallisation losses associated to the fact that the triplet state lies below the singlet energy level. To date, there are no stable deep blue phosphorescent emitters reported, due to the chemical degradation during both evaporation of the organic films as well as device operation. Therefore, OLED industry still relies heavily on the blue and to the lesser extent green fluorescent materials which calls for the research efforts to increase r_{ST} in OLEDs based on singlet state emission.

While r_{ST} close to 25 % as expected from the discussion above for fluorescent OLEDs was confirmed for a number of small-molecule [55] and polymer devices [56], positive deviations for the polymeric OLEDs were reported early [57, 58, 59, 60]. It was then followed also by works reporting higher efficiency values for the vacuum deposited devices as it would be expected from the spin statistics [61, 62].

In general, there can be two different possible ways to explain reported high efficiencies in fluorescent OLEDs. The first possibility assumes spin-dependent exciton recombination, which results in a higher singlet yield. It was proposed to occur via the alteration of exciton formation process in the intermediate CT state [63] or by spin dependent polaron capture mechanism [64]. Another explanation is to take into account additional exciton decay channels which would lead to the increase in singlets in fluorescent OLEDs. Delayed fluorescence resulting from the recycling of the triplet states, either from the *thermally activated delayed fluorescence* (TADF) or TTA mechanisms are considered to be the most probable causes for the high efficiency fluorescent OLEDs. On the other hand, various proposed mechanisms based on anomalies in the intermediate charge transfer exciton state formation which results in higher singlet yield still lacks both theoretical and experimental consensus and is highly debated in the OLED research community [65].

TTA associated emission also known as *P-type delayed fluorescence* or *triplet fusion*

mechanism is based on the fact that the interacting triplet states can also produce additional radiative singlet states which then add positively to the device efficiency. In the fluorescent emitters, TTA occurs via the physical collision of two excitons as spin selection rule dictates that it can only occur via the Dexter transfer. In the event of the collision of two uncorrelated triplets, the probability of forming a singlet state is only 1/9 [66]. Rest of the excitation decays into formation of triplet states (1/3 probability) and quintet states (5/9 probability). This results in $r_{ST} \approx 33$ %, which is not a significant enhancement. However, high lying quintet state energy level makes triplet annihilation into quintets a highly endothermic process, which can be out-competed by the triplet pair separation [67, 68]. Therefore, a more likely reaction is [69]

$$T_1 + T_1 \xrightarrow{k_{TTA}} \frac{1}{4}S_n + \frac{3}{4}T_n, \tag{4.1.9}$$

which leads to the maximum estimation of r_{ST} =25 %+75/5 %=40 %. It was even proposed that TTA can produce one singlet state out of the triplet pair, which would require deviation from the spin-statistical limit on singlet/triplet formation. In such case, the probability of forming an emissive state can be as high as r_{ST} =25 %+75/2 %=62.5 % [66, 68].

TADF mechanism is not limited by the number of triplets that can be recycled, and therefore provides a way for achieving r_{ST} =1. However, TADF relies on the efficient RISC mechanism to recycle triplet states back to the emissive singlet manifold. A prerequisite to achieve a high RISC rate at room temperature is the small energy splitting values between singlet and triplet excited states ΔE_{ST}. As discussed in Chapter 1, small ΔE_{ST} requires minimal overlap between the HOMO and LUMO orbitals which would lead to a low radiative transition rate and subsequent low radiative efficiency (Eq. (4.1.6)). For this reason, the efficiency enhancement in the first works on OLEDs based on Sn(IV)-porphyrin complex TADF emitters were not encouraging [70]. However, the breakthrough was achieved by realising highly efficient TADF OLEDs based on Cu(I) complexes [71] and purely organic molecules characterised by the broken conjugation between the donor and acceptor moieties. The latter approach resulted in OLEDs emitting in the green [72] and later in the blue [73] spectral region with the efficiencies on par with the best performing phosphorescent devices. Thus, TADF emitters are already dubbed as the "third generation" of OLED emitters [74]. Further research is focussed on realising efficient and stable deep blue TADF emitters [75].

4.1.6 Light Extraction

The amount of light, which escape the planar OLED, device is limited by the optical interfaces of materials characterized by the different refractive indexes resulting in trapped modes within the device. According to the most simple ray-optics approach, the outcoupling efficiency for the planar device with an isotropic emitter can be described by [58]

$$\eta_{\text{out}} \approx \frac{1}{2n_{\text{EML}}^2}, \tag{4.1.10}$$

where n_{EML} denotes the refractive index of the emitter medium. For most organic semiconductors, the refractive index is around 1.6-1.8, which leads to $\eta_{\text{out}} \approx$ 15-20 %. However, such model does not account for the spontaneous emission rate dependence on the dipole environment (Purcell effect), constructive and destructive interference effects within the OLED cavity or the loss associated with the excitation of the SPP modes at the organic/metal interface.

The modern approach to estimate the outcoupling efficiency of the OLED is to describe the emitter as an oscillating dipole and perform transfer-matrix calculations to account for different optical interfaces and the lossy media. The representative plots of the dipole power dissipation spectrum as the function of the in-plane wavevector k_x of the EML, for the case of the red bottom-emitting OLED stack on glass substrate, is shown in Figure 4.1.4 (a). The dissipated power depends strongly on the emission wavelength, therefore the whole emitter spectrum has to be considered for the calculation. The different modes can be analysed using wavevector k_x normalised to its modulus k. In such a case, the power dissipated in the range of $k_x/k < k_{\text{air}}/k$ corresponds to the far-field, that is, useful emission of the OLED. For $k_{\text{air}}/k < k_x/k < k_{subs}/k$ the light is guided in the substrate, and for $k_{\text{subs}}/k < k_x/k < 1$ the emission is trapped due to waveguiding in the organic films. Finally, $k_x/k > 1$ represents the evanescent regime, where light is lost due to the excitation of the SPP modes. Figure 4.1.4 (b) shows the power dissipation spectrum for the $\lambda = 620$ nm emission. The corresponding modes are also assigned. It can be seen that the vast majority of light does not escape the OLED and is lost instead, whether due to waveguide effects in the substrate or organic layers, or via the SPP channel. Therefore, increasing η_{out} by extracting guided light and minimizing SPP contribution is still pursued by many research groups worldwide [76].

For bottom-emitting OLEDs, the external outcoupling structures are applied on the substrate/air interface to extract guided light from the substrate. To reduce waveguide contribution in the organic layers, various light scattering micro- and nano- structures are fabricated for both bottom- and top-emitting OLEDs. Additionally, control of the emit-

(a)

(b)
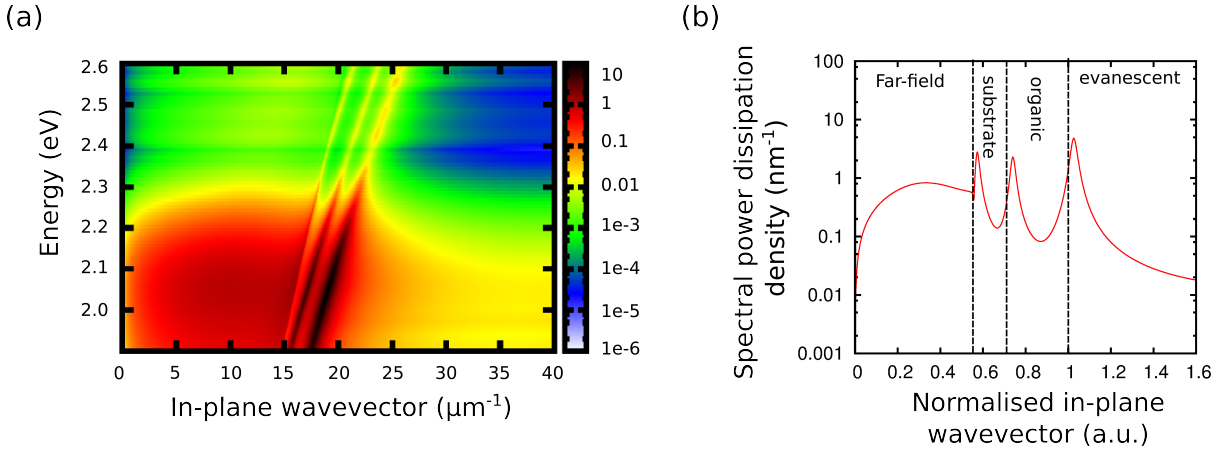
Figure 4.1.4: Simulated dipole emission power dissipation in OLEDs. (a) Two-dimensional power dissipation spectrum representing the spectral power density (false color) of a red bottom-emitting OLED as a function of in-plane wavevector k_x and photon energy. (b) Power dissipation spectrum for $\lambda = 620$ nm emission as a function of the normalised in-plane wavevector k_x/k. The power dissipated in the range of $k_x/k < k_{air}$ corresponds to the useful emission of the OLED to the far field. For $k_x/k > 1$ the emission is coupled to the evanescent plasmon polariton modes. Trapped optical modes exist in between, whether coupled to the guided modes travelling in the substrate or in the organic film.

ting dipole orientation can be used to enhance the outcoupling efficiency, with horizontal orientation being preferable. In general, 2-4 times boost in η_{out} has been reported when using light outcoupling enhancement structures (see reviews [77, 78, 76] for more details).

4.1.7 Efficiency Loss Mechanisms

OLED efficiency decrease at higher current density is referred to as "efficiency roll-off". It results from a number of exciton or charge carrier dependent physical mechanisms leading to decrease in the number of emissive excitons.

In phosphorescent devices, TTA is the most prominent emission quenching mechanism [54]. Contrary to fluorescent materials where it is mediated by the Dexter transfer, TTA in phosphorescent emitters can occur both in long range dipole-dipole and short range exchange mechanisms.

Additionally, triplet-polaron annihilation (TPA) plays a role at high current densities [79]. It can be described as

$$T_1 + P_+ \xrightarrow{k_{\mathrm{TP}}} S_0 + P_+^*, \tag{4.1.11}$$

$$T_1 + P_- \xrightarrow{k_{\mathrm{TP}}} S_0 + P_-^*, \tag{4.1.12}$$

where P_- and P_+ denote vibrationally coupled electron and hole states (see Chapter 1) and asterix denotes higher energy state. TPA, and similarly singlet-polaron annihilation (SPA) in fluorescent materials occurs mainly via Förster transfer.

Similar to TTA, singlet-singlet annihilation (SSA) can occur in fluorescent devices [80, 81]. However, due to the shorter exciton lifetime, high singlet densities needed to reach prominent SSA are unlikely. SSA is usually observed in high purity crystalline materials characterized by high charge carrier mobilities.

Additionally, field quenching, charge balance factor and Joule heating [81] can influence the OLED performance at elevated currents.

4.2 Applications of OLEDs

This section presents a brief overview about the main already existing and emerging uses of OLEDs, with the focus on the relevance and requirements of the printing technique associated with each application.

4.2.1 Information Displays

Compared to the liquid crystal display (LCD) technology, which dominates the market, OLED technology does not require the use of backlight illumination, since each of the pixel can be actively emissive. This leads to the higher contrast of the display due to the deeper black level ("true black" colour). Additionally, no colour filters and set of polarisers, which are essential components of the LCD, allows fabrication of extremely thin and light screens, with good color saturation and wide viewing angle. Finally, active-matrix OLED (AMOLED) displays have a more rapid response time compared to their LCD counterparts.

Together with backplane electronic components and highly efficient front plane light-emitting devices, the successful implementation of pixel patterning is a key requirement for the success of OLED displays. Prerequisites for patterning techniques include cost-efficiency, scalability to large area substrates ($\geq$Gen 8), registration between multiple layers, and compatibility with state-of-the-art OLED technology. At present, state-of-the-art OLEDs are predominantly based on multilayered thin films of thermally evaporated small molecules and frequently contain phosphorescent emitters, especially for covering the green and red spectral range. This approach enables internal quantum efficiencies reaching unity [82] and operational lifetimes suitable for commercial display applications [83, 84, 85, 86]. A common technique to fabricate multicolor pixelated OLEDs is shadow mask patterning. However, there are severe limitations with respect to providing simple and cheap pixel alignment on large scale substrates as well as in high resolution structuring (see Sec. 4.3.1), urging a search for more suitable alternatives [87].

Alternatively, full color OLED displays could also be achieved using a combination of a white emitting OLED and a color filter array [88] or using a blue device and fluorescent down-conversion layers [89]. Both methods offer considerable advantages compared to the structured OLED approach. However, by using color-filters, many advantages of AMOLED as compared to LCD technology are compromised. Both approaches are associated with increased power efficiency as compared to a patterned OLED display. Additionally, both methods rely on the use of stable and efficient blue emitters within the OLED stack, which, as described previously, is still an open issue.

76

4.2.2 Solid-State Lighting

WOLEDs comprising multiple phosphorescent emitters have been shown to exhibit performance equal or even surpassing the fluorescent tubes [90] and due to their inherent flexibility, light weight and large-area emission WOLEDs hold a huge promise to become the sources for the next generation solid-state-lighting. In addition, in recent years, the concept of colour-tunable WOLED emission for general and decorative lighting was gaining an increasing interest. There are three main approaches to achieve white light emission, namely, use of multiple emission layers (EMLs) within an OLED architecture, stacking two or more OLEDs vertically or aligning multiple monochrome devices laterally [91]. All of the aforementioned device concepts are also capable of allowing tuning of the WOLED colour.

WOLED stacks comprising multiple EMLs usually exhibit a voltage-dependent emission spectrum resulting from a variety of complex physical mechanisms. Changing the driving conditions of such device leads to spectral shifts arising due to the voltage dependent carrier trapping rate [92], or due to the migration of the exciton recombination zone [93]. Exciton density dependent triplet-polaron and/or triplet-triplet annihilation mechanisms leading to quenching of the emissive state, as well as field or temperature dependant carrier mobility [94] also play a role in determining the emission of the device. The complexity of the interplaying processes results in a difficult control of the device's color as well as the accompanied change in the WOLED brightness with change in the driving conditions.

To have a better control over the WOLED color, addressing several monochrome devices separately is preferred. It can be done either by stacking two or more separate monochrome OLEDs on top of each other [95, 96, 97, 98] or by aligning the striped OLEDs laterally [99, 100, 101]. However, both of the aforementioned approaches require more sophisticated processing as compared to the single device comprising multiple emitters. Lateral structuring provides possibility of the separate optical and electrical optimization of each of the monochrome subunits at a cost of the need of precise structuring of the devices.

4.2.3 OLED Based Sensors

Another rapidly emerging application of the OLED technology is in the use of integrated optoelectronics systems for medical purposes and biosensing [102, 103]. OLEDs integrated together with organic photodetector arrays were demonstrated for lab-on-a-chip based point-of-care systems [104, 105, 106]. The possibility to deposit OLEDs on flexible substrates enables fabrication of wearable optoelectronic sensors, which were demonstrated on various on-skin applications, including sensors for prosthetic devices [107], electronic

skin [108], photodynamic therapy of skin cancer [109, 110] and blood pressure/oxygenation sensing [107, 111]. Finally, high spatial and temporal resolution OLEDs show great potential for the use in the field of optogenetics [112, 113].

All of these applications often require integration of several optoelectronic components at high resolution and low-cost, thus, novel device structuring strategies are often required. The following section will review the current state-of-the-art of OLED patterning and discuss the efforts of developing new technologies to overcome current structuring limitations.

4.3 OLED Structuring

While both device and material engineering in OLED technology experienced a rapid development over the years, the structuring of OLEDs, i.e. the way devices are positioned and integrated into multi-component arrays, remained virtually unaltered. Namely, patterning using metal stencil masks (*shadow masks*) are universally employed to structure vacuum deposited organic films. On the other hand, to date there is no universal approach for printing of the solution-processed OLEDs. Among several research efforts, ink-jet printing technology is the most developed method for solution-processed devices. This section aims to summarise the main principles and resulting limitations of shadow mask and serial printing techniques. It is then followed by the overview of the emerging technologies aiming to replace the current printing methods for organic optoelectronic devices.

4.3.1 Shadow Mask Patterning

Full color active-matrix OLED displays are predominantly produced using thermally evaporated small molecule materials and are patterned using shadow mask technique. It results from the fact that vacuum deposition is a relatively cheap and well established technology, while use of the stencil masks provides a simple fabrication technique [114]. Despite its availability and compatibility with vacuum deposition, shadow mask patterning imposes several fundamental limitations on the OLED technology. These can be generally grouped into

1. Resolution limitation

2. Substrate size limitation

3. Maintenance

4. Material waste

The resolution achieved by the shadow mask is limited to ≥ 10 μm due to the material diffusion of the evaporated material in the gap between the mask and the substrate [115, 116]. Moreover, the maximal achievable pixel density using shadow mask structuring is dependent on the substrate size since the placement accuracy is affected by the bending of both the mask and the mother glass. The latter components experience the vertical spread (Δ_{VS}) due to the gravity which is defined as the difference between the maximum and minimum displacements of the mid plane of the sheet. Δ_{VS} is proportional to the

fourth power of the substrate sag and can be expressed as [117]

$$\Delta_{\mathrm{VS}} = C \cdot \frac{\mathrm{G}\rho_{\mathrm{subs}}(1 - \nu_{\mathrm{subs}}{}^2)}{\mathrm{E}_{\mathrm{subs}}} \frac{l^4}{d^2},$$
(4.3.1)

where G is the gravitational constant, material parameters ρ_{subs}, ν_{subs} and $\mathrm{E}_{\mathrm{subs}}$ denote density, Poisson's ratio and Young's modulus of the substrate, and d and l is the thickness and length of the substrate plate. The proportionality constant C in Eq. (4.3.1) can be reduced by using mechanical support at optimized positions on the substrate, which leads to a minimal Δ_{VS} value. However, due to the bending effect the shadow mask technology sets an upper limit for the available substrate size, which is expected to be Gen4 or Gen5 substrate [114]. Additionally, most of the material ends up being on the surface of the mask, rather than contribute to the active area of the device, which account only for $\approx 6\ \%$ of the total material volume per pixel. Due to clogging of the mask, it has to be repeatedly cleaned, which ultimately leads to the disposal of the mask after number of cleaning cycles. Finally, shadow mask technique is limited to small molecule devices only, and is not suitable for solution processed materials.

4.3.2 Serial Printing

In order for OLEDs to compete with LCDs, scalable RGB pixel patterning techniques such as photolithography or ink-jet printing that are well established in LCD technology should be implemented. Both lithographic and serial printing approaches are used for structuring color filter arrays in LCDs. Various serial printing techniques including ink-jet [118], molecular jet [119], and organic vapor jet printing (OVJP) [120] were proposed for OLED displays. So far, attempts to introduce liquid printing technologies into mass production have not succeeded. OVJP is a promising alternative since it is solvent-free and compatible with multilayer phosphorescent OLEDs comprising doped organic films. However, cross-contamination of adjacent organic layers at higher pixel densities still needs to be addressed [121].

4.3.3 Unconventional Patterning Techniques

As discussed in Chapter 1, organic semiconductors are characterized by strong covalent interactions within the molecules and relatively weak intermolecular interactions. This gives their unique mechanical properties, which can be modified by the external stimuli, such as temperature or pressure. There is a vast research devoted to applying these features of organic materials to produce patterned films via embossing, imprint lithography and

capillary molding, among others. The review by Menard *et al.* gives an overview of such structuring approaches [122]. However, applicability of such unconventional techniques to structure multicolor OLED displays is yet to be demonstrated.

More relevant to OLED technology, various laser based direct patterning techniques are being developed [123, 124]. Most advanced techniques include laser-induced thermal-imaging (LITI) and laser-induced pattern-wise sublimation (LIPS) methods. The former technology uses laser radiation absorbing donor films and a transfer organic layer. Laser light is then used to heat and subsequently evaporate certain parts of the donor film. Alternatively, in LIPS organic layers on glass are laser scanned and deposited on aligned AMOLED backplane. Recently, single color vacuum deposited OLEDs fabricated by precursor thermal head patterning were demonstrated [125]. The devices were structured down to 80 μm and exhibited encouraging EQEs of around 10 % on par with the thermally evaporated reference OLEDs. However, thermally patterned sub-pixels were characterised by very uneven profile, which would be a serious obstacle for display applications.

4.3.4 Photolithographic Patterning of OLEDs

Photolithography is a mature, cost-effective, inherently parallel patterning technique, with well-established registration protocols, high yield and resolution. Most importantly, there is a fully developed infrastructure for processing, since photolithography is the standard structuring technology in the inorganic semiconductor industry. However, up to now the application of this technique to pattern organic semiconductor devices has remained rather limited as most of the organic materials are incompatible with the resists, etchants, and developers used in the different processing steps of conventional lithography. The following section reviews various research efforts to implement lithographic processed OLEDs.

Traditional Photolithographic Patterning of Organic Films

In some cases, traditional photoresist/solvent combinations were shown to be compatible with certain robust organic polymers. Huang *et al.* [126] reported on placing commercially available photoresists SU8-10 beneath PEDOT:PSS and using a propylene glycol monomethyl ether acetate (PGMEA) developer, thus enabling pixel patterning on mechanically flexible substrates. Another approach based on conventional lithographic patterning takes advantage of the orthogonality between highly fluorinated light emitting polymers (LEPs) and standard photoresists [127, 128, 129]. However, the choice of materials for these traditional lithography approaches is limited, thus restricting the flexibility and performance of available OLED architectures. Recently, arrays of organic photodiodes [130]

and RGB OLEDs [131] were demonstrated using photolithographic structuring. The authors used modified photoresist, which enabled deposition and development which were compatible with organic semiconductors. However, details regarding the photoresist composition were not disclosed, except for a statement of its non-fluorinated nature.

Dry Lithographic Processing

Another strategy to circumvent the issue of incompatibility of OLED and wet processing is based on dry processing approaches [132, 133]. Hwang *et al.* [132] used super-critical CO_2 for the development of a fluorinated polymer photoresist. Electroluminescent polymer devices down to 5 μm in size were demonstrated with maximum current efficiency (luminous efficacy) of 22 cd/A (8 lm/W) at 1 mA/cm². This approach, however, is limited to patterning of the hole-transporting poly(3,4-ethylenedioxythiophene) poly(styrenesulfonate) (PEDOT:PSS) layers, with subsequent deposition of a LEP layer and is thus only suitable for single color structuring. Bahlke *et al.* [133] reported on lithographic patterning using frozen CO_2 gas as resist. While this provides a scalable patterning approach, the use of a cooled substrate (T_{subs} =77 K) during deposition of the organics leads to condensation of residual H_2O and might provoke changes in thin film morphology critical for OLED performance and yield.

Direct Writing of Organic Semiconductors

Various direct-writing techniques were established which employ the organic semiconductor itself as a photoresist. Multicolor RGB pixels were demonstrated by direct structuring of solution-processed LEPs based on UV induced oxetane photo-crosslinking reactions [134, 135, 136], polymer backbone cross-linking of poly(p-phenylene vinylene) (PPV) derivatives [137], as well as polymerisation of light-emitting liquid-crystalline monomers [138]. Despite offering relatively easy implementation, reformulation of the active layer is needed in order to utilize direct photolithography. Tailoring the involved materials to be photo-patternable and at the same time exhibit high stability as well as the desired electrical and optical properties, remains very challenging.

Use of Protective Films

Finally, protective metal layers [139, 140] or polymer films, such as Cytop [141] or parylene C [142] have been used to protect the organic semiconductor during conventional photolithographic processing. However, reports on photolithographic patterning of OLEDs with state-of-the-art efficiency and lifetime are missing.

4.3.5 Orthogonal Processing of Organic Semiconductors

The basic idea behind the emerging technology of orthogonal processing is to use per-fluorinated or very highly fluorinated liquids as developer solvents for photolithographic processing. Such materials are poorly miscible with non-fluorinated non-polar organic materials and water. Hydrofluoroethers (HFEs) stand out from the rest of the highly fluorinated or chlorinated compounds, since they were designed having in mind the environmental and toxicity related issues of the latter. HFEs are known to be environmentally friendly, "green" solvents, which are non-flammable, have a zero ozone-depletion potential, low global warming potential and low toxicity to humans [143].

The material compatibility with the developers used in photopatterning process is ensured by the orthogonality between the organic layers and the HFE solvents. The orthogonality between the material in question and HFE solvents can be evaluated quantitatively based on the solubility parameter concept. Hansen solubility parameters (HSP) are used to evaluate and predict molecular affinities, properties of solvents, solutes and solubility related phenomena [144]. The Hildebrand solubility parameter is defined as

$$\delta = \sqrt{\frac{E}{V_{\mathrm{M}}}}, \tag{4.3.2}$$

where V_{M} is the molar volume and E is the cohesive energy density

$$E = \Delta H_{\mathrm{vap}} - RT. \tag{4.3.3}$$

ΔH_{vap} and R in Eq. 4.3.3 denote heat of vaporisation and molar gas constant. In the three parameter Hansen approach, the total cohesion energy of the liquid, E, is divided into non-polar (dispersion) interactions, E_{D}, permanent dipole-permanent dipole (polar) interaction, E_{P}, and hydrogen bonding interaction, E_{H},

$$E = E_{\mathrm{D}} + E_{\mathrm{P}} + E_{\mathrm{H}}. \tag{4.3.4}$$

Dividing Equation (4.3.4) by the molar volume V_{M} leads to the respective Hansen solubility parameters (HSP)

$$\frac{E}{V_{\mathrm{M}}} = \frac{E_{\mathrm{D}}}{V_{\mathrm{M}}} + \frac{E_{\mathrm{P}}}{V_{\mathrm{M}}} + \frac{E_{\mathrm{H}}}{V_{\mathrm{M}}} \tag{4.3.5}$$

$$\delta^2 = \delta_{\mathrm{D}}^2 + \delta_{\mathrm{P}}^2 + \delta_{\mathrm{H}}^2, \tag{4.3.6}$$
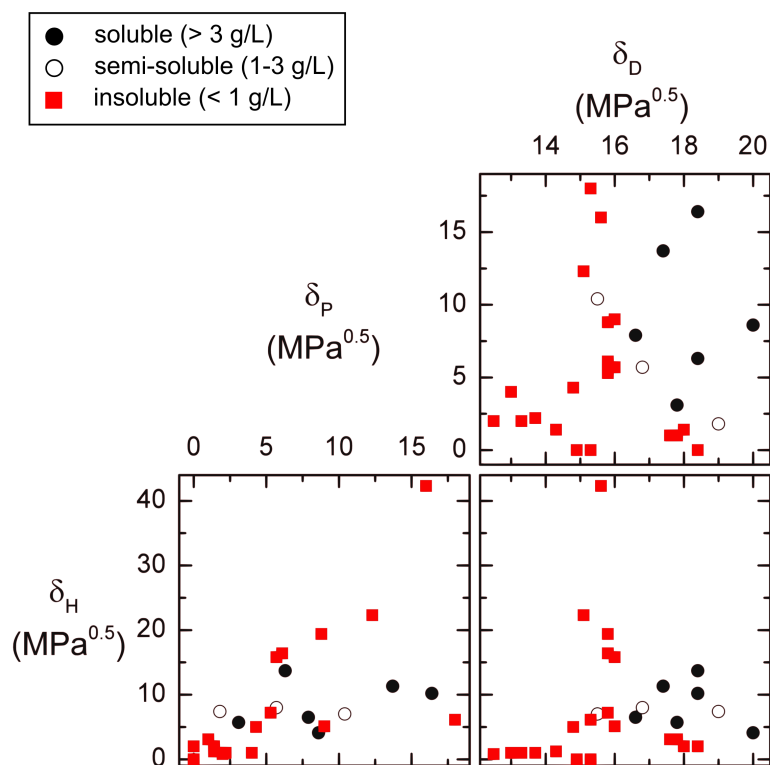
Figure 4.3.1: Solubility evaluation of Alq$_3$. Polar, dispersion and hydrogen interaction parameters δ_P, δ_D and δ_H are calculated to be by qualitative estimation of Alq$_3$ solubility in a number of solvents with known solubility parameters. The solvents are grouped to be soluble (solid black circles), semi-soluble (open circles) or insoluble (red solid squares). HSP estimated to be $\delta_D =18.10$ MPa$^{0.5}$, $\delta_P =9.33$ MPa$^{0.5}$ and $\delta_H =8.58$ MPa$^{0.5}$. HFE solvents are represented by low HSP values, concentrating in the lower left side of each graph. Thus, the HFE and Alq$_3$ have a low molecular affinity and can be considered orthogonal to one another.

where δ_D, δ_P, and δ_H denote the HSP for dispersion, polar and hydrogen interactions, respectively. Materials with similar valued solubility parameters are more likely to dissolve than dissimilar-valued materials.

Figure 4.3.1 presents an example of the HSP determination by evaluating solubility of the archetypal OLED emitter tris(8-hydroxyquinolinato)aluminium (Alq$_3$). The solubility parameters δ_P, δ_D and δ_H are estimated by qualitative evaluation of the concentration needed to dissolve Alq$_3$ molecule in a number of different solvent with known HSPs. The solvents are grouped into three groups, by arbitrary selection of the concentration required to be considered a "good" solvent. The good solvents (soluble > 3 g L^{-1}) are concentrated in a ellipsoid in the HSP space, with a center determined to be at $\delta_D =18.10$ MPa$^{0.5}$, $\delta_P =9.33$ MPa$^{0.5}$ and $\delta_H =8.58$ MPa$^{0.5}$. On the other hand, HSPs for HFE7100, a com-

mon commercially available HFE solvent, which is composed of two $C_5H_3F_9O$ isomers, are $\delta_D =13.7$ MPa$^{0.5}$, $\delta_P =2.2$ MPa$^{0.5}$ and $\delta_H =1.0$ MPa$^{0.5}$. Such disparity in HSP values reflects relatively high orthogonality between the materials. Therefore, HFEs are a good choice for the orthogonal processing and have been demonstrated to be compatible with a wide range of organic semiconductor materials [2, 145, 3, 146, 147] enabling photolithographic structuring of organic electronic devices.

5 Materials and Methods

This chapter aims to summarise the materials and the experimental techniques employed to fabricate and characterise organic films and devices studied in this work. Overview of the functional organic materials is given in Section 5.1. Section 5.2 reviews device fabrication techniques of organic films and devices. Finally, the main material and device characterisation techniques are discussed in Section 5.3.

5.1 Organic Functional Materials

State-of-the-art OLEDs comprise multilayer structure with each of the functional organic layer serving for a specific purpose to maximise device performance. Organic films based on small organic molecules (molecular mass < 2000 g/mol) each serve a specific function within the device. The following is the overview of the molecules used for charge injection, transport and blocking as well as emitter systems used throughout this work. Organic materials used in this work to fabricate OLEDs were commercially purchased from the sources specified below, purified by vacuum gradient sublimation and deposited via thermal vacuum evaporation.

5.1.1 Hole Injection/Transport Layers

The chemical structures of the materials employed for hole injection and transport are shown in Figure 5.1.1 (a). For simple single heterojuction devices N,N,N',N'-Tetrakis(4-methoxyphenyl)-benzidine (**MeO-TPD**, Sensient) and (**Spiro-TTB**, Lumtec) were used as a HTL. For the OLEDs employing p-i-n structure, Spiro-TTB doped with 4 wt% 2,2'-(perfluoronaphthalene-2,6-diylidene) dimalononitrile (**F6-TCNNQ**, Novaled GmbH) was used for an efficient charge injection and transport. Spiro-TTB was chosen to be used in p-i-n devices due to the comparable charge transport properties to Meo-TPD, but significantly higher glass transition temperature (T_g=146°C compared to 55 °C), which is crucial for stable OLED operation, especially when additional photolithographic processing is applied.

(a)

Meo-TPD   Spiro-TTB   F6-TCNNQ

(b)
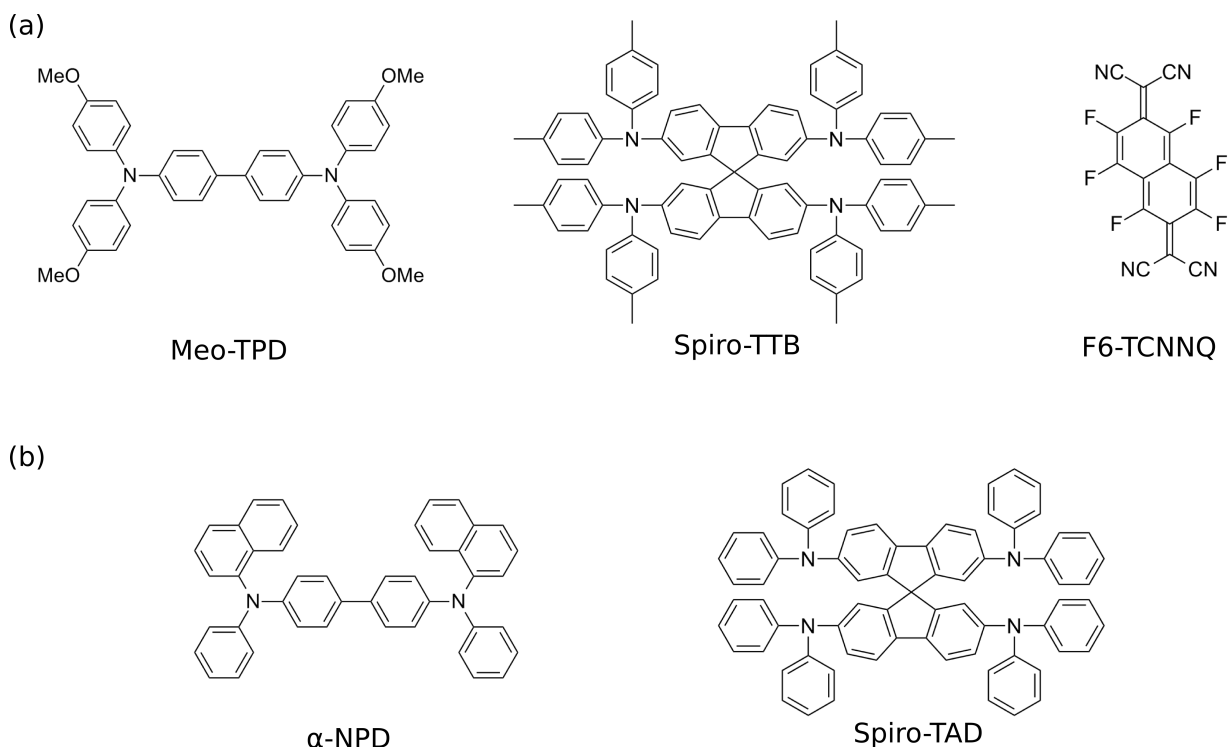
α-NPD   Spiro-TAD

Figure 5.1.1: Chemical structures of (a) hole transport materials Meo-TPD and Spiro-TTB and a p-type dopant F6-TCNNQ; (b) electron blocking materials used in this work: α-NPD and Spiro-TAD, characterised by high lying LUMO level.

5.1.2 Electron Blocking Materials

For efficient p-i-n device operation EBL and HBL are essential for optimal charge balance within the OLED. Sufficiently high LUMO level is a prerequisite for an efficient electron blocking. Chemical structures of (α-**NPD**, Sensient) and (**Spiro-TAD**, Lumtec) are shown in Figure 5.1.1 (b). The former material is also used as an matrix layer for red phosphorescent emitter (**Ir(MDQ)$_2$(acac)**, American Dye Source, Inc.) and is also a hole transport layer (hole mobility μ_h=6.1·10^{-5}cm^2/Vs [148]), hence, α-NPD is used in the red phosphorescent OLED stack. For yellow, green, and red emitting OLED Spiro-TAD was used instead. The corresponding LUMO values for α-NPD and Spiro-TAD are -2.6 eV and -2.4 eV [149], respectively.

5.1.3 Hole Blockers and Electron Transport Materials

For efficient hole blocking in p-i-n OLEDs aluminum(III)bis(2-methyl-8-quninolinato)-4-phenylphenolate (**BAlq$_2$**, Sensient) is used. It has a low lying HOMO at -6.1 eV which is required for HBL. As an electron transport and injection layer 4,7-diphenyl-1,10-
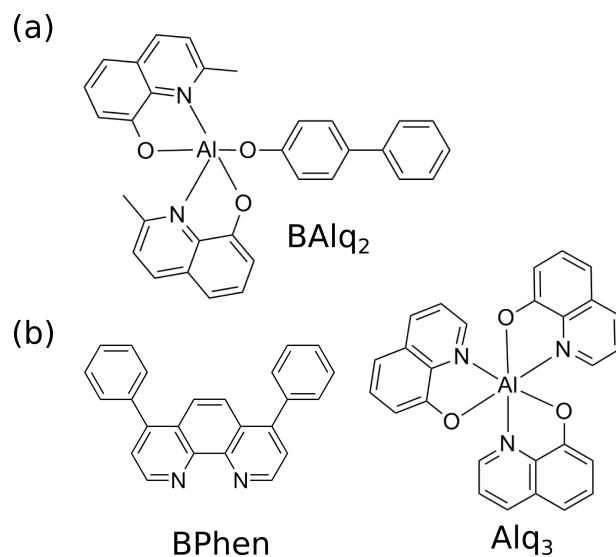
Figure 5.1.2: Chemical structures of (a) hole blocker BAlq$_2$ and (b) electron transport materials BPhen and Alq$_3$.

phenanthroline (**BPhen**, ABCR) co-evaporated with cesium (**Cs**, SEAS) is used. The doping ratio of the ETL is adjusted to obtain a conductivity of 10^{-5}S/cm. NET8 (Novaled GmbH), which has a HOMO at -6.0 eV and LUMO at -2.5 eV is also used as both HBL and ETL (doped with Cs). The rationale of replacing HBL and ETL materials with NET8 for use in photo-patterned OLEDs is described in Chapter 7. Alq$_3$ is used as both electron transport and emission layer in simple single heterojunciton OLEDs. The chemical structures of HBL and ETL materials are depicted in Figure 5.1.2.

5.1.4 Emitter Systems

As described in Chapter 3, for efficient OLED emission, materials with high electron-to-photon conversion efficiency are required. This implies not only high photoluminescence quantum yield of the corresponding excited molecular state, but also possibility to employ both singlet and triplet states. For this reason, phosphorescent Ir-based chromophores are used throughout this work. Use of the metal-organic compounds comprising heavy atom, results in an increased spin-orbit coupling leading to the high ISC rate and nearly 100 % EQE. For emission in the green, yellow and red, Tris(2-phenylpyridine) iridium(III) (**Ir(ppy)$_3$**, Covion GmbH), Bis(2-(9,9-dihexylfluorenyl)-1-pyridine) (acetylacetonate)iridium(III) (Ir(dhfpy)$_2$(acac), American Dye Source, Inc.) and Ir(MDQ)$_2$(acac) are selected. On the other hand, stability of the phophorescent blue emitters is very poor. For this reason, fluorescent chromophore 2,5,8,11-Tetra-tert-butylperylene (**TBPe**, Lumtec) is used. To prevent concentration quenching the emitters were incorporated into the wide band gap matrix layers. As mention previously, α-NPD was used as a matrix to red phosphorescent emitter. For the yellow and green devices, double matrix system, comprising emitters doped into 4,4',4"-tris(carbazol-9-yl)-triphenylamine (**TCTA**, Sensient) and 2,2',2"-(1,3,5-phenylen)tris(1-phenyl-1H-benzimidazol) (**TPBI**, Lumtec) in order to prevent emission quenching by shifting the emission zone away from the HBL layer with low-lying triplet state. For the blue emitter, (**MADN**, Lumtec) is used as a matrix.

The chemical structure, energy level diagram and spectral properties of emitter systems used in this work are summarised in Figure 5.1.3. HOMO values of matrix materials are determined by ultraviolet photoelectron spectroscopy (UPS), LUMO level is determined from the optical gap[1]. The excited singlet and triplet levels S_1 and T_1 are determined from the emission spectra[2].

5.1.5 Substrate and Electrodes

For all of the films and devices borofloat glass (Thin Film Devices Inc.) is used as a substrate. It has a thickness of 1.1 mm and, when used for OLED fabrication, is already coated with indium tin oxide (ITO), which serves as a bottom contact. The ITO has a thickness of 90 nm, a sheet resistance of 26 Ω/sq and around 92 % transmission in the visible. The work function of ITO is 4.7 eV. Top electrode, which serves as a opaque cathode in bottom-emitting OLED investigated in this work is metal aluminium (Al), which has a work function of 4.7 eV and average reflectivity of 90 % in the visible.

---

[1]UPS measurements were performed by Selina Olthof at IAPP.
[2]Measurements performed by Rene Michel and Caroline Murawski at IAPP.
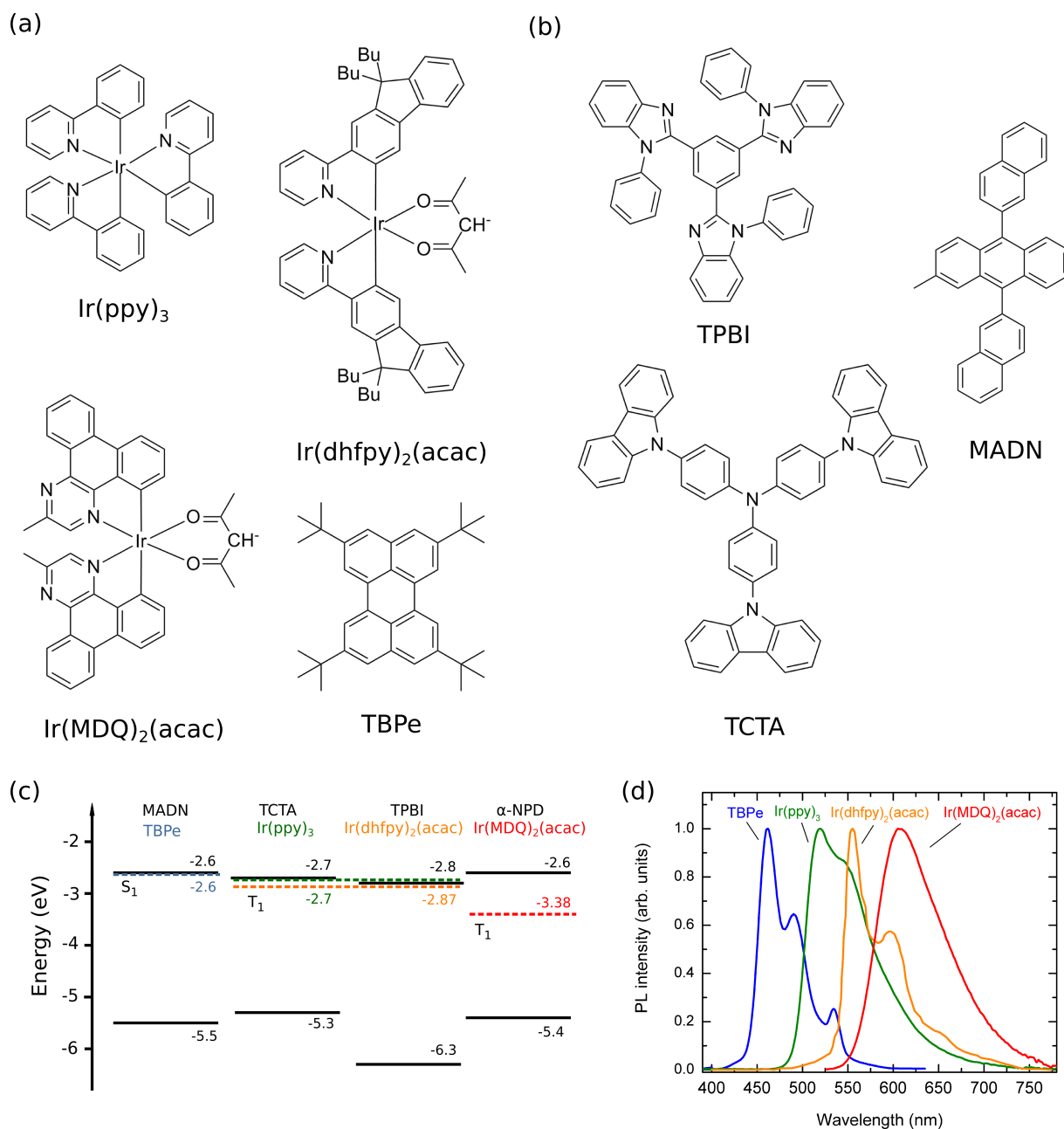
Figure 5.1.3: (a) Ir-based phosphorescent chromophores Ir(ppy)$_3$, Ir(dhfpy)$_2$(acac) and Ir(MDQ)$_2$(acac) emitting in green, yellow and red spectral region, respectively. For blue emission fluorescent molecule TBPe is used. (b) Chemical structures of matrix materials TPBI, TCTA and MADN. α-NPD was is as a matrix for Ir(MDQ)$_2$(acac).(c) HOMO and LUMO values of matrix materials (solid lines)and relevant singlet and triplet levels in corresponding chromophores (dashed lines). (d) Corresponding photoluminescence spectra of studied emitter systems.

5.2 Device Fabrication

5.2.1 Vacuum Deposition

Prior to device fabrication, the pre-structured 90 nm thick ITO coated glass substrates were cleaned using ultrasonic treatment in N-Methyl-2-pyrrolidon (**NMP**), distilled water, and ethanol. The single layer organic films and multilayered OLEDs are thermally evaporated in high vacuum. For simple device fabrication and sample testing a multichamber evaporation cluster system is used (Bestec), which is coined UFO2. Multilayered devices can be fabricated by transporting the sample from chamber to chamber wihtout breaking the vacuum. A single-chamber high vacuum tool (Kurt J. Lesker Co.) is used for OLED device preparation in big quantities. Organic and metal layers are thermally evaporated at a base pressure of 10^{-7} to 10^{-8} mbar without braking the vacuum. Evaporation rates and thicknesses of all layers are measured *in situ* via quartz crystals. Doping of organic film is achieved by co-evaporation. The organic layer sequence is based on the p-i-n device concept consisting of using doped charge transport layers, which enables low operational voltage and independent optimization of the device optics by varying transport layer thickness while maintaining the electrical performance [45]. The device is composed of HTL and ETL which ensure efficient charge injection from the electrodes and subsequent charge transfer. EML is then sandwitched between intrinsic EBL and HBL, whose role is to confine injected charges and excitons within the emission layer. In OLED stacks the overlap between bottom ITO contact and metal cathode defines the active area of the device, which is 6.76 mm^2 and 10.20 mm^2 for devices defined via evaporation through the shadow mask and photo-patterned pixels, respectively. After vacuum processing and lift-off, the OLEDs are encapsulated in nitrogen atmosphere using glass lids and UV-curing epoxy resin.

5.2.2 Photolithographic Structuring

Structuring via Lift-off

The simplified scheme of the photolithographic processing based on a bilayer method is depicted in Figure 5.2.1. It is used to structure films and devices based on organic semiconductors. Use of bilayer comprising fluorinated polymer and standard imaging resist is necessary, since fluoropolymer serves as a sacrificial layer for lift-off in HFEs, which are compatible with organics.

A glass substrate with the pre-patterned ITO (i) is subsequently covered by spin-coating of (ii) the fluorinated polymer film and (iii) the imaging resist layer (AZ nLOF-2020, AZ Electronic Materials GmbH). Fluoropolymer and imaging resist form 2.7 µm and 2 µm
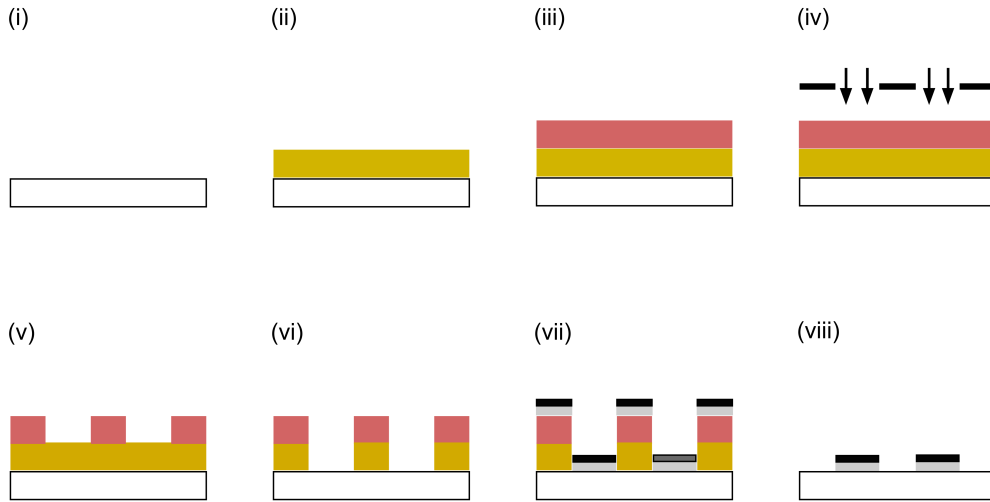
Figure 5.2.1: Simplified scheme of the photolithographic patterning procedure. (i) Substrate/electrode, (ii) spin-coat of the fluoropolymer, (iii) spin-coat of the imaging resist, (iv) UV exposure, (v) development of the imaging resist, (vi) development of the fluoropolymer, (vii) active layer deposition, (viii) lift-off in HFEs.

thick films, respectively. Mutual orthogonality between these two layers ensures that processing of the imaging resist does not alter the properties of the fluoropolymer and vice versa. The bilayer is patterned by (iv) exposing defined parts of the surface to the UV radiation (SF-100 broadband exposure system, Intelligent Micro Patterning) and subsequent (v) developing in the tetramethylammonium hydroxide (**TMAH**) based developer (ma-D 533 S, Microresist technology GmbH). The post-applied baking (PAB) and post-exposed baking (PEB) steps are performed for 1 min at 110 °C. Subsequently, the pattern is transferred into the fluoropolymer layer by (vi) spin-etching in a HFE solvent (**Novec7100**, 3M). To ensure the removal of resist leftovers an additional O_2 plasma treatment is applied. During the transfer step imaging resist serves as an etching mask. Next, the OLED stack is deposited (vii) under high vacuum on top of the pre-defined bilayer resist pattern. This procedure is followed by a lift-off in a fluorinated HFE solvent (viii), during which the parts of the OLED stack deposited on top of the given bilayer are removed yielding patterned organic layers.

Structuring via Etching

Standard photolithographic processing is applied to structure ITO anode into micro-sized stripes. AZ nLOF-2020 is deposited onto the glass substrate coated with ITO via spin-

coating. The desired structures are transferred to the photoresist film by UV exposure and subsequent development in TMAH developer. PAB and PEB steps are performed similar to the description above. The structured AZ nLOF-2020 film then serves as a mask for etching. Etching is performed using hydrochloric acid (37% concetration) for 3-4 min. The photoresist layer is removed by placing the sample in NMP solution for several minutes. Before further device fabrication the samples are cleaned by the standard procedure described in Sec. 5.2.1.

5.3 Measurements

5.3.1 OLED Characterisation

All measurements of encapsulated OLEDs are carried out under ambient conditions. Source measuring unit (SMU, Keythley SMU2400) together with a calibrated Si photodiode are used to obtain the current-voltage-luminance characteristics. The spectral radiance in the forward direction is recorded using a calibrated spectrometer (Instrument Systems GmbH CAS140). Angular emission properties of OLEDs are measured in an automated goniometer setup, consisting of a rotary table (OWIS GmbH), SMU and a USB4000 fiber optics spectrometer (OCEAN OPTICS). Spatially resolved electroluminescence spectra are acquired by recording OLED emission from a several micrometer spot using the combination of the imaging objective (63x, NA=0.8) and the near-field lens. The image plane is then focussed onto the entrance slit of an 0.6 m imaging spectrometer and recorded by a charge coupled device (CCD) camera [3]. Luminance decay curves were acquired by aging OLEDs under a constant current condition in a "Simple Lifetime" system (Novaled GmbH).

Three main parameters are used to evaluate and compare OLED performance. *The current efficiency* η_{CE} is obtained by simply measuring forward luminance $L_{0°}$ and dividing it by the current density passing through the device

$$\eta_{CE} = \frac{L_{0°}}{j}. \tag{5.3.1}$$

The η_{CE} is measured in cd/A units. Current efficiency does not account for the angular and spectral distribution of the emission, and therefore is relevant only for a basic initial comparison. As described in Chapter 3, *the external quantum efficiency* η_{EQE} is defined as the ratio between extracted photons and the injected electrons in OLED. Experimentally, it is estimated by measuring and integrating the spectral radiance intensity $I_e(\nu, \lambda)$ over

---

[3]Spatially resolved electroluminescence measurements were performed by Andreas Mischok at IAPP.

the whole emission hemisphere

$$\eta_{\text{EQE}} = \frac{2\pi q}{Ihc} \int \int \lambda I_{\text{e}}(\nu, \lambda) \sin \nu \, \mathrm{d}\nu \mathrm{d}\lambda. \tag{5.3.2}$$

η_{EQE} is a radiometric quantity. To account for the human vision, which perceives electromagnetic radiation in the visible spectral range with varying sensitivity, photometric *luminous efficacy* η_{LE} is introduced, which also takes into account human eye sensitivity function $V(\lambda)$

$$\eta_{\text{LE}} = 683 \frac{2\pi}{IU} \int \int I_{\text{e}}(\nu, \lambda) V(\lambda) \sin \nu \, \mathrm{d}\nu \mathrm{d}\lambda. \tag{5.3.3}$$

η_{LE} is measured in lm/W.

5.3.2 Optical and Morphological Inspection

The electroluminescence micrographs of OLEDs is taken using an optical microscope (Carl-Zeiss-Jena Jenaval). Photoluminescence micrographs and topography profiles are recorded using a fluorescence microscope (Nikon Eclipse High-resolution Microscope) and a Veeco Dektak 150 profilometer, respectively. AFM scans are acquired with CombiScope 1000 (AIST-NT) measurement setup. Measurements are performed in a tapping mode. A topographic view of the pixel surface is obtained using a laser scanning microscope (KEYENCE VR-3000).

5.3.3 Calcium Conductance Test

Barrier evaluation of the coated polymers is done using electrical calcium (Ca) tests. In this method, a thin, conducting, metallic calcium stripe reacts to non-conducting calcium hydroxide upon exposure to water. It is contacted electrically and acts as a sensor upon water ingress through the barrier, i.e. the investigated polymers. The quality of a moisture barrier is normally given by its water vapor transmission rate (WVTR), which is directly proportional to the derivative of the calcium's conductance over time [150]. The calcium sensor is contacted in a true four-point-probe conductivity measurement to avoid series resistance issues [151]. The Ca-Test stack comprises of three thermally evaporated layers. Deposited onto a 2.5×2.5 cm^2 BK7 glass substrate (Schott, Mainz, Germany) are 100 nm of aluminum electrode fingers, 100 nm of calcium sensor (length: 11 mm, width: 5 mm),

and 100 nm C_{60}. The latter is deposited over the whole sensor and acts as a mechanical decoupling of barrier and calcium [152]. Functional structuring of the evaporated layers was achieved by shadow masks placed in the evaporation path. Kapton tape is used to protect the samples' contact pads during spincoating deposition, which follows the evaporation process directly. All handling and processing before the measurement takes place in vacuum or in interconnected gloveboxes (MBraun). In the gloveboxes, an inert nitrogen atmosphere is kept with residual water and oxygen contents of below 0.1 ppm. Due to the fast reaction times of calcium thin-films, the measurements are performed under ambient conditions at 22°C and roughly 50% relative humidity. To keep fluctuations of the ambient climate to a minimum, all samples are measured consecutively in under an hour. For the WVTR measurement, each sample is taken from the glovebox individually and connected to a SMU in under 30 seconds. The SMU is connected to a measurement PC running a custom-made python program which performs a four point probe conductivity measurement with a set voltage of 20 mV every second. Measurements are done until complete calcium corrosion of each sample and generally takes between five to ten minutes. For more information on the electrical calcium test, see Klumbies *et al.* [152]

5.3.4 Time-of-flight Spectroscopy

Laser desorption/ionisation time-of-flight mass spectroscopy (LDI-TOF-MS) is an invasive technique to study material composition of OLEDs after lithographic processing. The mass spectra are obtained using tandem mass spectrometer (Bruker Daltonics Autoflex)[4]. The OLED stack is studied by peeling-off the Al cathode electrode. The bottom ITO contact then serves as the anode for producing electric field, required to separate ions produced by laser irradiation. Short pulses (ca. 10 ns) of N_2 laser emitting in UV (337 nm) is used to decompose the material of interest. The TOF-MS is based on a fact that, depending on the mass to charge ratio (m/z) the ions travel at different velocities in the electric field and are recorded at different times after the laser pulse, thus allowing to record and separate different contributions to the mass spectrum.

---

[4]LDI-TOF-MS experiment is performed by Florian Wölzl at IAPP.

6 Orthogonal Patterning of Organic Semiconductor Films and Devices

In this Chapter a summary of the initial study on patterning single organic films and simple devices using orthogonal photolithography is presented. It begins with the investigation on low molecular weight molecules, including fluorescent emitter and electron transporting Alq_3 and organic films doped with Ir-based metal-organic phosphorescent emitters. Some of these results are a part of a publication [153]. Experimental findings on the effect of lithographic processing applied to the simple single heterojunction OLEDs is discussed in Section 6.2. These initial results are meant to serve as a basis for the understanding the prerequisites and limits of the orthogonal photolithographic structuring of more complicated modern organic optoelectronic devices.

6.1 Patterned Low Molecular Weight Organic Films

Thermally evaporated small organic molecules are used to build most efficient state-of-the-art organic optoelectronic devices. Among those, Alq_3 stands out as an archetypal electron transport layer and green fluorescent emitter which was used as an active layer in the first demonstrated OLED [1]. As shown in the Chapter 3, due to the solubility parameter similarity with common organic solvents, the Alq_3 film would normally be severely damaged during various steps of the traditional photolithographic processing. Additionally, Alq_3 is known to crystallize after exposure to humidity [154], hence water-based developers and etchants would have an impact on the Alq_3 based device morphology and stability. For these reasons, photolithographic processing is not considered to be a viable option for Alq_3 films and devices.

To demonstrate the feasibility of the orthogonal processing based on bilayer method, stripe-patterning of a thin film of Alq_3 was performed. Shown in Figure 6.1.1, the width of the patterned stripes were 23 μm with 25 μm gap between the stripes. As seen from the fluorescence microscopy image of the film (Figure 6.1.1 (a)), highly regular features can be obtained. Profilometry measurements confirm that the structures exhibit well
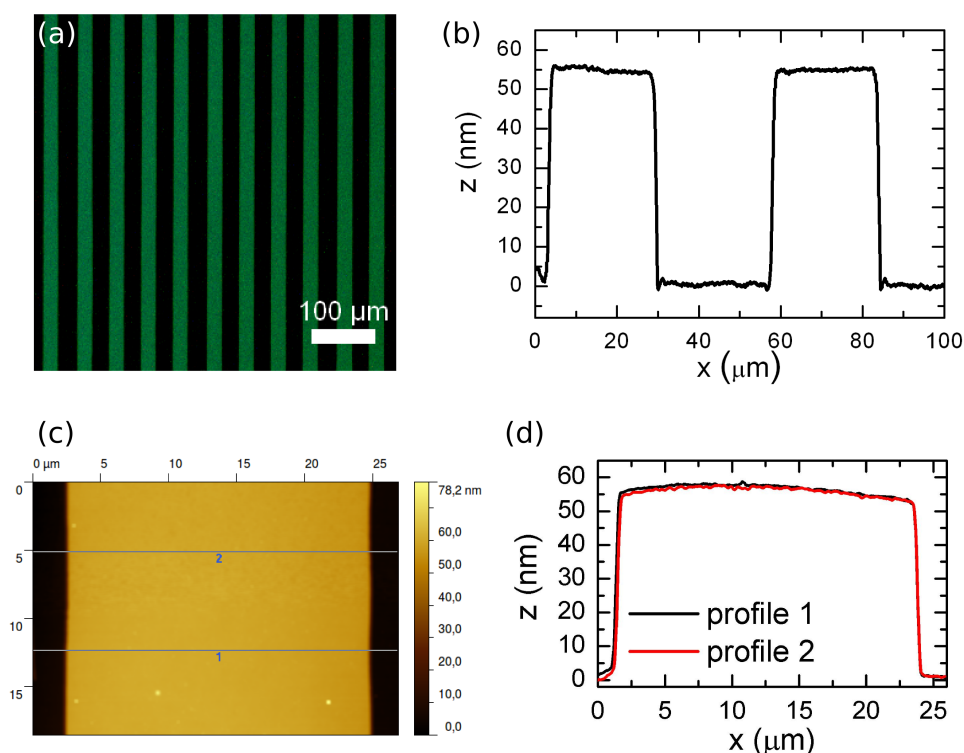
Figure 6.1.1: Photolithographic structuring of Alq$_3$ film. (a) Photoluminescence micrograph of a patterned Alq$_3$ thin film and (b) corresponding cross-section topography profile. (c) AFM scan of the structured feature and (d) corresponding edge profiles.

defined shapes and homogeneous thicknesses (Figure 6.1.1 (b)). AFM scans show that the films have well reproducible edges, with approx. 55 nm of film thickness reached over less than 1.5 µm in lateral dimension, in good agreement with the optical resolution of the lithography system used in this work (Figure 6.1.1 (c) and (d)). Such a profile is crucial for high-performance electrical operation as deviations from a rectangular profile would lead to inhomogeneous currents running through the device. In the past it has been proven challenging to achieve sharp edges and good thickness homogeneity with other methods including OVJP [121] and thermal patterning [125].

Organometalic phosphorescent materials represent the second generation of OLED emitters. They make the basis for most of the commercially available OLEDs, especially to cover the red and green spectral region. Two standard Ir based phosphorescent emitters doped into organic oligomer host material were investigated. TBPI film doped with 8 wt% Ir(ppy)$_3$ and α-NPD doped with 8 wt % Ir(MDQ)$_2$(acac) represent common green and red phosphorescent emitter systems, respectively, used throughout this work in state-of-the-art OLEDs.
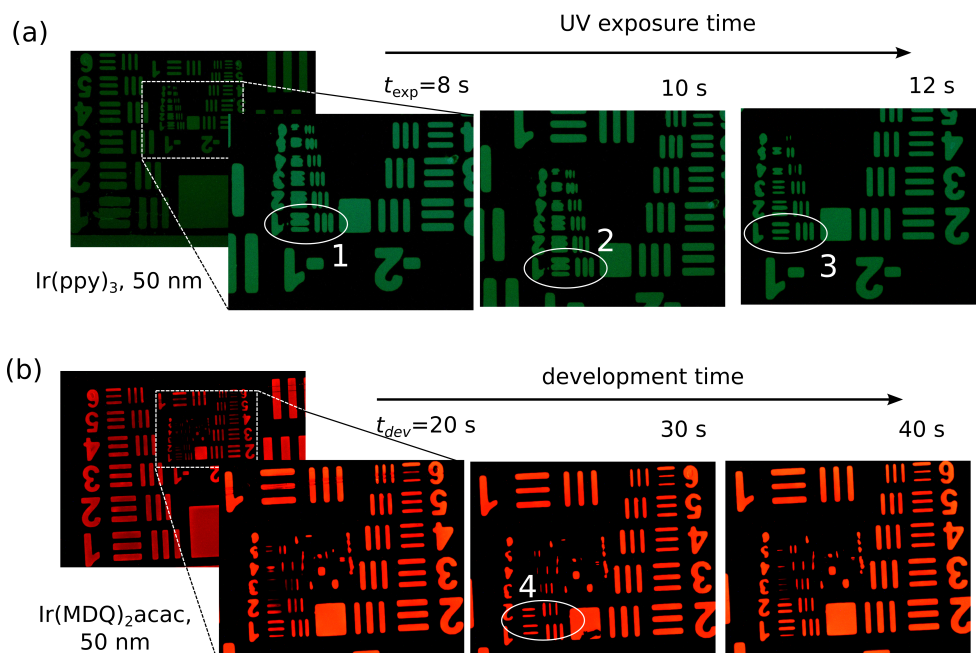
Figure 6.1.2: Photolithographic parameters study of structured small molecule organic films comprising phosphorescent emitters. (a) Photoluminescence micrographs of structured TBPI:Ir(ppy)$_3$ and (b) α-NPD:Ir(MDQ)$_2$(acac) films using the USAF1951 resolution target template. Regions 1-3 mark the observed feature change by varying the UV exposure time from 8 to 12 s. Smallest observed structured features (region 4) were ≈ 3.5 μm, limited by the capability of the exposure system.

A study of the structured phosphorescent 50 nm emitter films reveals the impact of the lithographic process parameters on the resulting patterned features. Figure 6.1.2 (a) depicts a structured TBPI:Ir(ppy)$_3$ film with varying UV exposure time t_{exp} applied to the imaging resist. The resulting patterned features are very sensitive to t_{exp}, with higher exposure times leading to higher resolution details. For example, marked regions 1, 2 and 3 in Figure 6.1.2 (a) represent ca. 5 μm features for t_{exp} =8, 10 and 12 s, respectively. Highest resolution is achieved with 12 s UV exposure.

On the other hand, change in the development time t_{dev} does not have a pronounced influence on the negative resist and the resulting structured organic film features (α-NPD:Ir(MDQ)$_2$(acac) film, Figure 6.1.2 (b)). The optimised parameters yield structures of around 3.5 μm (region 4), which is in line with the resolution limit of the exposure system. For the better sample reproducibility, $t_{\mathrm{dev}} \geq 30$ s is kept in all of the lithographic experiments.

6.2 Structuring Single Heterojunction OLEDs Based on Alq$_3$ Emitter

Simple single organic heterojunction devices similar to the first OLEDs reported by Tang and VanSlyke [1] were used as a model system to study effects of different processing steps of orthogonal photolithography applied to the electroluminescent device. Investigated OLEDs comprise a hole transporting layer (Meo-TPD or Spiro-TTB) and Alq$_3$ as both electron transport material and green emitter sandwiched between a semi-transparent ITO anode and an opaque Al cathode. Meo-TPD is a known hole transporter with HOMO level at -5.3 eV, LUMO of -1.9 eV and hole mobility $\mu_{\mathrm{h}} \approx 2.4 \cdot 10^{-5}$ cm^{2}V^{-1}s^{-1}. However it has a rather low glass transition temperature of T_{g} =55 °C. Hence, Spiro-TTB layer is also used, which is known to have similar electrical properties but higher morphological stability (T_{g} =143 °C).

While the electroluminescence efficiencies of the devices were poor, the simplicity of the studied OLED structure helps to identify how distinct lithographic processing steps influence certain functional layers or material interfaces, leading to the observed changes between shadow mask and photolithography patterned devices. In the following, the impact of the orthogonal processing applied directly to the Alq$_3$ film to structure the Al cathode is discussed. It is succeeded by the discussion on the observed changes in device efficiency and electroluminescence homogeneity after the O$_2$ plasma treatment.

6.2.1 Direct Emitter Patterning

The successful patterning of the emitter layer is the most simple approach to achieve RGB OLED array, as all of the structured emitters could be addressed by the same cathode which is evaporated as the last layer. Additionally, full color display could be achieved with only two patterning steps, by either conventional approach to use a common blue emitter layer as ETL for red and green devices [155, 87] or a common red emitter layer as HTL for green and blue devices [156]. Large area devices are studied in order to guarantee a reliable comparison of OLED characteristics not affected by the effects associated to the difficulties in fabrication and characterisation of microscale OLEDs. The corresponding active areas were 2.5 x 2.5 mm^2 for shadow mask structured OLEDs and 2.5 x 4.0 mm^2 for photo-patterned devices. Initial photolithographic processing experiment was performed directly after the deposition of the Alq$_3$ layer.

Despite apparent simplicity of the process and the promise to achieve an RGB array, direct structuring of the Alq$_3$ has never been successfully demonstrated in electrolumi-

nescent device, as the diode curve from the resulting photo-structured OLEDs was not recorded (a short circuit behaviour observed instead). Varying of HTL material did not yield successful results either. LDI-TOF-MS analysis was performed on shadow mask and photo-patterned OLEDs to gain insights into possible chemical degradation of the organic layers due to the orthogonal processing in HFE solvents. Figure 6.2.1 depicts the resulting mass spectra of the ITO/Spiro-TTB/Alq$_3$/Al devices, prepared by shadow mask (Figure 6.2.1 (a)) and photolithography (Figure 6.2.1 (b)).

The mass spectrum of shadow mask patterned device (Figure 6.2.1 (a)) has distinct peaks in around m/z=315, 900, 1006 and 1098. The peak at m/z $=$ 314.7 indicates the ionic peak of Alq$_2^+$. The analysis of the fine spectral features (Figure 6.2.1 (a), left inset) reveals a peak at m/z $=$ 458.9, which indicates the molecular ion state Alq$_3^+$ after the capture of an H atom. The existence of ionic Alq$^+$ state is difficult and the corresponding peak at m/z=171 is not observed. These observations are in line with similar analysis performed on a pristine Alq$_3$ film [157]. Additionally, the peak at m/z=774.3 can be attributed to the Al$_2$q$_5$ complex formed between Alq$_2^+$ ion and Alq$_3$ molecule.

Spiro-TTB exhibits higher T$_g$, but similar electrical properties to Meo-TPD, since it can be viewed as composition of cross-linked pair of Meo-TPD molecules (similar to Spiro-TTB). The presence of the peak at m/z=608.2 is then attributed to Meo-TPD$^+$ ion (Figure 6.2.1 (a), left inset). Then, m/z values which are approximately twice as large to Meo-TPD peak can be attributed the decomposition products of Spiro-TTB (Figure 6.2.1 (a), right inset).

The resulting mass spectrum after photo-patterning of the device is identical to the device structured by a shadow mask (Figure 6.2.1 (b)). Minor differences from peak positions in Figure 6.2.1 (a) (differences in m/z ratio ≤ 0.3) are observed, which can be attributed to the errors during sample preparation and LDI-TOF-MS measurement. Slight intensity variation can be observed in m/z=600-650 region (Figure 6.2.1 (b), right inset). The peak at around 608 attributed to the Meo-TPD moiety is less pronounced compared to the peak at 645 in shadow mask patterned OLED. Reversed situation is observed in photo-patterned device, which means there is slightly more pronounced decomposition into Meo-TPD than in the reference device. However, the effect is too small to account for the pronounced degradation observed in OLEDs after the photolithographic processing. To summarise, identical LDI-TOF-MS spectra between differently prepared OLEDs leads to the conclusion that no chemical bonding resulting in device degradation occurs during the multistep photolithography process. Therefore, different degradation pathways have to be responsible for the observed destruction of the devices, such as exposure to humidity and subsequent re-crystallisation or organic films, swelling of organic films due to HFEs, or water contamination at Alq$_3$/metal interface, among others.

6.2.2 Cathode as Protection Layer

Successful patterning of OLEDs is demonstrated by depositing an Al cathode before applying photolithographic processing. In such a case, Al is expected to stabilise the morphology of the underlying organic films and provide physical protection from the moderate levels of water contamination.

The current-voltage-luminance characteristics of OLEDs structured by photolithography is depicted in Figure 6.2.2 (open symbols). The performance of the standard shadow mask patterned devices are shown for comparison (solid symbols). EL spectra and current efficiency dependence on current density of the devices are shown in Figure 6.2.3. All of the devices are characterised by very low EQEs (≤ 0.5 %) and high turn-on voltage, which was around 7 eV for all of the measured OLEDs. All OLEDs emit at around 550 nm (Figure 6.2.3 (a)) in line with the emission spectrum of Alq$_3$. The EL spectra of the devices with similar HTLs are identical, while the differences between OLED emission from devices with different HTLs can be attributed to the differences between the refractive indexes of the materials used.

The observed differences between devices comprising different HTL materials can be understood by analysing the energy level diagram of the OLEDs (Figure 6.2.4 (a)). First of all, due to the very large injection barrier for the electrons from the cathode to Alq$_3$ (≈ 1.1

(a)

(b)
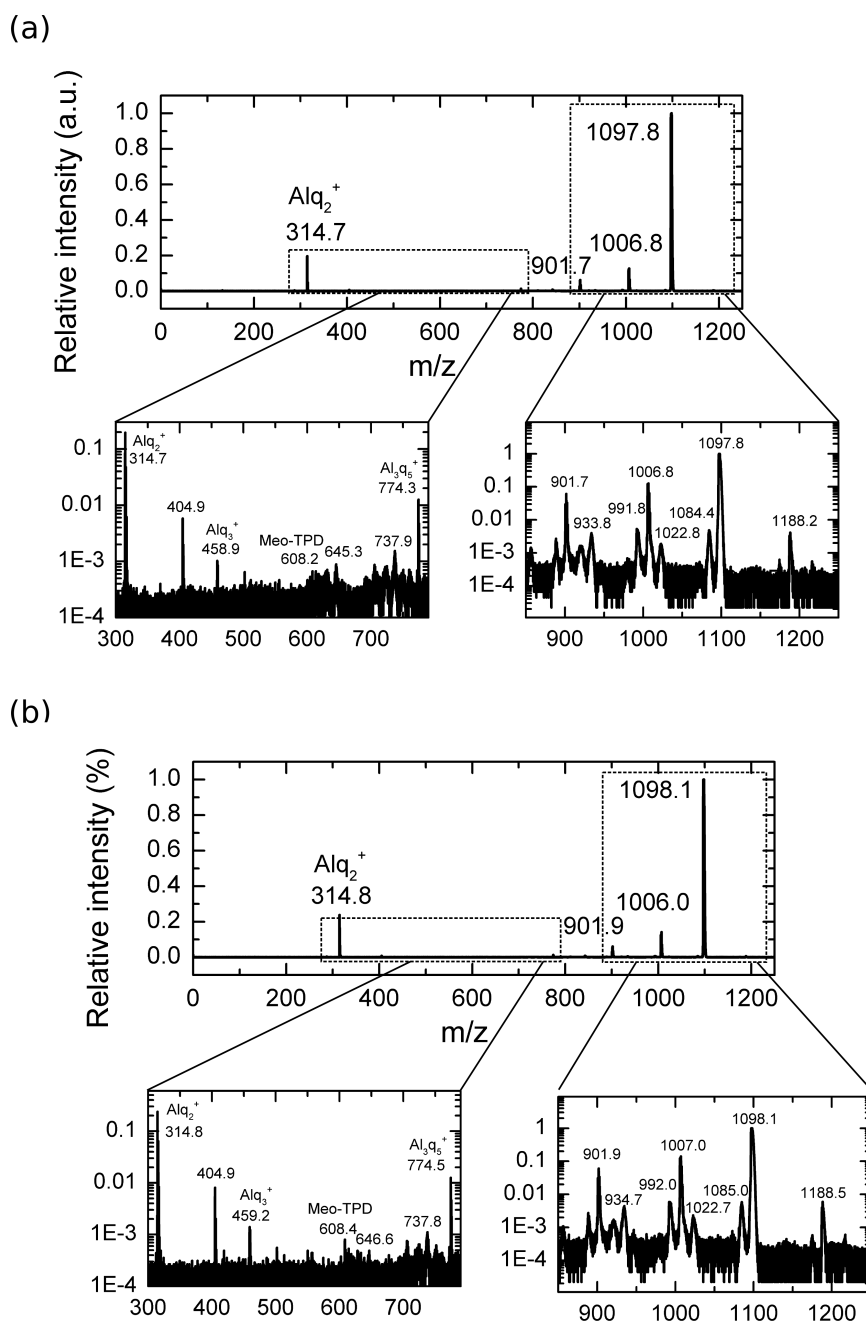
Figure 6.2.1: LDI-TOF-MS experiment results for single organic heterojunction ITO/Spiro-TTB/Alq$_3$/Al OLEDs. (a) Mass spectra of reference device patterned by shadow mask. (b) Mass spectra of OLED after the photolithographic patterning was applied to the EML (Alq$_3$).

(a)

(b)
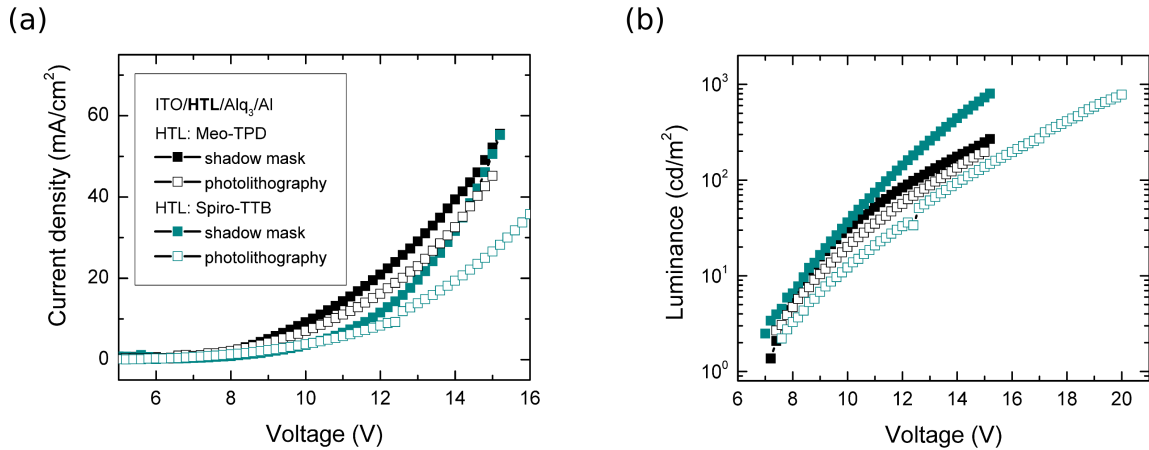
Figure 6.2.2: (a) Current-voltage and (b) luminance-voltage characteristics of ITO/HTL/Alq₃/Al devices. Black squares represent OLEDs with Meo-TPD as HTL, cyan squares represent devices with Spiro-TTB as HTL. Solid symbols denote vacuum deposited OLED patterned by standard shadow mask technique, open symbols represent photolithographic structuring of the OLEDs.

eV), the operation is injection limited from the n-side. This then explains the large turn-on voltage which was independent on the HTL used. However, even taking the large electron injection barrier and Alq₃ band gap ($\approx$2.25 eV) into account, this does not explain why the devices operate at $V_{ON} \geq 7$ V. This leads to the conclusion that due to the imbalance of electrons and holes, significant recombination current is present in investigated OLEDs. This claim is supported by the low hole injection barriers from ITO ($\approx$ 0.2 eV for Spiro-TTB and $\approx$ 0.6 eV for Meo-TPD as HTL) and ca. one order of magnitude higher charge carrier mobility values for holes in HTLs as compared to electrons in Alq₃. The three times smaller hole injection barrier for Spiro-TTB then results in overall lower current values compared to Meo-TPD devices due to the hole accumulation and capture close to the Alq₃/Al interface.

6.2.3 Impact of O₂ Plasma Treatment

Number of differences can be observed between the reference and photo-patterned devices for both Meo-TPD and Spiro-TTB based devices. The sample-to-sample variation was not high, therefore the observed differences cannot be attributed solely to the fabrication and characterisation errors. In general, lower currents are observed for OLED structured by photolithography. This leads to the lower luminance values for Meo-TPD/Alq₃ based OLED. Such device reaches 100 cd m⁻² at 13.4 V and 26.8 mA cm⁻² as compared to 12.5 V and 25 mA cm⁻² for the shadow mask structured device. Both of the devices
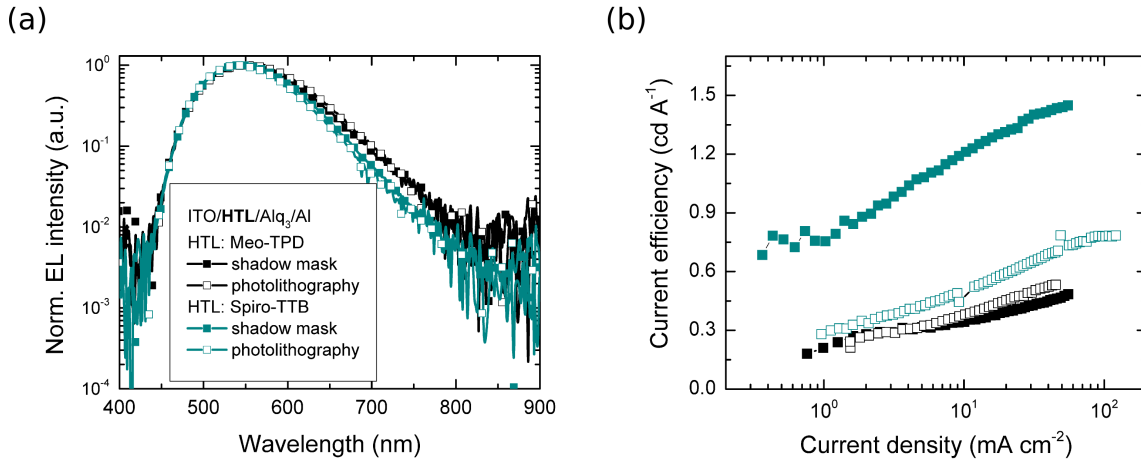
Figure 6.2.3: (a) Normalized electroluminescence spectra (b) current efficiency dependence on current density of Alq$_3$ based devices. Black squares represent OLEDs with Meo-TPD as HTL, cyan squares represent devices with Spiro-TTB as HTL. Solid symbols denote vacuum deposited OLED patterned by standard shadow mask technique, open symbols represent photolithographic structuring of the OLEDs.

exhibited comparable current efficiencies, reaching maximum value of ≈ 0.5 cd A^{-1}. The efficiency values for the structured device is slightly higher than its shadow mask structured counterpart.

However, the opposite situation is observed for Spiro-TTB devices, where significantly lower luminance values and current efficiencies are reached by the photo-patterned OLED. This device reaches 100 cd m^{-2} at 14.2 V and 20.7 mA cm^{-2} as compared to 11.5 V and 12 mA cm^{-2} for the shadow mask structured device. Overall Spiro-TTB devices exhibit higher efficiency values compared to Meo-TPD OLEDs, reaching 1.5 cd A^{-1} for shadow mask and 0.8 cd A^{-1} for photo-patterned devices.

The differences observed between OLEDs structured by the shadow mask and photolithography technique, are attributed to the changes in ITO work function after the O$_2$ plasma etching step during the lithographic processing. Due to its large work function of 4.7 eV ITO is a common choice as anode material for OLEDs and organic photovoltaic devices. ITO exhibits degenerate n-type conduction, which is attributed to the donation of a single free electron of Sn^{4+} dopant and pair of free electrons from O vacancy [158]. Changing the Sn/O ratio by increasing Sn deficient and O-rich areas by providing additional O$_{2-}$ ions via surface treatment [159], a reduction of carrier concentration can be achieved [160]. This results in larger surface band bending, lower conductance and a higher work function layer at the ITO surface. Additionally, removal of the carbon contaminants by the O$_2$ plasma treatment is attributed to the observed increase in the work function of
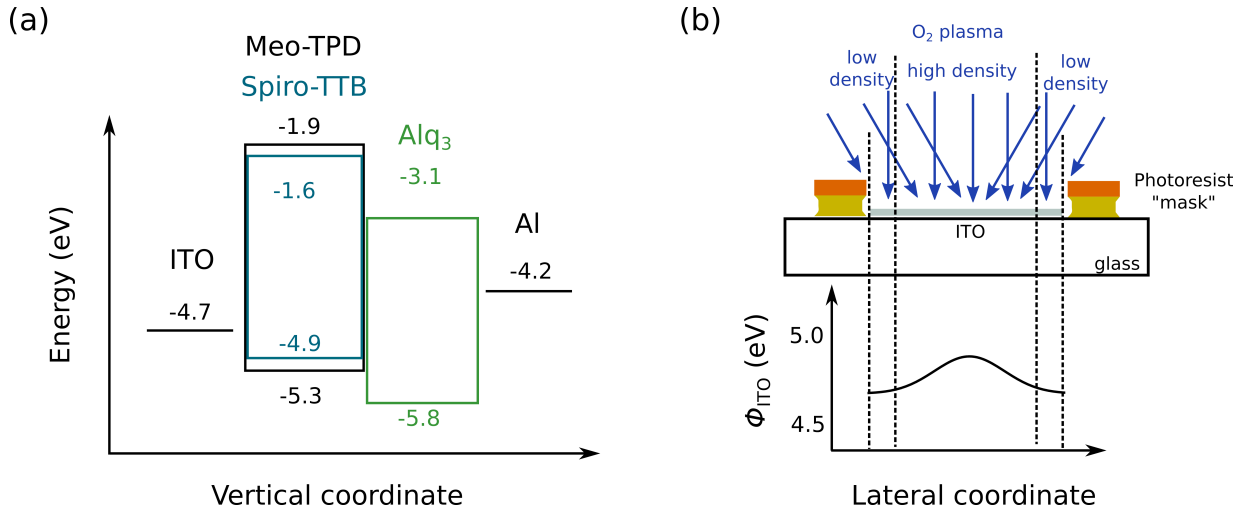
Figure 6.2.4: Energy level diagram for the Meo-TPD/Alq$_3$ and Spiro-TTB/Alq$_3$ devices. (b) Schematic illustration of the proposed mechanism for the O$_2$ plasma etching influence on OLED performance.

ITO [161]. It has been shown in the past that O$_2$ [162] or UV-ozone [160] treatment of ITO leads to better hole injection and improved OLED performance.

Since high deviation from the charge balance factor $\gamma = 1$ are expected in the simple double heterostructure devices studied in this work, additional O$_2$ plasma treatment before the evaporation of the organic layer sequence during the device fabrication and associated increase in the ITO work function overall results in diminished OLED performance in Spiro-TTB devices. This is attributed to the decrease in the hole injection barrier and increase in charge imbalance, resulting in two-fold decrease in current efficiency values for the photopatterned OLEDs (Figure 6.2.3 (b)). Additionally, strong inhomogeneity in EL emission was observed over the device area, with bright emission concentrated around the edges of the sample along with the strong reduction of the EL signal in the centre (Figure 6.2.5) opposed to the homogeneous EL profile exhibited by the shadow mask produced samples. Such inhomogeneous emission is explained by the shadowing effect of the photoresist mask during the O$_2$ etching step, shown schematically in Figure 6.2.4 (b). Large O$_2$ plasma density is expected in the center at the ITO surface with resulting increased anode work function and charge imbalance leading to the lower emission. The impact of this effect also depends on the position of the sample in the O$_2$ chamber leading to the sample-to-sample differences in the EL profiles of photo-patterned OLEDs, shown in Figure 6.2.5. Doping of organic charge transport layers, in order to reduce the impact of the work function of the anode, is expected to eliminate the impact of the anode material properties to the overall device performance. Such approach is pursued and presented in the following chapter on structuring p-i-n OLEDs.
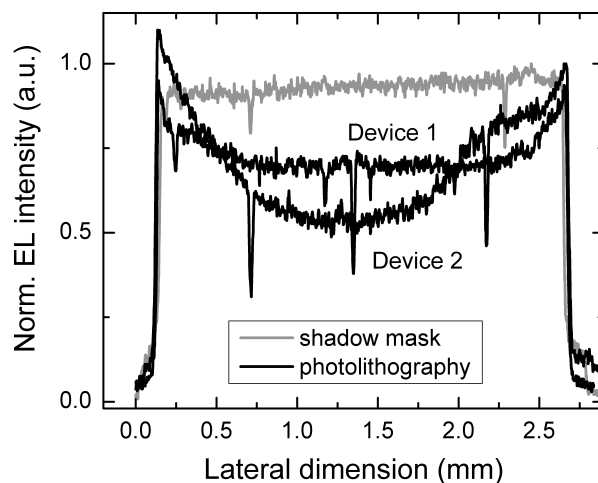
Figure 6.2.5: Typically observed electroluminescence profile of the large area ($\approx$ 6.4 mm^2) Spiro-TTB/Alq$_3$ heterojunction devices patterned by shadow mask (grey solid line) and photolithography (black solid line). The former is characterised by the homogeneous emission, while the latter exhibit pronounced decrease in EL signal in the center of the pixel compared to the emission at the edges.

6.3 Summary

In this chapter initial experiments demonstrating compatibility between various organic films and orthogonal lithographic processing are presented. Patterned films exhibit well-defined edge profiles and high resolution, which show great promise for the microscale optoelectronic device fabrication. Direct structuring of the Alq$_3$ layer as ETL led to the destruction of the device, which was further investigated by the mass spectroscopy analysis. No traces of the chemical degradation were found and the destruction of the OLED was attributed to the external factors affecting organic layers during device post processing. The degradation was circumvented by implementing cathode layer as a protective film, which enabled to demonstrate photolithographic structuring of simple single heterojunction OLEDs. A number of deviations from the performance of shadow mask fabricated OLEDs observed in photo-patterned devices were attributed mainly to the charge imbalance mediated by the change in the work function of the ITO anode during the lithographic processing.

7 Photolithographic Structuring of State-of-the-Art p-i-n OLEDs for Full-Colour RGB Displays

Following the proof-of-concept demonstration of the simple double heterojunction device structuring using lift-off in HFEs, this chapter presents the experiments on applying lithographic processing to the single colour multilayer p-i-n OLEDs. First, the compatibility between processing in HFE solvents and p-i-n OLEDs comprising phosphorescent emitters is investigated using tests of the prolonged exposure of the device to HFE environment and subsequent LDI-TOD-MS analysis (Section 7.2). Large area and microscale structured p-i-n OLEDs are demonstrated and investigated in Section 7.3 and Section 7.4, respectively. Finally, the chapter is closed with a discussion on the ways to extend the photolithographic processing to several steps for a multicomponent integration. Some of the results of this chapter are published in Ref. [153, 163].

7.1 Studied OLED Structures

Vacuum deposited OLED stacks comprising multilayered functional organic films are the basis of the commercial OLED displays found in smartphones, tablets and TVs. Vacuum deposition allows precise control of the thickness of each functional layer during the device fabrication. The standard multilayer p-i-n device architectures with optimised layer thicknesses studied in this work comprising phosphorescent red $Ir(MDQ)_2(acac)$ and green $Ir(ppy)_3$ emitters are shown in Figure 7.1.1 (a). The corresponding EL spectra are depicted in Figure 7.1.1 (b). Successful demonstration of photolithographic patterning of the red and green p-i-n OLEDs is a prerequisite for the realisation of the full-colour RGB display and is the focus of this chapter. The structuring of the blue pixel can then be achieved by a simple deposition through the shadow mask on the pre-patterned RG array. Hence, photolithographic structuring of blue OLEDs is left out in the following chapter and the possibility to deposit blue OLEDs after lithographic processing is discussed in the

subsequent chapter on two-colour microstructured device array.

The blocking and emission layers are typically few nanometers thick and any deviation from the optimal parameters can lead to pronounced changes in electrical and optical properties of OLEDs. Deviations from the optimal thicknesses can result from the film-solvent interactions during the lithographic OLED processing. Therefore, before structuring state-of-the-art p-i-n OLEDs by photolithographic means, a thorough initial compatibility study was performed by immersing the device into the HFE solvent for an extended period of time.
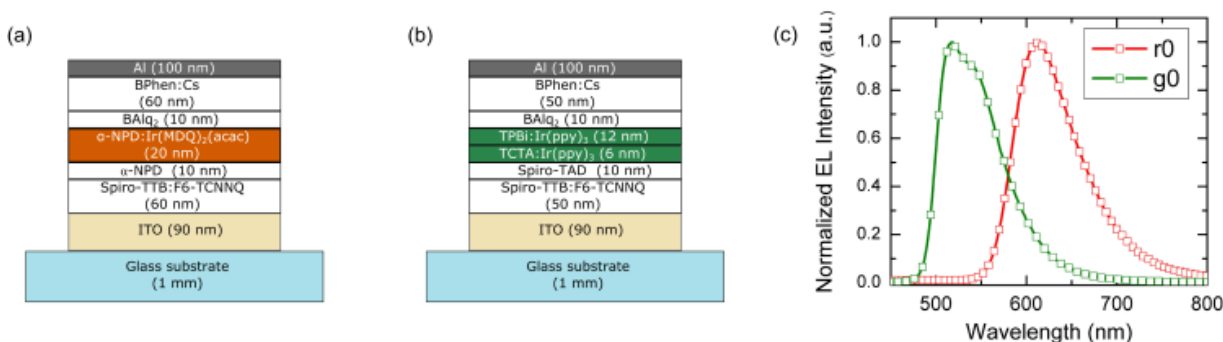
Figure 7.1.1: Standard electroluminescent devices used in this work: optimised red (a) and green (b) phosphorescent OLEDs comprising doped transport layers; (c) corresponding electroluminescence spectra of the reference devices (r0 and g0, respectively).

7.2 Compatibility Between HFEs and Multilayered OLED Stack

7.2.1 HFE Immersion Study

The impact of an HFE treatment on state-of-the art phosphorescent p-i-n OLEDs is investigated in terms of electrical and optical characteristics as well as long-term device stability. Non-encapsulated phosphorescent red-emitting OLEDs were immersed into the HFE for 5 h, i.e., more than twice as long as the time required for the lift-off step during patterning for large area devices. Afterwards the devices were characterized and their performance was compared to the performance of untreated reference devices structured by shadow mask. The red emitting OLED architecture was chosen for this test and is illustrated in the inset to Figure 7.2.1 (a). As majority of the charge transport and blocking layers are similar in red and green OLEDs, the focus of the compatibility study presented below is solely on red device. The reason for this is the relatively low glass transition temperature

of α-NPD (T_g=96 °C) which makes it more prone to the morphological instabilities during device post-processing, as compared to the Spiro-TAD (T_g=133 °C), TCTA (T_g=151 °C) and TPBi (T_g=122 °C) used in green phosphorescent OLED.

Figure 7.2.1 (a) shows the current-voltage-luminance (IVL) characteristics of reference and HFE treated devices. There is no detectable change in the IVL characteristics for the OLED immersed into HFE solution as compared to the reference device. Likewise, the EL spectra are not affected by the HFE treatment (Figure 7.2.1 (b)). It can therefore be concluded that the HFEs do not induce any significant change in the thickness of the organic layers, e.g., by swelling. Moreover, as shown in Figure 7.2.1 (c), the EQE and LE of the reference and the HFE treated OLEDs are nearly identical. Only at low luminance (< 30 cd m^{-2}), a slight reduction in EQE and LE is observed for the HFE treated device. This corresponds to operation in the low current density regime, where slightly higher leakage currents (not visible on the logarithmic scale used in Figure 7.2.1 (a)) are also observed for the HFE treated devices. The increase in leakage current is attributed to the additional sample handling step during which samples are immersed into HFE solvent. A more automated process is likely to further reduce the effect of HFE immersion.

In order to investigate the long-term stability of the devices after the HFE treatment, a series of OLED lifetime tests under different aging currents (i.e., different initial OLED luminance) were performed. Figure 7.2.1 (d) summarizes the $t_{0.75}$ lifetime of the HFE treated and the reference devices for the different aging currents (the $t_{0.75}$ lifetime is the time after which the device luminance has dropped to 75% of its initial value). It can be seen that OLED lifetimes of both reference devices and pixels immersed into HFE are similar (The slight difference in slope of the fits in Figure 7.2.1 (d) is within the range of sample-to-sample variation). For display applications, peak luminance requirements are in the range of 100-500 cd m^{-2}, i.e., more than one order of magnitude lower than the luminance at which the devices were operated during our test. In addition, in most display applications the pixels are not permanently operated at full brightness. The useful lifetime of OLEDs at relevant luminance levels can be estimated by assuming a power law correlation between the initial luminance L$_0$ and the $t_{0.75}$ lifetime. Even when assuming that the pixels are constantly operated at a luminance of 500 cd m^{-2} , a lifetime of $t_{0.75} >$ 100 000 h is expected for devices that were subject to the treatment in HFE. This confirms that the used HFE is fully compatible with the state-of-the-art phosphorescent OLED stack investigated in this work.
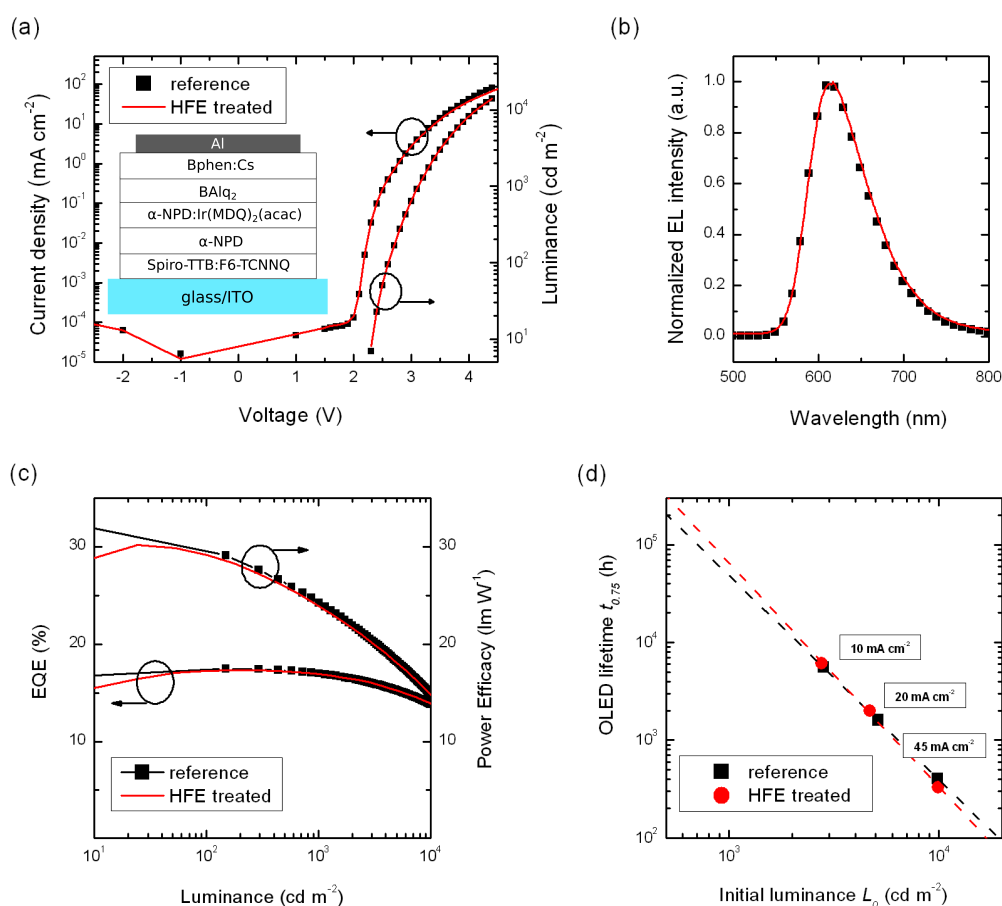
Figure 7.2.1: (a) Current density-voltage-luminance characteristics of OLEDs treated for 5 h in HFE (solid red line) and non-treated reference device (black squares); a schematic of the OLED stack used in this work is shown in the insert; (b) electroluminescence spectra, (c) external quantum efficiency and power efficacy vs luminance of the respective devices. (d) The $t_{0.75}$ lifetime vs initial luminance L_0 for HFE treated and untreated devices.

7.2.2 LDI-TOF-MS Analysis

Similarly to the study of simple single heterojunction Alq_3 devices, LDI-TOF-MS analysis was performed for p-i-n OLEDs comprising phosphorescent $Ir(MDQ)_2(acac)$ emitter for reference and HFE treated samples (Figure 7.2.2). Similarly to Alq_3 OLED case, the mass spectra before and after development in HFE solvents do not show significant differences. This again indicates the orthogonality between hydrofluoroethers and the multilayer OLED stack.

Additionally, both set of samples show similar characteristic peaks attributed to the chemical degradation and complexation of the emitter during electrical operation of OLEDs based on $Ir(MDQ)_2(acac)$. The signal around 1010 is attributed to the adduct between
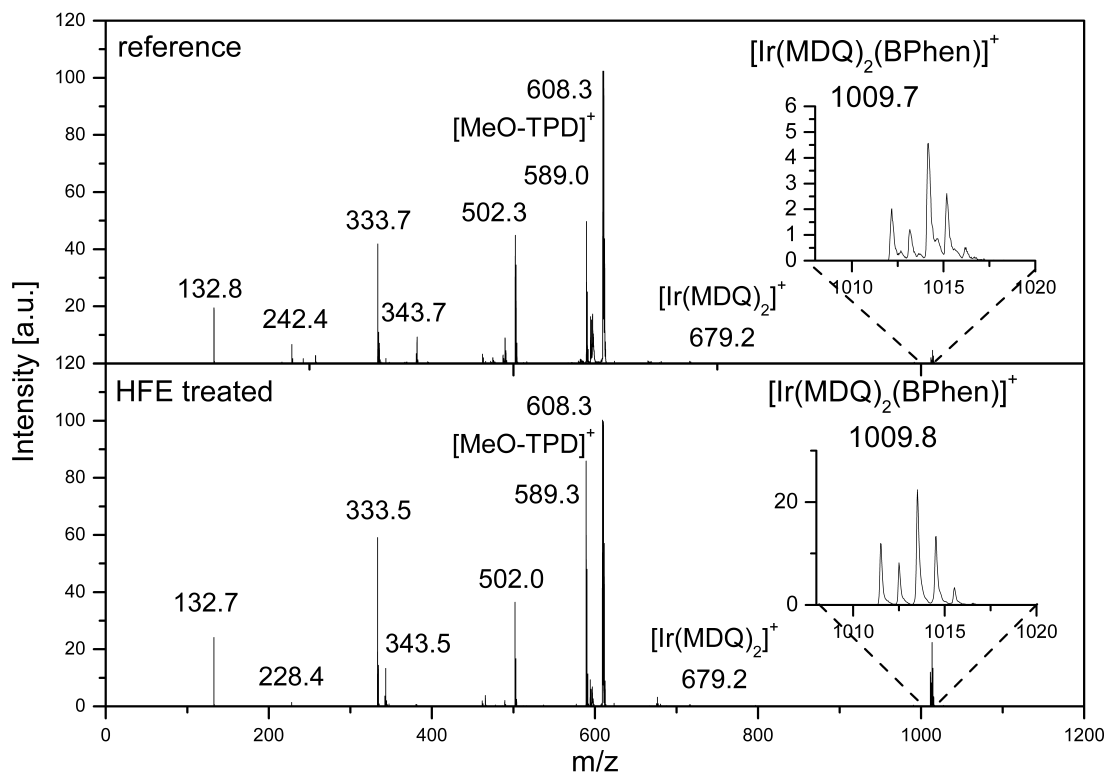
Figure 7.2.2: LDI-TOF-LS spectra of (a) untreated and (b) HFE treated devices comprising Ir(MDQ)$_2$(acac) emitter.

[Ir(MDQ)$_2$]$^+$ and BPhen [86], which is one of the possible pathways leading to the OLED degradation. The proposed scheme of the chemical changes in Ir(MDQ)$_2$(acac) is shown in Figure 7.2.3. Similar degradation products observed in LDI-TOF-MS analysis between reference and HFE treated devices is in line with the OLED lifetime study for reference and HFE treated devices (Figure 7.2.1 (d)).
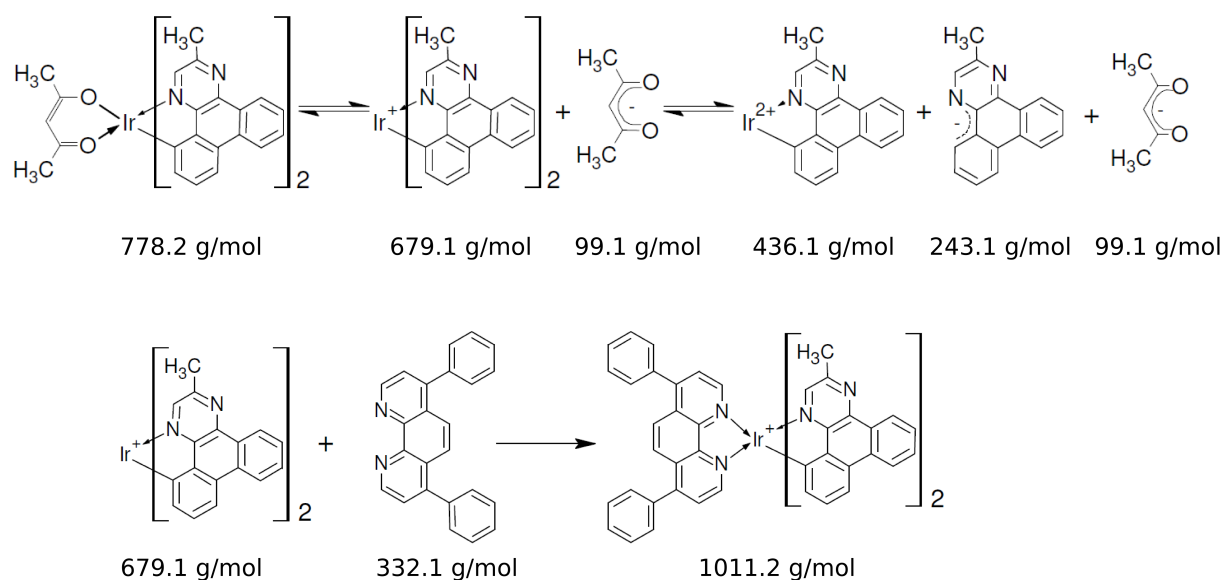
Figure 7.2.3: (a) Proposed dissociation pathway of Ir(MDQ)2(acac) and (b) the subsequent complexation with BPhen. After [86].

7.3 Photolithographic Structuring of Large Area p-i-n OLEDs

Large area OLEDs (2.5×2.5 mm^2 reference and 2.5×4.0 mm^2 patterned devices) were structured using photolithographic bilayer approach in order to guarantee a reliable comparison of device characteristics. Standard vacuum deposited red and green stacks defined via evaporation through shadow mask were used as a reference (r0 and g0, respectively). Figure 7.3.1 shows the current-voltage-luminance characteristics (jVL) and external quantum efficiency (EQE) and luminous efficacy (LE) of the reference and the photo-patterned devices (rP, gP). It can be seen that both rP and gP show comparable jVL performance under forward and reverse bias operation (Figure 7.3.1 (a)). Slight flattening of the jV curve is observed at higher current densities for a number of photo-patterned devices. This varied performance can be attributed to the morphological instability of certain organic films. Despite, emission properties of photo-patterned OLEDs are unaffected and both rP and gP reach EQE of 17.0 % and 14.9 % and LE of 28 lm/W and 57 lm/W at 1000 cd/m^2 without using additional light extraction structures, in line with state-of-the-art of the OLED technology. The performance of OLEDs structured by photolithography are higher than the best results achieved thus far by the OVJP technique [121]. Device yield was somewhat lower compared to the reference devices, but it is not surprising since in order to photo-structure the OLEDs, the devices were exposed to additional pre- and post-
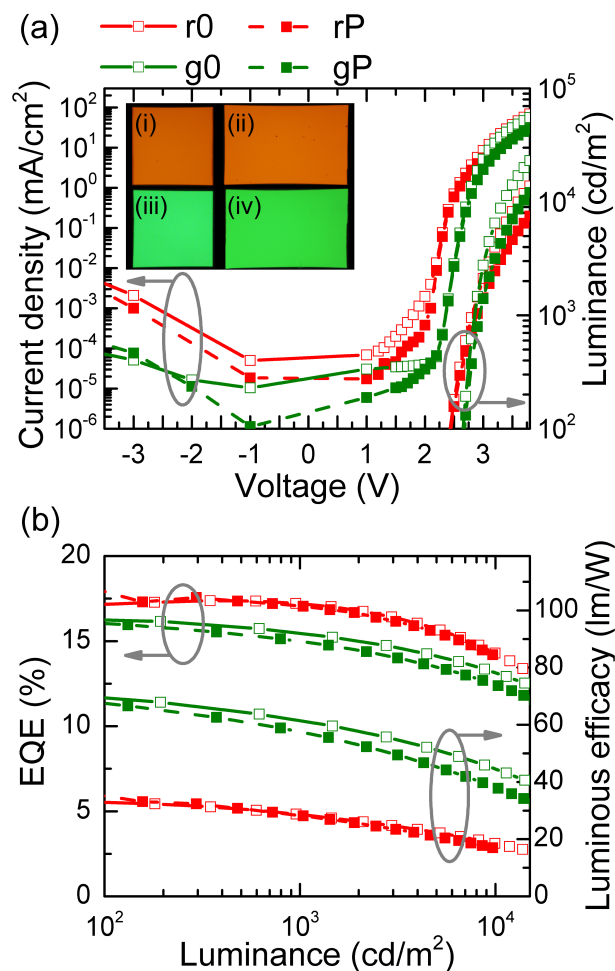
Figure 7.3.1: (a) Current density-voltage-luminance characteristics and (b) external quantum efficiency and luminous efficacy vs luminance of reference (r0, g0) and photo-patterned (rP, gP) devices. Insert in (a) shows microscope images of r0/g0 ((i)/(iii)) and rP/gP ((ii)/(iv)) pixels under electrical operation.

processing steps which increase the probability of substrate contamination and handling errors. Further improvement in the device yield could be achieved by exchanging current n-transport layers with materials exhibiting high glass transition temperatures and low tendency to recrystallize. Additionally low molecular affinity to HFE solvents is preferred as it is going to be discussed in the next chapter on the two-colour microstructured array fabrication. Finally, a higher class cleanroom facilities is expected to eliminate the impact of the substrate contamination and increase the overall yield of the photolithography process.

The long-term stability of the OLEDs is not affected by the photo-patterning. Figure 7.3.2 depicts the luminance decay of OLED pixels aged at a current density of 30 mA cm^{-2}, corresponding to a high initial luminance of 6500 cd m^{-2}. Overall, the aging behavior of photo-lithographically patterned pixels is nearly identical to the reference pixel. Only a slight initial decrease in luminance can be observed for the photolithographically patterned device over the first few hours. The lifetime of the photo-patterned device ($t_{0.75}$ =485 h) is comparable but somewhat shorter as compared to the shadow mask OLED ($t_{0.75}$ =505 h). Nevertheless, stable long-term operation of lithographically patterned OLEDs is demonstrated for over 1000 h.
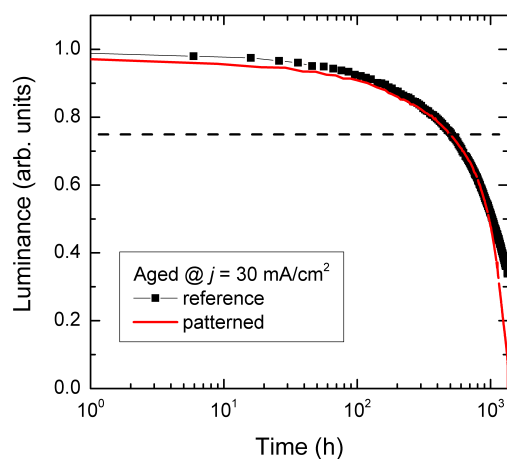
Figure 7.3.2: Aging of the Ir(MDQ)$_2$(acac) based OLED under constant current stress (j = 30 mA/cm^2). Black solid squares represent device structured by shadow mask technique, red solid line represent photo-patterned OLED. The dotted line represents the point at which $t_{0.75}$ lifetime is estimated.

In the previous chapter, EL profile inhomogeneities were described which were observed after the photolithographic processing of single heterojunction OLEDs. The deviations in EL profile and performance of photo-patterned devices compared to shadow mask structured OLEDs were attributed to the variation in the ITO work function due to the O_2 plasma etching during lithographic preparation. To reduce the impact of the ITO work function doping of organic films was suggested, as it is known to relax the requirements for the work function of the electrode by facilitating charge injection via tunnelling mechanism.
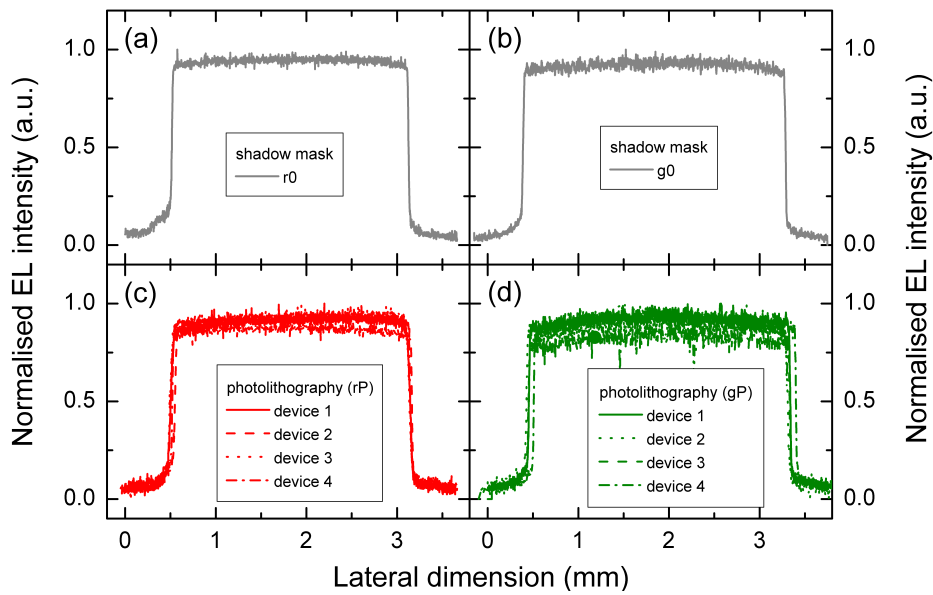
Figure 7.3.3: EL profile of shadow mask structured (a) red- and (b) green-emitting phosphorescent OLEDs. Corresponding profiles for devices patterned by photolithography are depicted in (c) and (d), respectively.

The p-i-n devices studied in this chapter represent OLEDs with both n- and p- type doping for efficient charge injection and transport. Indeed, as expected, homogeneous EL is observed after photolithographic patterning of large area p-i-n OLEDs. The corresponding EL profiles of red and green emitting reference devices r0 and g0 and a number of respective OLEDs patterned by photolithography rP and gP are depicted in Figure 7.3.3.

7.4 Electroluminescence from Microscale Devices

To demonstrate the capability of the photolithographic approach to structure electroluminescent organic devices on a scale relevant for OLED displays, a set of microstructured p-i-n OLEDs based on red phosphorescent emitter were fabricated (stack architecture shown in Figure 7.1.1 (a)). In display applications, pixel sizes in the range of 30-100 µm are used which requires defining stripes of the organic material with a width in the same range. Figure 7.4.1 (a) shows successful structuring and alignment of OLED stripes with a width of 65 µm placed on top of 15 µm wide pre-patterned ITO anode stripes. Well-defined stripes with homogeneous thickness are obtained as indicated by the excellent brightness homogeneity in the fluorescence micrograph (Figure 7.4.1 (b)). Under electrical operation, homogeneous EL is observed from the area of the film located on top of the ITO contact (Figure 7.4.1 (c)). The EL spectrum emitted by the patterned device is comparable to the spectrum obtained from pixels evaporated through a shadow mask (Figure 7.4.1 (d)).
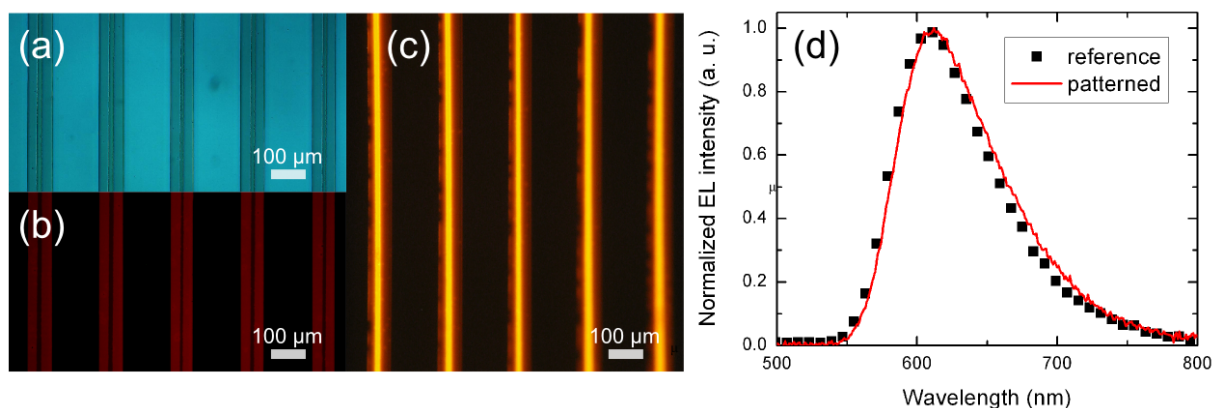
Figure 7.4.1: (a) Bright field and (b) fluorescence micrograph of 65 µm wide micropatterned stripes of red-phosphorescent OLEDs on a glass substrate with 15 µm wide ITO stripes. (c) Micrograph of photo-lithographically patterned OLEDs under electrical operation. (d) Electroluminescence spectra of micro-patterned device (red solid line) and unpatterned reference OLED (black squares).

Electroluminescence in such microstructured devices is expected to occur at the intersection of the ITO anode stripes and cathode, which defines the active area of the OLED. The Al cathode in this case is structured together with the functional organic layers by photolithographic means. Emission from the active area is most prominent in the EL micrograph depicted in Figure 7.4.1 (c). Additionally, there is a significant amount of emission outside the active area of the device also visible in Figure 7.4.1 (c). To investigate the observed emission outside the active area further, the EL profile was recorded for
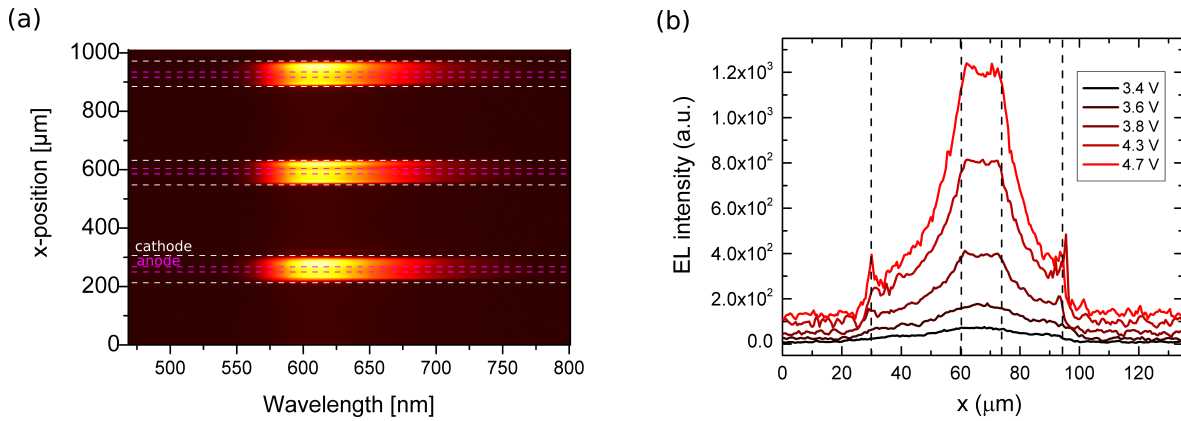
Figure 7.4.2: (a) Spatially resolved emission spectra of microstructured OLED array operating close to the tunr-on voltage and (b) EL profile of a structured OLED stripe recorded at different operating voltages. The lines indicate the corresponding position of corresponding electrodes. Intersecting area between anode and cathode defines the expected active area of the OLED. The emission observed outside the active area is attributed to the lateral charge transport in doped organic films.

different operating voltages of the microstructured OLEDs. Figure 7.4.2 (a) depicts the spatially resolved emission spectrum of device operated close to the turn-on voltage. The lines indicate the positions of the anode and cathode. The EL emission is homogeneous over the whole area of the organic films, there is no clear distinction between the regions where anode and cathode intersect and the rest of the device. With increasing voltage, EL localises as the emission from the active area becomes more pronounced. The observed EL profile change is depicted in Figure 7.4.2 (b).

EL emission outside the active area can be due to the reflection from the metal cathode, waveguided emission in organic films or extension of the recombination zone outside the active area whether due to the exciton diffusion or the lateral charge transport. The reflectivity of Al is around 90% and does not vary significantly in the spectral region of interest. Therefore, finite contribution of the back reflection is to be expected and is in line with the similar spectra recorded from the active area and outside of it (Figure 7.4.2 (a)). However, reflection from cathode fails to explain the observed emission intensity variation with the changing driving voltage of OLED. Similarly, confined optical modes in organic films should be independent on the applied voltage throughout the waveguide core region outside the active device area. Besides, additional outcoupling structures are required to extract guided light into the far-field. Since the studied microscale OLEDs are essentially planar, and the structure size is far greater than the coherence length of the emitted light
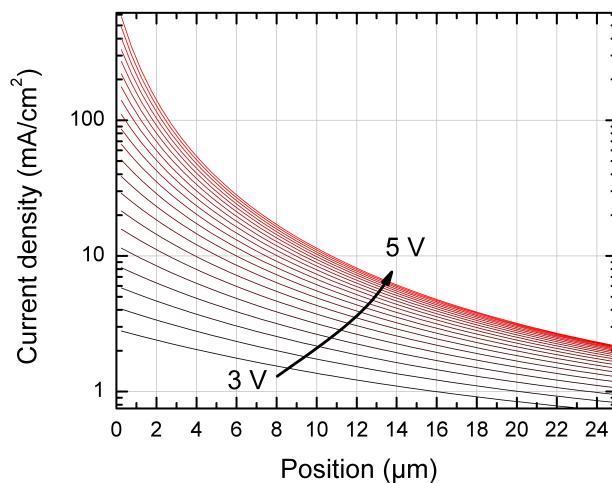
Figure 7.4.3: Simulated lateral current profile dependence on the applied voltage. Null position corresponds to the edge of the OLED active area (defined as intersection between anode and cathode electrodes). Current spread over tens of micrometers outside active area is predicted.

(in OLEDs the coherence length is typically $\approx$ 1-3 μm [164, 165]), the scattering effects are unlikely. On the contrary, coupling of the guided modes are observed at the edges of the device, where rougher device profile leads to the light scattering, which results in the observed EL intensity peaks (Figure 7.4.2 (b)), especially at the higher voltages. The effect is not observed at lower voltages. The effective length of the guided light beneath the leaky electrode is of the order of 10 μm [104]. It is comparable to the length the guided modes travel before reaching the cathode edge in the studied devices ($\approx$ 20 μm). Therefore, the absence of the EL intensity peaks at the cathode edges at low voltages can be attributed to the confined mode losses to the electrode, which makes the scattering effect too weak to observe.

Having ruled out the optical effects as an explanation of the observed EL outside the active area, it can be concluded that the emission occurs due to the spatial extension of the exciton recombination zone. Experimentally determined triplet exciton diffusion lengths in organic materials is typically few tens of nanometers [166, 167]. The effect is observed at order of magnitude higher scale, therefore significant exciton diffusion contribution into lateral recombination zone broadening is unlikely.

On the contrary, lateral charge transport in the doped organic semiconductors leading to the exciton formation and recombination outside the active area can fully explain the observed lateral EL. To demonstrate this, lateral charge transport was simulated using LT-

Spice IV package based on equivalent circuit method[1]. The spatial extent of the current transport was simulated by lateral discretisation of the device into diode subcells which are interconnected by the array of resistors, representing the sheet resistance of the doped organic films. The simulated current profile at different operating voltages is depicted in Figure 7.4.3. In accordance to the experimental findings, current is seen to spread over tens of micrometers outside the active area and is becoming more pronounced close to the active area as the voltage is increased.

---

[1]The simulations are performed by Axel Fischer at IAPP.

7.5 Bilayer Processing on p-i-n OLEDs

In order to successfully integrate three or more different OLED stacks on the same substrate, further processing steps and their influence on device performance have to be considered. Repetition of the bilayer processes would ultimately achieve the goal of multicolour patterning. However, several aspects different from the single colour structuring have to be considered. First of all, unless the fabrication utilities are equipped with photolithographic tools operating in the inert atmosphere, the effect of the exposure of devices to ambient conditions for a limited amount of time have to be accounted for (i). Secondly, fluoropolymer must be deposited and developed while being in direct contact with the OLED stack beneath (ii). Besides, deposition and development of the imaging resist (iii) together with baking of the resist at elevated temperatures (iv), plasma etching (v) and the UV exposure (vi) might as well harm the OLED stack. In the next section, the study focus on estimating the tolerance of the red OLEDs towards processing steps (i)-(iii), *i.e.* exposure device to air and deposition/development of the bilayer resist.

After the deposition in vacuum, various additional treatments were performed on non-encapsulated red phosphorescent OLEDs. Afterwards, test samples were encapsulated under inert atmosphere and their performance was compared to reference devices r0. Some of the OLEDs were exposed to ambient conditions for 4 h (test device r1). Fluoropolymer layer was spin-coated on the test device r2 in the inert N_2 atmosphere before 4 h air exposure and then developed in HFE solvent. In addition to the fluoropolymer processing, imaging resist was spin-coated in the inert atmosphere and developed in air with TMAH based developer (samples r3 (30 min air exposure) and r4 (4 h air exposure)). Table 7.5.1 summarizes the treatment of the test devices.

Initial jVL characteristics of reference OLED r0 and test samples r1 and r2 are shown in Figure 7.5.1(a). It can be seen that the electrical performance of r1 under forward bias operation is comparable to the reference device. However, exposure to air results in the decrease of the initial luminance L_0, which is observed from the onset of the emission and is increasingly more pronounced at higher luminance values. At a current density of $j = 100$ mA/cm^2, L_0 decreases from 18120 cd/m^2 for reference device r0 to 14690 cd/m^2 for r1. Comparison between r1 and r2 shows that additional fluoropolymer deposition and development does not alter device performance. This indicates that device exposure to the ambient conditions is the main factor affecting the OLED performance, while fluoropolymer processing is compatible with the OLED technology. Slight further drop in the initial luminance of r2 ($L_0 = 14090$ cd/m^2 at $j = 100$ mA/cm^2) is within the sample to sample variation range, and could be attributed to additional sample handling step.

Table 7.5.1: Samples tested for air exposure/bilayer processing. Fluoropolymer/imaging resist deposition and fluoropolymer development were performed in an inert atmosphere. Development of the imaging resist was done in the ambient conditions.

Sample name	Description	Air exposure	Fluoropolymer processing	Imaging resist processing
r0	reference	no	no	no
r1	air test	yes, 4 h	no	no
r2	fluoropolymer test	yes, 4 h	yes	no
r3	bilayer test (i)	yes, 30 min	yes	yes
r4	bilayer test (ii)	yes, 4 h	yes	yes

In order to compare long-term stability of the test devices, OLEDs were aged at constant current density of $j = 100$ mA/cm^2. At such elevated currents, various exciton annihilation mechanisms set in [168] and have to be considered to fully understand the degradation mechanism. However, since the device stack is kept constant throughout this work, therefore the changes in OLED performance of different test samples can be attributed to the extrinsic factors, such as oxygen and moisture [169, 170].

Figure 7.5.1(b) shows luminance decay curves of r0, r1 and r2 devices. Rapid decrease in luminance within the first several hours can be observed in all of the samples. Since Al cathode is porous to both oxygen and water[171, 172], initial drop in luminance is more pronounced in the samples r1 and r2, which were exposed to ambient conditions. This initial degradation is stronger in r1 device, as indicated in the faster normalized difference increase between r1 and r0 ΔL_{r01} as compared to ΔL_{r02} (normalized luminance difference between r2 and r0) over the first hours of device operation.

As shown in Figure 7.5.2, LT90 values extrapolated at $L_0 = 1000$ cd/m^2 drop from 810 h for reference sample to 401 h and 437 h for r1 and r2, respectively. This minor improvement in lifetime, together with slower initial increase and saturation of ΔL_{r02} indicates slight moisture barrier performance of the fluoropolymer layer. Electrical calcium tests (Ca-Tests) are performed to exclude OLED degradation by massive introduction of water into the device when using the imaging resist and to determine potential barrier qualities of the used spincoated materials. The corresponding drop in Ca was recorded due to the contact with water vapor (Figure 7.5.3). WVTRs of the fluoropolymer and bilayer resist were estimated to be 9.0±1.0 g/(m^{2}day) and 7.0±0.5 g/(m^{2}day), respectively. This indicates
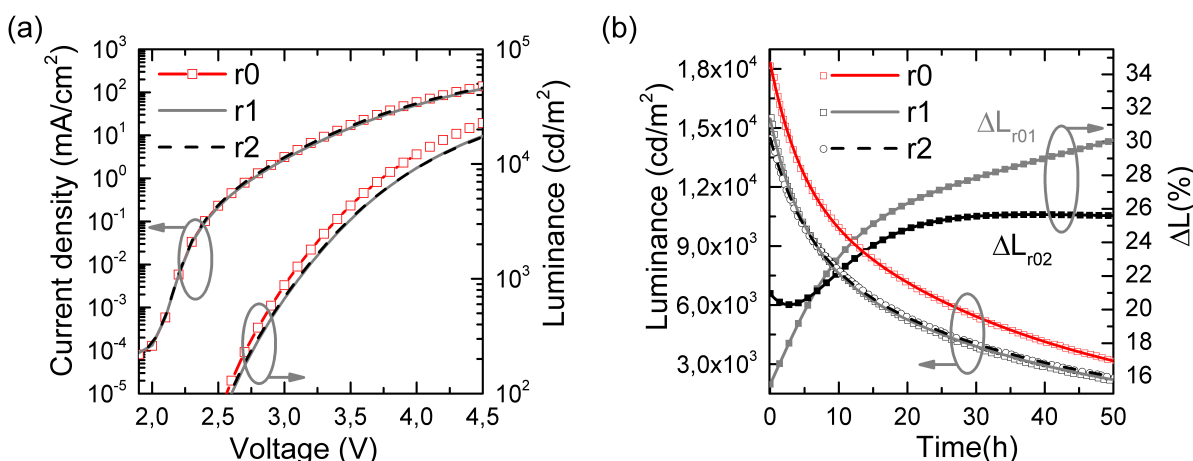
Figure 7.5.1: (a) Current density-voltage-luminance characteristics of reference (r0) and air exposed devices (r1 and r2). In between air exposure, additional fluoropolymer deposition and development were performed for sample r2. (b) Luminance decay curves of r0, r1 and r2 devices aged at $100\,\mathrm{mA/cm^2}$. Solid lines represent exponential decay fits. ΔL_{r01} (ΔL_{r02}) denote normalized change in luminance between the reference device and r1 (r2).

that additional imaging resist deposition does not introduce additional moisture into the vicinity of fluoropolymer/Ca interface, but results in a slightly improved WVTR due to the increase in overall film thickness compared to a single fluoropolymer layer.

Finally, full bilayer processing was performed on p-i-n OLED structure, including deposition and development of the imaging resist. Initial device performance is found to be severely diminished after 4 h air exposure and bilayer processing. More than 5-fold decrease in both EQE and LE is observed, together with an increase by approx. 130 mV in turn-on voltage, as compared to reference devices. However, the effect can be minimized significantly by reducing the time the bilayer is in contact with the OLED stack. Devices kept in ambient conditions with fluoropolymer/imaging resist for 30 min reach EQE of 13.08 % and LE of 18.40 lm/W at 1000 cd/m². As can be seen from Figure 7.5.2 both L_0 and LT90 are as well highly reduced after the bilayer processing (samples r3 and r4) and are higher for the sample with a lower tact time. Measurement results are summarized in Table 7.5.2.

Native solvent of the imaging resist is propylene glycol methyl ether acetate (PGMEA). Immersing of the OLED into the PGMEA results in a rapid destruction of the device. Considering this, together with Ca-test results and the pronounced dependence of OLED degradation on the time bilayer stays on the OLED structure, the degradation induced by the bilayer processing is attributed mainly to the diffusion of the PGMEA, which is introduced by the imaging resist, through the fluoropolymer layer and subsequent swelling
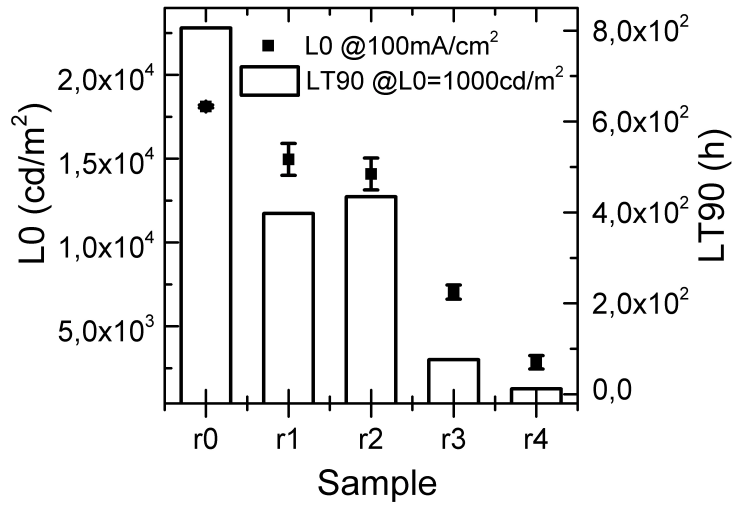
Figure 7.5.2: Initial luminance measured at 100 mA/cm^2 (black squares) and extrapolated device lifetime LT90 at $L_0 = 1000$ cd/m^2 of the tested samples.

of the active OLED layers.

Table 7.5.2: Accelerated degradation measurement of test devices. EQE and LE are measured at 1000cd/m^2, L_0 and LT90 are initial luminance and time at which luminance drops to 90 % to its initial value, respectively, measured at $j = 100$ mA/cm^2. LT90* is extrapolated lifetime at $L_0 = 1000$ cd/m^2

Sample	V_{on} [V]	EQE [%]	LE [lm/W]	L_0 [cd/m^2]	LT90 [hours]	LT90* [hours]
r0	2.35	17.0	27.8	18120	1.38±0.25	810±150
r1	2.38	15.0	23.5	14960	1.04±0.07	401±75
r2	2.33	13.7	21.9	14090	1.29±0.03	437±68
r3	2.40	13.1	18.4	7040	1.04±0.03	77±10
r4	2.48	3.0	4.1	2850	1.19±0.06	12.1±3.4

To sum up, deposition of the fluoropolymer in direct contact with non-encapsulated *p-i-n* device and subsequent processing in HFE solvents were found to be compatible with the OLED technology. Besides, slight improvement in the long-term operation of the devices with deposited fluoropolymer layer exposed to air can be attributed to the moisture barrier properties of the deposited film. Finally, full bilayer processing was performed on *p-i-n* devices and it was shown to be detrimental to both initial and long-term performance of the OLEDs. Further research is focused on search for imaging resist with better compatibility with organic semiconductors as well as for polymers exhibiting better barrier properties combined with solubility in HFEs.
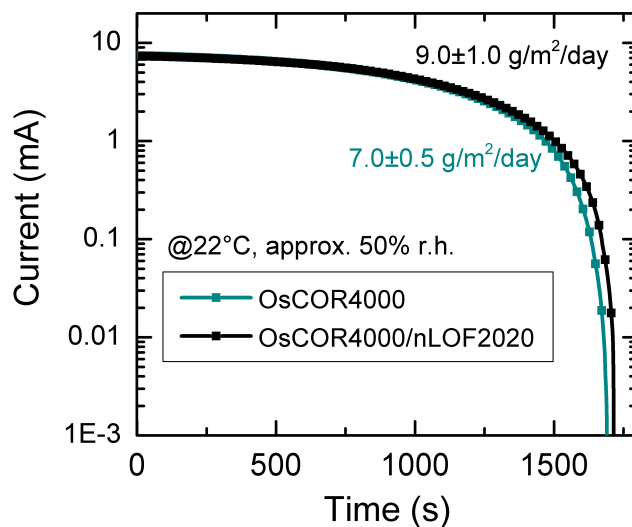
Figure 7.5.3: Conductive Ca test results for standalone fluoropolymer (OsCOR4000) and bilayer resist (OsCOR4000/AZ nLOF2020) films. The corresponding WVTRs are indicated.

7.6 Summary

The thorough investigation of photolithographic structuring of state-of-the-art OLEDs comprising doped organic films was presented. The compatibility between processing in orthogonal HFE solvents and multilayer OLED architectures was established by the immersion study and subsequent mass spectroscopy analysis. Photolithographic structuring of both large-area and microscale devices were demonstrated. The photo-patterned OLEDs show no significant deviations in performance compared to the vacuum deposited shadow mask counterparts. Use of doped organic films for charge injection/transport within the device allows to relax the requirements for the work function of the electrodes. Therefore, homogeneous electroluminescence over the whole active area of the photo-patterned OLEDs were demonstrated, contrary to the discussion on the devices comprising pristine organic films in previous chapter. The structured devices reach up to 17% EQE and $>10^5$ h lifetime at operating conditions relevant for display applications which is in line with the state-of-the-art technology. Successful structuring of the state-of-the-art OLEDs convincingly demonstrates the potential of orthogonal photolithography for producing large-area full-colour OLED displays, without the need of using additional colour filters. While the production of such display is beyond the scope of this work, the main challenges in extending the photolithograhic processing to multiple steps were also addressed. The influence of both, double resist processing on p-i-n OLEDs and exposure of the devices to ambient

conditions, on the basis of the electrical, optical and lifetime parameters of the devices were presented. By implementing thin Ca film conductance test to evaluate water vapor transmission rates of single and bilayer system, it was concluded that the diffusion of propylene glycol methyl ether acetate (PGMEA) through the fluoropolymer film is the main mechanism behind OLED degradation observed after bilayer processing.

8 White Light from Photo-structured OLED Arrays

This chapter presents the results on a two-colour microstructured OLED array, comprising side-by-side aligned fluorescent blue and phosphorescent yellow subunits. Demonstrated lateral alignment approach enables easy device optics optimization with a possibility to address subunits separately, resulting in high quality tunable white light emission, with excellent colour stability, desired in real applications. The chapter is split into two major parts - Section 8.1 describes the steps for device preparation and optimisation of various functional layer parameters, while Section 8.2 contains the presentation and the discusion of the main experimental findings.

8.1 Fabrication of Micro-OLED Array

White organic light-emitting diodes (OLEDs) are promising candidates for future solid-state lighting applications and backplane illumination in large-area displays. One very specific feature of OLEDs, which is currently gaining momentum, is that they can enable tunable white light emission. This feature is conventionally realized either through the vertical stacking of independent OLEDs emitting different colours or in lateral arrangement of OLEDs. The vertical design is optically difficult to optimize and often results in efficiency compromises between the units. In contrast, the lateral concept introduces severe area losses to dark regions between the subunits, which requires a significantly larger overall device area to achieve equal brightness. In the following, a colour-tunable, two-colour OLED device is demonstrated which is realized by side-by-side alignment of yellow and blue p-i-n OLEDs structured down to 20 μm by a simple and up-scalable orthogonal photolithography technique. This layout eliminates the problems of conventional lateral approaches by utilizing the complete area for light emission.

8.1.1 Structuring Procedure

The device architectures of fluorescent blue and phosphorescent yellow OLED subunits are depicted in Figure 8.1.1 (a). The organic layer sequence is based on the p-i-n device concept consisting of doped charge transport layers. The details regarding the layer thicknesses and material choice will follow in the next section.

The simplified scheme of the fabrication procedure of the microstructured OLEDs is depicted in Figure 8.1.1 (b). The OLED array is realized by photolithography, using fluorinated resist as a sacrificial layer in addition to the development of hydrofluoroethers enabling lithographic processing of organic semiconductors, as described in previous chapter. The photo-patterning of the sY device yields a structured yellow-emitting subunit array. A subsequent deposition of the sB device finishes the two-colour laterally structured OLED. Lateral dimensions W_Y and W_B define the widths of the yellow and blue subunits, respectively. The lateral subunit dimensions of microstructured devices W0, W1, W2, and W3 are WY/WB=50/50, 80/80, 80/20 and 100/30 µm, respectively. The following discussion is focused on the model device W0. The effect of different subunit size is detailed in the next Chapter. The photolithographic patterning also allows a precise allocation of the top electrode on the substrate, enabling each of the subunits to have separate drivers V_Y and V_B for yellow and blue subunits, respectively. The active area of microstructured devices W0-W3 is 7.75 mm^2.

The topography image of the microstructured OLED array W0 (W_Y/W_B=50/50 µm) is depicted in Figure 8.1.1 (c). The photolithography enables a homogeneous device profile and well-defined edges that are crucial parameters for reliable device operation at the microscale. Figure 8.1.1 (d) shows the micrograph of the same device under electrical operation when both yellow and blue subunits are activated simultaneously. When viewed from a larger distance, the emission of the subunits is indistinguishable to the viewer, and white light is instead perceived (Figure 8.1.1 (e)). This is achieved without additional optical diffusion components through the relatively small size of the monochrome devices, which is enabled by the photolithographic structuring.

8.1.2 Optical Device Optimisation

The devices were designed with a multilayered p-i-n architecture including charge transport and blocking layers [45, 44, 46, 47]. The p-i-n concept is based on the usage of the doped charge transport layers on both p- and n-transport side. It allows optical optimisation of OLED stack by varying transport layer thickness without negatively affecting electrical performance of the OLED. The ETL and HTL thicknesses were chosen according to the

(a)

Device sY

Al (100 nm)
NET8:Cs (1:1, 50 nm)
NET8 (10 nm)
TPBI:Ir(dhfpy)$_2$(acac) (8wt%, 12 nm)
TCTA:Ir(dhfpy)$_2$(acac) (8wt%, 6 nm)
Spiro-TAD (10 nm)
Spiro-TTB:F$_6$-TCNNQ (4wt%, 50 nm)
ITO (90 nm)

Device sB

Al (100 nm)
BPhen:Cs (1:1, 40 nm)
BAlq$_2$ (10 nm)
MADN:TBPe (1.5wt%, 10 nm)
Spiro-TAD (10 nm)
Spiro-TTB:F$_6$-TCNNQ (4wt%, 20 nm)
ITO (90 nm)

(b) Devices W0-W3

photo-patterning of sY

deposition of sB

(c) **(d)** **(e)**
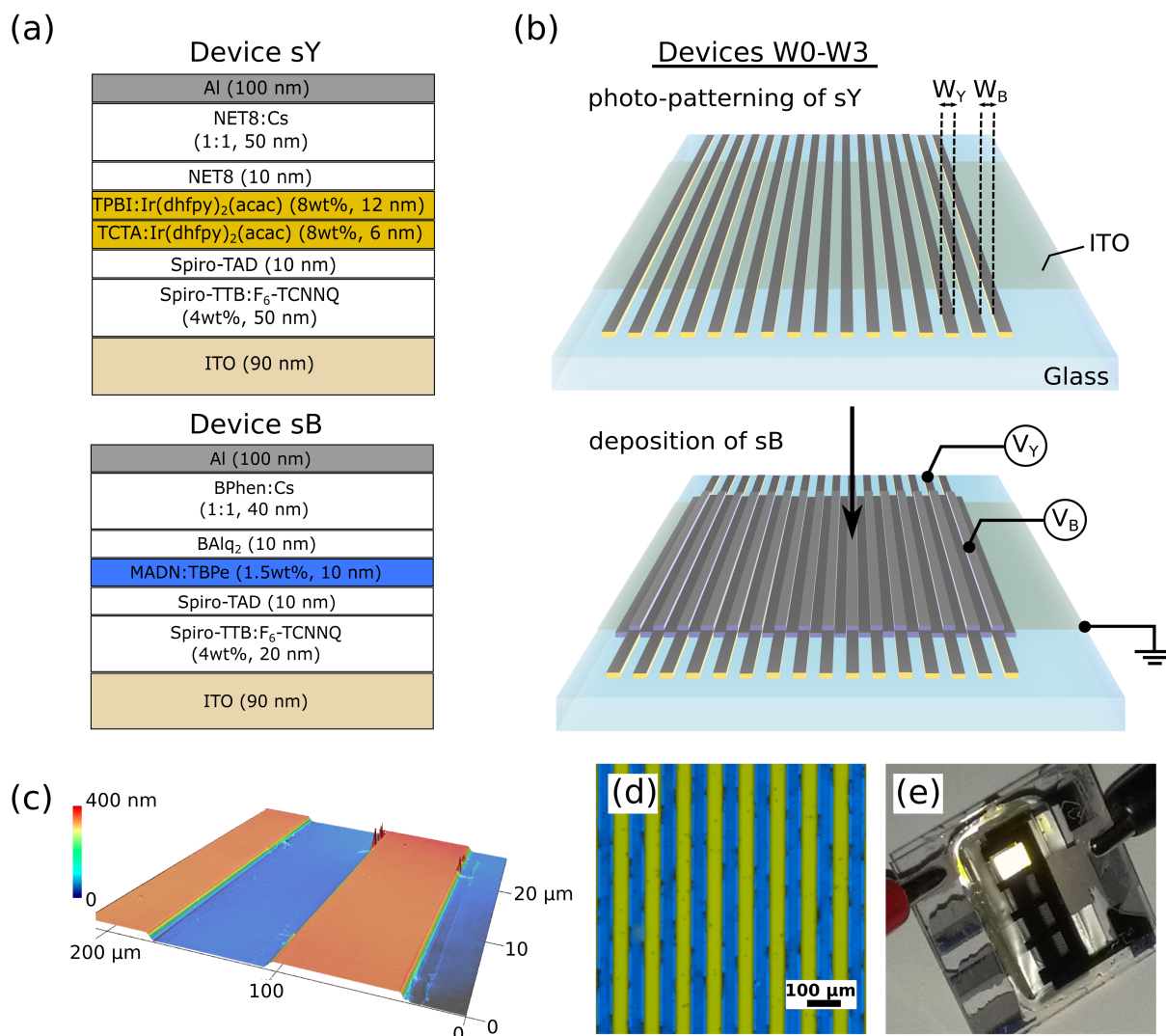
Figure 8.1.1: (a) Device architectures of yellow and blue p-i-n OLEDs (devices sY and sB, respectively). (b) simplified scheme of patterning procedure applied to achieve a microstructured OLED array. The widths W_Y/W_B of yellow/blue subunits are 50/50, 80/80, 80/20 and 100/30 μm for devices W0, W1, W2 and W3, respectively. V_Y and V_B denote corresponding electrode operation of yellow and blue subunits, respectively; (c) a false-colour topography image of microstructured device W0; (d) micrograph of the structured OLED under electrical operation; (e) photograph of the emission of the patterned device perceived as white light.

131
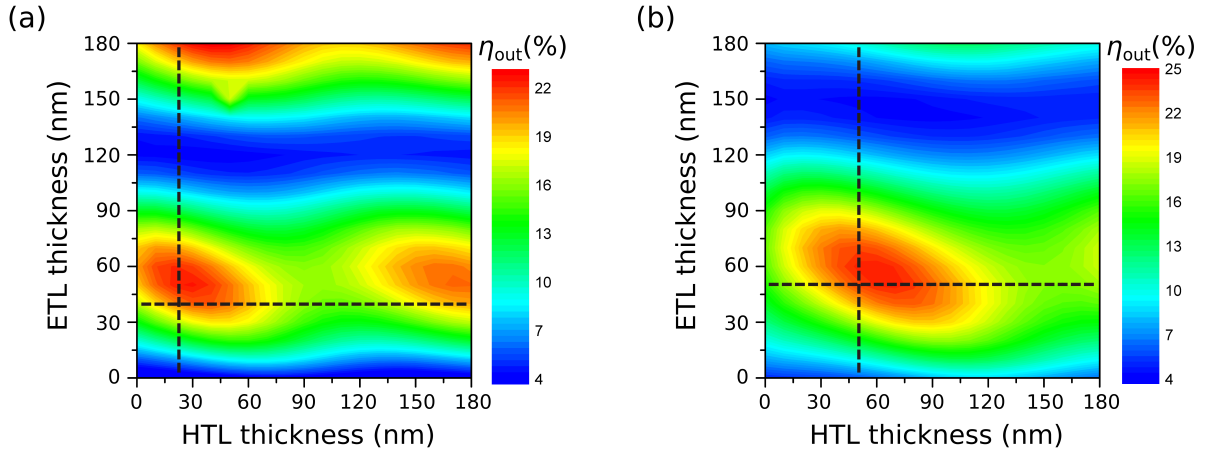
Figure 8.1.2: Light outcoupling efficiency dependence on thickness of electron and hole transport layers for (a) blue fluorescent device sB and (b) yellow phosphorescent OLED sY. Dotted lines represent the parameters used for the devices studied in this work.

optical simulation based on the transfer matrix algorithm [48]. The resulting light outcoupling efficiency η_{out} dependence on ETL and HBL thickness for devices sB and SY is depicted in Figure 8.1.2 (a) and (b), respectively. Dotted lines represent layer thicknesses chosen for the OLED architectures sB and sY used in this work, located in the vicinity of the peak value of η_{out}.

Figure 8.1.3 shows calculated electric field distribution (for s-polarised light) for (a) sB and (b) sY devices. The layer thicknesses were optimised for the first-order cavity with the electric field lying in the vicinity of the exciton recombination zone, where the light emission is expected to occur. Placing the emission zone near the field maximum ensures efficient coupling to the radiation modes [48]. The expected exciton recombination positions are shown as a dashed vertical lines. Bipolar matrix material MADN used in blue fluorescent device has electron and hole mobilities equal to $\mu_{\text{e,h}}^{\text{MADN}} = (2-3) \cdot 10^{-7}$ cm^2 V^{-1} s^{-1} [173]. Since the energy level alignment on the p-transport side contains lesser barrier compared to the n-transport side of the device sB, it is reasonable to expect the exciton recombination to occur at the EML/HBL interface. Device sY contains double EML layer, comprising matrix layers TCTA and TPBI. The former is used often as a hole transporting material [174], while the latter can be employed as a electron transporter, with a reported electron mobility of $\mu_{\text{e,h}}^{\text{TPBI}} = (6-18) \cdot 10^{-6}$ cm^2 V^{-1} s^{-1} [175]. Such bipolar system ensures the emission zone to be in the vicinity of the TCTA/TPBI interface, thus shifting it away from the EML/HBL junction, where emission quenching is known to occur.
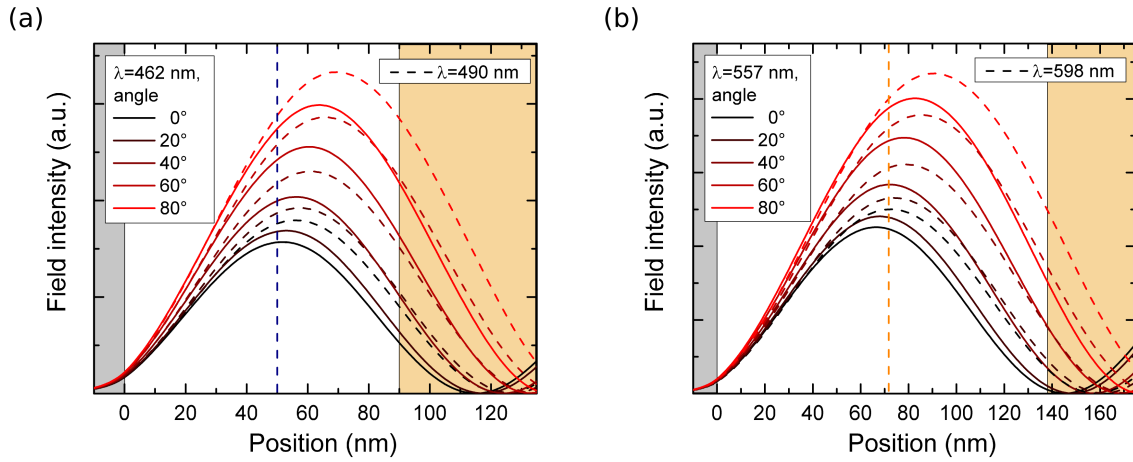
Figure 8.1.3: Electrical field distribution, angular and wavelength dispersion in (a) blue- and (b) yellow-emitting OLEDs studied in this work. Solid and dashed lines represent first and second EML emission peaks, respectively. The reference position is set at metal electrode (shaded grey area)/ETL interface. Shaded area on the right represents ITO anode. The vertical dashed line denotes the position of the exciton recombination/emission zone.

Optimal layer thickness selection is not a trivial task, especially if several emitters are used in the same OLED stack. Firstly, as discussed in the Chapter 1, due to the conformational disorder and several excited vibrational level deactivation, organic emitters are characterised by a broad luminescence spectrum, with FWHM> 100 nm, often with several emission maxima. The chemical structures of the emitter molecules and the resulting electroluminescence spectra of sB and sY devices are shown in Figure 8.1.4. The blue emitter has the emission peak at $\lambda = 462$ nm and a pronounced vibronic replica at $\lambda = 490$ nm. Similarly, the yellow emitter exhibits emission peaks at $\lambda = 557$ nm and $\lambda = 598$ nm. Moreover, as detailed in the previous chapter, apart from wavelength dependency, plane wave solutions of the Helmholtz equation exists for two separate polarisations, as well as exhibit strong angular dispersion. The electric field distribution for s-polarisation radiation at different emission angles is detailed in Figure 8.1.4. Having two separate subunits for each emitter simplifies the optical optimisation. Placing the EML position in the field maximum of the first emission peak at a normal angle resulted in high light outcoupling values η_{out} of $20-30$ % for both sB and sY devices, which are close to the theoretical limit for the OLED stack, when no additional light outcoupling structures are used.

Due to the optimised cavities for both yellow and blue devices, well coverage of the visible spectral region can be achieved. Figure 8.1.4, (a) compares the electroluminescence

(a)

(b)
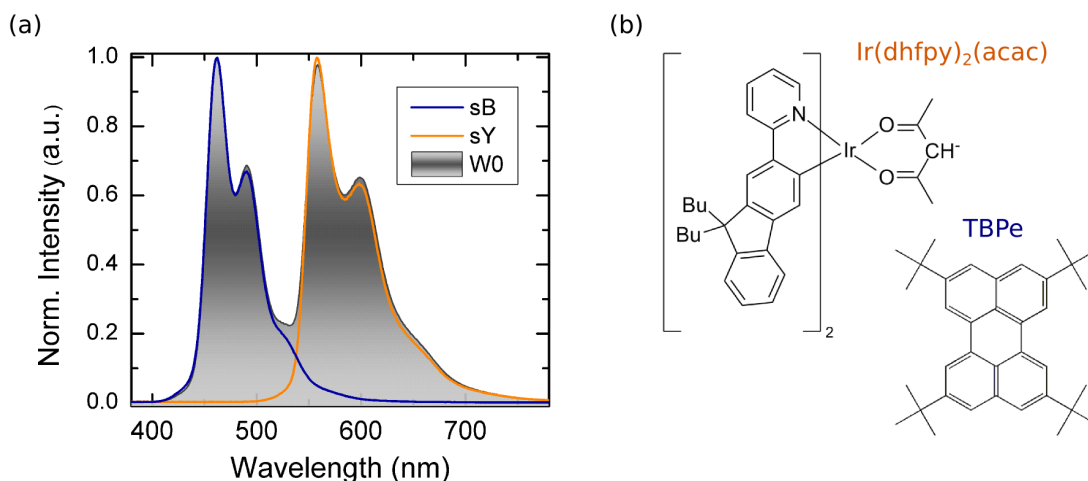
Figure 8.1.4: (a) Electroluminescence spectra of the monochrome devices sB (blue solid line) and sY (yellow solid line) and microstructured device W0 (shaded area) operating at current densities j_Y=26 mA/cm^2 and j_B=45 mA/cm^2, for yellow and blue units, respectively. The corresponding colour coordinates of white device is (0.33, 0.36) and CRI=68. (b) The chemical structures of the emitter molecules used in fluorescent blue (TBPe) and phosphorescent yellow (Ir(dhfpy)$_2$(acac)) OLEDs.

spectra from monochrome devices sB and sY, and two-colour OLED array (device W0). The emission spectra are nearly identical. Such well spectral coverage leads to high quality white light emission represented by high colour rendering index (CRI) values. Figure 8.1.4 shows normalised electroluminescence spectra of the monochrome devices sB and sY, as well as the resulting spectrum of micro-OLED array with 50 μm subunit stripes (device W0), when blue and yellow subunits are operated at current densities of j_B=45 mA/cm^2 and j_Y=26 mA/cm^2, respectively. This leads to the device W0 emission characterised by colour coordinates (0.33, 0.36) (near the equal-energy colour point E). The CRI of W0 at these colour coordinates is 68, which is among the best results reported for a two-colour system.

8.1.3 Choice of Hole Blocking and Electron Transport Layers

The p-i-n device concept ensures optimal electrical performance if the energy levels of transport materials are well matched, and allows the desired layer thicknesses according to the optical simulation. However, not all of the charge transport/blocking layers are compatible with the orthogonal photo-patterning processing steps. As discussed in a previous chapter, layers on the n-transport side in p-i-n OLEDs are the most susceptible

to degradation during the structuring of devices comprising multiple functional organic films. Thus, careful selection of hole blocking and electron transporting materials have to be performed to ensure high process yield and efficient OLED performance after the photo-structuring process. In the following, yellow-emitting OLED optimisation in terms of selecting materials with high morphological stability and low molecular affinity to hydrofluoroether solvents is presented. Finally, the optimisation of electrical performance of OLED comprising photo-patterning compatible organic films is discussed.

Solubility and Morphology Study

To ensure the compatibility between the multilayered p-i-n OLEDs and photolithographic processing, which is based on the development in hydrofluoroether (HFE) solvents, careful selection of the OLED device materials is required. First of all, due to the need for a good morphological film stability and low tendency of recrystallisation, materials exhibiting high glass transition temperatures (T_g) are preferred. For this reason, 4,7-diphenyl-1,10-phenanthroline (BPhen), which is known to have a low T_g value ($T_g = 62$ °C) [176], was omitted from the sY device.

Another important aspect is the material compatibility with the developers used in photopatterning process, which is ensured by the orthogonality between the organic layers and the HFE solvents. To determine the solubility limits relevant for the photopatterning application, drop casting of 6-9 µL droplets of a number of common organic solvents onto the surface of the evaporated organic film was performed. The solvent-film interaction was evaluated qualitatively, by observing whether film dewetting, inert (solvent spreading) or reactive (film swelling or dissolution) wetting of the surface occurs after the solvent deposition. Figure 8.1.5 shows the resulting HSP space for evaporated 70 nm-thick NET8 film. The corresponding HSP values determined for NET8 film were $\delta_D = 17 \pm 2$ MPa$^{0.5}$, $\delta_P = 7 \pm 2$ MPa$^{0.5}$ and $\delta_H = 11 \pm 3$ MPa$^{0.5}$. The vector distance to the HFE7100 solvent (marked with arrows in space, Figure 8.1.5) is then estimated to be $r_{\text{HFE7100}}^{\text{NET8}} = 133.9$ MPa$^{0.5}$. Corresponding values for the BAlq$_2$ film were estimated to be $\delta_D = 16 \pm 2$ MPa$^{0.5}$, $\delta_P = 6 \pm 2$ MPa$^{0.5}$, $\delta_H = 10 \pm 3$ MPa$^{0.5}$ and $r_{\text{HFE7100}}^{\text{BAlq2}} = 100.7$ MPa$^{0.5}$, thus showing a higher affinity to the HFE solvents, undesired in photopatterning application.

To evaluate and compare experimentally the morphological stability of the n-transport layers and their compatibility with the orthogonal photolithography process, the 70 nm thick films of BAlq$_2$, BPhen and NET8 were structured via lift-off in HFE7100 and investigated. Figure 8.1.6 shows the optical micrographs of the resulting structured organic films as well as corresponding cross-sections of patterned features. Both BAlq$_2$ and BPhen films (Figure 8.1.6 (a)-(c) and (d)-(f), respectively) exhibit strong morphological changes after
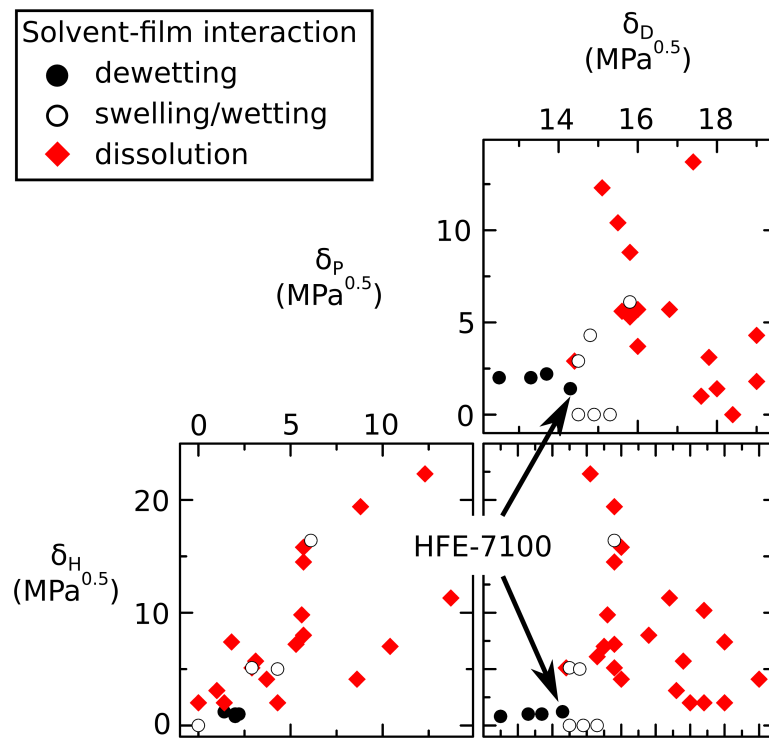
Figure 8.1.5: Hansen solubility parameter space for evaporated NET8 film, represented by a qualitative evaluation of the solvent-film interaction. Black solid circles represent film dewetting, open circles represent film swelling or solvent spreading and red diamonds represent film dissolution observed after the solvent deposition onto the film. Arrows indicate HFE7100 solvent used for photopatterning process.
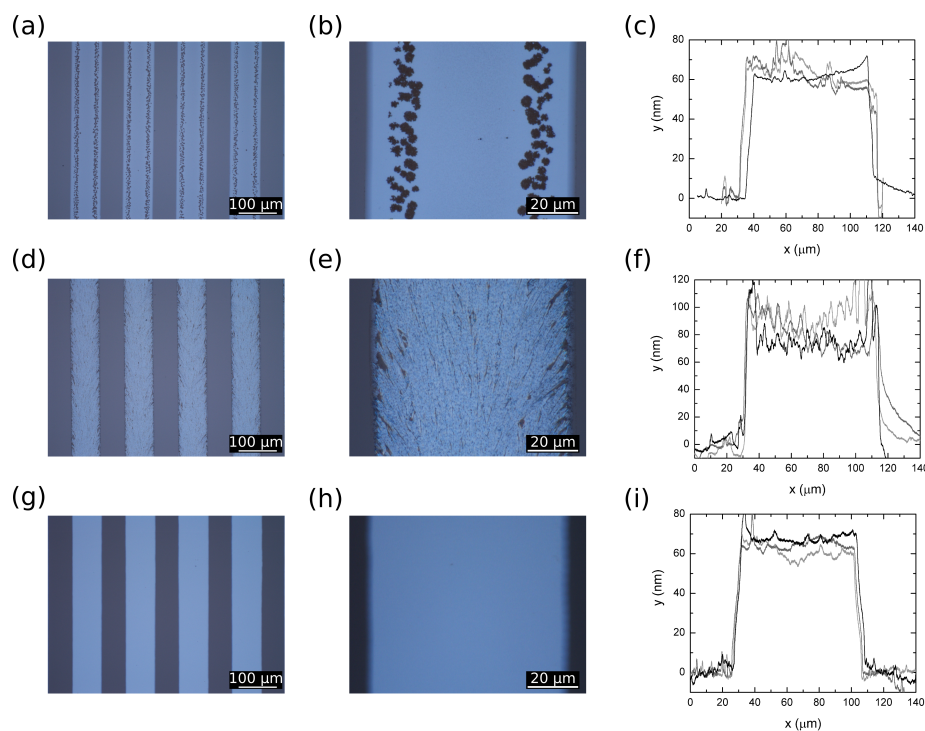
Figure 8.1.6: (a) Optical micrograph of the photo-structured BAlq$_2$ film, (b) closer view image of the patterned film and (c) corresponding film cross-section; (d)-(f) corresponding results for BPhen and (g)-(i) NET8 structured films.
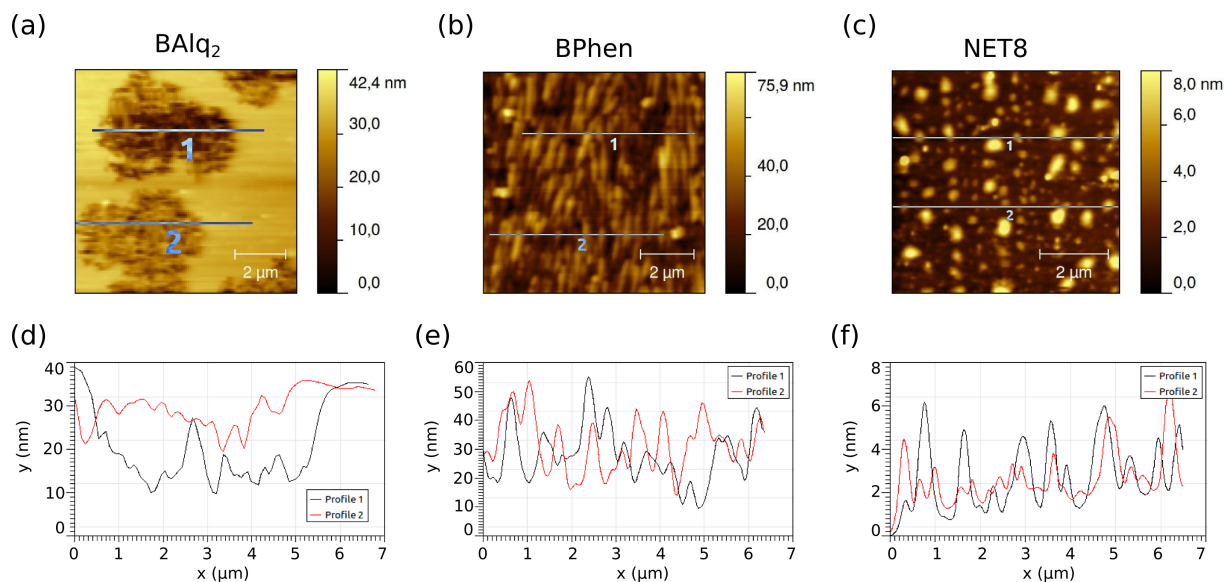
Figure 8.1.7: Morphology study of HBL/ETL films. (a)-(c), AFM pictures of finer details of layers of BAlq$_2$, BPhen and NET8, respectively; (e)-(g) corresponding film profiles.

patterning and exposure to air, represented by the inner microstructure visible in the optical micrographs as well as film inhomogeneities leading to high profile deviations. Atomic force microscopy (AFM) investigations of the finer structured film features are shown in Figure 8.1.7. On the other hand, NET8 exhibited relatively stable performance, resulting in a homogeneous structured layer. For the above mentioned reasons NET8 was chosen as a suitable replacement for both $BAlq_2$ and BPhen as a HBL and ETL layer, respectively.

Device Performance Using NET8

To evaluate the possibility of replacement of BPhen and $BAlq_2$ films with NET8, series of p-i-n containing yellow phosphorescent emitter and standard p-transport side, but comprising NET8 as both HBL and ETL were fabricated. To estimate NET8 performance as HBL, devices with $BAlq_2$ and NET8 were built and their electroluminescent operation compared. NET8 doped with Cs was used as an electron injection layer, instead of standard BPhen:Cs, due to morphological instability of the latter, detailed in the previous section.

Devices comprising $BAlq_2$/NET8:Cs and NET8/NET8:Cs combinations as HBL/ETL, show comparable leakage currents in a range of $1.5 - 2.5 \cdot 10^{-5}$ mA/cm^2 (Figure 8.1.8 (a)). The turn-on voltage (V_{on}) is slightly higher when using $BAlq_2$ as hole blocker ($V_{on} \approx 2.6$ V) as compared to $V_{on} \approx 2.5$ V using NET8. The turn-on voltages are higher than the so-called thermodynamic limit estimated from the optical band-gap of yellow emitter $Ir(dhfpy)_2(acac)$, which is around 2.22 V (estimated from the peak of the photoluminescence spectrum, Figure 8.1.8 (b)). Thus, both of the blockers can be associated with the electrical losses due to charge imbalance, with NET8 performing slightly better than $BAlq_2$. It can be caused by the different electron and hole mobilities in the corresponding transport layers, in addition to the energy barriers caused by the energy level mismatch. The charge imbalance is further exemplified by a lower voltage required to reach the same current density, e.g. for $j = 10$ mA/cm^2 device with NET8 requires 3.4 V, while the device with $BAlq_2$ needs 3.6 V to reach the same current running through the OLED. Such charge imbalance can be attributed to the energy barriers associated with $BAlq_2$/NET8 heterojunction as compared to HBL/ETL homojunction comprising pristine and doped NET8 layers, respectively.

(a)

(b)
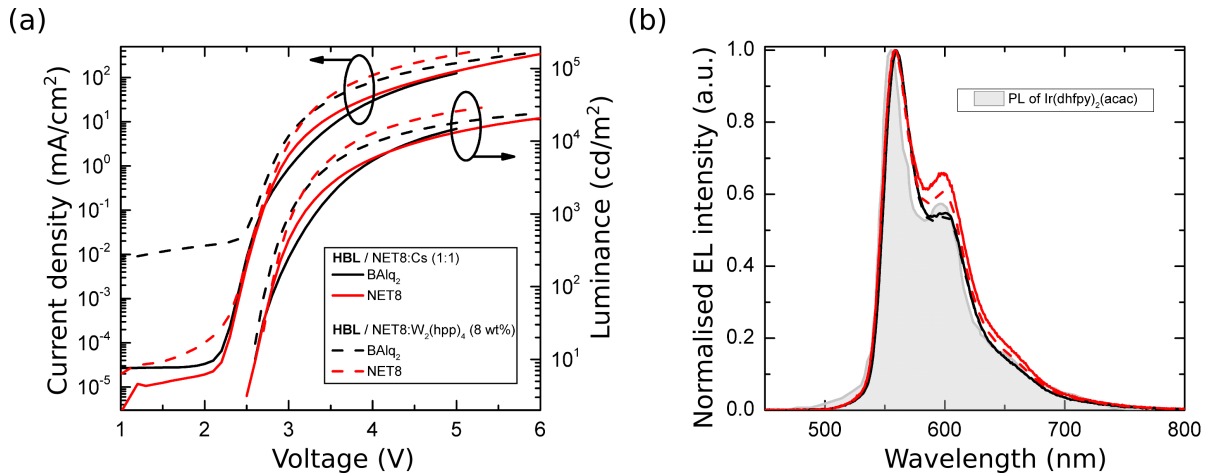
Figure 8.1.8: (a) Current density-voltage-luminance characteristics and (b) electroluminescence spectra of yellow OLEDs with varied hole blocking and electron transporting layers. Shaded grey area depicts photoluminescence spectrum of Ir(dhfpy)$_2$(acac) molecule for comparison.

Device with NET8 as a HBL reaches a luminance of $L = 1000$ cd/m^2 at $V \approx 3.15$ V and $j \approx 3.9$ mA/cm^2 as compared to $V \approx 3.35$ V and $j \approx 4.6$ mA/cm^2 for similar device containing BAlq$_2$. On the other hand, the external quantum efficiency value at $L = 1000$ cd/m^2 is comparable, and even slightly higher for BAlq$_2$ OLED: $\eta_{\mathrm{ext}} = 7.8$ % against 7.4 % for NET8 device (Figure 8.1.9, (b)). Higher or even comparable efficiency values contradicts lower charge balance factor when BAlq$_2$ is used as HBL, deduced above. Charge/exciton density dependant quenching of emitter molecules can explain the observed discrepancy. As will be discussed in Section 8.2.2, the triplet-triplet annihilation (TTA) model matches well the observed experimental data for the yellow phosphorescent OLED. TTA is an exciton density dependant mechanism leading to the decrease in the electrophosphorescence at elevated current densities [54]. Due to the higher charge injection in the emission layer TTA is more pronounced in the device with NET8 resulting in lower η_{ext} values even at moderate current densities. The efficiency roll-off at elevated currents is even more pronounced with critical current density of $j_0 = 52.4$ mA/cm^2 as compared to $j_0 = 69.4$ mA/cm^2 for BAlq$_2$ device. The performance of the device comprising BAlq$_2$/BPhen:Cs as HBL/ETL is also shown for comparison, as such device represents electrically optimised stack. Almost twofold improvement in the OLED performance could be achieved if BPhen:Cs is used as an ETL.

Electroluminescence of BAlq$_2$ OLED matches closely the photoluminescence spectrum of Ir(dhfpy)$_2$(acac) film shown in Figure 8.1.8 (b) as a reference. Slight red shift of ca. 3-4 nm of the EL spectrum as compared to PL emission can be explained by the OLED
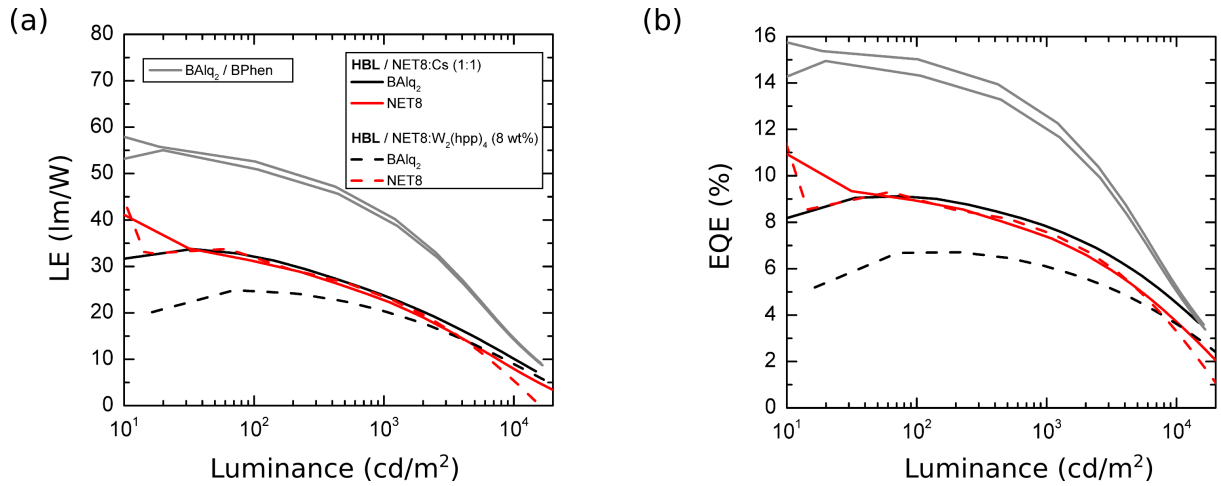
Figure 8.1.9: (a) Luminous efficacy and (b) external quantum efficiency dependence on luminance of devices with varied hole blocking and electron transport layers.

optical cavity effect. The differences (1-2 nm) between peak positions of EL spectra can be attributed to the errors in film thickness during device fabrication. The difference in intensity between first and second vibronic peaks (around $\lambda = 558$ nm and $\lambda = 600$ nm, respectively) in EL spectra of NET8 and BAlq$_2$ devices, can be due to the different refractive indexes of two HBLs, with BAlq$_2$ showing stronger absorption in the long-wavelength range.

Finally, OLEDs were aged at elevated currents in order to evaluate device lifetime at corresponding initial luminance. The data is shown Figure 8.1.10. Reducing the energy barriers associated with BAlq$_2$/NET8 interface by using NET8 as both HBL and ETL, allows to increase the device lifetime by one order of magnitude.

To directly dope OLED electron transport materials, dopants with high lying HOMO are required. Cesium, an alkali metal, is often used as an electron dopant of organic semiconductors, due to its low ionisation potential ($I_P = 3.89$ eV [44]), which leads to an efficient n-type doping resulting in highly efficient OLED operation. However, there are number of problems associated with the usage of Cs during the organic electronic device fabrication. It is not detectable using quartz crystal microbalance (QCM) - a standard equipment to measure amount of evaporated material - since Cs vapour do not stick to the QCM surface. Additionally, alkali metals, especially Li, due to their minute dimensions, have been reported to diffuse during OLED operation into adjacent organic films leading to detrimental effect on device lifetime [177, 178]. While Cs has a larger atomic dimension compared to Li, its diffusion at elevated temperatures, needed for Cs evaporation or reached

140
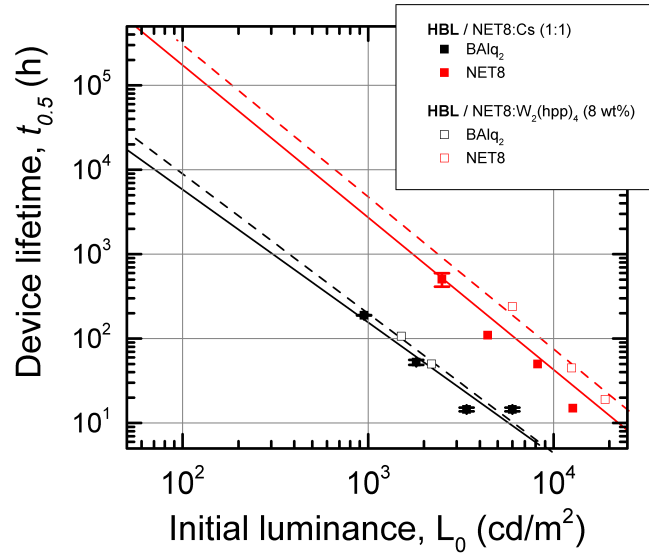
Figure 8.1.10: Device lifetime $t_{0.5}$ versus initial luminance L_0. Comparison between OLEDs comprising different HBL/ETL combinations. Solid and open squares represent the experimental results, solid and dashed lines are the power law fits.

during the device operation, might still be expected.

On the other hand, doping with controlled dopant concentration can be achieved using molecular dopants. Their larger dimension compared to atomic dopants, such as Li or Cs, ensures better device stability as the effect of dopant diffusion is minimized. The dimetal molecular complexes of chromium or tungsten with the anion of 1,3,4,6,7,8-hexahydro-2H-pyrimido[1,2-a]pyrimidine (hpp), forming $Cr_2(hpp)_4$ and $W_2(hpp)_4$ were shown to effectively dope organic films, such as C_{60}, with conductivities reaching well above 1 S/cm [44, 179]. $W_2(hpp)_4$ is reported to have the lowest ionisation potential of any chemical compound, with $I_P = 2.68 \pm 0.13$ eV [180, 181]. For these reasons, $W_2(hpp)_4$ was chosen as an alternative dopant to Cs, when using NET8 for electron injection/transport in photolithography-compatible OLEDs. The current-voltage-luminance curves and corresponding electroluminescence spectra of yellow phosphorescent devices containing $BAlq_2$ and NET8 as hole blockers with NET8 doped with Cs or $W_2(hpp)_4$ as an electron injection/transport layer are shown in Figure 8.1.8. Corresponding luminous efficacy and external quantum efficiency dependence on luminance is depicted in Figure 8.1.9.

For the devices comprising NET8 doped with 8 wt% $W_2(hpp)_4$, but containing different hole blocker materials, trends similar to the discussion above were observed. That is, usage of NET8 as HBL leads to a better charge balance within the device, as well as higher TTA

141

Table 8.1.1: Performance comparison of yellow phosphorescent OLEDs comprising different HBL/ETL combinations. $t_{0.5}$, LE and EQE are compared at L=1000 cd/m^2.

HBL	ETL	V_{on} [V]	$\lambda_1^{max}/\lambda_2^{max}$ [nm]	$t_{0.5}$ [h]	LE [lm/W]	EQE [%]
BAlq$_2$	NET8:Cs	2.6	559/600	150	23	7.7
BAlq$_2$	NET8:W$_2$(hpp)$_4$	2.6	559/602	200	19	6.1
NET8	NET8:Cs	2.55	558/597	2600	23	7.4
NET8	NET8:W$_2$(hpp)$_4$	2.6	557/598	4500	23	7.5

based efficiency roll-off, leading to the slightly lower efficiency values and quenching of the high energy band of EL emission. In general, higher currents were reached using molecular doping based on W$_2$(hpp)$_4$, as compared to NET doping with Cs. For the BAl$_2$ device, this resulted in even higher charge imbalance, which lead to a drastic increase (up to 3 orders of magnitude) in leakage currents and a pronounced decrease in luminous efficacy and external quantum efficiency. On the other hand, NET8 based OLED showed comparable leakage currents and efficiency performance to device with Cs doping, demonstrating that the charge balance factor within such architecture is close to unity and hence is almost independent on the charge density within the OLED. The performance of the yellow phosphorescent devices comprising different HBL/ETL combinations is summarised in Table 8.1.1.

Despite offering slight improvement in the electron injection using NET8 doped with W$_2$(hpp)$_4$, NET8:Cs was chosen for further work, due to the simplicity and low-cost of Cs doping. Additionally, n-type doping using molecular dopants has a general drawback of increasing instability of the dopants with respect to oxygen for higher HOMO values, requiring a continuous handling of the materials under inert conditions [44]. Due to the need of material stability with respect to external factors during photo-patterning procedure, Cs doping is also preferred over doping with W$_2$(hpp)$_4$, as the device performance is kept almost identical.

8.2 Performance of Microstructured Devices

The corresponding emission of the photo-patterned two-unit OLED can be tuned over a wide range from yellow to white to blue colours. The independent control of the different units allows the desired overall spectrum to be set at any given brightness level. Operated as a white light source, the microstructured OLED reaches a luminous efficacy of 13 lm/W and external quantum efficiency of 5.5% at 1000 cd/m^2 without an additional light outcoupling enhancement and exhibits a colour rendering index of 68 when operated near the colour point E. The following is a detailed discussion regarding the operation of the microstructured devices.

8.2.1 Colour Temperature Tuning

Each of the laterally aligned OLED subunits can be independently operated, resulting in the adjustable emission colour of the structured device. Figure 8.2.1 depicts corresponding changes in the micro-OLED array emission, when the subunits are operated at different driving conditions. Demonstrated in Figure 8.2.1, (a), the spectral intensity control of one of the subunits is possible while maintaining constant emission of the other unit. This allows emission control over all available colour points in CIE coordinate space lying on the straight line between the yellow emitter (CIE colour coordinates (0.5, 0.5)) and that of the blue emitter (CIE (0.14, 0.18)). Thus, white light from the micro-OLED array can be tuned from warm colour near colour point A (0.45, 0.41) to equal energy emission point E (0.33, 0.33) corresponding to cold white light while maintaining a constant luminance value (Figure 8.2.1, (b)).

The device luminance levels of the microstructured OLED array can also be adjusted over a wide range, of more than 3 orders of magnitude, from ca. 100 cd/m^2 up to over 10000 cd/m^2. The corresponding current combinations running through different subunit arrays j_Y and j_B and the resulting OLED brightness are shown in Figure 8.2.2, (a). The brightness of the device can be adjusted continuously in a easy-to-predict fashion once the current density is > 3 mA/cm^2 for each of the subunits. Perturbations in luminance observed when $j_{Y,B} < 3$ mA/cm^2 can be attributed to the measurement errors due to lower light intensity as well as device instabilities close to the diode turn-on condition.
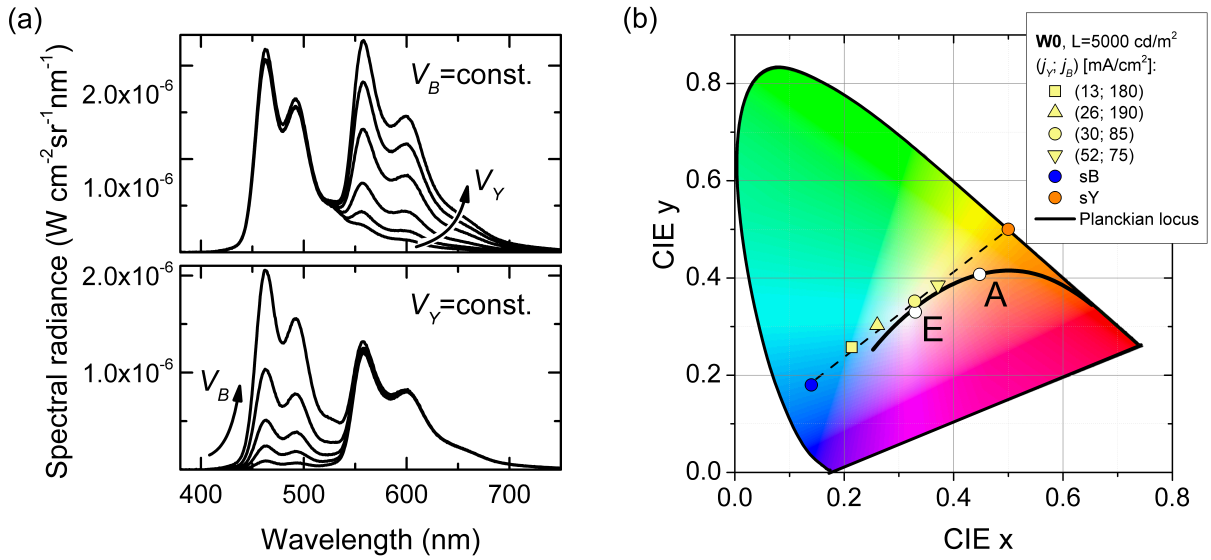
Figure 8.2.1: (a) Electroluminescence spectra at different operating conditions of the separately operated subunits: the blue unit is kept at a constant voltage while the voltage of the yellow unit is varied (top), and the yellow unit is kept at a constant voltage as different operating voltages are applied to the blue unit (bottom); (b) colour coordinates corresponding to the different driving conditions of the subunits at a constant luminance of 5000 cd/m^2. Colour points E and A are also depicted for comparison.

The corresponding colour coordinates, when one of the subunits is kept at constant driving conditions, while the current running through the other is ramped up, is shown in Figure 8.2.2 (b) and (c), for the j_Y =const. and varied j_B, and j_B =const. and varied j_Y, respectively. Fine tuning of the colour coordinates of the microstructured OLED array can be achieved, with the colour change step of $\Delta < 0.01$ for both CIE x and CIE y values. Such fine colour tuning available at any desired luminance value is hardly possible with OLED containing multiple emission layers within the stack to achieve white light emission.
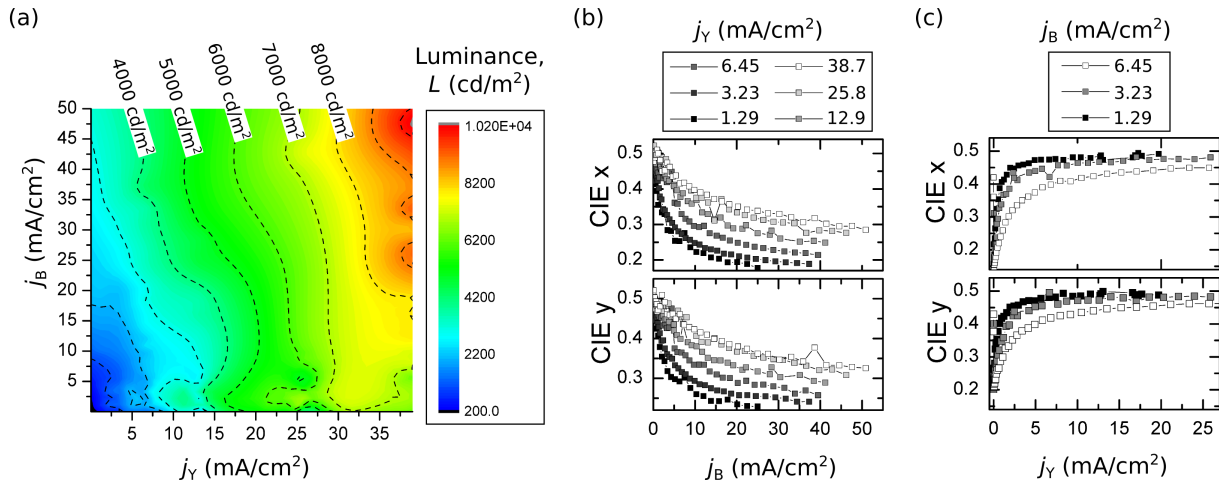
Figure 8.2.2: Emission colour tuning at different device brightness levels. (a) Luminance dependence on current density running through each of the subunits. Dashed lines represent constant luminance condition; emission colour coordinates corresponding to different device driving operation: (b) j_B is varied at different j_Y =const. values and (c) j_B =const. and j_Y is varied.

8.2.2 Compatibility with Photo-patterning

The current-voltage-luminance profile, external quantum efficiency and luminous efficacy of the OLED in device W0 when emitting light at colour point (0.40, 0.41) are depicted in Figure 8.2.3. For comparison, the characteristics of single-colour devices (sB and sY) are shown. Device W0 with laterally aligned 50 μm subunits exhibits intermediate performance between the equivalent of yellow unit sY comprising a phosphorescent emitter and a fluorescent blue device, sB. The white OLED (W0) reaches an EQE of 5.5 % and a LE of 13 lm/W at an illumination-relevant luminance of 1000 cd/m^2 (cf. Figure 8.2.3, (b)), compared with 8 % (22 lm/W) and 3 % (4 lm/W) for monochrome devices sY and sB, respectively. A detailed analysis of the efficiency roll-off characteristics shows that the EQE data of the microstructured device (Figure 8.2.3, (b), solid black line) can be well matched by the sum of the EQE values of large-area blue and yellow devices (devices sB and sY, respectively), weighted by the corresponding area of the device. The efficiency roll-off characteristics of devices sB and sY are modeled using singlet EPQ and TTA mechanisms [182, 54], respectively (Figure 8.2.3, (b), red solid line). The good match between the experiment and the model leads us to conclude that the photolithographic process applied to achieve a structured array does not introduce significant losses in the device performance normally observed after photo-patterning of organic semiconductor devices. Thus, this

result demonstrates good compatibility between the photo-patterning process comprising lift-off in hydrofluoroethers and the OLED stack used in this work and is consistent with the best results of photo-patterning of p-i-n OLEDs demonstrated in previous chapter. A further increase in both EQE and LE is expected if common light extraction techniques are applied to the microstructured device, which conventionally boosts the performance by a factor of up to 2-3 [77, 78, 76]. In the following, a detailed discussion regarding the external quantum efficiency description of microstrutured OLED array is presented.

Due to the long-lived triplet state, high exciton densities can be reached in phosphorescent OLEDs operated at elevated current densities. Under such conditions triplet-triplet annihilation (TTA) is expected to play the major role in determining external quantum efficiency η_{ext} dependence on the current density j [54]. Assuming that TTA is the only process responsible for the efficiency roll-off, the following equation holds

$$\frac{\eta_{\text{ext}}^{\text{Ph}}(j)}{\eta_0^{\text{Ph}}} = \frac{j_0^{\text{Ph}}}{4j}\left(\sqrt{1 + 8\frac{j}{j_0^{\text{Ph}}}} - 1\right), \tag{8.2.1}$$

where j_0^{Ph} is the critical current density at which external quantum efficiency drops to half of its initial value η_0^{Ph}. While other competing mechanisms, such as triplet-polaron annihilation, Joule heating and charge imbalance within the device, might play a role in determining roll-off characteristics of the phosphorescent OLED [79, ?], the simplified model was in a good agreement with the measured data of phosphorescent yellow device sY. The best fit is found with $\eta_0^{\text{Ph}} = 8.86$ % and $j_0^{\text{Ph}} = 56.42$ mA/cm^2.

Since the radiative decay rate of the singlet emitter is ca. 3 orders of magnitude higher than that of the triplets, exciton annihilation in fluorescent devices is less pronounced at high current densities compared to the phosphorescent OLED. Efficiency roll-off characteristics of fluorescent devices has been shown to be successfully fitted assuming singlet exciton-polaron quenching (EPQ) mechanism [182, 183, 184, 185]. As a first approximation, j-V characteristics are described by the trap charge limited current $j \propto V^{l+1}$ [186, 187, 188]. Then, efficiency dependence on the current density can be described as

$$\frac{\eta_{\text{ext}}^{\text{Fl}}(j)}{\eta_0^{\text{Fl}}} = \frac{1}{1 + \left(\frac{j}{j_0^{\text{Fl}}}\right)^{\frac{1}{l+1}}}. \tag{8.2.2}$$

The best fit for the sB device was achieved with the critical current density $j_0^{\text{Fl}} = 429.84$ mA/cm^2 and corresponding parameters $\eta_0^{\text{Fl}} = 3.21$ %, $l = 1.25$.

For the microstructured two-colour OLED array, assuming identical roll-off behaviour for each of the yellow and blue subunit stripes, $\eta_{\text{ext,m}}^{\text{Ph}}(j)$ and $\eta_{\text{ext,n}}^{\text{Fl}}(j)$, respectively, as for their
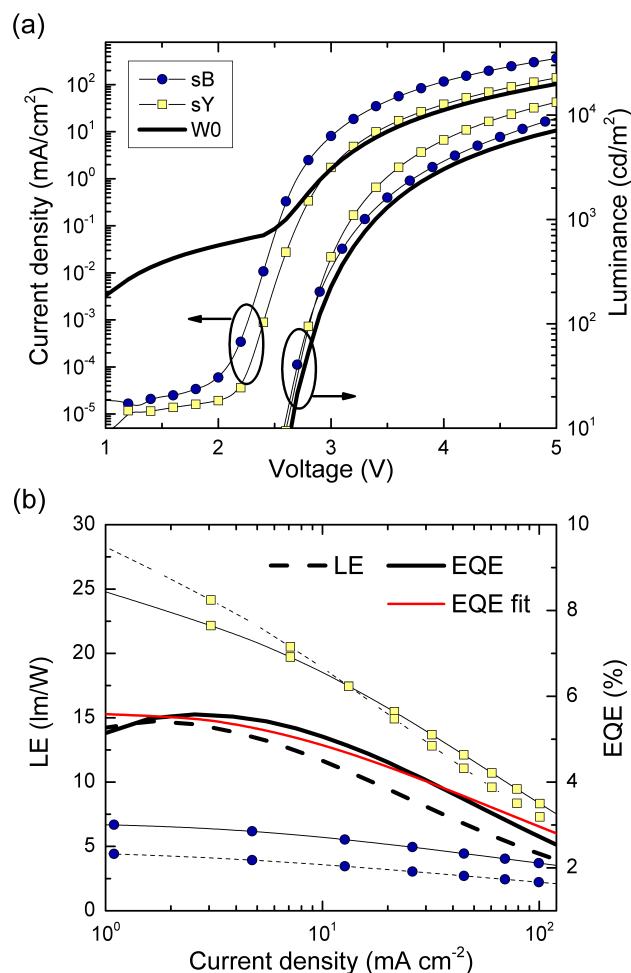
Figure 8.2.3: (a) Current density-voltage-luminance characteristics and (b) external quantum efficiency (solid lines) and luminous efficacy (dashed lines) of reference blue (blue circles, device sB), yellow (yellow squares, sY) and photo-patterned white OLED (solid black line, W0). The red solid line is the efficiency fit for device W0, considering the TTA and EPQ mechanisms for the yellow and blue subunits, respectively.
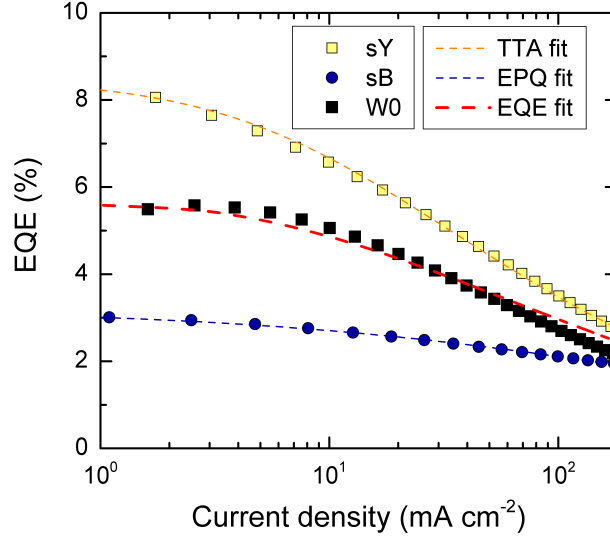
Figure 8.2.4: External quantum efficiency dependence on current density for large area yellow (sY), blue (sB) and microstructured (W0) devices. Scattered data points represent measured data, dashed lines represent data fit with respective efficiency roll-off models (see text for details).

large area counterparts sY and sB, described by equations 8.2.1 and 8.2.2, respectively, one can write for the device W0

$$\eta_{\text{ext}} = \frac{1}{N} \sum_{m,n=1}^{N/2} \left(\eta_{\text{ext,m}}^{\text{Ph}}(j) + \eta_{\text{ext,n}}^{\text{Fl}}(j) \right) = \frac{\eta_{\text{ext}}^{\text{Ph}}(j) + \eta_{\text{ext}}^{\text{Fl}}(j)}{2}, \tag{8.2.3}$$

where N is the total number of subunit stripes.

The measured data of sY, sB and W0 devices, together with the corresponding fits are shown in Figure 8.2.4. While a good match of the experimental data and the model fit was found at the low current regime $j < 2$ mA/cm², the roll-off characteristics are not represented well at elevated currents. The more detailed discussion regarding the roll-off character of microstructured device is reserved for Chapter 8.

An increase of up to 3 orders of magnitude in the leakage currents can be observed in the OLED array when subunits are served by a common voltage source (Figure 8.2.3, (a)). However, when the subunits are separately measured, leakage is comparable to that of devices sB and sY (Figure 8.2.5). This can be explained assuming the crosstalk between subunits, which can occur owing to the relatively high lateral conductivity of doped organic films. Additional patterning of the anode electrode and subsequent photolithographic alignment of the subunits are expected to eliminate this effect at a cost of decreasing the
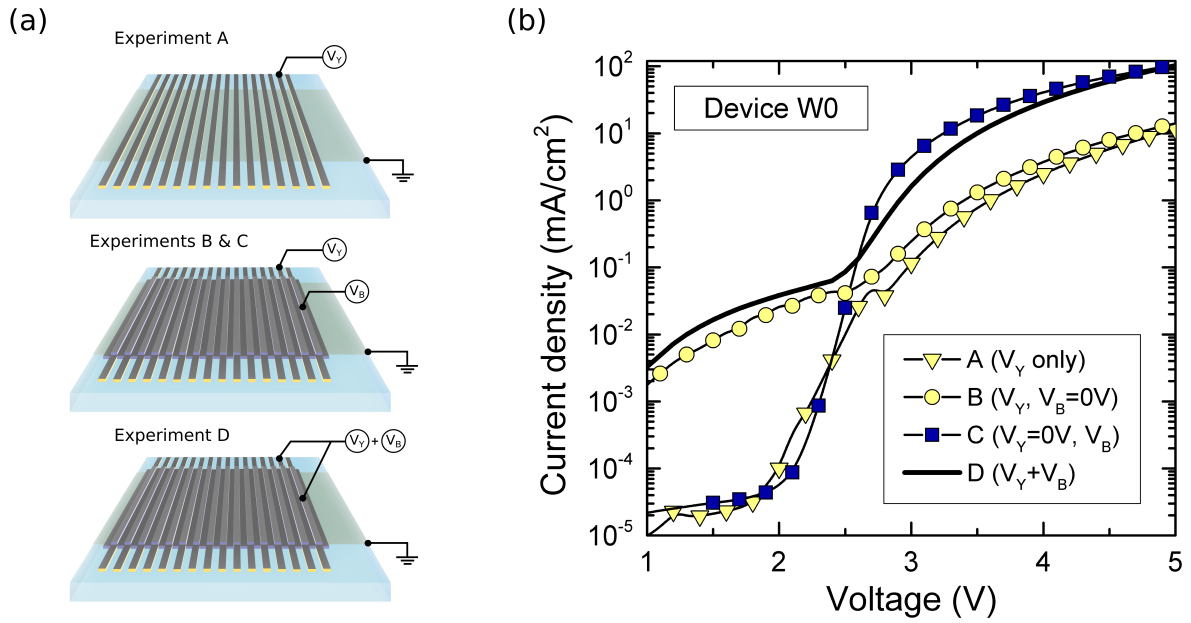
Figure 8.2.5: (a) Different measurement setups for measuring subunit cross-talk; (b) corresponding current density-voltage characteristics of microstructured device W0.

coverage of the active device area.

To elucidate the origin of elevated leakage in the device, the following experiments were performed. The current density-voltage characteristics of patterned yellow subunit stripes with a width $W_Y = 50$ μm without and with a subsequent deposition of the blue subunit were measured (Figure 8.2.5 (a), experiments A and B, respectively). Figure 8.2.5 (b) shows that high leakage currents are observed in B measurement configuration only, which leads us to conclude that the lateral conductivity of the yellow subunit is the main reason for the leakage. On the other hand, when only blue subunit is operated (Figure 8.2.5 (c), experiment C), leakage level is comparable to the large area reference device sB. Current-voltage characteristics when both subunits are operated simultaneously are also shown for comparison (Experiment D).

The higher lateral conductivity of the yellow subunit can be attributed to the charge imbalance within the device. Possible explanation is the following. External quantum efficiency of the OLED can be described as

$$\eta_{\text{ext}}^{\text{Ph}} = \gamma \cdot r_{\text{S/T}} \cdot \Phi_{\text{PL}}^* \cdot \eta_{\text{out}}, \tag{8.2.4}$$

where γ is the charge balance factor, $r_{\text{S/T}}$ is the singlet-triplet ratio, Φ_{PL}^* is the effective

149

photoluminescence efficiency of the emitter molecule, which takes into account change in the radiative rate due to the microcavity environment (Purcell effect) and η_{out} is the light outcoupling efficiency, which is around 20-30 % if no additional light extraction structures are used (Figure 8.1.2). The yellow monochrome device reaches maximum $\eta_{\mathrm{ext}}^{\mathrm{Ph}} = 8\%$ which is below its optimal value of 15-16 % (see Figure 8.1.9 (b)). Parameters $r_{\mathrm{S/T}}$, Φ_{PL}^{*} and η_{out} are expected to be nearly identical between stacks differing in HBL/ETL layers only. This leads to the conclusion that low value of γ and therefore pronounced charge imbalance within the device is the main reason behind lower observed efficiency values of the sY. On the other hand the fluorescent blue OLED operates close to its optimal electrical performance, which makes it less prone to the charge accumulation and subsequent lateral conductivity.

8.2.3 Colour Stability

Stability of the emission colour of white OLEDs is another challenge which needs to be overcome in order for OLED technology to compete in lighting industry. Colour coordinate change at different brightness levels or different viewing angles is usually undesired in real-life applications. As described in Chapter 3, white OLEDs comprising multiple EMLs show characteristic voltage dependent emission, which is hard to control since only single set of electrodes is used. On the other hand, vertically stacked monochrome OLEDs which can be addressed separately exhibit stable white light emission at wide range of brightness levels. However, need of interstack metal electrodes leads to the difficult optical optimisation of the device. In addition, high reflectivity of the electrodes results in a pronounced optical cavity effects which leads to the strong angular dependence of the emission. Lateral alignment of the monochrome OLEDs can in principle offer both, stable emission operation at varying brightness levels as well as unpronounced angular colour characteristics. In the following, the stability white emission from the two colour photo-structured micro-OLED array is discussed, in terms of EL spectral change at different driving conditions and different viewing angles.

Colour Change at Elevated Brightness

The colour coordinates at different device brightness levels of the laterally structured white OLED is depicted in Figure 8.2.6. The device exhibits very good colour stability when operated at elevated driving conditions. This quality is of key importance because lighting applications require the tolerance of the CIE colour coordinate change to be $\Delta < 0.01$ for varying brightness levels of differing orders of magnitude [189]. Depicted in Figure 8.2.6 (a),

the microstructured device shows tolerable colour stability up to 5000 cd/m^2, consistent with the brightness requirements for solid-state lighting applications [190].

A further increase in the current density running through the subunits results in an additional EL band observed at around 430 nm which leads to the change in CIE coordinates (Figure 8.2.6 (b)). One possible explanation is that elevated currents in the device can lead to a charge accumulation and the resulting broadening of the exciton recombination zone. This, in turn, results in an additional emission from one of the charge blocking material leading to a colour shift. The EL spectrum at elevated currents of the blue emitting sB device, depicted in Figure 8.2.7 (a), also show similar additional high energy emission band. On the other hand, yellow-emitting device sY, shown constant EL emission over the measured brightness levels. This is in line with the attribution of the additional band to BAlq$_2$ emission (also shown in Figure 8.2.7 (a)), since BAlq$_2$ is present in sB OLED and absent in sY device. However, emission of BAlq$_2$ extends over a broad wavelength range, covering the emission of the blue emitter TBPe and peaking at $\lambda_{\text{BAlq}_2} \approx 493$ nm. Therefore, one would expect to see differences in sB emission also in the low energy band and not only in the high energy side, since the BAlq$_2$ emission is not too far away from the optical cavity mode in sB device (see Figure 8.1.3 (a)).

Alternative explanation could be the emission from the MADN matrix layer. As seen from the emission spectrum of MADN (Figure 8.2.7 (a)), it has a peak around 430 nm, and its broad emission spectrum is less pronounced at the lower photon energies. In the sB device, due to the optical cavity being optimised for $\lambda \approx 460$ nm emission, the low energy emission of MADN should play even lesser role, allowing to explain the observed additional EL band in high energy tail only.

While it is hard to pin-point the actual mechanism behind additional high energy tail at elevated currents, it is clear that it is a charge carrier density dependant effect occurring in the blue OLED stack. It is interesting to note, that the additional EL band does not depend on size of the device, as identical relative EL emission intensity was recorded from both sB and W0 devices, shown in Figure 8.2.7 (b).

Angular Colour Change

The microstructured device also exhibits good angular colour stability. The angular distribution of the emission intensity of device W0 is depicted in Figure 8.2.8 (a). The colour coordinates of both, monochrome OLEDs sB and sY, and microstructured device W0, operated at 15 mA/cm^2 is shown in Figure 8.2.8 (b). The angular emission profile of W0 follows a Lambertian emission pattern (Figure 8.2.8 (a)), and the colour change of the device with changing emission angle can be attributed to the corresponding change in
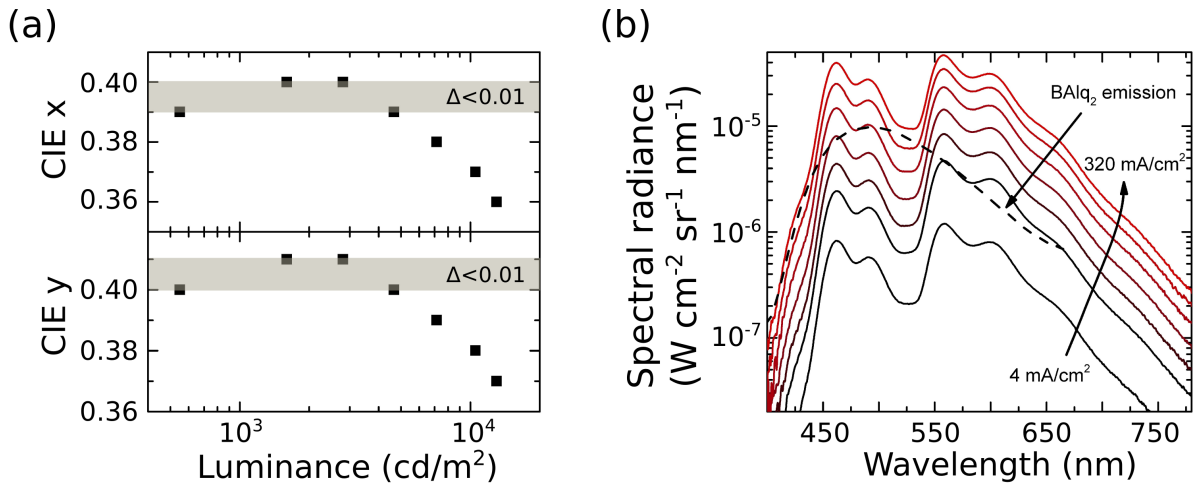
Figure 8.2.6: (a) CIE colour coordinates at different luminance values for white OLED device W0; the shaded area depicts common colour stability requirements (see text for details); (b) corresponding electroluminescence spectra dependence on current density; the photoluminescence emission of BAlq2 is depicted for comparison.
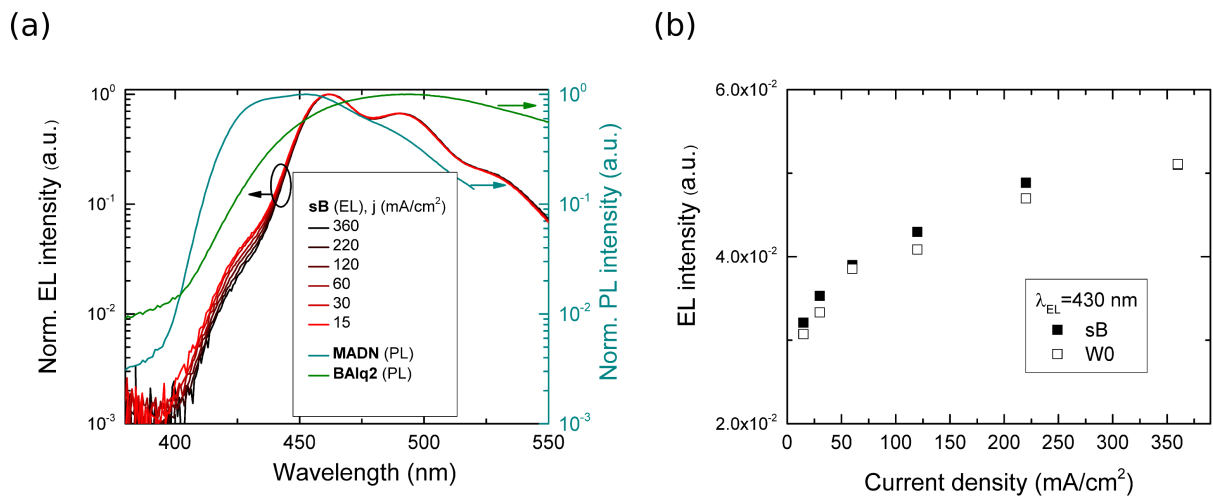
Figure 8.2.7: (a) Normalised EL spectra of large area blue OLED (sB) recorded at different current density values. PL spectra of matrix molecule MADN and hole blocking molecule BAlq2 are depicted for comparison; (b) relative EL intensity dependence on current density for the $\lambda = 430$ nm emission of sB (solid black squares) and W0 (open black squares) devices.
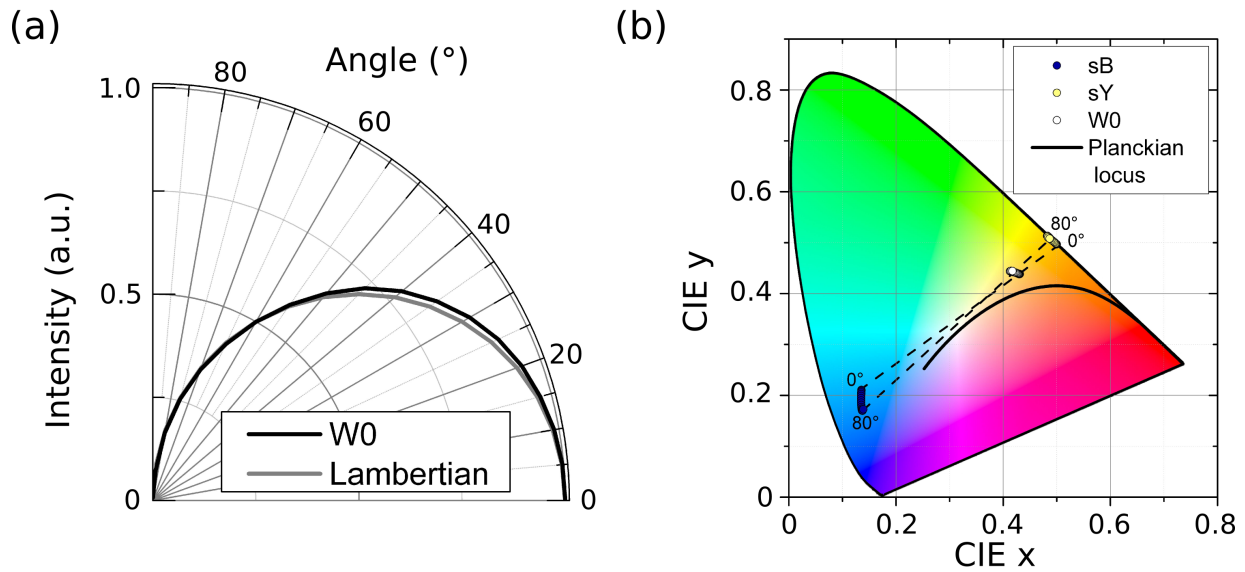
Figure 8.2.8: (a) Angular emission dependence of W0 measured at 15 mA/cm^2; the Lambertian emission profile is depicted for comparison; (b) corresponding CIE colour coordinate change versus viewing angle of microstructured device W0 and monochrome devices sB and sY.

the emission of the monochrome blue and yellow devices (Figure 8.2.8 (b)), as one would expect from a combination of two separately addressed monochrome devices.

Figure 8.2.9 depicts the angular dependence of the EL spectra of devices sB, sY and W0, corresponding to the colour coordinates depicted in Figure 8.2.8 (b). The shape of the emission spectrum at each different viewing angle from the microstructured OLED array is identical to the combination of EL spectra of sB and sY devices. The intensity of the emission is similar at small angles, however, discrepancies occur between large area device and microstructured OLED at high viewing angles, especially when comparing yellow emission band of W0 and sY. While the discrepancies for the blue emission is not as pronounced is could be attributed to the measurement errors, which are highest at high angles, since the recorded signal is low. However, there are clear differences observed already at relatively small viewing angles ($\approx 20°$) for the yellow emission band, suggesting that additional effects, corresponding to the micro-scale size of the subunits of W0 device, might play a role. Among the other effects, reduced Joule heating or reabsorption of the lateral emission of blue subunit by the yellow subunit might lead to the increased emission of the microstructured device. The next chapter is dedicated to elucidate the differences between the performace of the large area devices and microscale OLEDs.
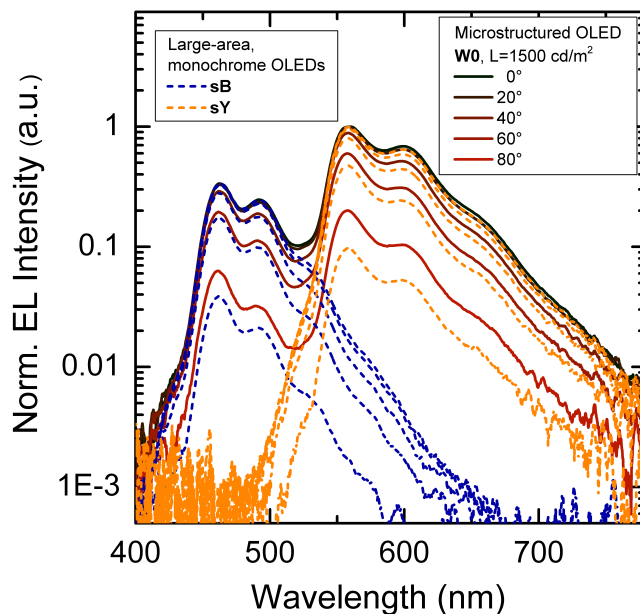
Figure 8.2.9: Angular dependence of EL spectra of large area monochrome devices sB
(dashed blue lines) and sY (dashed yellow line), and microstructured
OLED array W0 (solid lines) emitting close to the colour point A at
normal incidence.

8.3 Summary

An efficient, colour-tunable OLED device concept based on a lateral alignment of fluo-
rescent blue and phosphorescent yellow microstructured OLEDs. Lateral alignment of
OLEDs enabled electrical and optical optimisation of each individual device. Addition-
ally, the organic layer sequence was chosen to minimise the impact of photolithographic
structuring, by selecting layers with high glass transition and low molecular affinity to
HFE solvents. The latter was empirically estimated using Hansen solubility parameter
approach. The resulting photo-patterned OLED array enabled colour tuning over a wide
range, from blue to yellow, including warm white and cold white-light emission without
unwanted change in the brightness level of the device. The microstructured OLED array
reached EQE and luminous efficiency values of 5.5 % and 13 lm/W, respectively, at lumi-
nance of 1000 cd/m^2. At colour coordinates (0.33, 0.36), the device shows a CRI of 68,
which is among the highest values to date reported for two-emitter systems. Finally, the
next chapter will present further investigation on micro-OLED array, with a focus on the
impact of the spatial subunit dimensions on the device emission colour and performance.

9 Efficiency Roll-off and Emission Colour of Microstructured OLEDs

After the successful demonstration of white OLED comprising side-by-side structured fluo-rescent blue and phosphorescent yellow subunits, further investigation focus on the impact of the dimension of each of the subunits to the device performance. This chapter discusses the observed changes in OLED emission colour, lifetime and efficiency after the variation of the size of each of the subunits. Section 9.1 gives an overview of the performance of fabricated microstructured OLEDs with varied dimension. It is followed by the discussion of the differences in emission spectra (Section 9.2) and efficiency roll-off (Section 9.3) of the devices with varied subunit dimension. The results are rationalised by considering the effect of elevated temperatures in investigated OLEDs (Section 9.4) and an analytical model is developed to evaluate the Joule heat mediated exciton quenching (Section 9.5).

9.1 Photolithographic Control of the Subunit Dimension

Photolithographic processing applied to achieve structured OLED arrays offers an easy control of the dimension of each of the subunit stripe. To demonstrate the lithographic dimension control and to investigate its effect on microstructured device performance, a series of devices with a variable size of blue and yellow subunits were fabricated. Table 9.1.1 presents the data on subunit size combinations used in the experiment and summarizes the performance of the microstructured white-emitting OLED devices at a current density of 15 mA/cm^2. Changing the dimension of the subunit stripes lead to the change in device lifetime, emission colour and efficiency. For example, the colour of the devices W0 and W2 is kept almost identical with CIE coordinates of (0.40, 0.41) for W0 and (0.39, 0.40) for W1. However, increasing the subunit pitch leads to the 3.5 times longer W1 lifetime. By varying the size ratio of the blue and yellow subunits from 1:1 (devices W0 and W1) to 1:4 (W2) and 1:3 (W3), the emission colour of the device can be tuned. In the following,

the differences between emission colour and the roll-off characteristics of microstructured devices of varying dimensions will be addressed.

Table 9.1.1: Performance comparison of photo-structured white OLED devices with varied subunit sizes at a current density of $j = 15$ mA/cm^2. The yellow and blue subunits are operated simultaneously with one power supply.

Device	W_B/W_Y [µm]	V [V]	L [cd/m^2]	CRI	CIE	LE [lm/W]	EQE [%]	LT75 [h]
W0	50/50	3.60	1610	57	(0.40,0.41)	10.87	4.9	2.4
W1	80/80	3.55	1500	61	(0.39,0.40)	10.65	4.8	8.2
W2	30/100	3.40	1600	56	(0.41,0.42)	11.32	4.3	9.2
W3	20/80	3.50	2000	50	(0.44,0.44)	13.07	5.2	5.0

9.2 Control of the Emission Colour

As described above, changing the subunit width ratio between yellow and blue subunits results in varied emission colour of the microstructured OLED array. The corresponding EL spectra of devices W0 ($W_Y=W_B=50$ µm, $m = 0.5$) and W3 ($W_Y= 80$ µm, $W_B=20$ µm, $m = 0.2$) operated with shared power supply for both of the subunits at a current density of $j = 15$ mA/cm^2 are shown in Figure 9.2.1 (a). Here, m denotes the ratio

$$m = \frac{W_B}{W_B + W_Y}. \tag{9.2.1}$$

The corresponding colour coordinates are depicted in Figure 9.2.1 (b). Device W0 emits white light characterised by the correlated colour temperature (CCT) of 4000 K and CRI=57. As expected, due to the decreased value of m, device W3 emission is shifted to yellow compared to W0, towards warm white point A. However, the emission colour cannot be qualified as a white light, since the colour coordinates do not match any of the chromaticity quadrangles.

As expected for both devices, there is more spectral contribution in the yellow-red spectral region (550-700 nm) than in the blue spectral region (450-550 nm). Even when the total areas covered by the blue and yellow subunits are equal (device W0, $m = 0.5$), due to more than 2-fold higher efficiency (for $j < 50$ mA/cm^2) in the phosphorescent sY compared to the fluorescent sB device, yellow emission dominates. It is interesting to note, that the difference between the ratios of the emission intensities in the yellow and blue spectral regions for devices W0 and W3 is less pronounced compared to the simple prediction based on the large area OLED performances. In other words, there seems to be more contribution in the blue spectral region from the device structured down to 20 µm width,
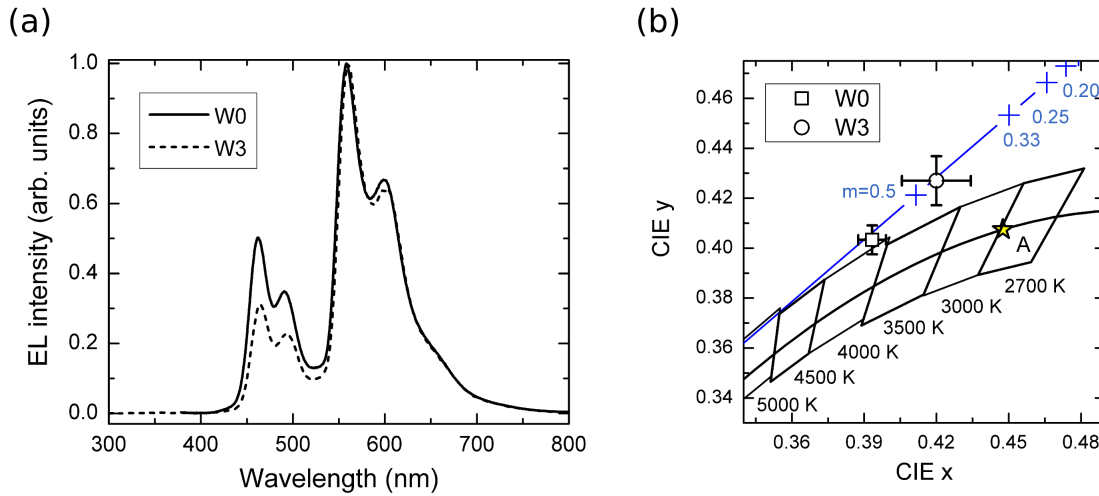
Figure 9.2.1: (a) Normalised EL spectra of devices W0 (W_Y=W_B=50 μm, $m = 0.5$, black solid line) and W3 (W_Y= 80 μm, W_B=20 μm, $m = 0.2$, black dashed line) at $j = 15$mA/cm^2. (b) Corresponding colour coordinates of W0 (open square) and W3 (open circle). Blue solid line indicates theoretical predictions of the colour coordinates based on the large area OLED performances. Colour point A (yellow star), Planckian locus (black solid line) and 7-step chromaticity quadrangles of equal correlated colour temperature are indicated for comparison.

as it would be expected considering linear EL intensity dependence on the OLED size. The effect is further exemplified by comparing the colour coordinates of the corresponding microscale devices (Figure 9.2.1 (b)). Both W0 and W3 show blue shifted emission compared to the theoretically predicted values (solid blue line). The blue shift is more pronounced in W3, indicating the subunit size dependence on the OLED performance. This dependence is further investigated considering the roll-off characteristics of the microstructured and large-area devices.

9.3 Suppression of Efficiency Roll-off in Microscale Devices

Efficiency roll-off characteristics of devices W0 and W3 are depicted in Figure 9.3.1. Device W3 shows higher values compared to the device W0, especially elevated current densities ($j > 10$ mA/cm^2). In order to account for the impact of the subunit size variation, a model describing microstructured device characteristics based on TTA and EPQ mechanisms

(Eq.(8.2.3)) is extended to include the parameter m

$$\eta_{\text{ext}} = m \cdot \eta_{\text{ext}}^{\text{Fl}}(j) + (1 - m) \cdot \eta_{\text{ext}}^{\text{Ph}}(j). \tag{9.3.1}$$

Naturally, increasing the contribution of the more efficient phosphorescent unit by increasing its relative area (decreasing m) is expected to boost the overall efficiency of the microstructured OLED array, as is shown in Figure 9.3.1 (red solid lines). The increase in efficiency due to increasing yellow device contribution is expected at lower currents. At low current density ($j < 10$ mA/cm^2) the predicted efficiency values for device W3 are higher than experimentally observed. W3 exhibits strong efficiency "roll-on", which is usually attributed to the charge imbalance (see Chapter 3), hence it can be the reason for the mismatch between predicted and observed values. The model also cannot fully account for the increase in W3 efficiency at elevated current density. A closer inspection into the efficiency fit of the device W0 characteristics shows reasonable well match at low currents, however at higher current densities the model underestimates the EQE of microstructured device. Such discrepancies between the predicted and observed EQE values at elevated currents suggest that there are different physical mechanisms responsible for the roll-off suppression in microscale devices and the large area devices, which the model represented by Eq. 9.3.1 is based on.

One possibility to explain the efficiency increase when device is structured to the tens of micrometers in size can be the suppression of the EPQ mechanisms. It has been shown by separating the exciton generation and emission zones within the OLED by structuring its injection layer down to 50 nm [80]. The effect of the EPQ suppression and resulting increase in EQE was observed too a lesser extent also in the microscale structures. However, in this work, structuring is done to the whole OLED and not only to the injection layer, therefore exciton generation and emission regions are not separated and are expected to be distributed evenly throughout the device area.

On the other hand, Joule heating is considered to be one of the mechanisms leading to the efficiency roll-off in OLEDs [81]. Thermal management is especially important in large area lighting panels, where Joule heat contributes greatly to the observed EL inhomogeneities over large areas [191]. To reduce the Joule heat impact on OLED performance, several approaches have been proven successful in the past, including pulsed operation [182, 81, 192, 193], the use of high thermal conductivity substrates [194, 195], and fabricating small area devices for efficient thermal runaway [195, 196]. Based on this prior knowledge, thermal effects in large area and microscale OLEDs are investigated in order to account for the differences observed between these devices and presented in the following sections.
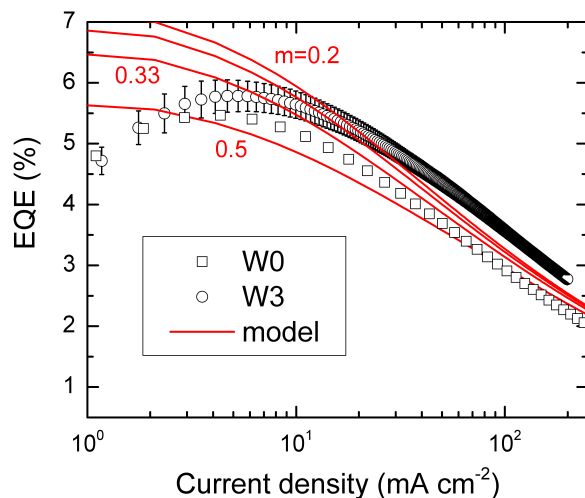
Figure 9.3.1: External quantum efficiency dependence on current density of devices W0 ($m = 0.5$, open squares) and W3 ($m = 0.2$, open circles). Red solid lines represent modelling of the roll-off characteristics of microstructured devices at high currents based on TTA and EPQ mechanisms for phosphorescent and fluorescent subunit devices, respectively. Different lines depict effect on varying ratio of subunit size for $m = 0.2, 0.25, 0.33$ and 0.5.

9.4 Thermal Management in OLEDs

To show that the thermal effects are playing a role in large area devices sB and sY, the voltage sweep is performed with increasing and decreasing voltage values. Upper graph in Figure 9.4.1 depicts typical current hysteresis observed in DC operation in large area device sB. Such hysteresis is explained by the temperature dependent conductivity of the charge carriers in organic semiconductors [191, 197, 198]. During operation, the OLED heats up, thus the current rises due to the exponentially increasing conductivity. Since temperature dissipation takes certain amount of time, decreasing the voltage values results in different (higher) current running through the OLED, since the system still has not reached thermal equilibrium.

The current elevation and the hysteresis are not observed in pulsed operation (pulse duration 1 ms) of the same device, thus confirming the explanation relating the effect to the Joule heating. Additionally, reducing the device area by structuring it to 20 μm stripes separated by 80 μm gap, results in similar suppression of the current hysteresis in DC mode. Only a slight increase in the current at high operating voltages is observed in such device in DC mode, compared to the pulsed operation.
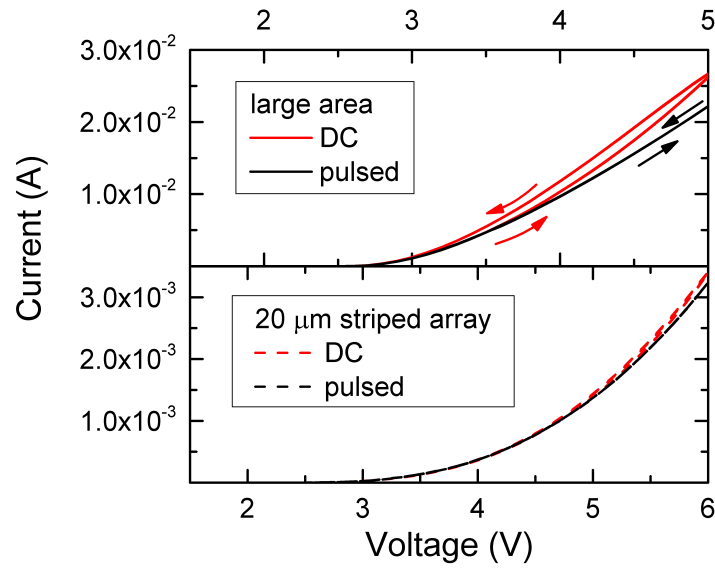
Figure 9.4.1: Current elevation and hysteresis due to self-heating in large area fluorescent OLEDs (device sB, top). Arrows indicate the direction of the voltage sweep. Hysteresis is observed in DC mode (red solid line), but is suppressed in pulsed device operation (1 ms pulse, black solid line). Bottom: microscale OLED array show no pronounced current elevation and hysteresis in both pulsed (dashed black line) and DC (dashed red line) modes.

In order to evaluate the effect of the temperature rise in the working OLED in determining its efficiency, controlled heating of samples sB and sY is performed from room temperature to 340 K. Corresponding temperature-dependent current-voltage characteristics and EQEs are shown in Figure 9.4.2. In general, in both sB and sY devices, current density rises with increasing temperature (Figure 9.4.2 (a) and (c), respectively), in line with the observation of the current hysteresis in Figure 9.4.1. In addition, EQE values decrease with the rising temperature, which supports the hypothesis of the efficiency increase in the microscale devices due to a better thermal management. However, the efficiency drop is not continuous in the fluorescent blue device. This can be attributed to the thermal instability of the n-transport layers which, as discussed in Chapter 7, are characterised with low glass transition temperature. On the other hand, device sY comprising temperature stable materials show steady decrease in efficiency with increasing temperature.
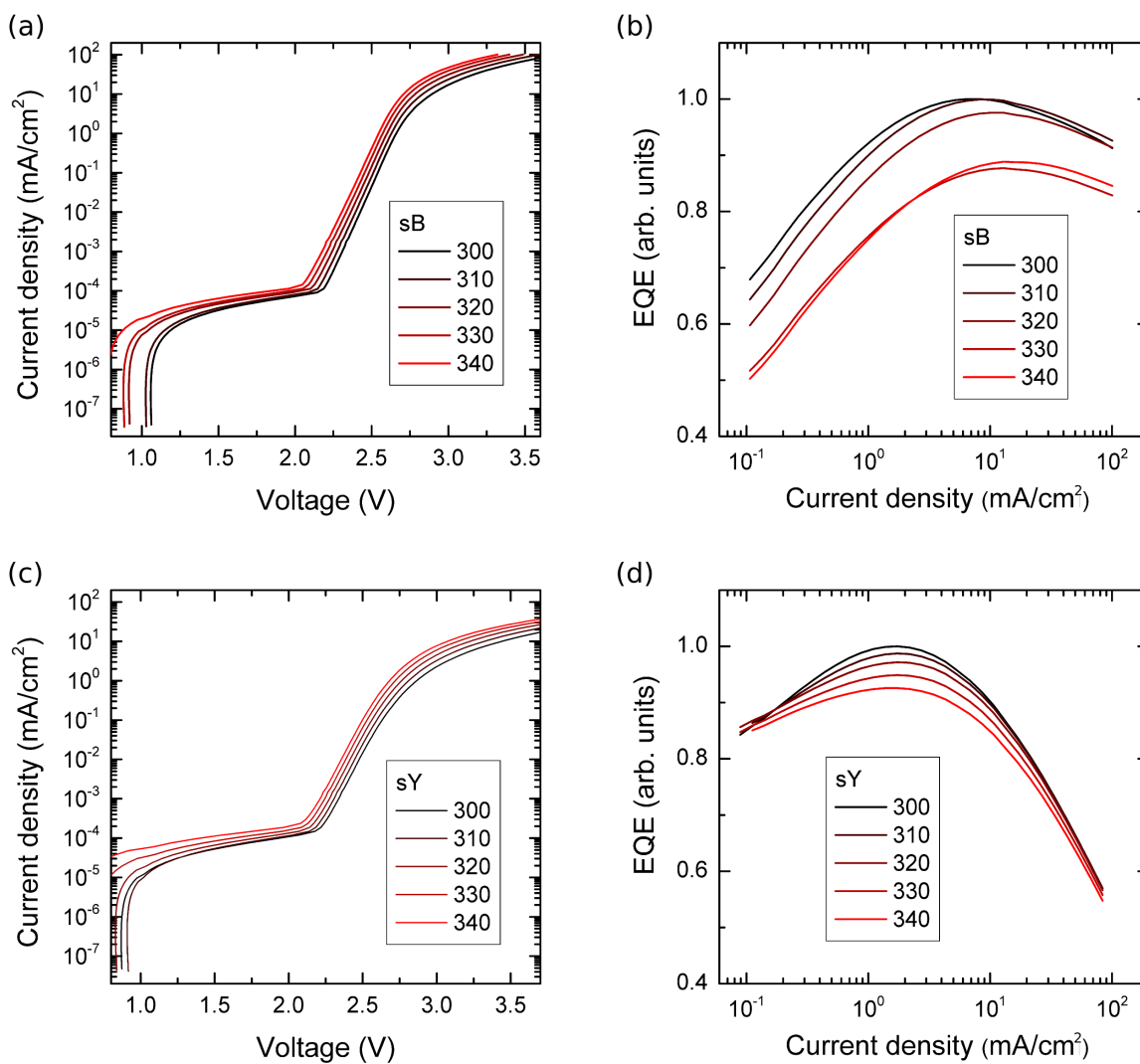
Figure 9.4.2: Temperature dependence of OLED characteristics. (a) Current-voltage characteristics and (b) EQE of device sB dependence on temperature from 300 K to 340 K. Similar current-voltage and EQE characteristics for device sY, (c) and (d), respectively.

9.5 Modelling Impact of Joule Heat on Roll-off Characteristics

Finally, a simple analytical model is introduced to quantitatively estimate the suppression of the Joule heat quenching observed by structuring the devices down to 20 μm. As shown previously, efficiency roll-off of the fluorescent blue device sB is modelled assuming EPQ mechanism. In order to account for the thermal quenching, a term $-k_{\mathrm{th}}jVn_{\mathrm{S}}$ is introduced to the rate equation for singlet excitons

$$\frac{\mathrm{d}n_{\mathrm{S}}}{\mathrm{d}t} = -\frac{n_{\mathrm{S}}}{\tau} - k_{\mathrm{P}}Cj^{\frac{1}{l+1}}n_{\mathrm{S}} - k_{\mathrm{th}}jVn_{\mathrm{S}} + \frac{j}{4qw}, \tag{9.5.1}$$

where k_{th} denotes thermal quenching parameter [81], n_S is the singlet exciton density, τ is the fluorescence lifetime, k_{P} is the polaron quenching rate and w is the thickness of the carrier recombination zone. This model assumes trap charge limited current (TCLC) model [187, 188] for the description of current-voltage characteristics, i.e. $j = \alpha V^{l+1}$, with

$$\alpha = \frac{N_0\mu q^{1-l}}{d^{2l+1}}\left(\frac{\epsilon l}{N_{\mathrm{T}}(l+1)}\right)^l\left(\frac{2l+1}{l+1}\right)^{l+1}, \tag{9.5.2}$$

where N_0 is the effective density of states in the transport level, N_{T} is the total trap density, μ is the charge carrier mobility, d is the thickness of the sample and

$$l = \frac{E_{\mathrm{T}}}{k_{\mathrm{B}}T}, \tag{9.5.3}$$

where E_{T} denotes the effective energy of traps states.

In the steady-state case, Eq.(9.5.5) can be solved to obtain the efficiency roll-off characteristics

$$\frac{\eta_{\mathrm{ext}}}{\eta_0} = \left(1 + k_{\mathrm{P}}C\tau j^{\frac{1}{l+1}} + k_{\mathrm{th}}\alpha^{-(l+1)}j^{\frac{l+2}{l+1}}\right)^{-1}. \tag{9.5.4}$$

Figure 9.5.1 shows the analytical expression Eq.(9.5.4) applied to fit the experimental results of large area device sB and microstructured OLED array. The differences in EQE data can be successfully described by varying only the thermal quenching rate k_{th} and keeping the rest of the parameter virtually identical. Joule heating term k_{th} is estimated to be 1.7 times higher in device sB compared to its microstructured counterpart.
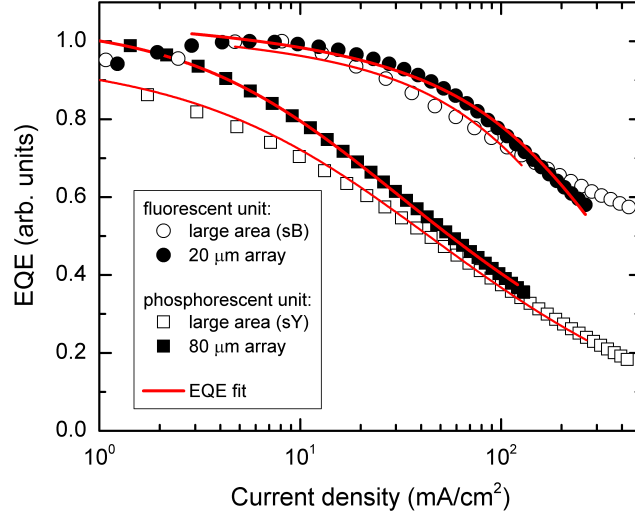
Figure 9.5.1: Evaluation of the impact of the thermal exciton quenching in large area OLEDs. EQE dependence on current density of device sB (open circles) and microstructured 20 μm OLED array (solid circles), as well as device sY (open squares) and its structured counterpart (solid squares). Red solid lines represent EQE fits based on corresponding exciton quenching model including Joule heating term. Estimated thermal quenching rate k_{th} is 1.7 times higher in large area device compared to microscale OLED array.

Similarly, the rate equation for triplet excitons

$$\frac{\mathrm{d}n_{\mathrm{T}}}{\mathrm{d}t} = -\frac{n_{\mathrm{T}}}{\tau} - \frac{1}{2}k_{\mathrm{TTA}}n_{\mathrm{T}}^2 - k_{\mathrm{th}}jVn_{\mathrm{T}} + \frac{j}{qw}. \tag{9.5.5}$$

Then, the steady state solution for the efficiency roll-off reads

$$\frac{\eta_{\mathrm{ext}}}{\eta_0} = \frac{4j}{j_0}\Big(1 + \tau k_{\mathrm{th}}\alpha^{-(l+1)}j^{\frac{l+2}{l+1}}\Big[\sqrt{1 + \frac{8j}{j_0}\big(\tau k_{\mathrm{th}}\alpha^{-(l+1)}j^{\frac{l+2}{l+1}}\big)^{-1}} - 1\Big]\Big). \tag{9.5.6}$$

Similarly to the case of fluorescent OLEDs, phosphorescent devices can be modelled to have a lower Joule heat term, which explains the higher efficiency of small area devices. However, at high current densities, TTA dominates, and strong efficiency roll-off behaviour is observed (Figure 9.5.1).

9.6 Summary

In this chapter, the effect of decreasing the OLED size to tens of micrometers is investigated. Lithographic device size variation enabled control of the emission colour of the microstructured OLED array. Additionally, the possibility to vary device lifetime and efficiency roll-off characteristics by controling OLED dimension was demonstrated. Experimental findings were compared to the theoretical predictions of the corresponding efficiency roll-off model for fluorescent OLEDs, which led to the conclusion that different physical mechanisms are responsible for the efficiency roll-off at elevated currents in microscale and large-area devices. The observed efficiency enhancement in microscale OLEDs were attributed to the suppression of the Joule heating due to the better management of heat dissipation. Simple analytical expression to account for the thermal exciton quenching was developed and applied to show an almost two-fold higher Joule quenching in the large area devices compared to the microstructured OLEDs.

10 Conclusions and Outlook

10.1 Conclusions

In this work, the orthogonal processing, which is based on the development in highly fluorinated hydrofluoroether (HFE) solvents, is shown to be compatible with the p-i-n OLED technology, thus enabling photolithographic structuring of state-of-the-art organic electroluminescent devices. It is demonstrated that the careful selection of the organic functional layers is needed to establish the compatibility between the orthogonal processing and multilayered OLEDs. In this regard, materials with high glass transition temperature and low molecular affinity to HFEs are preferred. The latter is evaluated using the solubility study based on Hansen solubility parameter approach. Impact of different lithographic processing steps on OLEDs are evaluated by first investigating the simple single heterojuntion devices based on archetypical Alq_3 emitter, and then realising complex multilayer OLEDs based on doped charge transport films and phosphorescent emitters. The lithographic processing is shown to induce changes in the work function of the semi-transparent ITO electrode. Thus, in order to achieve a homogeneous EL profile, which is required for OLED applications, doping of the charge transport layers is proven essential. Phosphorescent devices based on green emitter $Ir(ppy)_3$ and red emitter $Ir(MDQ)_2(acac)$, which are structured by photolithography, reach nearly 100 % internal quantum efficiency and device lifetime of > 100000 h, in line with the state-of-the-art shadow mask patterned OLEDs. The possibility to integrate multiple devices using orthogonal processing based on a bilayer approach is explored and the main limitation, i.e. solvent permeability of the fluoropolymer films, is discussed. Furthermore, proof-of-concept demonstration of the white OLED based on side-by-side patterning of yellow and blue devices is presented. The novel device concept involves a single lithography step and allows 100 % usage of the active area for light emission, thus avoiding limitations of the lateral structuring approaches. The device architecture allows simultaneous electrical and optical optimisation of each of the subunit devices. What is more, the emission colour of the microstructured OLED array can be tuned by individually addressing separate subunits. Essential for the solid-state lighting applications, the device exhibits excellent colour stability with increasing brightness up to

the lighting application relevant value of 5000 cd/m^2.

   Microscale OLEDs are shown to exhibit a number of features seldom reported in the large area devices. Due to a high conductivity of doped organic semiconductor films, significant contribution of lateral charge transport results in the electroluminescence emission outside of the active area of the OLED. While the effect is minor in the large area devices, the lateral emission contributes significantly in microscale OLEDs, especially at low driving conditions. When OLED operates close to its turn-on voltage, the lateral charge transport is shown to extend up to tens of micrometers outside of the active device area, i.e. distance comparable to the device itself. The subunit cross-talk and the resulting increase in the current leakage in two-color microstructured arrays is also attributed to the lateral conductivity of doped organic films. Finally, it is shown that decreasing the lateral OLED dimension down to 20 μm leads to the better heat management in the electroluminescent device. Series of experiments were conducted to investigate the impact of the Joule heating on different OLED architectures, employing temperature dependent and pulsed device operation measurements. The study clearly shows the effect of the self-heating in large area OLEDs and the decrease of external quantum efficiency with increasing temperature in such devices. In addition, an analytical expression is developed to account for the heat induced exciton quenching processes in fluorescent OLEDs. Up to two times lower thermal quenching term leads to the suppression of the Joule heating and the corresponding efficiency roll-off characteristics at elevated currents that are shown in microstructured OLED arrays as compared to their large area counterparts. This allows the demonstration of the roll-off suppression in white OLEDs based on lithographically structured subunits at operating conditions relevant to solid-state lighting.

10.2 Outlook

The actual demonstration of the RGB display is beyond the scope of this work. However, the presented results suggest that the full colour, large area displays fabricated using lithographic techniques could, in principle, be achieved. Further, the resolution of the investigated OLEDs was limited by the photolithography exposure tool used in this work. However, micron or even sub-micron structuring could be achieved with the currently available optical lithography tools. The limiting factor, however, is the use of the bilayer resist which limits the resolution down to the undercut formed by the fluoropolymer layer beneath the imaging resist. The latter is of the order of few microns in the investigated samples. Once the size of the patterned structures is comparable to the depth of the bespoke undercut, the structures are expected to collapse. Therefore, reducing the undercut and the bilayer thickness is a way to achieve sub-micron structures using the bilayer method.

Material screening based on HSP approach could be further expanded by including DFT based calculations in order to guide the material development. Novel transport layers compatible with the direct photolithographic patterning would simplify the fabrication of the RGB array to only two patterning steps, in addition to enable novel device concepts based on lithographically patterned cathode layer placed on top of the organic films.

A promising proof-of-concept microstructured solid-state-lighting devices were demonstrated. The electrical performance of the phosphorescent unit could be further optimised by using HFE compatible n-transport layers with a better aligned energy transport levels, which would more than double the luminous efficacy of the yellow unit. The MADN:TBPe emitter system in the fluorescent blue subunit could be replaced by one of the EMLs based on TADF emitters. In such case, the efficiency of the blue OLED could be increased by 3-4 times. Additionally, TADF emitters are characterised by a broad emission spectrum, originating from the CT state, and thus would improve the CRI, due to a better coverage of the visible spectrum. Further improvements of such OLEDs are expected by extending the structuring procedure to two steps, in order to incorporate green emitting unit. In such case, CRI > 90 could be easily achieved, without compromising any of the benefits of microstructured OLEDs, e.g. colour stability at high brightness and possibility to optimize each colour individually. Adding an efficient green subunit, which can be achieved either using phosphorescent (e.g. $Ir(ppy)_3$) or TADF based emitter, would improve the luminous efficacy considerably. To sum up, by implementing three unit array comprising structured efficient red, green and the TADF based blue units, the device could easily reach 30-40 lm/W at 1000 cd/m^2, matching state-of-the-art white OLED performace. Fol-

lowing the optimisation based on OLED dimension variation the efficiency values could be maintained up to lighting relevant brightness and with the possibility to shift the emission colour towards warm white point A. Including additional external light outcoupling structures, the performance could be improved by 2-3 times, which would lead to performance comparable to commercially available fluorescent lighting bulbs.

Orthogonal processing is an enabling technology, thus, the lithographic implementation of OLEDs for novel uses can be envisioned in the future. A vast number of emerging applications based on OLED microdisplay, as well as the integration of OLEDs with transistor or photodiode arrays, will benefit further from the advances in photolithographic structuring of organic semiconductors.

List of Solvents for HSP Screening

Solvent	δ_D [MPa$^{0.5}$]	δ_P [MPa$^{0.5}$]	δ_H [MPa$^{0.5}$]	δ [MPa$^{0.5}$]
Acetone	15.5	10.4	7	19.94
Benzene	18.4	0	2	18.51
Chlorobenzene	19	4.3	2	19.58
Chloroform	17.8	3.1	5.7	18.95
Diethyl ether	14.5	2.9	5.1	15.64
Dimethyl sulfoxide	18.4	16.4	10.2	26.68
1,4-Dioxane	19	1.8	7.4	20.47
Ethanol	15.8	8.8	19.4	26.52
Ethyl acetate	15.8	5.3	7.2	18.15
Hexane	14.9	0	0	14.9
Methanol	15.1	12.3	22.3	29.61
Nitromethane	15.8	18.8	5.1	25.08
Tetrahydrofuran	16.8	5.7	8	19.46
Toluene	18	1.4	2	18.16
HFE7100	13.7	2.2	1	13.91
HFE7200	13.3	2	1	13.49
HFE7300	12.5	2	0.8	12.68
HFE7600	14.3	1.4	1.2	14.42
N,N-dimethylformamide	17.4	13.7	11.3	24.86
Acetonnitrile	15.3	18	6.1	24.4
Isopropyl alcohol	15.8	6.1	16.4	23.58
N-butyl alcohol	16	5.7	15.8	23.2
Nitrobenzene	20	8.6	4.1	22.15
Methyl tert-butyl ether	14.8	4.3	5	16.2
P-xylene	17.6	1	3.1	17.9
N-heptane	15.3	0	0	15.3
PGMEA	15.6	5.6	9.8	19.26
2,6-dimethyl-4-heptanone	16	3.7	4.1	16.9
2-butanol	15.8	5.7	14.5	22.19
pentane	14.5	0	0	14.5
dibutyl ether	14.4	2.9	5.1	15.55

List of Abbreviations

AFM	Atomic-Force Microscpopy
AMOLED	Active-Matrix Organic Light-Emitting Diode
CIE	Comission Internationale d'Eclairage
CRI	Colour Rendering index
CT	Charge Transfer
DFT	Density Functional Theory
EBL	Electron Blocking Layer
EL	Electroluminescence
EML	Emission Layer
EPQ	Exciton-Polaron Quenching
EQE	External Quantum Efficiency
ETL	Electron Transport Layer
FWHM	Full Width at Half Maximum
HBL	Hole Blocking Layer
HFE	Hydrofluoroether
HOMO	Highest Occupied Molecular Orbital
HSP	Hansen Solubility Parameter
HTL	Hole Transport Layer
ISC	Intersystem Crossing
ITO	Indium Tin Oxide

LCAO	Linear Combination of Atomic Orbitals
LCD	Liquid Crystal Display
LDI-TOF-MS	Laser Desorption/Ionisation Time-of-Flight Mass Spectroscopy
LE	Luminous Efficacy
LEP	Light-Emitting Polymer
LIPS	Laser Induced Patternwise Sublimation
LITI	Laser Induced Thermal Imaging
LP	Localised Plasmon
LUMO	Lowest Unoccupied Molecular Orbital
MO	Molecular Orbital
OLED	Organic Light-Emitting Diode
OVJP	Organic Vapour-Jet Printing
p-i-n	p-doped, Intrinsic, n-doped
QCM	Quartz Crystal Microbalance
RGB	Red, Green, Blue
RISC	Reverse Intersystem Crossing
SPP	Surface Plasmon Polariton
SSA	Singlet-Singlet Annihilation
TADF	Thermally Activated Delayed Fluorescence
TE	Transverse Electric
TIR	Total Internal Reflection
TM	Transverse Magnetic
TPA	Triplet-Polaron Annihilation
TTA	Triplet-Triplet Annihilation
UV	Ultraviolet
WVTR	Water Vapour Transmission Rate

List of Figures

List of Tables

Acknowledgements

from physics to chemistry to engineering.

I am grateful to the students whom I had an opportunity to supervise, Toni Bärschneider, Ulrich Kemper, and Paulius Imbrasas for their curiosity, enthusiasm and all the long hours spent in the lab. I learned many new things discussing your project outcomes with you. I thank Robby Janneck and Shrujan Kalkura for our collaborative efforts with the orthogonal lithography.

I thank Dr. Frederik Nehm, Dr. Donato Spoltore, Dr. Franz Selzer, Irma Slowik, Bernhard Siegmund, Felix Dollinger, Toni Mayer and Matthias Böhm for a range of outdoor and indoor activities that we jointly had.

Finally, I want to thank my friends and family for their continuous support and encouragement. A special thanks goes to my special ones, Corinna and Lukas, for enriching my days with joy and wonder.

Bibliography

[1] C. W. Tang and S. A. VanSlyke, "Organic electroluminescent diodes," *Applied Physics Letters*, vol. 51, no. 12, 1987.

[2] P. G. Taylor, J.-K. Lee, A. A. Zakhidov, M. Chatzichristidi, H. H. Fong, J. A. DeFranco, G. G. Malliaras, and C. K. Ober, "Orthogonal patterning of PEDOT:PSS for organic electronics using hydrofluoroether solvents," *Advanced Materials*, vol. 21, no. 22, pp. 2314–2317, 2009.

[3] A. A. Zakhidov, J.-K. Lee, H. H. Fong, J. A. DeFranco, M. Chatzichristidi, P. G. Taylor, C. K. Ober, and G. G. Malliaras, "Hydrofluoroethers as orthogonal solvents for the chemical processing of organic electronic materials," *Advanced Materials*, vol. 20, no. 18, pp. 3481–3484, 2008.

[4] H. Shirakawa, E. J. Louis, A. G. MacDiarmid, C. K. Chiang, and A. J. Heeger, "Synthesis of electrically conducting organic polymers: halogen derivatives of polyacetylene, (ch)," *J. Chem. Soc., Chem. Commun.*, pp. 578–580, 1977.

[5] P. Atkins and J. de Paula, *Atkins' Physical Chemistry*. OUP Oxford, 2010.

[6] Y. Zhao and D. G. Truhlar, "A new local density functional for main-group thermochemistry, transition metal bonding, thermochemical kinetics, and noncovalent interactions," *The Journal of Chemical Physics*, vol. 125, no. 19, 2006.

[7] P. Hohenberg and W. Kohn, "Inhomogeneous electron gas," *Phys. Rev.*, vol. 136, pp. B864–B871, 1964.

[8] N. Allinger and D. Rogers, *Molecular Structure: Understanding Steric and Electronic Effects from Molecular Mechanics*. Wiley, 2010.

[9] I. Levine, *Quantum Chemistry 5Th Ed.* Prentice-Hall Of India Pvt. Limited, 1999.

[10] A. Stone, *The Theory of Intermolecular Forces*. OUP Oxford, 2013.

[11] J. Waals, *Over de continuiteit van den gas- en vloeistoftoestand*. A. W. Sijthoff, 1873.

[12] W. H. Keesom, "The second viral coefficient for rigid spherical molecules, whose mutual attraction is equivalent to that of a quadruplet placed at their centre," *Koninklijke Nederlandse Akademie van Wetenschappen Proceedings Series B Physical Sciences*, vol. 18, pp. 636–646, 1915.

[13] W. Duffin, *Electricity and Magnetism.* W. J. Duffin, 2001.

[14] F. London, "The general theory of molecular forces," *Trans. Faraday Soc.*, vol. 33, pp. 8b–26, 1937.

[15] J. Huheey, E. Keiter, and R. Keiter, *Inorganic Chemistry: Principles of Structure and Reactivity.* Pearson Education, 2000.

[16] T. S. Moore and T. F. Winmill, "The state of amines in aqueous solution," *J. Chem. Soc., Trans.*, vol. 101, pp. 1635–1676, 1912.

[17] L. Pauling, *The Nature of the Chemical Bond and the Structure of Molecules and Crystals: An Introduction to Modern Structural Chemistry.* George Fisher Baker Non-Resident Lecture Series, Cornell University Press, 1960.

[18] J. J. Dannenberg, L. Haskamp, , and A. Masunov, "Are hydrogen bonds covalent or electrostatic? a molecular orbital comparison of molecules in electric fields and h-bonding environments," *The Journal of Physical Chemistry A*, vol. 103, no. 35, pp. 7083–7086, 1999.

[19] W. Koch and M. Holthausen, *A chemist's guide to density functional theory.* Wiley-VCH, 2000.

[20] J. E. Jones, "On the determination of molecular fields. ii. from the equation of state of a gas," *Proceedings of the Royal Society of London A: Mathematical, Physical and Engineering Sciences*, vol. 106, no. 738, pp. 463–477, 1924.

[21] B. Valeur and M. N. Berberan-Santos, *Absorption of Ultraviolet, Visible, and Near-Infrared Radiation*, pp. 31–51. Wiley-VCH Verlag GmbH Co. KGaA, 2012.

[22] M. Kasha, "Characterization of electronic transitions in complex molecules," *Discuss. Faraday Soc.*, vol. 9, pp. 14–19, 1950.

[23] P. Klán and J. Wirz, *Photochemistry of Organic Compounds: From Concepts to Practice.* Postgraduate Chemistry Series, Wiley, 2009.

[24] N. Djeu and W. T. Whitney, "Laser cooling by spontaneous anti-stokes scattering," *Phys. Rev. Lett.*, vol. 46, pp. 236–239, 1981.

[25] D. Andrews and A. Demidov, *Resonance Energy Transfer*. Wiley, 1999.

[26] T. Förster, "Zwischenmolekulare energiewanderung und fluoreszenz," *Annalen der Physik*, vol. 437, no. 1-2, pp. 55–75, 1948.

[27] D. L. Dexter, "A theory of sensitized luminescence in solids," *The Journal of Chemical Physics*, vol. 21, no. 5, 1953.

[28] N. Karl, "Charge carrier transport in organic semiconductors," *Synthetic Metals*, vol. 133-134, pp. 649 – 657, 2003. Proceedings of the Yamada Conference LVI. The Fourth International Symposium on Crystalline Organic Metals, Superconductors and Ferromagnets (ISCOM 2001).

[29] V. Coropceanu, J. Cornil, D. A. da Silva Filho, Y. Olivier, R. Silbey, , and J.-L. Bredas, "Charge transport in organic semiconductors," *Chemical Reviews*, vol. 107, no. 4, pp. 926–952, 2007.

[30] N. Tessler, Y. Preezant, N. Rappaport, and Y. Roichman, "Charge transport in disordered organic materials and its relevance to thin-film devices: A tutorial review," *Advanced Materials*, vol. 21, no. 27, pp. 2741–2761, 2009.

[31] M. Pope and C. Swenberg, *Electronic Processes in Organic Crystals and Polymers*. Monographs on the physics and chemistry of materials, Oxford University Press, 1999.

[32] H. Bässler, "Charge transport in disordered organic photoconductors a monte carlo simulation study," *physica status solidi (b)*, vol. 175, no. 1, pp. 15–56, 1993.

[33] J. Maxwell, *A Treatise on Electricity and Magnetism*. No. 1 tom. in A Treatise on Electricity and Magnetism, Clarendon Press, 1873.

[34] M. Born, E. Wolf, A. Bhatia, D. Gabor, A. Stokes, A. Taylor, P. Wayman, and W. Wilcock, *Principles of Optics: Electromagnetic Theory of Propagation, Interference and Diffraction of Light*. Cambridge University Press, 2000.

[35] O. Heavens, *Optical Properties of Thin Solid Films*. Dover Books on Physics Series, Dover Publications, 1991.

[36] T. Tamir and R. Alferness, *Guided-wave optoelectronics.* Springer series in electronics and photonics, Springer, 1988.

[37] D. Marcuse, A. Telephone, and T. Company, *Theory of Dielectric Optical Waveguides.* Quantum Electronics–Principles & Applications, Academic Press, 1991.

[38] R. Hunsperger, *Integrated Optics: Theory and Technology.* Advanced texts in physics, Springer New York, 2009.

[39] F. Abelès, "La théorie générale des couches minces," *J. Phys. Radium*, vol. 11, no. 7, pp. 307–309, 1950.

[40] S. Maier, *Plasmonics: Fundamentals and Applications.* Springer US, 2010.

[41] M. Scully and M. Zubairy, *Quantum Optics.* Cambridge University Press, 1997.

[42] T. Tsutsui, "Progress in electroluminescent devices using molecular thin films," *MRS Bulletin*, vol. 22, pp. 39–45, 1997.

[43] M. Aldissi and N. A. T. O. S. A. Division, *Intrinsically Conducting Polymers: An Emerging Technology.* E]: [Nato ASI series, Springer, 1993.

[44] K. Walzer, B. Maennig, M. Pfeiffer, and K. Leo, "Highly efficient organic devices based on electrically doped transport layers," *Chemical Reviews*, vol. 107, no. 4, pp. 1233–1271, 2007.

[45] M. Pfeiffer, K. Leo, X. Zhou, J. Huang, M. Hofmann, A. Werner, and J. Blochwitz-Nimoth, "Doped organic semiconductors: Physics and application in light emitting diodes," *Organic Electronics*, vol. 4, no. 2-3, pp. 89 – 103, 2003.

[46] R. Meerheim, S. Scholz, G. Schwartz, S. Reineke, S. Olthof, K. Walzer, and K. Leo, "Efficiency and lifetime enhancement of phosphorescent organic devices," *Proc. SPIE*, vol. 6999, pp. 699917–699917–9, 2008.

[47] R. Meerheim, S. Scholz, S. Olthof, G. Schwartz, S. Reineke, K. Walzer, and K. Leo, "Influence of charge balance and exciton distribution on efficiency and lifetime of phosphorescent organic light-emitting devices," *Journal of Applied Physics*, vol. 104, no. 1, 2008.

[48] M. Furno, R. Meerheim, S. Hofmann, B. Lüssem, and K. Leo, "Efficiency and rate of spontaneous emission in organic electroluminescent devices," *Phys. Rev. B*, vol. 85, p. 115205, 2012.

[49] N. C. Giebink and S. R. Forrest, "Quantum efficiency roll-off at high brightness in fluorescent and phosphorescent organic light emitting diodes," *Phys. Rev. B*, vol. 77, p. 235215, 2008.

[50] G. A. Crosby and J. N. Demas, "Measurement of photoluminescence quantum yields. review," *The Journal of Physical Chemistry*, vol. 75, no. 8, pp. 991–1024, 1971.

[51] E. Schubert, *Light-Emitting Diodes*. Cambridge University Press, 2006.

[52] J. Wang, A. Chepelianskii, F. Gao, and N. C. Greenham, "Control of exciton spin statistics through spin polarization in organic optoelectronic devices," *Nat Commun*, vol. 3, p. 1191, 2012.

[53] M. A. Baldo, D. F. O'Brien, Y. You, A. Shoustikov, S. Sibley, M. E. Thompson, and S. R. Forrest, "Highly efficient phosphorescent emission from organic electroluminescent devices," *Nature*, vol. 395, no. 6698, pp. 151–154, 1998.

[54] M. A. Baldo, C. Adachi, and S. R. Forrest, "Transient analysis of organic electrophosphorescence. ii. transient analysis of triplet-triplet annihilation," *Phys. Rev. B*, vol. 62, pp. 10967–10977, 2000.

[55] M. A. Baldo, D. F. O'Brien, M. E. Thompson, and S. R. Forrest, "Excitonic singlet-triplet ratio in a semiconducting organic thin film," *Phys. Rev. B*, vol. 60, pp. 14422–14428, 1999.

[56] M. Segal, M. A. Baldo, R. J. Holmes, S. R. Forrest, and Z. G. Soos, "Excitonic singlet-triplet ratios in molecular and polymeric organic materials," *Phys. Rev. B*, vol. 68, p. 075211, 2003.

[57] M. Wohlgenannt, K. Tandon, S. Mazumdar, S. Ramasesha, and Z. V. Vardeny, "Formation cross-sections of singlet and triplet excitons in [pi]-conjugated polymers," *Nature*, vol. 409, no. 6819, pp. 494–497, 2001.

[58] J.-S. Kim, P. K. H. Ho, N. C. Greenham, and R. H. Friend, "Electroluminescence emission pattern of organic light-emitting diodes: Implications for device efficiency calculations," *Journal of Applied Physics*, vol. 88, no. 2, 2000.

[59] C. Rothe, S. M. King, and A. P. Monkman, "Direct measurement of the singlet generation yield in polymer light-emitting diodes," *Phys. Rev. Lett.*, vol. 97, p. 076602, 2006.

[60] L. C. Lin, H. F. Meng, J. T. Shy, S. F. Horng, L. S. Yu, C. H. Chen, H. H. Liaw, C. C. Huang, K. Y. Peng, and S. A. Chen, "Triplet-to-singlet exciton formation in poly(p-phenylene-vinylene) light-emitting diodes," *Phys. Rev. Lett.*, vol. 90, p. 036601, 2003.

[61] D. Y. Kondakov, "Characterization of triplet-triplet annihilation in organic light-emitting diodes based on anthracene derivatives," *Journal of Applied Physics*, vol. 102, no. 11, 2007.

[62] D. Y. Kondakov, "Role of triplet-triplet annihilation in highly efficient fluorescent devices," *Journal of the Society for Information Display*, vol. 17, no. 2, pp. 137–144, 2009.

[63] M. Segal, M. Singh, K. Rivoire, S. Difley, T. Van Voorhis, and M. A. Baldo, "Extrafluorescent electroluminescence in organic light-emitting devices," *Nat Mater*, vol. 6, no. 5, pp. 374–378, 2007.

[64] T. Ford, H. Ohkita, S. Cook, J. Durrant, and N. Greenham, "Direct observation of intersystem crossing in charge-pair states in polyfluorene polymer blends," *Chemical Physics Letters*, vol. 454, no. 4–6, pp. 237 – 241, 2008.

[65] A. P. Monkman, "Singlet generation from triplet excitons in fluorescent organic light-emitting diodes," *ISRN Materials Science*, vol. 2013, p. 19, 2013.

[66] R. E. Merrifield, "Theory of magnetic field effects on the mutual annihilation of triplet excitons," *The Journal of Chemical Physics*, vol. 48, no. 9, pp. 4318–4319, 1968.

[67] B. Dick and B. Nickel, "Accessibility of the lowest quintet state of organic molecules through triplet-triplet annihilation; an indo ci study," *Chemical Physics*, vol. 78, no. 1, pp. 1 – 16, 1983.

[68] D. Y. Kondakov, T. D. Pawlik, T. K. Hatwar, and J. P. Spindler, "Triplet annihilation exceeding spin statistical limit in highly efficient fluorescent organic light-emitting diodes," *Journal of Applied Physics*, vol. 106, no. 12, 2009.

[69] D. Y. Kondakov, "Triplet–triplet annihilation in highly efficient fluorescent organic light-emitting diodes: current state and future outlook," *Philosophical Transactions of the Royal Society of London A: Mathematical, Physical and Engineering Sciences*, vol. 373, no. 2044, 2015.

186

[70] A. Endo, M. Ogasawara, A. Takahashi, D. Yokoyama, Y. Kato, and C. Adachi, "Thermally activated delayed fluorescence from sn4+–porphyrin complexes and their application to organic light emitting diodes — a novel mechanism for electroluminescence," *Advanced Materials*, vol. 21, no. 47, pp. 4802–4806, 2009.

[71] J. C. Deaton, S. C. Switalski, D. Y. Kondakov, R. H. Young, T. D. Pawlik, D. J. Giesen, S. B. Harkins, A. J. M. Miller, S. F. Mickenberg, and J. C. Peters, "E-type delayed fluorescence of a phosphine-supported cu2(-nar2)2 diamond core: Harvesting singlet and triplet excitons in oleds," *Journal of the American Chemical Society*, vol. 132, no. 27, pp. 9499–9508, 2010.

[72] H. Uoyama, K. Goushi, K. Shizu, H. Nomura, and C. Adachi, "Highly efficient organic light-emitting diodes from delayed fluorescence," *Nature*, vol. 492, no. 7428, pp. 234–238, 2012.

[73] Q. Zhang, B. Li, S. Huang, H. Nomura, H. Tanaka, and C. Adachi, "Efficient blue organic light-emitting diodes employing thermally activated delayed fluorescence," *Nat Photon*, vol. 8, no. 4, pp. 326–332, 2014.

[74] Y. Tao, K. Yuan, T. Chen, P. Xu, H. Li, R. Chen, C. Zheng, L. Zhang, and W. Huang, "Thermally activated delayed fluorescence materials towards the breakthrough of organoelectronics," *Advanced Materials*, vol. 26, no. 47, pp. 7931–7958, 2014.

[75] L. Bergmann, D. M. Zink, S. Bräse, T. Baumann, and D. Volz, "Metal–organic and organic tadf-materials: Status, challenges and characterization," *Topics in Current Chemistry*, vol. 374, no. 3, pp. 1–39, 2016.

[76] M. C. Gather and S. Reineke, "Recent advances in light outcoupling from white organic light-emitting diodes," *Journal of Photonics for Energy*, vol. 5, no. 1, p. 057607, 2015.

[77] K. Saxena, V. Jain, and D. S. Mehta, "A review on the light extraction techniques in organic electroluminescent devices," *Optical Materials*, vol. 32, no. 1, pp. 221 – 233, 2009.

[78] W. Brütting, J. Frischeisen, T. D. Schmidt, B. J. Scholz, and C. Mayr, "Device efficiency of organic light-emitting diodes: Progress by improved light outcoupling," *physica status solidi (a)*, vol. 210, no. 1, pp. 44–65, 2013.

[79] S. Reineke, K. Walzer, and K. Leo, "Triplet-exciton quenching in organic phosphorescent light-emitting diodes with ir-based emitters," *Phys. Rev. B*, vol. 75, p. 125328, 2007.

[80] K. Hayashi, H. Nakanotani, M. Inoue, K. Yoshida, O. Mikhnenko, T.-Q. Nguyen, and C. Adachi, "Suppression of roll-off characteristics of organic light-emitting diodes by narrowing current injection/transport area to 50nm," *Applied Physics Letters*, vol. 106, no. 9, 2015.

[81] H. Nakanotani, H. Sasabe, and C. Adachi, "Singlet-singlet and singlet-heat annihilations in fluorescence-based organic light-emitting diodes under steady-state high current density," *Applied Physics Letters*, vol. 86, no. 21, 2005.

[82] C. Adachi, M. A. Baldo, M. E. Thompson, and S. R. Forrest, "Nearly 100% internal phosphorescence efficiency in an organic light-emitting device," *Journal of Applied Physics*, vol. 90, no. 10, 2001.

[83] M. A. Baldo, S. Lamansky, P. E. Burrows, M. E. Thompson, and S. R. Forrest, "Very high-efficiency green organic light-emitting devices based on electrophosphorescence," *Applied Physics Letters*, vol. 75, no. 1, 1999.

[84] X. Zhou, M. Pfeiffer, J. S. Huang, J. Blochwitz-Nimoth, D. S. Qin, A. Werner, J. Drechsel, B. Maennig, and K. Leo, "Low-voltage inverted transparent vacuum deposited organic light-emitting diodes using electrical doping," *Applied Physics Letters*, vol. 81, no. 5, 2002.

[85] G. He, O. Schneider, D. Qin, X. Zhou, M. Pfeiffer, and K. Leo, "Very high-efficiency and low voltage phosphorescent organic light-emitting diodes based on a p-i-n junction," *Journal of Applied Physics*, vol. 95, no. 10, 2004.

[86] R. Meerheim, S. Scholz, S. Olthof, G. Schwartz, S. Reineke, K. Walzer, and K. Leo, "Influence of charge balance and exciton distribution on efficiency and lifetime of phosphorescent organic light-emitting devices," *Journal of Applied Physics*, vol. 104, no. 1, 2008.

[87] S. Chen and H.-S. Kwok, "Full color organic electroluminescent display with shared blue light-emitting layer for reducing one fine metal shadow mask," *Organic Electronics*, vol. 13, no. 1, pp. 31–35, 2012.

[88] M. Kashiwabara, K. Hanawa, R. Asaki, I. Kobori, R. Matsuura, H. Yamada, T. Yamamoto, A. Ozawa, Y. Sato, S. Terada, J. Yamada, T. Sasaoka, S. Tamura, and

T. Urabe, "29.5l: Late-news paper: Advanced am-oled display based on white emitter with microcavity structure," *SID Symposium Digest of Technical Papers*, vol. 35, no. 1, pp. 1017–1019, 2004.

[89] A. P. Ghosh, W. E. Howard, I. Sokolik, R. Zhang, V. M. Shershukov, A. V. Tolmachev, N. I. Voronkina, and V. A. Dudkin, "40.3l: Late-news paper: Color changing materials for oled microdisplays," *SID Symposium Digest of Technical Papers*, vol. 31, no. 1, pp. 983–985, 2000.

[90] S. Reineke, F. Lindner, G. Schwartz, N. Seidler, K. Walzer, B. Lüssem, and K. Leo, "White organic light-emitting diodes with fluorescent tube efficiency," *Nature*, vol. 459, no. 7244, p. 234–238, 2009.

[91] S. Reineke, M. Thomschke, B. Lüssem, and K. Leo, "White organic light-emitting diodes: Status and perspective," *Rev. Mod. Phys.*, vol. 85, pp. 1245–1293, 2013.

[92] M. C. Gather, R. Alle, H. Becker, and K. Meerholz, "On the origin of the color shift in white-emitting OLEDs," *Advanced Materials*, vol. 19, no. 24, p. 4460â"4465, 2007.

[93] S. Liu, R. Wu, J. Huang, and J. Yu, "Color-tunable and high-efficiency organic light-emitting diode by adjusting exciton bilateral migration zone," *Appl. Phys. Lett.*, vol. 103, no. 13, p. 133307, 2013.

[94] S. Chen, Q. Wu, M. Kong, X. Zhao, Z. Yu, P. Jia, and W. Huang, "On the origin of the shift in color in white organic light-emitting diodes," *Journal of Materials Chemistry C*, vol. 1, no. 22, p. 3508, 2013.

[95] Z. Shen, "Three-color, tunable, organic light-emitting devices," *Science*, vol. 276, no. 5321, p. 2009â"2011, 1997.

[96] G. Parthasarathy, G. Gu, and S. R. Forrest, "A full-color transparent metal-free stacked organic light emitting device with simplified pixel biasing," *Advanced Materials*, vol. 11, no. 11, pp. 907–910, 1999.

[97] C. W. Joo, J. Moon, J.-H. Han, J. W. Huh, J. Lee, N. S. Cho, J. Hwang, H. Y. Chu, and J.-I. Lee, "Color temperature tunable white organic light-emitting diodes," *Organic Electronics*, vol. 15, no. 1, pp. 189–195, 2014.

[98] M. Fröbel, T. Schwab, M. Kliem, S. Hofmann, K. Leo, and M. C. Gather, "Get it white: color-tunable AC/DC OLEDs," *Light Sci Appl*, vol. 4, no. 2, 2015.

[99] B. D'Andrade, V. Adamovich, R. Hewitt, M. Hack, and J. J. Brown, "Phosphorescent organic light-emitting devices for solid-state lighting," *SPIE proceedings*, 2005.

[100] Y. Jiang, J. Lian, S. Chen, and H.-S. Kwok, "Fabrication of color tunable organic light-emitting diodes by an alignment free mask patterning method," *Organic Electronics*, vol. 14, no. 8, pp. 2001–2006, 2013.

[101] M. S. Weaver, X. Xu, H. Pang, R. Ma, J. J. Brown, and M.-H. Lu, "Color tunable phosphorescent white OLED lighting panel," *SID Symposium Digest of Technical Papers*, vol. 45, no. 1, pp. 672–674, 2014.

[102] A. Acharya, M. Packirisamy, and R. Izquierdo, "Oled hybrid integrated polymer microfluidic biosensing for point of care testing," *Micromachines*, vol. 6, no. 9, p. 1406, 2015.

[103] G. Williams, C. Backhouse, and H. Aziz, "Integration of organic light emitting diodes and organic photodetectors for lab-on-a-chip bio-detection systems," *Electronics*, vol. 3, no. 1, p. 43, 2014.

[104] M. Ramuz, L. Buergi, R. Stanley, and C. Winnewisser, "Coupling light from an organic light emitting diode (oled) into a single-mode waveguide: Toward monolithically integrated optical sensors," *Journal of Applied Physics*, vol. 105, no. 8, 2009.

[105] E. L. Ratcliff, P. A. Veneman, A. Simmonds, B. Zacher, D. Huebner, S. S. Saavedra, and N. R. Armstrong

[106] F. Lefevre, A. Chalifour, L. Yu, V. Chodavarapu, P. Juneau, and R. Izquierdo, "Algal fluorescence sensor integrated into a microfluidic chip for water pollutant detection," *Lab Chip*, vol. 12, no. 4, pp. 787–793, 2012.

[107] A. K. Bansal, S. Hou, O. Kulyk, E. M. Bowman, and I. D. W. Samuel, "Wearable organic optoelectronic sensors for medicine," *Advanced Materials*, vol. 27, no. 46, pp. 7638–7644, 2015.

[108] C. Wang, D. Hwang, Z. Yu, K. Takei, J. Park, T. Chen, B. Ma, and A. Javey, "User-interactive electronic skin for instantaneous pressure visualization," *Nat Mater*, vol. 12, no. 10, pp. 899–904, 2013. Letter.

[109] I. D. Samuel, J. Ferguson, and A. McNeill, *Organic Light-Emitting Diodes (OLEDs): Next-Generation Photodynamic Therapy of Skin Cancer*. Wiley-VCH Verlag GmbH Co. KGaA, 2013.

[110] S. Attili, A. Lesar, A. McNeill, M. Camacho-Lopez, H. Moseley, S. Ibbotson, I. Samuel, and J. Ferguson, "An open pilot study of ambulatory photodynamic therapy using a wearable low-irradiance organic light-emitting diode light source in the treatment of nonmelanoma skin cancer," *British Journal of Dermatology*, vol. 161, no. 1, pp. 170–173, 2009.

[111] C. M. Lochner, Y. Khan, A. Pierre, and A. C. Arias, "All-organic optoelectronic sensor for pulse oximetry," *Nat Commun*, vol. 5, 2014. Article.

[112] A. Steude, M. Jahnel, M. Thomschke, M. Schober, and M. C. Gather, "Controlling the behavior of single live cells with high density arrays of microscopic oleds," *Advanced Materials*, vol. 27, no. 46, pp. 7657–7661, 2015.

[113] A. Steude, E. C. Witts, G. B. Miles, and M. C. Gather, "Arrays of microscopic organic leds for high-resolution optogenetics," *Science Advances*, vol. 2, no. 5, 2016.

[114] Z. Kafafi, *Organic Electroluminescence*. Optical Science and Engineering, CRC Press, 2005.

[115] R. K. Kummamuru, L. Hu, L. Cook, M. Y. Efremov, E. A. Olson, and L. H. Allen, "A close proximity self-aligned shadow mask for sputter deposition onto a membrane or cavity," *Journal of Micromechanics and Microengineering*, vol. 18, no. 9, p. 095027, 2008.

[116] M. M. Ling, , and Z. Bao*, "Thin film deposition, patterning, and printing in organic thin film transistors," *Chemistry of Materials*, vol. 16, no. 23, pp. 4824–4840, 2004.

[117] G. Meda, "Support designs for reducing the sag of horizontaly supported sheets," *Technical Information Paper*, vol. TIP, no. 303, 2004.

[118] H. Sirringhaus, T. Kawase, R. H. Friend, T. Shimoda, M. Inbasekaran, W. Wu, and E. P. Woo, "High-resolution inkjet printing of all-polymer transistor circuits," *Science*, vol. 290, no. 5499, pp. 2123–2126, 2000.

[119] J. Chen, V. Leblanc, S. Kang, P. Benning, D. Schut, M. Baldo, M. Schmidt, and V. Bulovic, "High definition digital fabrication of active organic devices by molecular jet printing," *Advanced Functional Materials*, vol. 17, no. 15, pp. 2722–2727, 2007.

[120] M. Shtein, P. Peumans, J. B. Benziger, and S. R. Forrest, "Direct, mask-and solvent-free printing of molecular organic semiconductors," *Advanced Materials*, vol. 16, no. 18, pp. 1615–1620, 2004.

[121] G. J. McGraw and S. R. Forrest, "Vapor-phase microprinting of multicolor phosphorescent organic light emitting device arrays," *Advanced Materials*, vol. 25, no. 11, pp. 1583–1588, 2013.

[122] . Etienne Menard, . Matthew A. Meitl, . Yugang Sun, . Jang-Ung Park, . Daniel Jay-Lee Shir, . Yun-Suk Nam, . Seokwoo Jeon, , and . John A. Rogers*, "Micro- and nanopatterning techniques for organic electronic and optoelectronic systems," *Chemical Reviews*, vol. 107, no. 4, pp. 1117–1160, 2007.

[123] M. Makrygianni, S. Papazoglou, and I. Zergioti, *Direct Laser Printing for Organic Electronics*. John Wiley Sons, Inc., 1999.

[124] S. H. Ko and C. P. Grigoropoulos, *Unconventional, Laser Based OLED Material Direct Patterning and Transfer Methods*. InTech, 2011.

[125] D. Goto, M. Mohri, K. Morimoto, A. Mzhavia, and C. Adachi, "100 m-order patterning of organic semiconductor layers using a thermally converted precursor technique and its application to organic light emitting diodes," *Advanced Optical Materials*, vol. 2, no. 2, pp. 110–114, 2014.

[126] J. Huang, R. Xia, Y. Kim, X. Wang, J. Dane, O. Hofmann, A. Mosley, A. J. de Mello, J. C. de Mello, and D. D. C. Bradley, "Patterning of organic devices by interlayer lithography," *J. Mater. Chem.*, vol. 17, pp. 1043–1049, 2007.

[127] J.-K. Lee, H. H. Fong, A. A. Zakhidov, G. E. McCluskey, P. G. Taylor, M. Santiago-Berrios, H. D. Abruna, A. B. Holmes, G. G. Malliaras, and C. K. Ober, "Semiperfluoroalkyl polyfluorenes for orthogonal processing in fluorous solvents," *Macromolecules*, vol. 43, no. 3, pp. 1195–1198, 2010.

[128] H. H. Fong, J.-K. Lee, Y.-F. Lim, A. A. Zakhidov, W. W. H. Wong, A. B. Holmes, C. K. Ober, and G. G. Malliaras, "Orthogonal processing and patterning enabled by highly fluorinated light-emitting polymers," *Advanced Materials*, vol. 23, no. 6, pp. 735–739, 2011.

[129] A. A. Zakhidov, J.-K. Lee, J. A. DeFranco, H. H. Fong, P. G. Taylor, M. Chatzichristidi, C. K. Ober, and G. G. Malliaras, "Orthogonal processing: A new strategy for organic electronics," *Chem. Sci.*, vol. 2, pp. 1178–1182, 2011.

[130] P. E. Malinowski, A. Nakamura, D. Janssen, Y. Kamochi, I. Koyama, Y. Iwai, A. Stefaniuk, E. Wilenska, C. S. Redondo, D. Cheyns, S. Steudel, and P. Heremans, "Pho-

tolithographic patterning of organic photodetectors with a non-fluorinated photoresist system," *Organic Electronics*, vol. 15, no. 10, pp. 2355 – 2359, 2014.

[131] P. E. Malinowski, T. Ke, A. Nakamura, P. Vicca, M. Wuyts, D. Gu, S. Steudel, D. Janssen, Y. Kamochi, I. Koyama, Y. Iwai, and P. Heremans, "74-3: Multicolor 1250 ppi oled arrays patterened by photolithography," *SID Symposium Digest of Technical Papers*, vol. 47, no. 1, pp. 1009–1012, 2016.

[132] H. S. Hwang, A. A. Zakhidov, J.-K. Lee, X. Andre, J. A. DeFranco, H. H. Fong, A. B. Holmes, G. G. Malliaras, and C. K. Ober, "Dry photolithographic patterning process for organic electronic devices using supercritical carbon dioxide as a solvent," *J. Mater. Chem.*, vol. 18, pp. 3087–3090, 2008.

[133] M. E. Bahlke, H. A. Mendoza, D. T. Ashall, A. S. Yin, and M. A. Baldo, "Dry lithography of large-area, thin-film organic semiconductors using frozen co2 resists," *Advanced Materials*, vol. 24, no. 46, pp. 6136–6140, 2012.

[134] C. D. Müller, A. Falcou, N. Reckefuss, M. Rojahn, V. Wiederhirn, P. Rudati, H. Frohne, O. Nuyken, H. Becker, and K. Meerholz, "Multi-colour organic light-emitting displays by solution processing," *Nature*, vol. 421, no. 6925, pp. 829–833, 2003.

[135] M. C. Gather, A. Koehnen, A. Falcou, H. Becker, and K. Meerholz, "Solution-processed full-color polymer organic light-emitting diode displays fabricated by direct photolithography," *Advanced Functional Materials*, vol. 17, no. 2, pp. 191–200, 2007.

[136] M. C. Gather, N. M. Kronenberg, and K. Meerholz, "Monolithic integration of multi-color organic leds by grayscale lithography," *Advanced Materials*, vol. 22, no. 41, pp. 4634–4638, 2010.

[137] X. Deng and K. Y. Wong, "Cross-linked conjugated polymers for achieving patterned three-color and blue polymer light-emitting diodes with multi-layer structures," *Macromolecular Rapid Communications*, vol. 30, no. 18, pp. 1570–1576, 2009.

[138] M. P. Aldred, A. E. Contoret, S. R. Farrar, S. M. Kelly, D. Mathieson, M. O'Neill, W. C. Tsoi, and P. Vlachos, "A full-color electroluminescent device and patterned photoalignment using light-emitting liquid crystals," *Advanced Materials*, vol. 17, no. 11, pp. 1368–1372, 2005.

[139] P. F. Tian, P. E. Burrows, and S. R. Forrest, "Photolithographic patterning of vacuum-deposited organic light emitting devices," *Applied Physics Letters*, vol. 71, no. 22, 1997.

[140] B. Lamprecht, E. Kraker, G. Weirum, H. Ditlbacher, G. Jakopic, G. Leising, and J. R. Krenn, "Organic optoelectronic device fabrication using standard uv photolithography," *physica status solidi (RRL) – Rapid Research Letters*, vol. 2, no. 1, pp. 16–18, 2008.

[141] J.-F. Chang, M. C. Gwinner, M. Caironi, T. Sakanoue, and H. Sirringhaus, "Conjugated-polymer-based lateral heterostructures defined by high-resolution photolithography," *Advanced Functional Materials*, vol. 20, no. 17, pp. 2825–2832, 2010.

[142] J. A. DeFranco, B. S. Schmidt, M. Lipson, and G. G. Malliaras, "Photolithographic patterning of organic electronic materials," *Organic Electronics*, vol. 7, no. 1, pp. 22 – 28, 2006.

[143] W.-T. Tsai, "Environmental risk assessment of hydrofluoroethers HFEs," *Journal of Hazardous Materials*, vol. 119, no. 1-3, pp. 69 – 78, 2005.

[144] C. M. Hansen, *Hansen Solubility Parameters: A User's Handbook*. CRC Press, 2007.

[145] H. Kleemann, A. Zakhidov, M. Anderson, T. Menke, K. Leo, and B. Lüssem, "Direct structuring of c60 thin film transistors by photo-lithography under ambient conditions," *Organic Electronics*, vol. 13, no. 3, p. 506–513, 2012.

[146] A. A. Zakhidov, S. Reineke, B. Lüssem, and K. Leo, "Hydrofluoroethers as heat-transfer fluids for OLEDs: Operational range, stability, and efficiency improvement," *Organic Electronics*, vol. 13, no. 3, p. 356–360, 2012.

[147] F. Selzer, N. Weiß, D. Kneppe, L. Bormann, C. Sachse, N. Gaponik, A. Eychmüller, K. Leo, and L. Müller-Meskamp, "A spray-coating process for highly conductive silver nanowire networks as the transparent top-electrode for small molecule organic photovoltaics," *Nanoscale*, 2015.

[148] T. Saragi, T. Fuhrmann-Lieker, and J. Salbeck, "Comparison of charge-carrier transport in thin films of spiro-linked compounds and their corresponding parent compounds," *Advanced Functional Materials*, vol. 16, no. 7, pp. 966–974, 2006.

[149] P. van Gemmern, V. van Elsbergen, S. P. Grabowski, H. Boerner, H.-P. Loebl, H. Becker, H. Kalisch, M. Heuken, and R. H. Jansen, "Influence of carrier conductivity and injection on efficiency and chromaticity in small-molecule white organic light-emitting diodes based on 4,4'-bis(2,2'-diphenylvinyl)-1,1'-spirobiphenyl and rubrene," *Journal of Applied Physics*, vol. 100, no. 12, 2006.

[150] R. Paetzold, A. Winnacker, D. Henseler, V. Cesari, and K. Heuser, "Permeation rate measurements by electrical analysis of calcium corrosion," *Review of Scientific Instruments*, vol. 74, no. 12, pp. 5147–5150, 2003.

[151] S. Schubert, H. Klumbies, L. Mueller-Meskamp, and K. Leo, "Electrical calcium test for moisture barrier evaluation for organic devices," *Review of Scientific Instruments*, vol. 82, no. 9, 2011.

[152] H. Klumbies, P. Schmidt, M. Haehnel, A. Singh, U. Schroeder, C. Richter, T. Mikolajick, C. Hossbach, M. Albert, J. W. Bartha, K. Leo, and L. Mueller-Meskamp, "Thickness dependent barrier performance of permeation barriers made from atomic layer deposited alumina for organic devices," *Organic Electronics*, vol. 17, pp. 138 – 143, 2015.

[153] S. Krotkus, F. Ventsch, D. Kasemann, A. A. Zakhidov, S. Hofmann, K. Leo, and M. C. Gather, "Photo-patterning of highly efficient state-of-the-art phosphorescent OLEDs using orthogonal hydrofluoroethers," *Advanced Optical Materials*, vol. 2, no. 11, pp. 1043–1048, 2014.

[154] H. Aziz, Z. Popovic, S. Xie, A.-M. Hor, N.-X. Hu, C. Tripp, and G. Xu, "Humidity-induced crystallization of tris (8-hydroxyquinoline) aluminum layers in organic light-emitting devices," *Applied Physics Letters*, vol. 72, no. 7, 1998.

[155] M. H. Kim, M. W. Song, S. T. Lee, H. D. Kim, J. S. Oh, and H. K. Chung, "11.3: Control of emission zone in a full color amoled with a blue common layer," *SID Symposium Digest of Technical Papers*, vol. 37, no. 1, pp. 135–138, 2006.

[156] H. Lee, J. Kwak, C.-M. Kang, Y.-Y. Lyu, K. Char, and C. Lee, "Trap-level-engineered common red layer for fabricating red, green, and blue subpixels of full-color organic light-emitting diode displays," *Opt. Express*, vol. 23, no. 9, pp. 11424–11435, 2015.

[157] K. Thangaraju, P. Amaladass, K. S. Bharathi, A. Mohanakrishnan, V. Narayanan, and J. Kumar, "Studies on influence of light on fluorescence of tris-(8-

hydroxyquinoline)aluminum thin films," *Applied Surface Science*, vol. 255, no. 11, pp. 5760 – 5763, 2009.

[158] M. Mizuno, T. Miyamoto, T. Ohnishi, and H. Hayashi, "Effects of tin doping and oxygen vacancies on the electronic states of indium oxide," *Japanese Journal of Applied Physics*, vol. 36, no. 6R, p. 3408, 1997.

[159] W. Song, S. So, D. Wang, Y. Qiu, and L. Cao, "Angle dependent x-ray photoemission study on uv-ozone treatments of indium tin oxide," *Applied Surface Science*, vol. 177, no. 3, pp. 158 – 164, 2001.

[160] S. Y. Kim, J.-L. Lee, K.-B. Kim, and Y.-H. Tak, "Effect of ultraviolet ozone treatment of indium tin oxide on electrical properties of organic light emitting diodes," *Journal of Applied Physics*, vol. 95, no. 5, 2004.

[161] K. Sugiyama, H. Ishii, Y. Ouchi, and K. Seki, "Dependence of indium–tin–oxide work function on surface cleaning method as studied by ultraviolet and x-ray photoemission spectroscopies," *Journal of Applied Physics*, vol. 87, no. 1, 2000.

[162] B. Low, F. Zhu, K. Zhang, and S. Chua, "Improvement of hole injection in phenyl-substituted electroluminescent devices by reduction of oxygen deficiency near the indium tin oxide surface," *Applied Physics Letters*, vol. 80, no. 24, 2002.

[163] S. Krotkus, F. Nehm, R. Janneck, S. Kalkura, A. Zakhidov, M. Schober, O. Hild, D. Kasemann, S. Hofmann, K. Leo, and S. Reineke, "Influence of bilayer resist processing on p-i-n oleds: towards multicolor photolithographic structuring of organic displays," *Proceedings of the SPIE 9360, Organic Photonic Materials and Devices XVII*, vol. pp93600W, 2015.

[164] F. J. Duarte, L. S. Liao, and K. M. Vaeth, "Coherence characteristics of electrically excited tandem organic light-emitting diodes," *Opt. Lett.*, vol. 30, no. 22, pp. 3072–3074, 2005.

[165] G. Xie, M. Chen, M. Mazilu, S. Zhang, A. Bansal, K. Dholakia, and I. D. W. Samuel, "Measuring and structuring the spatial coherence length of organic light-emitting diodes," *Laser Photonics Reviews*, pp. n/a–n/a, 2015.

[166] M. Samiullah, D. Moghe, U. Scherf, and S. Guha, "Diffusion length of triplet excitons in organic semiconductors," *Phys. Rev. B*, vol. 82, p. 205211, 2010.

[167] O. V. Mikhnenko, R. Ruiter, P. W. M. Blom, and M. A. Loi, "Direct measurement of the triplet exciton diffusion length in organic semiconductors," *Phys. Rev. Lett.*, vol. 108, p. 137401, 2012.

[168] C. Murawski, K. Leo, and M. C. Gather, "Efficiency roll-off in organic light-emitting diodes," *Advanced Materials*, vol. 25, no. 47, pp. 6801–6827, 2013.

[169] A. Turak, "Interfacial degradation in organic optoelectronics," *RSC Advances*, vol. 3, no. 18, pp. 6188–6225, 2013.

[170] H. Yamamoto, J. Brooks, M. S. Weaver, J. J. Brown, T. Murakami, and H. Murata, "Improved initial drop in operational lifetime of blue phosphorescent organic light emitting device fabricated under ultra high vacuum condition," *Appl. Phys. Lett.*, vol. 99, no. 3, p. 033301, 2011.

[171] K. Norrman, N. Larsen, and F. Krebs, "Lifetimes of organic photovoltaics: Combining chemical and physical characterisation techniques to study degradation mechanisms," *Solar Energy Materials and Solar Cells*, vol. 90, no. 17, p. 2793–2814, 2006.

[172] M. Hermenau, M. Riede, K. Leo, S. A. Gevorgyan, F. C. Krebs, and K. Norrman, "Water and oxygen induced degradation of small molecule organic solar cells," *Solar Energy Materials and Solar Cells*, vol. 95, no. 5, p. 1268–1277, 2011.

[173] M.-H. Ho, Y.-S. Wu, S.-W. Wen, M.-T. Lee, T.-M. Chen, C. H. Chen, K.-C. Kwok, S.-K. So, K.-T. Yeung, Y.-K. Cheng, and Z.-Q. Gao, "Highly efficient deep blue organic electroluminescent device based on 1-methyl-9,10-di(1-naphthyl)anthracene," *Applied Physics Letters*, vol. 89, no. 25, 2006.

[174] Y. Kuwabara, H. Ogawa, H. Inada, N. Noma, and Y. Shirota, "Thermally stable multilared organic electroluminescent devices using novel starburst molecules, 4,4',4"-tri(n-carbazolyl)triphenylamine (tcta) and 4,4',4"-tris(3-methylphenylphenylamino)triphenylamine (m-mtdata), as hole-transport materials," *Advanced Materials*, vol. 6, no. 9, pp. 677–679, 1994.

[175] Y. Li, M. Fung, Z. Xie, S.-T. Lee, L.-S. Hung, and J. Shi, "An efficient pure blue organic light-emitting device with low driving voltages," *Advanced Materials*, vol. 14, no. 18, pp. 1317–1321, 2002.

[176] P. Kathirgamanathan, S. Surendrakumar, R. R. Vanga, S. Ravichandran, J. Antipan-Lara, S. Ganeshamurugan, M. Kumaraverl, G. Paramaswara, and V. Arkley,

"Arylvinylene phenanthroline derivatives for electron transport in blue organic light emitting diodes," *Organic Electronics*, vol. 12, no. 4, pp. 666 – 676, 2011.

[177] J. Kido and T. Matsumoto, "Bright organic electroluminescent devices having a metal-doped electron-injecting layer," *Applied Physics Letters*, vol. 73, no. 20, 1998.

[178] G. Parthasarathy, C. Shen, A. Kahn, and S. R. Forrest, "Lithium doping of semi-conducting organic charge transport materials," *Journal of Applied Physics*, vol. 89, no. 9, 2001.

[179] T. Menke, D. Ray, J. Meiss, K. Leo, and M. Riede, "In-situ conductivity and seebeck measurements of highly efficient n-dopants in fullerene c_60," *Applied Physics Letters*, vol. 100, no. 9, 2012.

[180] F. A. Cotton, N. E. Gruhn, J. Gu, P. Huang, D. L. Lichtenberger, C. A. Murillo, L. O. Van Dorn, and C. C. Wilkinson, "Closed-shell molecules that ionize more readily than cesium," *Science*, vol. 298, no. 5600, pp. 1971–1974, 2002.

[181] F. A. Cotton, J. P. Donahue, D. L. Lichtenberger, C. A. Murillo, , and D. Villa-gran, "Expeditious access to the most easily ionized closed-shell molecule, $w_2(hpp)_4$," *Journal of the American Chemical Society*, vol. 127, no. 31, pp. 10808–10809, 2005. PMID: 16076168.

[182] M. A. Baldo, R. J. Holmes, and S. R. Forrest, "Prospects for electrically pumped organic lasers," *Phys. Rev. B*, vol. 66, p. 035321, 2002.

[183] Y. Setoguchi and C. Adachi, "Suppression of roll-off characteristics of electrolumi-nescence at high current densities in organic light emitting diodes by introducing reduced carrier injection barriers," *Journal of Applied Physics*, vol. 108, no. 6, 2010.

[184] I. A. Howard, J. M. Hodgkiss, X. Zhang, K. R. Kirov, H. A. Bronstein, C. K. Williams, R. H. Friend, S. Westenhoff, and N. C. Greenham, "Charge recombination and exciton annihilation reactions in conjugated polymer blends," *Journal of the American Chemical Society*, vol. 132, no. 1, pp. 328–335, 2010. PMID: 19961228.

[185] M.-K. Lee, M. Segal, Z. G. Soos, J. Shinar, and M. A. Baldo, "Yield of singlet excitons in organic light-emitting devices: A double modulation photoluminescence-detected magnetic resonance study," *Phys. Rev. Lett.*, vol. 94, p. 137403, 2005.

[186] K. Kao and W. Hwang, *Electrical transport in solids: with particular reference to organic semiconductors*. International series in the science of the solid state, Pergamon Press, 1981.

[187] P. E. Burrows, Z. Shen, V. Bulovic, D. M. McCarty, S. R. Forrest, J. A. Cronin, and M. E. Thompson, "Relationship between electroluminescence and current transport in organic heterojunction light-emitting devices," *Journal of Applied Physics*, vol. 79, no. 10, 1996.

[188] P. E. Burrows and S. R. Forrest, "Electroluminescence from trap limited current transport in vacuum deposited organic light emitting devices," *Applied Physics Letters*, vol. 64, no. 17, 1994.

[189] M. C. Gather, A. Köhnen, and K. Meerholz, "White organic light-emitting diodes," *Advanced Materials*, vol. 23, no. 2, pp. 233–248, 2011.

[190] A. M. Marconnet, M. A. Panzer, and K. E. Goodson, "Thermal conduction phenomena in carbon nanotubes and related nanostructured materials," *Rev. Mod. Phys.*, vol. 85, pp. 1295–1326, 2013.

[191] A. Fischer, T. Koprucki, K. Gärtner, M. L. Tietze, J. Brückner, B. Lüssem, K. Leo, A. Glitzky, and R. Scholz, "Feel the heat: Nonlinear electrothermal feedback in organic leds," *Advanced Functional Materials*, vol. 24, no. 22, pp. 3367–3374, 2014.

[192] I. H. Campbell, D. L. Smith, C. J. Neef, and J. P. Ferraris, "Charge transport in polymer light-emitting diodes at high current density," *Applied Physics Letters*, vol. 75, no. 6, 1999.

[193] D. Kasemann, R. Brückner, H. Fröb, and K. Leo, "Organic light-emitting diodes under high currents explored by transient electroluminescence on the nanosecond scale," *Phys. Rev. B*, vol. 84, p. 115208, 2011.

[194] H. Yamamoto, H. Kasajima, W. Yokoyama, H. Sasabe, and C. Adachi, "Extremely high density carrier injection and transport over 12000 A/cm^2 into organic thin films," *Applied Physics Letters*, vol. 86, no. 8, 2005.

[195] T. Matsushima and C. Adachi, "Observation of extremely high current densities on order of mA/cm^2 in copper phthalocyanine thin-film devices with submicron active areas," *Japanese Journal of Applied Physics*, vol. 46, no. 12L, p. L1179, 2007.

[196] C. I. Wilkinson, D. G. Lidzey, L. C. Palilis, R. B. Fletcher, S. J. Martin, X. H. Wang, and D. D. C. Bradley, "Enhanced performance of pulse driven small area polyfluorene light emitting diodes," *Applied Physics Letters*, vol. 79, no. 2, 2001.

[197] A. Fischer, P. Pahner, B. Lüssem, K. Leo, R. Scholz, T. Koprucki, K. Gärtner, and A. Glitzky, "Self-heating, bistability, and thermal switching in organic semiconductors," *Phys. Rev. Lett.*, vol. 110, p. 126601, 2013.

[198] E. Knapp and B. Ruhstaller, "Analysis of negative capacitance and self-heating in organic semiconductor devices," *Journal of Applied Physics*, vol. 117, no. 13, 2015.

Erklärung

Die vorliegende Dissertation wurde am Institut für Angewandte Physik an der Technischen Universität Dresden unter der wissenschaftlichen Betreuung von Prof. Dr. Sebastian Reineke angefertigt.

Hiermit versichere ich, dass ich die vorliegende Arbeit ohne unzulässige Hilfe Dritter und ohne Benutzung anderer als der angegebenen Hilfsmittel angefertigt habe. Die aus fremden Quellen direkt oder indirekt übernommenen Gedanken sind als solche kenntlich gemacht. Die Arbeit wurde bisher weder im Inland noch im Ausland in gleicher oder ähnlicher Form einer anderen Prüfungsbehörde vorgelegt.

Weiterhin versichere ich, dass bisher keine Promotionsverfahren stattgefunden haben.

Ich erkenne die Promotionsordnung der Fakultät Mathematik und Naturwissenschaften der Technischen Universität Dresden in der Fassung vom 23.02.2011 an.

Simonas Krotkus
Dresden, Oktober 2016